Evaluation of Cost-Effective Technologies for Highly Efficient Silicon-Based Solar Cells

THÈSE N° 4851 (2010)

PRÉSENTÉE LE 8 NOVEMBRE 2010
À LA FACULTÉ SCIENCES ET TECHNIQUES DE L'INGÉNIEUR
LABORATOIRE D'ÉLECTRONIQUE GÉNÉRALE 1
PROGRAMME DOCTORAL EN MICROSYSTÈMES ET MICROÉLECTRONIQUE

ÉCOLE POLYTECHNIQUE FÉDÉRALE DE LAUSANNE

POUR L'OBTENTION DU GRADE DE DOCTEUR ÈS SCIENCES

PAR

Luca GAUTERO

acceptée sur proposition du jury:

Prof. M. A. Ionescu, président du jury
Dr J.-M. Sallese, Dr J. Rentsch, directeurs de thèse
Prof. C. Ballif, rapporteur
Prof. G. Hahn, rapporteur
Prof. J. Schmidt, rapporteur

ÉCOLE POLYTECHNIQUE
FÉDÉRALE DE LAUSANNE

Suisse
2010

Table of Content

This dissertation shall start with some words from previous prominent colleagues. Indeed, the photovoltaic effect was first discovered as a chemical interaction.

"Dans le dernier Mémoire que j'ai eu l'honneur de présenter à l'Académie,

dans sa séance du lundi 29 juillet 1839, je me suis attaché à mettre en évidence, à l'aide des

courants électriques, les réactions chimiques qui ont lieu au contact de deux liquides, sous

l'influence de la lumière solaire. Le procédé que j'ai employé nécessitait l'emploi de deux

lames de platine, en relation avec les deux extrémités du fil d'un multiplicateur très

sensible et qui plongeaient chacune dans une des dissolutions superposées. Or comme ces

deux lames éprouvaient elles-mêmes les effets de la radiation, il a dû en résulter des

phénomènes composés, dont je vais m'occuper dans ce nouveau Mémoire. On sera à même

en suite de faire la part de chacun des effets produits."[1]

{Becquerel 1839}

Since then many things have changed, nowadays some photovoltaic devices are solid matter. Therefore, the next sentence is maybe more appropriate.

"Intorno a questo stromento si aggira principalmente la mia nuova

dissertazione elettrica".[2]

{Volta 1782}

---

[1] In the last memory I had the honor to present to the Academy, during its meeting on Monday, July 29, 1839, I sought to demonstrate, using electric currents, chemical reactions that occur at the contact of two liquids under the influence of sunlight. The method I used required the use of two platinum plates in conjunction with the two wire ends of a very sensitive multiplier and which were each plunged into overlapping solutions. Now as these two blades themselves experience the effects of radiation, it had to result in compounded phenomena, which I will look in this new essay. It will be my charge to separate each of the effects. (own translation)

[2] Around this instrument is principally my new electrical dissertation about (own translation)

Abstract:

The work underscores the feasibility of highly efficient silicon solar cell structures manufactured with high throughput machines. The main challenge consists in the implementation of more performant structures of intrinsic higher complexity. These structures are meant to be fabricated within similar constraints on time and on cost as for conventional devices of industrial manufacture. Achievements in this direction foster larger economical deployment of this kind of renewable energy.

The structure chosen for the implementation of "high efficiency" concepts requires an advanced machining of the silicon substrate. Etching techniques, dielectric coating preparations, and metal to semiconductor contact formation were evaluated for their integration in a complete silicon solar cell fabrication sequence. These sequences were later tested to gain knowledge regarding the effects of the aforementioned advanced processing.

Prototypes were created using the fabrication sequence. They were analysed to acquire a further understanding of the advanced processing influences. Statistical interpretation of the data obtained was used to support physical interpretation of the observed phenomena. For one particular implementation of a surface passivation (floating junction passivation) an attempt of modelling aiming to unveil its specific dynamics is reported.

A resulting solar cell concept compatible with high throughput equipment achieved a certified efficiency of 18% (V_{OC} = 635 mV, J_{SC} = 37.3 mA/cm², FF = 76 %) on substrate with a reduced thickness (120 μm). The resulting sequence prepares the back surface with a thermal oxidation for passivation purposes and with a laser technique to locally contact the bulk. The thickness is compatible with the intent of cost reduction through the decrease in material consumption. Other approaches performed on the same substrate achieved 17.1% efficiency (V_{OC} = 617 mV, J_{SC} = 36.1 mA/cm², FF = 75 %). In this case the passivation was achieved with deposited dielectric layers on the back surface.

Furthermore, the investigated dynamics of the floating junction passivation allows for better insight into its traits.

The proposed solution has an interesting ratio of efficiency versus costs. The general consequence is a higher market appeal of this particular renewable source on the energy market.

The study on the floating junction passivation allows a better exploitation of this particular implementation towards more performant silicon solar cells.

Keywords:

Solar cell, silicon, passivation, metal (Al) semiconductor (Si) contact, inline processing, PECVD, high efficiency, PERC, floating junction, inversion region

Sommario:

Il lavoro pone l'accento sulla fattibilità di strutture ad alta efficienza in cella solare al silicio realizzate con macchine ad alta capacità produttiva. La sfida principale consiste nell'implementazione di strutture più performanti aventi intrinsecamente una maggiore complessità. Queste strutture sono destinate ad essere fabbricate all'interno di vincoli di tempi e di costi analoghi ai dispositivi convenzionali di fattura industriale. Realizzazioni in questa direzione favorirebbero un maggiore utilizzo, economicamente valido, di questo tipo di energia rinnovabile.

La struttura scelta per l'attuazione di concetti "ad alta efficienza" richiede una lavorazione avanzata del substrato di silicio. Tecniche di corrosione, preparazioni di rivestimento dielettrico, e la formazione di contatti metallo-semiconduttore sono state valutate per la loro integrazione in una sequenza completa di fabbricazione di celle solari in silicio. Queste sequenze sono state in seguito sottoposte a dei test per acquisire conoscenze sugli effetti della suddetta lavorazione avanzata.

Dei prototipi sono stati creati utilizzando la sequenza di fabbricazione. Essi sono stati analizzati per acquisire una maggiore comprensione delle influenze delle lavorazioni avanzate. Sono state utilizzate interpretazioni statistiche dei dati ottenuti allo scopo di dimostrare l'interpretazione fisica dei fenomeni osservati. Per una particolare implementazione di una passivazione superficiale (passivazione a "floating junction") si presenta un tentativo di modellazione teso a svelarne la specifica dinamica.

Una risultante cella solare, compatibile con apparecchiature ad alta capacità produttiva, ha raggiunto un'efficienza certificata del 18% (V_{OC} = 635 mV, J_{SC} = 37.3 mA/cm^2, *FF* = 76 %) su un substrato di spessore ridotto (120 micron). La sequenza risultante prepara la superficie posteriore con un'ossidazione termica con finalità di passivazione e con una tecnica laser per creare un contatto locale con il volume della cella. Lo spessore è compatibile con l'intento di riduzione dei costi attraverso la diminuzione del consumo di materiale. Altri approcci eseguiti sullo stesso substrato hanno raggiunto il 17,2% di efficienza (V_{OC} = 617 mV, J_{SC} = 36.1 mA/cm^2, *FF* = 75 %). In questo caso la passivazione è stata raggiunta tramite il deposito di strati dielettrici sulla superficie posteriore.

Inoltre, l'indagine sulla dinamica della passivazione a "floating junction" permette una comprensione migliore delle sue caratteristiche.

La soluzione proposta ha un rapporto di efficienza/costo molto vantaggioso. La conseguenza generale è un'attrattiva più alta, per questa particolare fonte rinnovabile, sul mercato dell'energia.

Lo studio sulla passivazione a "floating junction" consente un migliore sfruttamento di questa particolare implementazione verso celle solari in silicio più performanti.

Keywords:

Cella solare, silicio, passivazione, contatto metallo (Al) semiconduttore (Si), processi inline, PECVD, alta efficienza, PERC, floating junction, regione invertita.

Chapter 1   Introduction

*Within this first chapter, social and environmental aspects of the present
time will be depicted, which will help define the reason for a thorough research
into the photovoltaic domain.*

1.1   Motivation

The aim of this thesis is to suggest and explore technical solutions to a need of society. This need is intrinsic to the development towards goals of common prosperity and wealth. This need is energy with the least negative consequences on society.

This work will explore methods for the fabrication of devices able to convert one of the main energy sources external to our planet into a useful form. This energy source is our closest star, the Sun. This nuclear reactor delivers its power in the form of electromagnetic radiations (the radiated spectrum contains visible and invisible parts). Hence, an optimal device will capture and convert light energy to a usable form of energy (mechanical, gravitational, thermal, and electric, to cite a few examples). For the design of the device, electric energy is chosen as output energy form. This form is, as a result, convenient for transmission and acceptable for storage. Another interesting property of electric energy is the accessible conversion into other forms of energy. Furthermore, unrelenting studies on the increase of conversion efficiency guarantee a reduction of unnecessary losses.

The device itself has an efficiency of conversion. The efficiency, together with the effort needed to produce the device, rates its quality. This device exploits the photovoltaic effect which was first discovered almost a century ago in liquid solution {Becquerel 1839}. Nowadays, this effect is synthesised from many different materials. This work will focus on the implementation based on silicon. Advantages of this choice are the vast documentation on its material properties, the market level availability of ultra high purification processes, the abundance of this element on the earth's crust, and the well developed knowledge on solid state physics. Furthermore, together with gallium arsenide and cadmium telluride, it is one of the semiconductors that best exploit the solar spectrum.

The device treated in this work is therefore a photovoltaic silicon solar cell.

Comparing the use of the Sun's radiation energy and the energy sources and conversion methods employed by our current society helps to underscore the importance of the former and the urgency to adopt it in the future. Below the arguments about the advantages of solar energy are reported. These are followed by few comments on the popular acceptance of these topics. Finally, a short paragraph on the role of photovoltaic in the use of solar energy is given. Furthermore, a few words will be spent on the function of this thesis in the photovoltaic domain.

1.1.1   Arguments against the dependency on fossil fuel

Society currently exploits other, presently convenient, ways of harnessing energy. More than 90 % of this energy is severely based on the resources present on our planet and almost 95 % of

the sources are fossil fuels {BP 2010}. Our planet with its 6E+24 kg of mass is by and large assumed to be an infinite source of raw materials. In fact, if the earth were a huge tank of oil, with the present consumption it would take more or less 224 Tera-year[3] before the last drop is burned or converted to a polymer.

Unfortunately, as of today, the statistics speak of about 1333,1 Gbarrel left and an annual consumption of 30 Gbarrel (which was, incredibly enough, stable from 2009 to 2010) {BP 2010}.

For example, if we want to see our children and grandchildren benefit from the versatility of polymers, energy has to be produced in some other way. Therefore, oil has to be preserved for functions which cannot be performed otherwise. The mentioned polymerization is one tangible example.

Aside from the love we nurture for our progeny and the interest we have in guaranteeing them an adequate lifestyle, other issues are emerging against fossil fuel consumption.

♦ *Avoid international disputes*

From the current prediction on the distribution of the fuel reserves, it is clear to see that very few countries, and even more precisely, very few people, have decision power on all the energy of the next 30 years.

In the past, this situation was somewhat reversed, with significant amounts of oil relatively close to the earth's surface in politically stable regimes. Even now, oil exploitation must more and more take the form of deeper and more dangerous expeditions under the surface of the sea, or other difficult and hostile environments, and in politically unstable or illiberal (to put it mildly) regimes. This will arguably increase global instability, cartellisation of the energy market, and further deleterious effects for the globally disadvantaged.

Providing an alternative source, which by nature is disseminated everywhere, would contribute to a fairer partition of the energy.

♦ *Avoid economic crises due to limited and localized energy sources*

Even when assuming our society will attain a peaceful behaviour, market conditions will rule the distribution until the last drop is available. This will create enormous differences in the years to come. Rich countries will have access to energy while other, less prosperous countries, will see their potential of production decreasing. Technical progress cannot be applied in the absence of energy. More likely than not, present economic differences will become even greater.

♦ *Avoid reduction of oxygen on Earth*

An interesting logical conclusion {Würfel 2005} can be introduced when arguing that primordial matter on earth, due to the high temperature present on the surface, was lacking in oxygen and carbon in their molecular form. Instead, they were to be found together in the form of carbon dioxide.

All the oxygen present in the atmosphere (≈ 20 % of it) is therefore a by-product of all plants photosynthesis. This took place through the ages and fixed carbon in the plants. It is possible to balance the photo-reaction and find out how much carbon has been produced and could be now available for consumption in form of fossil fuel. The calculation would result in several tens if not hundreds of years of availability. This ensures frighteningly small margin of time compared to the age of human society. Although even more frightening is that if we count on burning everything to ensure our lifestyle, then threats to the normal breathing of living creatures will emerge in the long run.

1.1.2   Reduce the creation of carbon dioxide

The Intergovernmental Panel on Climate Change (IPCC) stated in its fourth assessment report {Metz, Davidson et al. 2007} that the climate is changing and (cautiously) declared that the change is very likely due to human activities producing greenhouses gasses. Starting from these sentences, different scenarios were forecasted, where the activity of human society was

---

[3] 224 000 000 000 000 years

correlated to the increase in global temperature. There are several reasons why our society cannot afford the risk of climate change.

The strength of weather events, which can develop in this new climate, can reach extremes that almost all regions in the world are simply incapable or unable[4] of facing. The economies of entire countries could collapse trying to support victims and maintain a necessary capital infrastructure.

♦ *Avoid unsafe carbon dioxide storage*

One of the promising solutions is in the storage of the created greenhouse gasses. Although the solution definitively reduces the presence of carbon dioxide in the air, eventually it will resemble closely to the challenge of nuclear waste, which, to the knowledge of the author, has not yet found a definitive and safe answer.

If the storage is completely passive and no material is meant to re-enter the natural matter cycle, everlasting monitoring costs will be created. The carbon dioxide, though not ignitable, can be a severe risk if stored at high pressures. Severe leaks can be dangerous for any nearby population. Indeed, carbon dioxide is toxic at high concentrations. Similar accidents were investigated for medical interest {Pinchas, Yosef et al. 2004} and revealed to be harmful to humans if not immediately treated.

1.1.3   Increased public concern

Green is deemed to make people feel more at ease due to its similarity to the flora colour {Wiseman 2010}. This works marvellously for increasing "environmentally friendly" products sales. However, in between all of the hype on environmentally friendly products, media communications are reawakening an environmental sensibility in many.

Large dissemination started with documentaries which described with few words the presence and awkwardness of the severe human situation (i.e. {Gore 2006}). All have been targeted to the sensitisation of the public at large to the climatic/conservation challenge. In the press the argument was treated as well; a noteworthy example is a special issue on energy from National Geographic {McKibben, Nijhuis et al. 2009}, which exploits the strength of images to deliver quantitative messages on the energy production and use worldwide.

As a result the attention has now arisen. The efforts of the people involved in climate change counteraction are publicly presented the way they should be. One prominent example is the award of the Nobel Prize for peace to the IPCC and Al Gore in 2009.

1.1.4   Increase the PV market penetration

Photovoltaics, with their clean source and diffused availability, represent a true alternative to fossil fuel. Below the contributions of this PhD thesis in direction of the dissemination of solar energy conversion will be delineated.

As mentioned above, the quality of a photovoltaic product is evaluated from the cost of creation compared to the power delivered. This thesis suggests ways to reduce this ratio. This will foster the penetration of photovoltaic devices into this energetic market.

The physical challenge of solar cells is to increase their efficiency. However, silicon structures for light energy conversion have been investigated for several years. Indeed, eminent results in terms of efficiency have been achieved. Although these paved the way for their large scale realisation, they do not confront the necessity of applicability.

Therefore an additional constraint of applicability is added in this thesis. An important example is the implementation of a solution that decreases the raw material use.

By reducing the production cost and increasing the efficiency, and in turn the power generated by a cell, the ratio can be brought down to market acceptability.

---

[4] „incapable" indicates the availability of economic resources, however a significant scarcity of means/work power. Instead, „unable"indicates both capability and economic means are lacking.

1.2   Overview of the work

The first chapter describes realities that put pressure on the argument of the thesis. However, the generality of this chapter introduces the more scientifically addressed remaining parts of the book.

The second chapter introduces the reader to the physics that better describe the device on which the work is focussed. The arguments written are well known from the literature, though some liberties have been taken to make the explanation better corresponding to the point of view of the author.

The third chapter introduces the technological part of the work. A short initial section explains the present state of the art of industrial solar cells. The rest of the chapter describes experiments which were significant to understand the potential for the desired structural implementation.

The fourth chapter takes the reader to the most interesting result of any work on photovoltaic devices: the complete realisation of working solar devices. As many other complex systems, the effort spent in the preparation of the single parts is finally tested. The solar cells results are presented and furthermore analysed in depth. This guarantees an understanding of the principles and therefore a correct assessment of the latent issues.

The fifth chapter presents theoretical aspects which have been developed in the frame of this work to increase the comprehension of the phenomena that characterized several cells. The work is then validated when possible or compared to previous literature.

In the sixth and final chapter a short conclusion on the work and an outlook on future development is presented.

After these content rich chapters follows a series of appendices. The first, labelled "A", contains explanations of the characterisation tools used to develop the work. Afterwards follows "B", with a short explanation of the methods and plotting used for the description of experiment design and analysis used in this work. Furthermore an additional attempt to solve a problem posed in the work is proposed. In the appendix "C" a complete list of symbols used and a succinct description can help the reader to read more fluidly. Noteworthy for the reader is the appendix "D" which contains all the bibliographic entries that are found between accolades throughout the text.

Chapter 2   Existing and advanced applied solid state physics theories for photovoltaic

Starting from the description of electron energy levels in a material it is possible to understand how the photovoltaic effect can be exploited. The specific relations are listed in this chapter and will be recalled in the rest of the work. Sources are quoted, nevertheless similar treatments can be found in graduate books. Worth mentioning are a classical and a fully interactive free online textbook (respectively {Sze and Ng 2006; Van Zeghbroeck 2007}). Photovoltaic physics, however, underline particular arguments, especially related to illumination conditions. Textbooks with this emphasis are equally worth consulting {Green 1995; Green 1998; Würfel 2005}. The detailed understanding will translate in a simple circuit model which fits the experimentally observed behaviour of photovoltaic semiconductor devices.

2.1   Physics of semiconductors for solar cells

A rigorous approach to understand why semiconductor materials, and silicon foremost, are used for the production of solar cells starts from the description of the allowed electron wavefunctions in the material bulk.

Fig. 2:1 Calculated and measured diagrams of energy band structure for different materials. The top of the valence band is aligned to the zero energy level. All the area from the zero level upwards belong to the energy bandgap until an energy level is available (from {Rohlfing, Krüger et al. 1993}).

2.1.1   Wavefunctions

Wavefunctions assume discrete energy levels in the case of single atoms. In crystallised solids, however, the vicinity of atoms and the periodicity of this spatial configuration allow a continuum of configurations. Single energetic orbital levels split in energy bands. The

distribution of energy levels in these bands is given based on material properties and spatial crystal structure, or, in other words, by the interactions of charge and momentum of particles (electrons) with the periodic potential or nuclei. For example silicon, germanium, and gallium arsenide share the same crystal structure, namely diamond cubic crystal structure.

Nevertheless their band configurations differ (Fig. 2:1). The drawings represent all allowed combinations of momentum and energy in the crystal. Additionally, from this graph we can learn that forbidden energy levels exist. These regions are called band gaps, and, as it will be seen, are of great interest in semiconductor physics.

Similar band structures exist for every material with spatial periodicity, and the electrons present in the material are distributed on the allowed energy levels starting from the least energetic one, filling always first more convenient levels (for which less energy is required). It is helpful for the following discussion to define few names: the band of highest energy filled with electrons is defined as the conduction band (CB), the energetic band immediately before is called the valence band (VB).

This assigning procedure differentiates materials in three groups: metals, insulators and semiconductors. The first group has the electron of highest energy allotted in a band (Fig. 2:2); this allows the charged particle to move freely, furthermore there are plenty of energy levels for incoming electrons. This permits the good electrical conductivity typical of metals. In contrast, the second has its last electron on the lower edge of a band gap. The band gap is several eV wide. Hence, it is highly improbable for electrons to move inside the band already filled to the brim. Furthermore the material cannot accept further electrons. The third are semiconductors, their configuration is similar to that of the insulator, but their bandgap is smaller. Notwithstanding these insulating properties, at room temperature they can conduct electrical charges, although to a lesser degree in respect to metals. Following the assigning scheme it results that for the case of semiconductors and insulators, CB and VB surround the band gap (see Fig. 2:2).
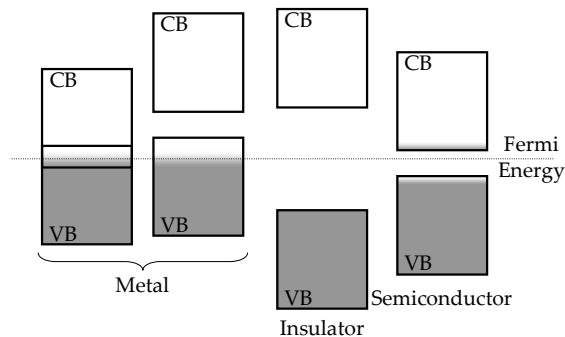
Fig. 2:2 Material differentiations on bands filling. The dotted energy level, indicated as Fermi energy, is the average energy of an electron added to the system.

An already mentioned example of the third set is silicon. This material is abundant on the earth's crust, and has assumed recently a big importance in the everyday life[5]. Since it is also the main character of this book, a little more attention to its band diagram (Fig. 2:1) is paid here below. Remarkable is that the maximum allowed state of the VB does not share the same momentum of the minimum allowed state of the CB. Silicon is consequently defined as indirect band gap semiconductor. As it will be seen, this has consequences in the absorption of photons. A typical example of a direct bandgap semiconductor is gallium arsenide, also displayed in (Fig. 2:1).

---

[5] "You can't see it, but it's everywhere you go." – Bridget Booher, journalist, on silicon.

2.1.2   Carrier Density

The assigning procedure at each energy level is described as proportional to the availability of states and the probability that this state will be occupied. By integrating this description it is possible to obtain the density of carriers present in the band of interest (Fig. 2:3).

$$N(E) = g_B(E) \cdot f(E)$$
$$n = \int_{E_B}^{E_{void}} N(E) dE$$

<div align="right">Eq. 2−1</div>

In this formula $N(E)$ indicates the density of occupied states, which is obtained by multiplying the density of states $g_B(E)$ and the probability distribution $f(E)$.

The calculation of the allowed states in a volume $g_B(E)$ ("density of states") is performed assuming a well shaped potential, limited by the size of the material L. In the expression of Eq. 2−2 a cube of size L is assumed and is then normalized to its volume (L^3).

$$g_B(E)\Big|_{E \geq E_B} = \frac{8\pi\sqrt{2}}{h^3}\left(m_{particle}*\right)^{\frac{3}{2}}\sqrt{E-E_B}$$
$$g_B(E)\Big|_{E < E_B} = 0$$

<div align="right">Eq. 2−2</div>

Where the energy level is related to the CB (VB) minimum (maximum) and indicated with E_B. Furthermore, $m_{particle}$ is the effective particle mass (m_e* for the case of CB and m_h* for the case of VB), containing information related to the material, extracted from the band diagrams (Fig. 2:1). This value accounts for the influence of a periodic potential of the band on an electron movement, therefore resulting as a mass modification. Furthermore, it corresponds closely to the curvature of the minimum (maximum) of the CB (VB).

The Pauli principle forbids the presence of more than one electron on one energy level. Abiding by this principle, electrons act as Fermions and make the interpretation of the assigning very similar to filling a bucket with powder. The probability distribution is mathematically expressed by a Fermi-Dirac function Eq. 2−3.

$$f(E) = \frac{1}{1+e^{\frac{E-E_F}{kT}}}$$

<div align="right">Eq. 2−3</div>

The E_F term represents the average energy necessary for adding an electron to the semiconductor under conditions of conservation of entropy. For semiconductors, as it is possible to see in Fig. 2:2, this value lies in between the CB and VB edges, named E_C and E_V respectively.

Albeit this being the best representation, it does not guarantee the analytical integration of Eq. 2−1, therefore the Boltzmann distribution is used (Boltzmann approximation). This distribution is obtained removing the unity at the numerator of the Fermi distribution function (see Eq. 2−3).

The formulation of the density of carriers in Eq. 2−1 is transformed and can therefore be integrated correctly in a closed form. The result is a product of a constant and a Boltzmann term. The first depends on the density of states in the band; the second depends on the distance between the Fermi energy and the band edge.

$$n(E_F) = N_C e^{-\frac{E_C-E_F}{kT}}$$

<div align="right">Eq. 2−4</div>

The calculation results in the density of electrons in the CB, however these are not the only electrons which can represent mobility, also on the highest energetic levels of the VB free states are available. Whilst it would be completely legitimate to calculate the electron density of the whole band, it is more convenient and elegant to introduce another particle, namely a hole, which considers the voids which move as consequence of displacing electrons.

Under these conditions, the hole density becomes of interest, the treatment is identical, however the Fermi distribution must be used by inverting the sign of energy (Eq. 2—5).

$$p(E_{\mathrm{F}}) = N_{\mathrm{V}} e^{-\frac{E_{\mathrm{F}} - E_{\mathrm{V}}}{kT}}$$

Eq. 2—5

♦ *Mass action law*

The product of electron and hole densities is a material property dependent on temperature. This product is called intrinsic carrier density. The definition of the intrinsic carrier density follows from the mass action law and gives therefore a value for thermal equilibrium.

$$n(E_{\mathrm{F}}) p(E_{\mathrm{F}}) = n_{\mathrm{i}}^2 = N_{\mathrm{V}} N_{\mathrm{C}} e^{\frac{-E_{\mathrm{g}}}{kT}}$$

Eq. 2—6

In Eq. 2—6 E_{g} represents the band gap and n_{i} indicates the intrinsic density of carriers.
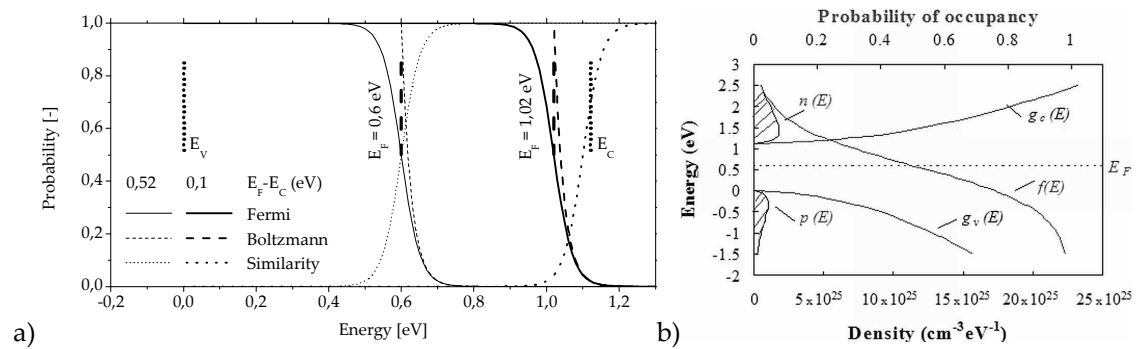
Fig. 2:3 a) Two configurations of the distribution, the first (E_{F} =0.6 eV) can safely be approximated by a Boltzmann function (Boltzmann approximation) while the second (E_{F} =1.02 eV) has a similarity[6] well below 1 at the CB edge E_{C}. b) Graphical representation of the carriers' calculation. (from {Van Zeghbroeck 2007}).

♦ *Doping*

Relation Eq. 2—6 is also valid when electrons or holes are inserted in the system, creating a change in $n(E_{\mathrm{F}})$ and $p(E_{\mathrm{F}})$. This is normally achieved by introducing impurities substitutionally in the lattice. Impurities which give an electron are called donors (i.e. arsenic, phosphorus). On the other hand, the ones taking an electron (creating therefore a hole) are called acceptors (i.e. gallium, boron, aluminium).

Since the medium (silicon) has a high permittivity, the binding energy (energy to vacuum) of either the donor or the acceptor particle is below 0.1 eV. Furthermore convenient donors and acceptors have their energy state in the vicinity of a band. Applications require that thermal energy alone at room temperature frees the particle from its atom and make it jump to the closer band where states are available. The doping matter is hence thermally ionized at room temperature.

When introducing impurities in the melt of the semiconductor, already a low ratio of donors (or acceptors) to semiconductor weight move the particle density in a sensible way. The low intrinsic population of silicon, in the order of 1E+9 to 1E+10, can be easily overcome. The presence and thermal ionisation of donors (acceptors) creates a large availability of electrons (holes) and the material is said to be n-type (p-type). Coexistence of donors and acceptors is possible, Eq. 2—6 is valid and the material is called compensated. The type is determined by the most abundant doping impurity. This kind of material is becoming of interest in photovoltaic for its promisingly low production costs. However, it will not be the subject of this work.

---

[6] The similarity is calculated as the ratio of the fermi function over the Boltzmann function

When the material has only one doping type and the energy level of the impurity is shallow, it is common practice to assume the density of carriers to be equal to the density of the atoms introduced. The doping indeed introduces mobile charges in the material. Two phenomena permit this. The first is thermal ionization already occurring at room temperature for shallow impurities. The second is the difference between the intrinsic and the introduced dopant density. This spans over several orders of magnitude (typical substrates present density of impurities which ranges from 1E+15 to 1e+17 cm^{-3}). Common nomenclature refers to the carrier with the higher density as majority carriers and the other as minority carrier.

♦ *Intrinsic level*

Another noteworthy value is the intrinsic level; this is the energy level of E_F when the density of $n(E_F)$ and $p(E_F)$ are equal.

$$E_F \quad = \quad E_i \quad = \quad \frac{E_V + E_C}{2} + \frac{kT}{2}\ln\left(\frac{N_V}{N_C}\right) \qquad \text{Eq. 2−7}$$

This energy is of interest for reference of potentials, since it lies in the middle of the bandgap.

♦ *Non equilibrium conditions*

Sources of energy, other than thermal, impinging on the bulk of the semiconductor (i.e. photons or external bias), excite electrons for a jump of level. With a sufficient energy, electrons leave the VB and reach the CB. An electron-hole pair (EHP) is injected. Their density, indicated as Δn, does not obey the mass action law anymore (Eq. 2−6). One way to mathematically represent them is to assign two different average energy levels to the two particle populations. These are called quasi Fermi levels. The injection of carriers, occurring due to the external sources of energy, splits the Fermi level in two. The quasi Fermi levels are indicated with E_{Fn} and E_{Fp} for electrons and holes respectively.

By introducing these energetic quantities new relations can be introduced

$$p\left(E_{Fp}\right) \quad = \quad N_V e^{-\frac{E_{Fp}-E_V}{kT}}$$

$$n\left(E_{Fn}\right) \quad = \quad N_C e^{-\frac{E_C-E_{Fn}}{kT}} \qquad \text{Eq. 2−8}$$

$$n\left(E_{Fn}\right)p\left(E_{Fp}\right) \quad = \quad n_i^2 e^{\frac{-qV_{oc}}{kT}} \quad = \quad N_V N_C e^{\frac{-E_G}{kT}} e^{\frac{-qV_{oc}}{kT}}$$

where V_{oc} is the absolute difference between the two Quasi-Fermi levels. Two regimes of injection are identified: the measure for their distinction is the doping of the excited region. Injections higher than the doping are named high-level injections (hli) while below this threshold are indicated as low-level injection (lli).

$$\Delta n \quad = \quad \sqrt{n_i^2\left(e^{\frac{qV_{oc}}{kT}}-1\right)+\left(\frac{p_0+n_0}{2}\right)^2} - \frac{p_0+n_0}{2}$$

$$\Delta n_{lli} \quad = \quad \frac{n_i^2}{N_{dop}}\left(e^{\frac{qV_{oc}}{kT}}-1\right) \qquad \text{Eq. 2−9}$$

In case of p-type, an exact relation and an approximation for lli was proposed {Aberle 1991; Dauwe 2004} to relate the amount of injected carriers and the splitting of the quasi Fermi levels (V_{oc}). Mutatis mutandis also the relation for n-type material can be obtained.

2.2 Out of equilibrium: generation and recombination

2.2.1 Generation and absorption

In case of illumination, impinging photons contribute to the upward energetic displacement of electrons in, as well as amongst, the bands. Photons are absorbed depending on their energy and the energetic distance of unoccupied and occupied states in the bands. Photovoltaic devices base their principle on the inter-band shift rather than the intra-band one. Indeed, in the first case an electron absorbs the photon energy and, if momentum can be conserved, reaches the CB, and leaves a hole in the VB. This procedure is called electron-hole pair (EHP) generation and is characterised by its rate G_L in s^{-1} cm^{-3}. This term, integrated over the injection volume and multiplied by the charge quantity q results in a current density. Therefore, the G_L term can be adopted to evaluate the total photo-generated current potential $J_{L\,total}$ of a wafer of thickness W. However, the direction of the complete current in the wafer is given by external phenomena (electric field and diffusion, see below 2.3.2)

$$J_{L\,total} = q\int_0^W G_L \mathrm{d}x$$

Eq. 2−10

Since photons carry a very small momentum, the first inter-band energetic distance in silicon that can be covered by photon energy alone corresponds to 3.4 eV. The corresponding wavelength is of low interest for a solar cell aimed to exploit the maximum of the terrestrial irradiation (see Fig. 2:4). Less probable, but valuable for the photovoltaic use, is the indirect absorption. In this case a third particle assists the capturing of photon energy by giving or accepting the necessary momentum. By this process all energetic distances above 1.12 eV can be accepted. The additional particles needed are phonons, they represent lattice vibration modes. Their presence is strictly related to temperature.
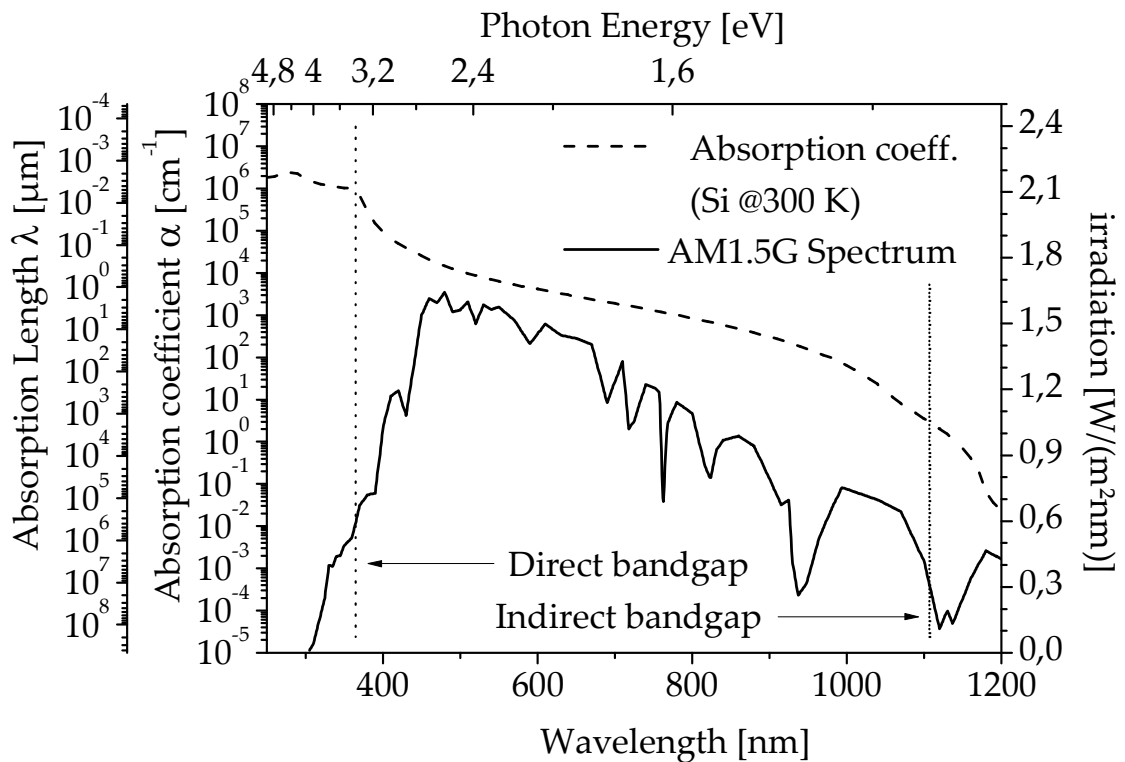

Fig. 2:4 Silicon spectral absorption and standardised terrestrial solar irradiation. The indirect and direct energetic distance of silicon is also indicated (from {Clugston and Basore 1997})

The absorption at a certain wavelength is proportional to its probability of capture in the material. Its description relates the decay of intensity to a single parameter known as absorption coefficient α_c. Another way to understand the concept, closer to the reality, is detailing the thickness of material needed before absorption reduces the intensity of the incoming wavelength to approximatively 34%. The term is known as absorption length λ_a (see Fig. 2:4). The term highlights the need of thick solar cells for the complete absorption of light in crystalline silicon. Since using centimetre thick substrates becomes cumbersome and expensive, other concepts are implemented for the best exploitation of the solar spectrum.

♦ *Concepts of light trapping*

As previously mentioned, the thickness of the solar cell cannot be extended endlessy. Instead, considerations regarding cost tend to economize the use of this material. Photons have to find a long optical path in order to be absorbed, and luckily these paths do not need to be perpendicular to the substrate depth.

As it was possible to see in the graph (see Fig. 2:4) a part of the solar spectrum (long wavelengths, infra-red part) travels long distances, up to several hundreds of micrometres, before being absorbed. To overcome this issue, the path of perpendicularly incoming long wavelength photons is slanted upon entering the silicon. This is accomplished by tilted facets on the silicon surface.

However, a typical silicon substrate for photovoltaic has a thickness around 200 μm. The slanting procedure ensures a slightly higher effective normal thickness, though long wavelength photons will be able to hit the back surface of the cell and recoil. There a structure must be ready for an internal reflection and possibly a scattering of the incoming ray.

The need of the scattering comes from the validity of the reversibility principle on optical paths. This states that any valid optical path can be performed by a ray in both directions. In case a ray reaching the back surface is mirror reflected, then the ray has a probability to find its way back to its source equal to the incoming probability (net of the absorption probability).

Several works have developed platforms for the evaluation of the optical properties of the solar cell. A comprehensive study has been developed by Kray in his dissertation. In Fig. 2:5 a representative diagram of the ray slanting is proposed for pyramidal texture with an ARC made of silicon oxide. In this figure the case of a perpendicular ray is followed along with its partition at interfaces. The normal ray enters the silicon and splits in two different angles (A and B in Fig. 2:5). The rays travel straight through the bulk and reach the back surface. The back surface is in this case assumed to be flat, although a small surface roughness can contribute to a light scattering[7]. To evaluate the scattering component the Phong model has been chosen. This distributes the intensity of the incoming light on a packet of angles close to the exact Fresnel law reflection angle. The intensity distribution over the rays depends on a parameter (the power exponent W of the cosine, see Fig. 2:5) and on the deviation α from the angle of the totally reflected ray. Again the description is done for the case A and B. One additional information important for light trapping schemes is the concept of the escape cone. This solid angle considers all the ray directions which can escape the silicon bulk.

This model helps to evaluate how close the surface is to a Lambertian plane. Another model, closer to a direct application, which does not make use of angles, is the so called Basore model. This model specifies the probability of first and subsequent bounces at both surfaces; in this way it is possible to insert all details of how the reflection takes place in four parameters. This model is implemented in the PC1D simulator (see 2.4.3).

Considerations from the studies detail a flat surface with lambertian property as a good back surface to attain the highest internal reflection and in turn the best light trapping.

---

[7] This phenomenon does not appear on the front side since the facets present a high flatness due to the crystallographic orientation.
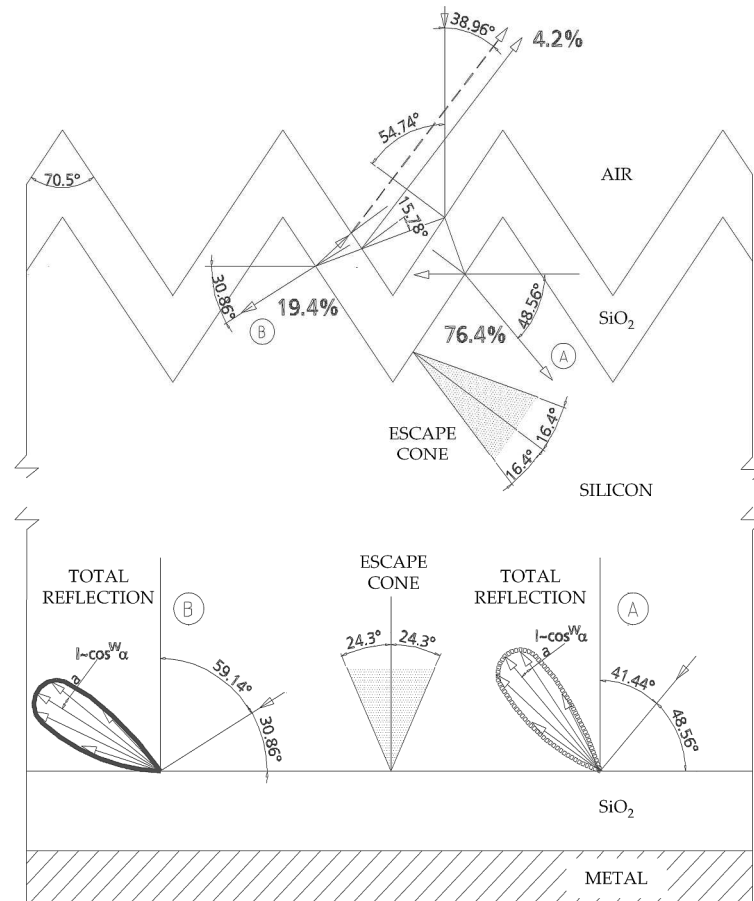
Fig. 2:5 Example of light propagation in a structured solar cell (out of scale). The silicon bulk is here presented with an oxidised surface. With a specific thickness, SiO₂ can act as a good antireflection coating. The angles of deviation have been calculated for a wavelength of 1100 nm (From {Kray 2004})

♦ *Absorption losses*

As previously mentioned, absorption is not entirely devoted to the shift of electrons from one band to an upper one. The photon energy can also be used to shift electrons within the same band. This phenomenon, known under the name of free carrier absorption (FCA) {Pankove 1975}, is foe to the photovoltaic effect and is fostered by an increased amount of free charges in almost empty bands.

2.2.2 Recombination in the bulk

Thermal equilibrium (Eq. 2—6) expresses a situation of balance between generation and recombination. Indeed, in presence of injection, the speed of recombination mechanisms is put to the test[8].

$$G_0 \quad = \quad R_0 \quad = \quad \frac{n_{p0}}{\tau_n} \quad = \quad \frac{p_{n0}}{\tau_p} \qquad \text{Eq. 2—11}$$

Absence of injection[9] results in a value of recombination R_0, completely balanced by the generation G_0 at any time.

Out of equilibrium, generation exceeds the equilibrium value G_0. As an effort to re-establish equilibrium conditions, recombination rises above the equilibrium value. This increase is

---

[8] This last sentence suggests a good way to verify the existence and quantify recombination that will be pursued in the Appendix (A.f).

[9] or extraction

denoted net recombination $U(\Delta n)$. This term expresses the dependence on injection (see Eq. 2—12).

The energy of an absorbed photon for an interband jump is stored temporarily in a travelling EHP if an interband charge jump happened. The EHP has to be gathered (we will see later how) before any recombination occurs. Hence, another foe of photovoltaic conversion of harvested light is recombination of light-injected EHP. For the study of this phenomenon only the net recombination is of interest.

$$ R \;=\; R_0 + U(\Delta n) \;=\; \frac{n_{p0}}{\tau_n} + \frac{\Delta n}{\tau_{net}} \qquad\qquad \text{Eq. 2—12} $$

Recombination theory of direct and indirect semiconductor differs. The first is strongly influenced by the doping density. On the other hand, the second depends on the availability of assisted transitions. For the matter of this work only the latter will be treated.

Below is a short list of the equivalent mathematical models of net recombinations. The mathematical models will report clearly the dependence of each net recombination on the carrier densities. As will be observed later, recombination mechanisms have useful fingerprints which help their identification.

♦ *Auger*

Auger recombination is a multiple particles recombination. In addition to an EHP, this mechanism transfers the energy of the coupling pair to excite another particle to a higher energetic level. This particle then transfers its energy to the lattice in forms of phonon. Its major limitation is the abundance of free carriers, for this reason its influence on total recombination is prominent with higher doping or higher injection.

$$ \begin{aligned} U_{Aug} &= C_n\left(n^2 p - n_0^{\,2} p_0\right) + C_p\left(n p^2 - n_0 p_0^{\,2}\right) \\ R_{Aug} &= C_n\left(n^2 p\right) + C_p\left(n p^2\right) \;=\; n p\left(C_n n_0 + C_p p_0 + C_a \Delta n\right) \end{aligned} \qquad \text{Eq. 2—13} $$

The coefficients were investigated and measured for the total recombination. In this work the formulation of Kerr will be used {Kerr and Cuevas 2002}, this parametrization takes also into account the Coulomb enhanced Auger effect.

♦ *Radiative*

With the help of a phonon, the coupling EHP could release their energy in form of photons. The wavelength of these emissions corresponds to the width of the bandgap. Therefore, emitted photons have a narrow spectrum around 1100 nm.

$$ U_{rad} \;=\; B\left(n p - n_i^{\,2}\right) \;=\; B\Delta n\left(\Delta n + p_0 + n_0\right) \qquad\qquad \text{Eq. 2—14} $$

The effect, as it can be seen from the mathematical expression (Eq. 2—14) {Kerr, Cuevas et al. 2003}, depends strongly on the availability of carriers.

♦ *SRH*

With this acronym the name of the three physicists Shockley, Read, and Hall is indicated. They presented a mathematical description of recombination at localized electronic states within the band gap, denoted as traps. Traps are located in space; what is more, they have levels in the bandgap. Electrons can use these energy sites effectively to recombine with two (or more) halfway travels. The theory demonstrates that deep level traps, close to the intrinsic level, foster high recombination rates and in turn limit severely the carrier lifetime (see Fig. 2:6).

This model applies to the whole semiconductor, few modification are introduced to take into account specific regions

◊ *Bulk*

The classical example is the recombination due to a material defect (i.e. dislocations) or an impurity (substitutional or interstitial) in the bulk of the material. Remarkable examples in

silicon photovoltaic devices are Boron-Oxygen, especially in Cz-Si, and Iron-Oxygen complexes. Their importance stems from their light induced activation/deactivation. However, especially in cast material, many more impurities are found creating traps and therefore contributing to recombination.

Rarely the energetic impurity level can be seen as a mere donor or acceptor. Rather they create recombining levels. Additionally, specific dislocations of the lattice contribute to this recombination mechanism inserting levels in the middle of the bandgap.

A statistical treatment relating the occurrence of traps and the recombination effect was proposed {Shockley and Read 1952}, a complete treatment can be found elsewhere {Rein 2005}.

$$U_{SRHb} \quad = \quad \frac{\left(np - n_i^2\right)v_{therm}N_t}{\left(n+n_t\right)\sigma_p^{-1} + \left(p+p_t\right)\sigma_n^{-1}} \qquad \text{Eq. 2—15}$$

The formulation describes the traps by their density N_t, their energetic level E_t, and the capture cross section σ_P and σ_n for respectively electron and holes. In addition, the quantities p_t and n_t indicate statistical terms to calculate the probability of capture. Present in the formula is also the silicon constant of maximum carrier velocity v_{therm}.

$$n_t \quad = \quad N_C e^{-\frac{E_t - E_C}{kT}} \quad = \quad n_i e^{\frac{E_t - E_i}{kT}} \qquad \text{Eq. 2—16}$$
$$p_t \quad = \quad N_V e^{-\frac{E_t - E_V}{kT}} \quad = \quad n_i e^{-\frac{E_t - E_i}{kT}}$$

The net recombination modelled with SRH statistics can be investigated for its effect on net lifetime. The definition of the capture time constant for electrons $\tau_{n0} = \sigma_n v_{therm} N_t$ and for holes $\tau_{p0} = \sigma_n v_{therm} N_t$ describes the characteristic of a trap level in two parameters. This allows reformulating Eq. 2—15 and present the net lifetime (see Eq. 2—17). Exploiting the relation in thermal equilibrium the expression of the net lifetime is obtained.

$$\tau_{netSRH} \quad = \quad \frac{\tau_{p0}\left(n_0 + n_t + \Delta n\right) + \tau_{n0}\left(p_0 + p_t + \Delta n\right)}{p_0 + n_0 + \Delta n} \qquad \text{Eq. 2—17}$$

Further assumptions on injection reduce the complexity of the formula. For example, assuming a low level injection (lli), equation Eq. 2—17 simplifies to the point that it strongly depends on the doping type (see Eq. 2—18). The behaviour of the low injection is interesting for solar cells since this is the normal operation condition. The expressions obtained are proposed for a p-type material in a plotted version in Fig. 2:6.

$$\underbrace{\tau_{netSRH}\big|_{\Delta n < N_D}}_{\text{n-type}} \quad = \quad \tau_{n0}\left(1 + \frac{p_t}{p_0}\right) + \tau_{p0}\frac{n_t}{p_0}$$
$$\underbrace{\tau_{netSRH}\big|_{\Delta n < N_A}}_{\text{p-type}} \quad = \quad \tau_{p0}\left(1 + \frac{n_t}{n_0}\right) + \tau_{n0}\frac{p_t}{n_0} \qquad \text{Eq. 2—18}$$

Instead, increasing the injection to a high level (hli) the type and the doping does not play a role anymore Eq. 2—19. Indeed, due to equal population of carriers, the mechanism is only limited by the concurrency of the recombination.

$$\left.\tau_{\text{netSRH}}\right|_{\Delta n > (N_D + N_A)} \quad = \quad \tau_{p0} + \tau_{n0} \qquad\qquad \text{Eq. } 2-19$$
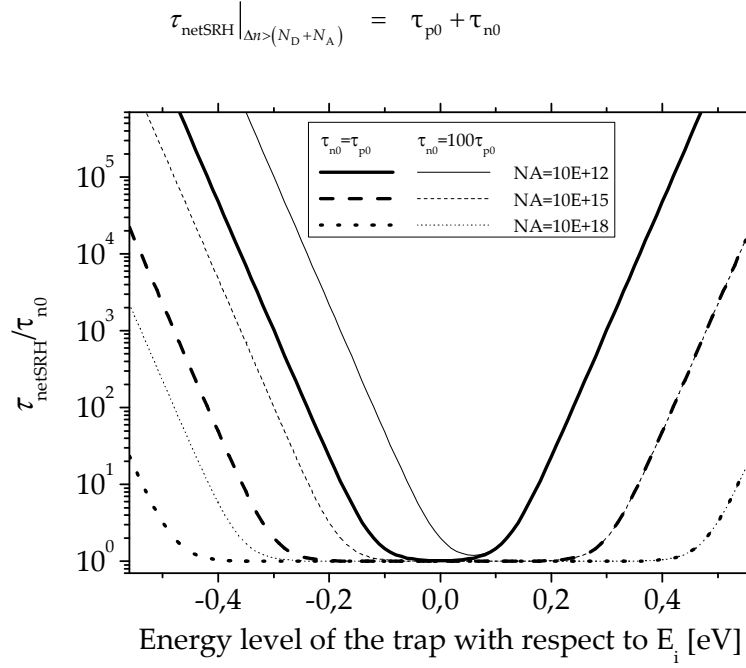

Fig. 2:6 Resulting ratio of net lifetime due to recombination following SRH statistics for different combination of doping and capture time constant. Notice the shift for unequal capture time constant.

◊ *Depletion regions*

In a drift/diffusion equilibrium region (called also space charge region SCR) a crossing point of the carrier density can be found, geometrically speaking a crossing plane for a planar diffusion. The existence of the crossing point ensures that also another recombination prone point can be found. This is called (ironically?) sweet point and is defined as $n_s/p_s = \sigma_P/\sigma_n$. This condition fosters SRH recombination at their maximum {Aberle, Glunz et al. 1993}.

This high recombination mechanism is always present. Below it will be indicated as U_{SRHdr}. More detailed analyses were conducted and result in a different dependency of the net recombination on the injection {McIntosh, Altermatt et al. 2000}.

2.2.3   Recombination at the surface

The surface recombination has been investigated in detail in several occasions to date {Girisch, Mertens et al. 1982; Nicollian and Brews 1982; Aberle, Glunz et al. 1992; Aberle, Glunz et al. 1993; Dauwe 2004}. The review and further interpretation of {Dauwe 2004} are suggested for more detailed reading.

Before undertaking the explanation of the mathematical modelling proposed to date, few definitions will be given.

A clear distinction between several aspects of surface recombination is due. In Eq. 2−20 starting from the term of net surface recombination, we use the advantage of dealing with a recombining surface. Indeed recombined EHPs can also be interpreted as charges that have been sucked from the interface. Therefore, the information on the direction, which is missing in case of generation and recombination, here is completely evident. For this reason, the first equation results legitimate.

$$U_s \;=\; \frac{J_s}{q} \;=\; U_{\text{SRH it}} + U_{\text{SCR}} \;=\; \frac{J_{\text{it}}}{q} + \frac{J_{\text{SCR}}}{q} \;=\; \left.\Delta n\right|_{x=0} S_{\text{it}} + \left.\Delta n\right|_{x=d_{\text{scr}}} S_{\text{SCR}} \;=\; \left.\Delta n\right|_{x=d_{\text{scr}}} S_{\text{pass}} \qquad \text{Eq. } 2-20$$

The second equation of Eq. 2−20 goes already further in the description of the interface. A distinction between a recombination at the interface (U_{SRHit}) and a recombination in the space charge region SCR (U_{scr}) describes the possibility of two different recombination mechanisms.

Their description can once again be made in terms of current, or as proposed by Dauwe, in terms of surface recombination velocity (S_{it} and S_{SC}) . The understanding of these recombination mechanisms delivers the value of the total S_{pass}. However, this value corresponds to an effective surface. This surface is chosen to be positioned at the end of any present space charge region (SCR). This depth is conventionally named d_{SC} (see Fig. 2:7).
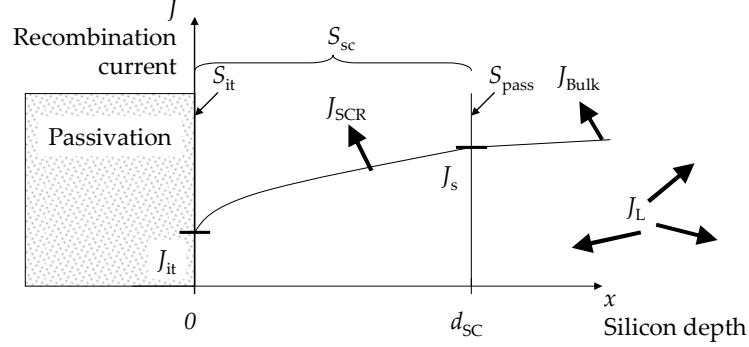

Fig. 2:7 Sketch of the recombinative surfaces and the direction of the currents. The illustration of the recombination current wants to underscore how they are partitioned spatially.

This theory is of great importance for a solar cell device. Indeed, nowadays realisations have always increasing ratios of surface to volume. The consequence of the reduced thickness on the device will be evident in section 2.5.

♦ *Interface recombination*

The termination of a crystal can be seen as a plane of dislocations/defects. Their high density (even more than one dangling bond per Si atom is possible) distributes on the forbidden bandgap. The SRH theory is used as the continuous sum of all the effects, in this setting the theory takes the name of extended SRH formalism.

$$U_{SRHs} \quad = \quad \frac{S_{it}}{\Delta n}\bigg|_{x=0} \quad = \quad \left(n_s p_s - n_i^2\right) \int_{E_V}^{E_C} \frac{v_{th} D_{it}\left(E_t\right)}{\dfrac{\left(n_s + n_t\left(E_t\right)\right)}{\sigma_p\left(E_t\right)} + \dfrac{\left(p_s + p_t\left(E_t\right)\right)}{\sigma_n\left(E_t\right)}} dE_t \qquad \text{Eq. 2—21}$$

Albeit the similarity of formula Eq. 2—21 with Eq. 2—15, the few differences are the consequence of treating a surface. Thus, the values n_s and p_s refer to carrier density at the surface and the quantity D_{it}, which depends on energy, introduces the distribution of the trap levels at the surface. Furthermore, the values of n_s and p_s correspond to the density values of the bulk only if the energy bands are flat from the bulk to the surface. In the case of bands having a bending towards the surface ($E_C|_{x=0}$ - $E_C|_{x=dsc} \neq 0$), this is taken into consideration modifying these two terms adopting Eq. 2—4 and Eq. 2—5.

The band bending is a consequence of a number of situations. A rather simple case is a doping of the surface, as consequence of a very shallow diffusion. The two terms, n_s and p_s, will therefore correspond to the doping concentration following the mass action law.

Another case is a hetero-junction, the surface that is analysed as recombinative surface is indeed an interface to another semiconductor. The interface will therefore create a space charge region and for this reason the amount of carriers can differ from the bulk.

The third case is an external bias imposed through a dielectric. The dielectric hinders conduction and therefore the situation is in thermal equilibrium. This situation is used in the microelectronics to test the performances of the interface between dielectric and silicon.

The fourth and most interesting case for us is the bending as a consequence of an unbalance between charges contained in the dielectric. These will impose a redeployment of the carriers. However, carriers will have to obey the relations described above, such as the mass action law.

For the Gauss law, the charges in the dielectric must be matched in the depth of the semiconductor, from 0 to d_{SC}. Different amounts of fixed charges in the dielectic (Q_f) will introduce different bending. Furthermore, in case of illumination of the samples, the additional amount of injected carrier density contributes to the charge compensation. Therefore the bands will bend less. Indeed, if the injection is high enough, the band bending disappears (see Fig. 2:8). The shift of the band $E_C|_{x=dsc}$ - $E_C|_{x=0}$ will be defined as ψ_{surf}.

These relations have been previously described {Schroder 2001}, in Eq. 2−22 the main results are summarized.

$$Q_{SC} \;=\; -\varepsilon_{Si} E_S \;=\; \left.\frac{d\psi}{dz}\right|_{z=0} \;=\; \mp\frac{\sqrt{2}\varepsilon_{Si}k_B T}{qL_{Dn}} F(p_{p0},\psi_{Surf},\Delta n) \;=\; -Q_f \qquad \text{Eq. 2−22}$$

In this equation ε_{Si} represents the permittivity of the silicon, E_S is the electric field at the surface, k_B is the Boltzmann constant, T is the temperature, q is the electron charge, L_{Dn} is the diffusion length of the electrons, and F is the normalized field expression. This latter depends on the amount of majority carriers, which at room temperature is close to the doping N_A, the surface voltage ψ_{surf} and the injection level Δn.

In Fig. 2:8 a bilateral relation between the amount of charges and the bending is plotted for different doping and illumination. The illumination is represented as the number of the injected carriers Δn in d_{SC}. However, it has been demonstrated that injection, and in turn the quasi Fermi levels, can be assumed constant from the d_{SC} to the bulk {Dauwe 2004}.
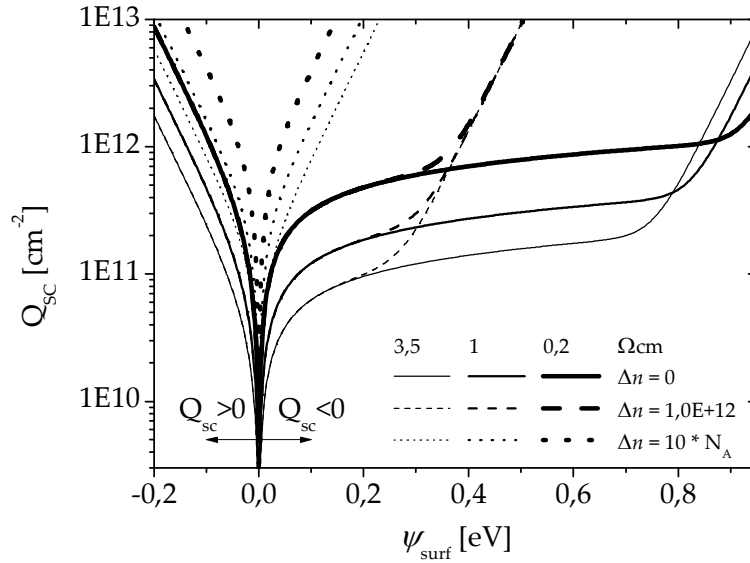
Fig. 2:8 Plot of the relation between the amount of charges in the semiconductor and the resulting surface voltage, defined as the difference between the band level at the surface and in the bulk. The relation is calculated for a p-type material. The doping level explored for the calculations are: 4E+15 cm^{-3} (3.5 Ω·cm), 1.5E+16 cm^{-3} (1 Ω·cm), and 1E+17 cm^{-3} (0.2 Ω·cm). This graph takes in consideration both positive and negative charges are considered (see the regions defined by the arrows). The illumination effect is reported for low level illumination (Δn = 1E+12) and for high level injection (ten times the doping level).

The curves can also be reported plotting the Fermi level and the quasi-Fermi levels with respect to the band gap (see Fig. 2:9). In this view, it results easier to understand that the deployment of charges in the semiconductor lead the surface to be in different states. In the specific case of the picture (p-type material), the surface is in accumulation when the Q_{SC} is positive (negative charges in the dielectric), on the other hand, when the Q_{SC} is negative, three different partitioning of the graph can be described. The first part presents low values of charges. This is called depletion. The surface is partly ionised to compensate the external

charges. The second part is called weak inversion and can be found as soon as the Fermi level goes below the intrinsic energy level. Indeed few minority carriers will gather at the interface, however, their number is not sufficient to compensate the substrate doping. The last part is strong inversion. Minority carriers gathered at the surface balance the external charges and are sufficient to compensate the doping and therefore change locally the type of semiconductor.
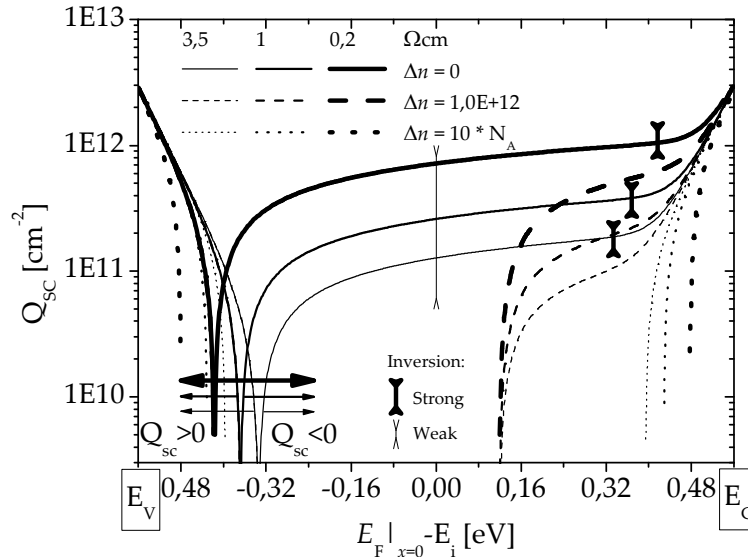
Fig. 2:9 Plot of the relation between the amount of charges in the semiconductor and the position of the Fermi level at the surface. As in Fig. 2:8, the arrows indicate the region of positive and negative charges. From the calculation it is possible to see that an amount of charges Q_{SC} below (above) 2E+12 cm^{-2} is able to set the Fermi level at the edge of the conduction (valence) band
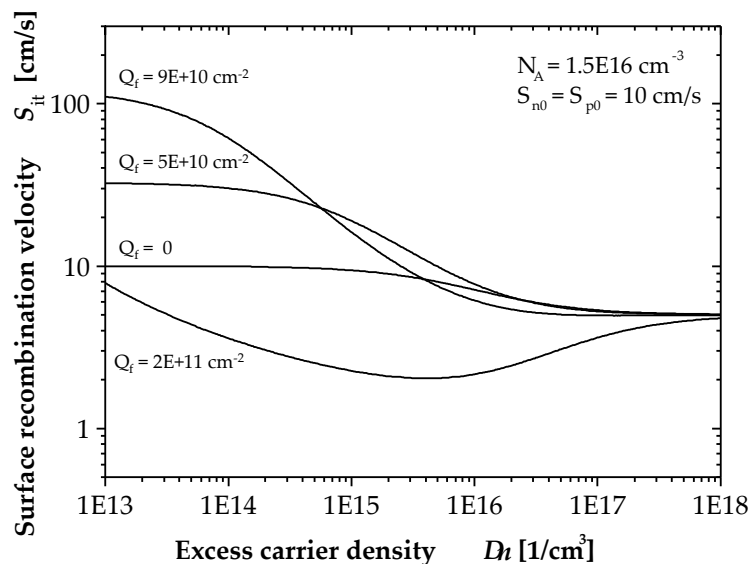
Fig. 2:10 Plot of the surface recombination velocity at the interface. The dependency on the charges and on the injection level shows the variety of the surface passivation (from {Hofmann 2008}).

The amount of saturated traps at the surface influences the number of charges in the semiconductor. Filled states can balance or summate to external charges. Therefore only a numerical approach is able to establish the correct surface potential and the correct surface velocity {Girisch, Mertens et al. 1988}. However under the assumption of negligible D_{it} and in turn negligible Q_{it}, the surface potential ψ_{surf} depends only on the external charges to balance.

The knowledge of Q_f gives therefore access to the value of the carrier density at the surface (n_s and p_s).

With the additional simplification at the interface surface of having only one trap level in the middle of the bandgap Eq. 2—21 simplifies to Eq. 2—23. The term Q_{SC} plays an important role in the resulting passivation benchmark (S_{it}) (see Fig. 2:10).

$$U_{SRHs} \quad = \quad S_{it}\,\Delta n\big|_{x=0} \quad = \quad \frac{n_s p_s - n_i^2}{\dfrac{(n_s + n_t)}{S_{p0}} + \dfrac{(p_s + p_t)}{S_{n0}}}$$

$$\Rightarrow$$

$$S_{it} \quad = \quad \frac{n_{s0} + p_{s0} + \Delta n}{\dfrac{(n_{s0} + \Delta n + n_t)}{S_{p0}} + \dfrac{(p_{s0} + \Delta n + p_t)}{S_{n0}}}$$

Eq. 2—23

♦ *Space charge region recombination*

Dauwe, while treating the case of dielectric loaded with positive charges on p-type material, developed an expression to take into account the recombination in the space charge region which balances the external charges (Eq. 2—24). The formulation takes into account the dependence of the region extension d_{SC}. In turn, this distance depends on the level of carrier injection, on the doping of the material and on the amount of external charges.

$$S_{SCR} \quad = \quad \frac{1}{\Delta n\big|_{x=d_{SC}(Q_f, N_A, \psi_{Surf})}} \int\limits_0^{d_{SC}(Q_f, N_A, \psi_{Surf})} U_{SCR}(x)\,\mathrm{d}x$$

Eq. 2—24

As for the case of recombination in the depletion region of a p-n junction, he considers the SRH mechanism the main responsible for the increased recombination rate. The sweet point is present as soon as inversion conditions are met. Then a peak of recombination can be found in the space charge region.

Furthermore in his treatment, while detailing the correspondence of behaviour between an inverted surface and a junction, he explains this SCR recombination channel as the non-ideality of the junction. This introduces the understanding of injection dependent passivations.

2.3 Mechanism of a solar cell

2.3.1 Continuity equation

Of uttermost importance for solar cell devices is the continuity equation. In static conditions, its definition encloses the main photovoltaic principle: what is generated in a volume of semiconductor can either escape the block or recombine. Recombination has to be reduced so that the generated carriers can escape the block (diffusing out).

The mathematical expression in one dimension (Eq. 2—25) can be represented with a simple sketch (Fig. 2:11)

$$\frac{\mathrm{d}n(t)}{\mathrm{d}t} \quad = \quad G_n - R_n + \frac{1}{q}\frac{\mathrm{d}J_n(x)}{\mathrm{d}x}$$

$$\frac{\mathrm{d}p(t)}{\mathrm{d}t} \quad = \quad G_p - R_p + \frac{1}{q}\frac{\mathrm{d}J_p(x)}{\mathrm{d}x}$$

Eq. 2—25

The terms in the equation Eq. 2—25 represent the total generation rate and the total recombination rate. These, in case of thermal equilibrium, assume the same value,

conventionally designated as R_0. The differences between the total and the thermal equilibrium generation are indicated with the prefix "net",

$$
\begin{aligned}
G &= G_0 + G_L &&= R_0 + G_L \\
R &= R_0 + \sum_i U_i &&= R_0 + U_{Aug} + U_{rad} + U_s + U_{SRHb} + U_{SRHdr}
\end{aligned}
$$

Eq. 2—26

and represented by a U_i, where the "i" stands for the various recombination mechanisms: <u>Aug</u>er, <u>rad</u>iative, <u>s</u>urface, <u>SRH</u> in the <u>b</u>ulk, <u>SRH</u> in the <u>d</u>epletion <u>r</u>egion. The subscripts which distinguish the particle are omitted to enhance visibility, the reader is intended to interpret Eq. 2—26 for specifically one particle type at a time.
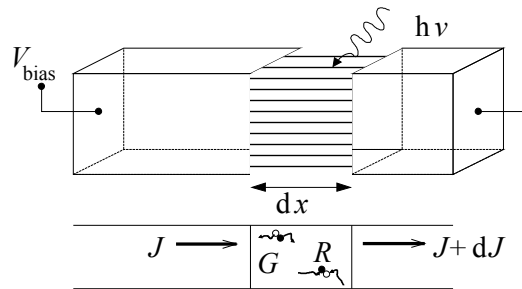
Fig. 2:11 Continuity sketch

To illustrate in further detail the working principle of a solar cell we will suppose a p-type bulk. The continuity equation (Eq. 2—25) can be rewritten

$$
\frac{dn(t)}{dt} = G_L - \left(U_{Aug} + U_{rad} + U_s + U_{SRHb} + U_{SRHdr} \right) + \frac{1}{q} \frac{dJ_n(x)}{dx}
$$

Steady state condition

$$
\frac{1}{q} \frac{dJ_n(x)}{dx} = U_{Aug} + U_{rad} + U_s + U_{SRHb} + U_{SRHdr} - G_L
$$

Eq. 2—27

and it becomes clear that current increases along the x axis are expected only outside of equilibrium conditions. The condition for a positive current is a generation higher than the sum of all recombination mechanism.

Net recombinations are also characterised by the lifetime of carriers undergoing this mechanism only. The definition relates to the amount of carriers and the net recombination

$$
\tau_i = \frac{\Delta n}{U_i}
$$

Eq. 2—28

The definition applies always. However for recombinations taking place at the surfaces, a more suitable term is defined.

$$
S = \frac{U_s}{\Delta n}
$$

Eq. 2—29

The surface recombination velocity S assumes a low value for low recombinative surface and is limited by the thermal velocity v_{therm}, since the carrier cannot travel to the surface faster that this speed.

The harmonic sum[10] of each lifetime associated with a recombination is called effective lifetime.

---

[10] The harmonic sum is here defined as the inverse of the sum of the inverses.

$$\tau_{\text{eff}} \quad = \quad \frac{1}{\sum_i \tau_i} \qquad\qquad \text{Eq. 2—30}$$

Another value helpful to determine the spatial extent of the recombination effect is the diffusion length. It is convenient to define it by using the effective lifetime

$$L \quad = \quad \sqrt{D \cdot \tau_{\text{eff}}} \qquad\qquad \text{Eq. 2—31}$$

and the diffusion coefficient, which, through the Einstein relation, depends on the mobility of the carrier and on temperature. Since the diffusion coefficient and the effective lifetime are supposed to change depending on the type of the material, the subscript n or p applies on both right and left side of the equation (Eq. 2—31).

2.3.2 Carrier transport

The densities of carriers are sensitive to unbalances and fields, for this reason a treatment of their movement (transport) has to be properly understood.

For the following description the convention of electron and holes will be chosen. Furthermore, to make the writing closer to the application used in this book, only the one dimensional case will be described. Textbooks contain detailed multidimensional treatments {Sze and Ng 2006} and will be quoted when necessary in the text.

The first relation which applies to the system is the so called Poisson's law

$$\frac{\mathrm{d}^2 \psi(x)}{\mathrm{d}x^2} \quad = \quad -\frac{\mathrm{d}E(x)}{\mathrm{d}x} \quad = \quad -\frac{\rho_{\text{charge}}(x)}{\varepsilon_0 \varepsilon_{\text{Si}}} \qquad\qquad \text{Eq. 2—32}$$

where ρ_{charge} represents the carriers in the point x; $E(x)$ is the field and $\psi(x)$ is the potential corresponding to the intrinsic energy level.

Eq. 2—32 will be used to take into account external fields created by fixed charges or, generally, to evaluate built-in fields.

Another set of equations expresses the transport as consequence of two factors: the carrier diffusion, which plays an important role in photovoltaic devices, and the carrier drift under a field influence.

$$
\begin{aligned}
J_n(x) &= q D_n \frac{\mathrm{d}n(x)}{\mathrm{d}x} + q \mu_n n(x) E(x) &=& \mu_n n(x) \frac{\mathrm{d}E_{\text{Fn}}(x)}{\mathrm{d}x} \\
J_p(x) &= -q D_p \frac{\mathrm{d}p(x)}{\mathrm{d}x} + q \mu_n p(x) E(x) &=& \mu_n p(x) \frac{\mathrm{d}E_{\text{Fp}}(x)}{\mathrm{d}x}
\end{aligned}
\qquad \text{Eq. 2—33}
$$

With E_{Fn} and E_{Fp} the two quasi-Fermi levels are indicated. Eq. 2—33 is valid for low electric fields. Departing from this condition derecognise the validity of the right hand side equalities. High electric field finds in v_{therm} the limit of mobility and electric field product (diffusion mechanism are also limited by this velocity).

2.3.3 Junctions on the entire wafer substrates

Before introducing the matter of this subsection a short summary is a prerequisite:
- Illumination creates carriers
- Continuity equation insures that, if they don't recombine, the carriers escape their creation volume.
- The transport of these carriers is driven by fields or by diffusion.

Extracting carriers by fields would require energy to create these fields, and this is not the point of a solar cell. Much more convenient is diffusion, and also coherent with the goal: having a stable creation of carriers in the bulk and taking out these energetic carriers on one of the

sides, a gradient of carrier will create as a consequence. Therefore, diffusion will feed the extracting side.

One way to extract the exceeding minority carriers on one of the sides, is to create a region where even though carriers are created, many more states are available at the same energy level. This will allow that, even under the same injection, the energetic level of generated carriers in the bulk is higher. One way to create this is to create a built in field, this will bend the bands and allows more states to be present at the same energetic level.
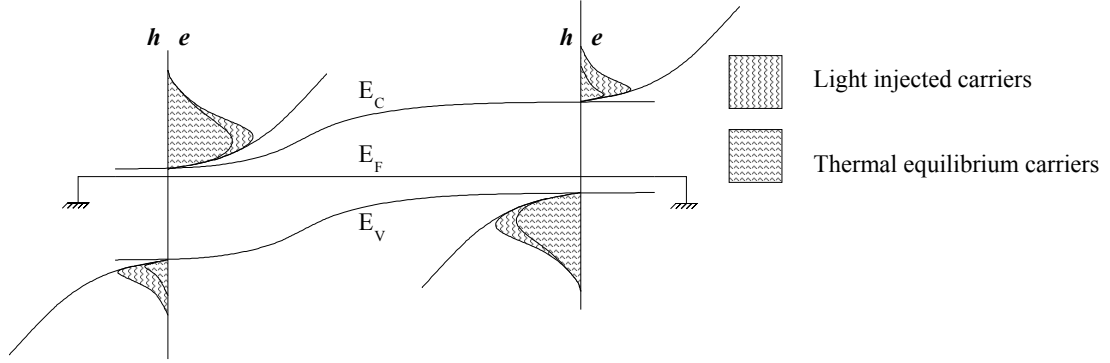

Fig. 2:12 Sketch of a cell at the short circuit condition.

This is achieved by locally inverting the doping type in the material. As we described earlier, one side would be enough, though many different designs have been proposed in the years. A complete overview of the existing alternatives is obtained by consulting recent publications (i.e. concepts as: metal wrap through {Clement 2009}, emitter wrap through con {Mingirulli 2009}, and back-contacted back junction (BC-BJ) {Granek 2010}).

A large flat substrate of silicon is a perfect volume where this structure can be implemented, the light will impinge on the large surface and cross its thickness (most of the spectrum could be captured in few hundreds micrometres thickness), the overcompensation of the bulk doping type can be performed, for example on the front side.

This area is normally called emitter, and a very common procedure to create such a configuration is to dope the material, general knowledge on the diffusion of materials in silicon {Jones 2008} is used to bring the dopants into the near-surface bulk region of the targeted side.

The minority carrier flow which is created by such a structuring can be evaluated. Since the mechanism is diffusion driven, the gathering of carriers is taking place at maximum at a certain characteristic distance: the minority carrier diffusion length (L_{Dn} for electrons in p-type and L_{Dp} for holes in n-type). The calculation is performed along the depth of the material, normal to the emitter plane. The origin of this set of coordination is the interface between the two doped regions

For the sake of simplicity, the analysis will limit to the one dimensional case and only radiative recombination (Eq. 2—14) will be taken into account.

$$ R \quad = \quad R_{rad} \quad = \quad R_0 \frac{np}{n_i^2} \quad = \quad R_0 e^{\frac{E_{Fn} - E_{Fp}}{kT}} \qquad \text{Eq. 2—34} $$

From the continuity equation we can say that the sum of the current escaping one side of the cell will be the sum of the diffusing minority carrier on each side (Eq. 2—27).

$$ J \quad = \quad \int_{-L_p}^{0} \frac{dJ_p(x)}{dx} dx + \int_{0}^{L_n} \frac{dJ_n(x)}{dx} dx \quad = \quad -q \left(\int_{-L_p}^{0} \left(G_p - R_p \right) dx + \int_{0}^{L_n} \left(G_n - R_n \right) dx \right) \qquad \text{Eq. 2—35} $$

The generation can be substituted with the sum of its equilibrium term and a function G_L representing the net generation. This term G_L depends on the depth and on the light spectrum

only. Indeed, it can be safely extracted from both integrals and defined on the whole range of interest ($-L_{Dp}$ to L_{Dn}). Furthermore, the recombination depends only on the local injection (Eq. 2—34) and the generation at thermal equilibrium ($G_0 = R_0$). From these definitions of generation and recombination out of thermal equilibrium (Eq. 2—34) we can write

$$J \;=\; -q\int_{-L_p}^{L_n} G_0\left(1-e^{\frac{E_{Fn}-E_{Fp}}{kT}}\right)dx - q\int_{-L_p}^{L_n} G_L dx \;=\; qG_0\left(L_p+L_n\right)\left(e^{\frac{qV}{kT}}-1\right)-J_L \qquad \text{Eq. 2—36}$$

a relation between the equilibrium and the excited state (valid for both bias or illumination excitation). In this case the total current which can be gathered is represented as J_L. Due to the absence of resistive path and potential barriers of this treatment, the splitting of the quasi Fermi levels depends directly by any external bias V and is independent of the depth. For this reason the exponential relation can come out of the integral. The definition of G_0 for each region is given in Eq. 2—37 by applying Eq. 2—11.

$$
\begin{aligned}
L_{Dn} &= \sqrt{D_n\tau_n} & L_{Dp} &= \sqrt{D_p\tau_p} \\
n_{p0} &= n_i^2/N_A & p_{n0} &= n_i^2/N_D \\
G_0\big|_{-L_{Dp}}^{0} &= \frac{n_i^2 D_n}{N_A L_{Dn}^2} & G_0\big|_{0}^{L_{Dn}} &= \frac{n_i^2 D_p}{N_D L_{Dp}^2}
\end{aligned}
\qquad \text{Eq. 2—37}
$$

From these simplifications Eq. 2—36 can be finally rewritten

$$J \;=\; qn_i^2\left(\frac{D_n}{N_A L_n}+\frac{D_p}{N_D L_p}\right)\left(e^{\frac{qV}{kT}}-1\right)-J_L \;=\; J_0\left(e^{\frac{V}{m_{const}\cdot V_{Th}}}-1\right)-J_L \qquad \text{Eq. 2—38}$$

in terms describing the material properties. The last equation introduces a term J_0 called saturation current and a term m_{const} which in this case is constant and equal to 1 (m_1).

As the radiative recombination also the SRH in the bulk and the SRH on the surface can be expressed in the same way. In this case the term J_0 must be adapted to take into account the loss mechanisms.

However, for the case of recombination of the type Auger and SHR in the depletion region, the relation Eq. 2—38 is not enough to describe the whole relation. These have a relation to the injection different from the radiative recombination seen in Eq. 2—34 (for a list, see {Kaminski, Marchand et al. 1998}), and lead therefore to different terms in the final equation. The Auger recombination takes part only at very high injections ($V_{forward} > 700mV$ or an illumination of hundreds of Suns) and is therefore neglected in the model. On the other hand, recombination in the space charge region is most effective at low bias. Therefore, this is represented by an additional term in the equation. This represents a second diode and assumes an ideality factor close to two (m_2).

$$J \;=\; J_{01}\left(e^{\frac{V_{oc}}{m_1\cdot V_{Th}}}-1\right)+J_{02}\left(e^{\frac{V_{oc}}{m_2\cdot V_{Th}}}-1\right)-J_L \qquad \text{Eq. 2—39}$$

The presence of unclassified non idealities makes this rigid interpretation valid for very few cells. To dilate the description of the model, often the ideality factor of the second term can depart form the initial value of 2 to achieve best fits of solar cell characteristics.

2.4 Characterisation of a solar cell

2.4.1 Loss mechanisms and the two diode model

On real cells all the described recombination mechanism are found, furthermore other deviations from this ideal picture are found. Coexisting loss mechanisms can be listed with a classification.

The first category and the most important comprehends optical losses. They are best represented by shadows on the absorbing material, these can increase the reflection locally up to 100 % (i.e. front metallisation), though other optical losses are represented by ineffective light trapping, rays of light are meant to enter the device and have low probability of escaping the material without being absorbed. A perfect device would look therefore completely black.

This first loss is best represented by the current that escapes the cell in short circuit condition J_{SC}, this current can be approximated in most cases with the photogenerated current J_L.

A second category is represented by loss in heat creation. Under this category are all losses which employ gathered photon energy to heat up the device with the Joule effect[11]. This effect describes power dissipation of a current flowing through a resistance.

These losses limit the voltage or the current depending how the electrical resistance is connected to the active device (the illuminated power-generating solar cell). They are represented by resistance in series R_s, which limits the voltage delivered to the outside world and by parallel resistances R_{shF}, which represent an internal path for the photogenerated current.

In the third category are the recombination mechanisms. These were already described in length. Recombination mechanisms are best represented by a diode with a saturation current J_{01} and an ideality factor $m_{const} = 1$, and additionally a second diode with saturation current J_{02} and an ideality factor $m_2 \approx 2$ (see 2.2.2, SRH and Depletion regions paragraphs).

Each category is represented in a lumped model, normally called "two diode" model. A sketch of the circuit is given in Fig. 2:13. The influence on the cell efficiency that each part can represent is well documented in previous literature (i.e. {Glunz 1995}).

The cell characteristic can be measured under several excitation modes, in the rest of the work they will be indicated as follows

- JVDark: The cell is kept in dark, with a stabilized temperature of 25 °C. Under these conditions the potential of the base is decreased with respect to the emitter. The current coming out at each bias is tracked.
- JV1Sun: The cell is kept under illumination, the illumination follows a standard {IEC 2008}, it can be a fixed light intensity or a decaying light intensity. In the latter case the measurement of the current during the voltage sweep has to be adjusted to the varying intensity. Instructions for this procedure are standardized (sound alternatives to this procedures have been also developed {Burgers 2004}). Also in this case the temperature is stabilized to 25 °C. Under these conditions the potential of the base is decreased with respect to the emitter. The current coming out at each bias is tracked. The current is then normalized to the area of the cell. This helps the comparison of cells with different area. During this measurement it is possible to evaluate the efficiency of the cell at imposed illumination level. Different combinations of load will receive from the solar cell a different power. The load for which this power is maximal creates in the cell the condition of maximum power point. This point is indicated with J_{mpp} and V_{mpp}.

---

[11] This definition takes inspiration from the illuminated lock-in thermography (ILIT). This characterisation instrument bases its principle on the observation of heat related light emissions.

- SunsVoc: The cell is kept at constant temperature and in open circuit conditions. The cell is then exposed to varying illumination intensity, and the voltage for each illumination intensity is tracked.
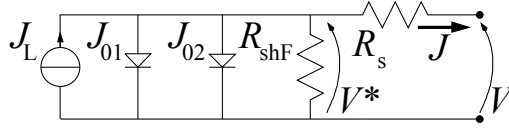

Fig. 2:13 Circuital representation of the two diode model.

Largely adopted is the JV1Sun measurement. Indeed the solar conversion efficiency (η) is obtained from this curve. Furthermore, on this curve the fill factor (*FF*) can be measured. This quantity expresses the ability of the cell to deliver to the outside world the power left after the most prominent loss mechanisms. These are optical losses and recombinative losses which can be described with an ideal diode having an ideality factor of one. A detailed discussion on this term and two other strictly correlated values is given in the appendix A.h.

The characteristic of a solar cell can be fitted to the lumped parameter model described above. Popular fitting algorithms were developed and are now freely available {Burgers 2004}.

2.4.2   Another point of view on the cell, the local ideality factor

In order to understand the behaviour of the cell, it would be helpful to know which kind of loss mechanism (Joule effect or recombination) is the most prominent at every single bias. As biases the following can be considered:

- electric bias (dark I-V curves);
- illumination bias (SunsV_{OC} curves or J_{SC}-V_{OC} curves));
- a mixture of the two previous biases (illuminated I-V curves);

Below a voltage bias in the dark will be assumed. Adopting these conditions, an ideal diode device is measured for its JVDark curve. In a logarithmic-linear plot its curve resembles a straight line. The mathematical model of an ideal diode (Eq. 2−40) describes a temperature dependency through the variable V_{th}

$$\log \frac{J_{ideal}}{J_0} \quad = \quad \frac{V}{V_{th} m_{const}} \qquad\qquad \text{Eq. 2−40}$$

and additionally delineates an ideal single recombination mechanism having a "$m_{const} = 1$" fingerprint.

The mechanism which dominates the whole curve of the ideal device is evinced from the m_{const}. Its constant value indicates a locus of points for the current. This tidy arrangement is not observable in real diodes. Indeed, different recombination mechanisms and resistance losses influence the JVDark. Therefore, they will alternate their fingerprints changing the resulting slope of the curve.

A slope comparison of the JVDark between an ideal and a real device would show which limitations are preventing the real diode from ideality. As it was mentioned above, the ideal curve has an ideality factor of one.

$$\frac{d \log \frac{J_{real}}{J_0}}{dV} \quad \neq \quad \frac{d \frac{V}{V_{th} m_{const}}}{dV} \quad \Rightarrow \quad \frac{d \log \frac{J_{real}}{J_0}}{dV} \quad = \quad \frac{1}{m_{loc}(V)} \cdot \frac{d \frac{V}{V_{th} m_{const}}}{dV} \qquad \text{Eq. 2−41}$$

In Eq. 2−41 the derivative of the logarithm of the current obtained with a JVDark measurement is compared to the derivative of an ideal behaviour (the right hand side of Eq. 2−40). Indeed they are found to be different. It is decided to describe this difference through a term that will be called local ideality factor m_{loc}. This term by definition entangles all the non

idealities and depends on the bias. Furthermore, its definition makes it a multiplication term for the constant ideality factor m$_{const}$.

Once the derivation on the right hand side of Eq. 2—41 is performed, it is possible to solve the equation for m_{loc}.

$$m_{loc}\left(V\right) \quad = \quad \frac{dV}{V_{th}\,m_{const}\,d\log\dfrac{J_{real}}{J_0}}$$

Eq. 2—42

The comparison of the derivatives allows an independence from value of currents. Indeed, the analysis focuses on the slope. Comparing the current values of the real and ideal instead would give a result with little interpretability. This new term describes the constant ideality factor of the diode which assumes the same current value as the real cell. This description neglects predominant recombination or loss mechanisms of the real device. This value, indicated for clarity in Fig. 2:14, is of scarce interest for the understanding of the cell behaviour.

The knowledge that is gained from this curve has to be carefully analysed. Several treatments introduce causes for shifts of the curve from the ideal path. The ideal path description can be found in textbooks {Sze and Ng 2006}. There a $m_{loc} = 2$ describes the recombination happening in the SCR, which have only at low injection a significant impact on the cell behaviour. Whereas, the high injection case is dominated by a recombination linked to SRH mechanism which portrays a $m_{loc} = 1$. More elaborated theories and characterisations were detailed by mainly two authors in the photovoltaic community, {McIntosh, Altermatt et al. 2000} and {Breitenstein, Altermatt et al. 2006}. In the work part of their treatment will be used and then correctly explained.
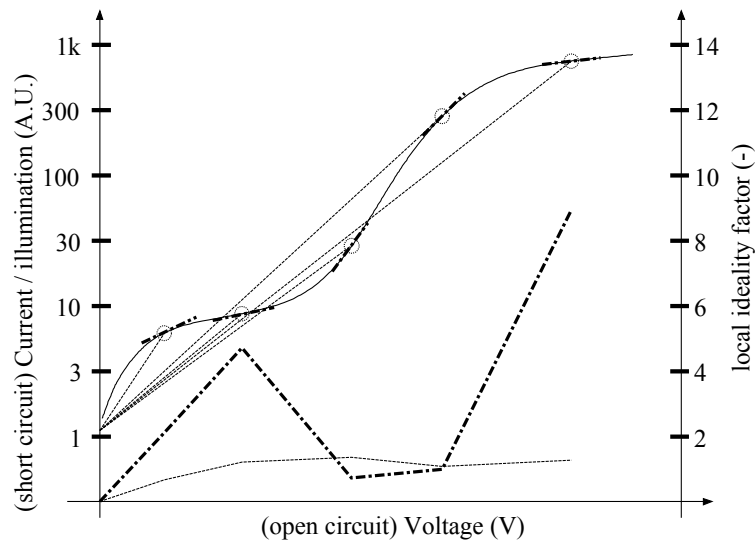
Fig. 2:14 A log-linear plot of, for example, an I-V curve taken in dark (thin full line) and the "manual" calculation of the m_{loc} (thick dot dash line) and of the secant (thin dash-dash line). The values of the I-V curve slope are used to reproduce a m_{loc} curve at the bottom. The slopes of the secant warn about the difference from the former.

Together with this alternative point of view on solar cells it is worthy to mention that exotic recombination channels can be identified by measurements at different temperatures {Kaminski, Marchand et al. 1998}. In this measurement setting, the calculation of the local ideality factor identifies the different parts of the curve.

This knowledge was used for specific analyses. The objective was to detect if recombination mechanisms, other than the ones observed with other tools, were affecting the realised solar cell.

2.4.3 Numerical simulation

Excellent tools to examine the potential of solar cells are now freely available. Namely these tools are:

- `PC1D` {Clugston and Basore 1997} from the University of New South Wales, In this tool sophisticated models for light trapping analyses and high doping phenomena are included (though the model implements the "Boltzmann approximation").
- QSS Model V3 offered by the Australian National University {Cuevas, Sinton et al. 2008}, Cuevas and many other authors contributed to its realisation and implemented many of the known SRH parameters for specific defects.

Both proposes numerical approach to the solution of the equations describing the cell.

2.5   Thin substrate solar cells

The relation Eq. 2—38 is valid for an infinite thickness substrate or at least a substrate with a thickness of the doped side much larger than the diffusion length of the minority carriers. This situation is far from reality, due to material cost, the use of thinner cells is promoted. To consider this factor in Eq. 2—38 an elegant method is to include geometrical factors {Kray 2004}.

$$
\begin{aligned}
F_n &= \frac{S_h \cosh(W_n/L_h) + D_h/L_h \sinh(W_n/L_h)}{D_h/L_h \cosh(W_n/L_h) + S_h \sinh(W_n/L_h)} \\
F_p &= \frac{S_e \cosh(W_p/L_e) + D_e/L_e \sinh(W_p/L_e)}{D_e/L_e \cosh(W_p/L_e) + S_e \sinh(W_p/L_e)}
\end{aligned}
\qquad \text{Eq. 2—43}
$$

The saturation current will vary depending on the thickness and the termination of the surfaces. The latter is modelled through the extended SRH treatment.

$$
J_0 = \left(\frac{q n_i^2 D_n}{N_A L_n} F_p + \frac{q n_i^2 D_p}{N_D L_p} F_n \right)
\qquad \text{Eq. 2—44}
$$

Reducing the thickness is an approach to reduce material, at the same time, an increase of the efficiency could be gained under certain conditions described below.

Eq. 2—44 gives an insight of the important terms in the downscaling of the solar cell thickness. With few more assumptions the results of the equation can be used to simulate an entire solar cell. In the plot Fig. 2:15 constant values are assumed for the diffusion length, photo-generated current (J_L and therefore J_{SC}), and fill factor (*FF*). The variations of surface recombination velocity on the back surface and of cell thickness show the influence directly on the efficiency. We remind though that when J_{SC} and *FF* are fixed, the efficiency is driven by the value of V_{OC}. Hence the explanation below will focus on the open circuit condition of a solar cell under 1 Sun illumination.

In the attempt to explain the curves it is paramount to mention that the same amount of net generation is obtained independently from the actual volume of the bulk. This is consequence of imposing a fix short circuit current which in turn represents the term J_L. It has to be mentioned that this consequent anti-proportional carrier density behaviour with respect to the thickness, does not explain movements in open circuit voltage alone.

When the back surface recombination velocity is low, the carrier will have a higher probability to recombine in the bulk, therefore their density in the bulk will increase. This will also increase the injection level at the front. This injection in turn expresses the potential at the front following the law of the junction.

$$\Delta n\big|_{x=0} = \frac{n_i^2}{N_A}\left(e^{\frac{V_{OC}}{V_{th}}} - 1\right) \Leftrightarrow V_{OC} = V_{th} \ln\left(\frac{N_A \cdot \Delta n\big|_{x=0}}{n_i^2} + 1\right) \qquad \text{Eq. 2—45}$$

On the other hand, when the back surface represents a sink for the carriers, having a thicker base protects carriers by decreasing their chance of encounter with the highly recombining surface. Thick wafers benefit (see Fig. 2:15) even in the surface limited condition.
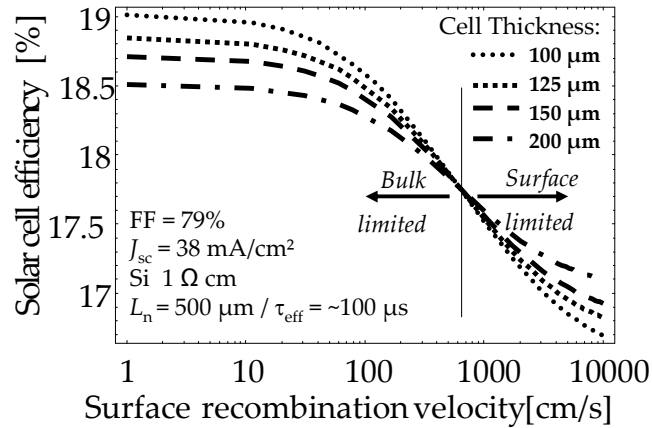

Fig. 2:15 Result of the calculation from the Kray additional terms {Kray 2004} in the one diode model. In the picture two regions are individuated, in the left region the limiting recombination is found in the bulk, on the right, the bulk is still active, in addition the surface contributes. It can be seen that the thinner the cell the stronger the contribution. Indeed thicker cells find relief in a diffusion limitation mechanism. The carriers need actually to be delivered to the surface before recombining with the velocity specific to the surface. Similar argumentations for the advantages of thin silicon solar cells are obtained analytically {Kray 2004} and by numerical simulations {Hofmann 2008}.

2.6   Limits of a silicon single band gap solar cell

This section has its perfect end in the exploration of the photovoltaic limits of the device presented until now. What can be achieved with silicon when the technologies do not hinder the realisation of an ideal solar cell?

This argument was treated previously {Green 1986; Aberle, Altermatt et al. 1995} as an extension of an analysis of a laboratory prototype of high efficiency solar cells. For that occasion the losses were decomposed, hence, the knowledge of the maximum attainable efficiency limit deserved attention.

The limit must be calculated first by eliminating all possible recombination mechanism on which the human action could put remedy. What remains are radiative recombination and Auger recombination. Bulk can be supposed defect and contamination free. Indeed, the technology level of the silicon crystal growth allows this assumption for FZ-Si substrate. Surfaces can be prepared so that the effective surface recombination has as much influence as the bulk terms.

The second limitation to the final efficiency is the absorption capability and EHP generation. Different optimal thicknesses are suggested depending on the maximum generation possible.

A third issue related to the material is the thermal dissipation of all energy gathered by the EHP above the band gap energy. This is the direct consequence of using a single band gap solar cell.

In conclusion, of interest for the application of this thesis is the calculated limit stating 30.1 % maximal efficiency. Several assumptions for the calculation were made. First, light is absorbed

under the "one phonon limit". This states that only one phonon is assisting the creation of EHPs, and one photon with energy above the bandgap generates a single EHP. Second, the light trapping of this structure randomizes the direction of the rays in the bulk. Third only recombination of the Auger type is considered. For such hypothesis the ideal thickness is calculated to be around 100 µm {Green 1986}. Sunpower realised recently a full size prototype (probably 125mm pseudo square) with an efficiency of 24.2% {Sunpower 2010}. This realisation profits from years of experience on their specific cell concept (back-contacted back junction cells).

Chapter 3   Experimental, conventional and advanced processing

In the PVTEC laboratory at the Fraunhofer ISE institute, the evaluation of solar cell processing is an ongoing work. Within the goals of this thesis several processes were of main importance since their evaluation can lead to the realisation of a high efficiency structure within industrial settings. The process evaluation targets the possibilities of structuring and takes the setting that is most likely to achieve the properties required.

The work started with a familiarization with the material and conventional technologies, which are also briefly presented below (3.1 and 3.2). Furthermore advanced processing has been evaluated for the implementation of a particular device structure. The motivation and the processing details are detailed below (3.3 and following).

3.1   Brief introduction to silicon wafer fabrication

The base material for the research of this thesis is silicon, in this section a brief introduction on its preparation is given for completeness.

Silicon is an abundant material on earth, albeit it is found in stable compounds with other elements, most notably oxygen. The silicon creation begins from the purification of quartz (SiO_2); a carbothermic arc reduction accomplishes this task. Review articles listing the challenges of this procedure for the production of solar grade silicon can be found in specialized literature (i.e. {Lynch 2009}).

Silicon chunks of different material purity are prepared through this first metallurgical step. They are classified by the number of 9 in the purity percentage (i.e. 6N = 99.9999%)
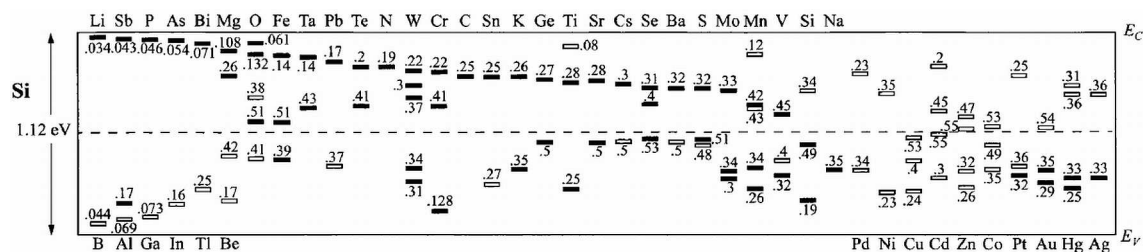

Fig. 3:1 Donors (solid bars) and acceptors (hollow boxes) level in silicon (from {Sze and Ng 2006}).

As it was mentioned above (2.2.2), elements introduced in the silicon crystal can act as donors or acceptors (see Fig. 3:1). However, if they cannot ionize at room temperature they represent a trap level, therefore a bulk recombination mechanism.

A bath of almost pure silicon is obtained melting the chunks. From this point, the wafers are fabricated using several techniques: a first method, largely widespread, is the thermally controlled solidification of the molten silicon. This leads to small (µm to mm range) crystals. A second technique is a pull of material out of silicon molten in a basin. This second method, called after its inventor, J. Czochralski, lead to a mono-crystalline cylindrical ingot. Both of these techniques require sawing to create wafers for solar cell production.

For the cast approach the solidified block is deprived of parts in direct contact with the crucible, the remaining brick is sawn in blocks, and then sliced in wafers. These have a squared shape.

For the pulled ingot the approach is almost similar: tops and tails of the ingots are sawn away because of their higher impurity content, the remaining cylinder is sliced in wafers[12].

The wafer slicing is similar for both the cast and the pulled material. A continuous wire of few km runs at high speed against silicon. Before entering in contact with the silicon block the wire is wetted with slurry, a substance containing hard particles which help the silicon graving. The resulting wafer thickness corresponds to the distance between the wire paths minus a quantity which is called kerf. This quantity is the amount of silicon which is eroded by the wire cutting.
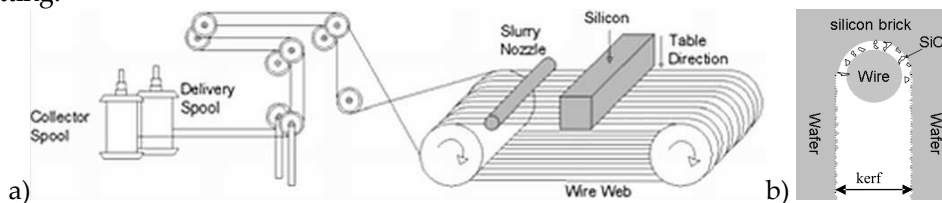

Fig. 3:2 a) principle sketch of a multi-wire saw b) Schematic of the cutting process in one cutting channel. (both from {Schumann, Singh et al. 2009})

Other techniques (EFG {Kaes, Hahn et al. 2007}, RGS {Seren, Kaes et al. }, Mono[2] {Prajapati, Cornagliotti et al. 2009} etc.) are interesting procedures to reduce the cost of silicon wafer production, especially avoiding most of the otherwise necessary cutting.

New sawing techniques are in sight, based on lift off techniques {Dross, Milhe et al. 2008} or proton blast cracking {Henley, Lamm et al. 2008; Podewils 2009}. These could both overcome the issue of kerf loss when reducing the wafer thickness.

3.2   Conventional processing

Significant knowledge of the solar cell processing can be gathered looking at the conventional process. This process will be largely referred to in this work. Few adaptations are required changing from mono- to multi-crystalline cells, this basically reduces to the roughening procedure of the side exposed to the sun.

The material is chosen amongst a wide range of dopant levels, common material is found between $0.2\,\Omega{\cdot}cm$ and $6\,\Omega{\cdot}cm$. The absence of standardization is due to the absence of requirements on the matter. Indeed cells and modules are qualified by power generated under standard illumination conditions.

Different is the issue on the sizes, since the business model allows horizontal stratification of the value chain, geometrical features need to be known for the vertical integration. For example, the products of a cell company must fit in the equipments of a module company. To the present moment, a big part of the market is taken by squared cells with a side dimension of 125 mm and

---

[12] As a compromise between expensiveness of the procedure and maximal use of the surface, the cylindrical ingot are cut longitudinally on 4 chords, each perpendicular to another one, the wafers results then in a shape commonly named pseudo-square, and is characterised by a diameter (the ingot diameter, still visible in most case) and the distance between two chords.

156 mm. The size influences directly the amount of current that flows out from the device. This variability of the size introduces the need for a normalisation. The current is therefore divided on the total cell area and the concept of current density (indicated with J) is introduced.

A depiction of a conventional cell (in this case a mono-crystalline cell Fig. 3:3) gives the possibility to explore its main features. Most of the structure is composed by the silicon, the second most abundant material in the cell is the aluminium on the back surface and finally the silver on the front; dielectric coating and diffused doping material are a small fraction of the whole.
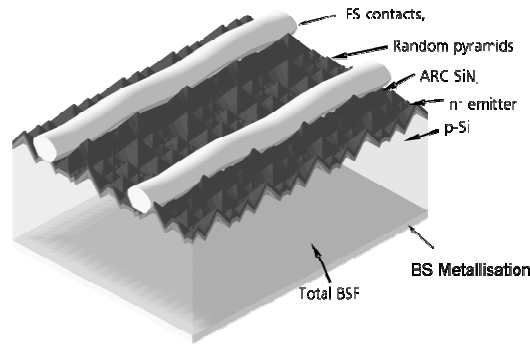

Fig. 3:3 A section of a solar cell realised with the nowadays conventional process.

Below, in chronological order, the steps for the preparation of a conventional solar cell are presented. This structure is identified in the rest of this work by its particular anode structure. This is on the back surface and consists of an aluminium doped layer of silicon in contact with the metal. Indeed, this structure is known as aluminium back surface field (Al-BSF).

♦ *Texturing*

The surface of the silicon is treated in order to create a high number of tilted facets. This exploits ray theory of light propagation, indeed light coming from a perpendicular direction towards the device will have more occasions to penetrate the medium-to-silicon interface before being bounced back.
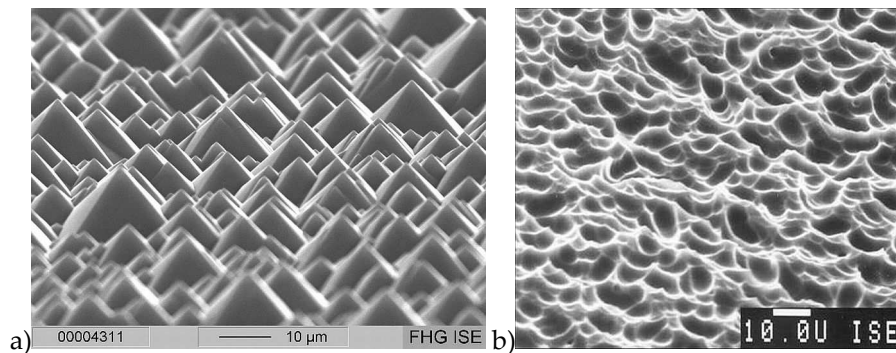
Fig. 3:4 Solar cell texturised surfaces: a) random pyramids. This surface is prepared by alkaline etching on mono-crystalline material with a crystal orientation of 100. b) Rough texture created by wet acidic etching of silicon (from internal image archive).

The substrate undergoes a process which transforms the roughness at the surface. Its starting condition can be flat, as of a polishing procedure or it can be raw as it comes from the cast/ingot sawing. In the latter case, the damaged layer of silicon due to the mechanical stress of sawing has to be removed. The new roughness is therefore created digging specific structures in the silicon. A clear distinction comes with the availability of a prevailing crystal orientation. Of great interest is the case of a mono-crystalline wafer with a specific crystallographic orientation (100). There anisotropic alkaline etching solution creates pyramidal structures. Their

distribution can be imposed with creation of masks or can be random. In the latter case the necessary local masking is performed fostering the formation of bubbles on the surface increasing the surface tension of the liquid {Zimmer, Oltersdorf et al. 2007}.

On the other hand as the crystal orientation is random and varies along the surface, isotropic etching processes are preferred, both dry (SF_6 Plasma Enhanced) and wet (HNO_3 : HF combinations) implementations are available.

♦ *Diffusion*

The $POCl_3$ source is inserted in the furnace through a carrying gas, once the gas reaches the furnace at high temperature a new chemical compound is formed, the P_2O_5. This fixes in the furnace on every surface and especially on the wafers. Once this P source is on the silicon, the diffusion of this specific element, which is now solid matter on the surface, can start. The molecule breaks and the oxygen left on the surface starts to oxidise the surface, much P is incorporated in this SiO_2 and therefore the characteristic of this silicon oxide deviates a bit from a pure one and is named Phosphosilicate glass (PSG).

This kind of quartz glass is better known under the name of Phosphorous Silicon Glass, or PSG. Although insulating, its low thickness and high intrinsic doping allows an electrical contacted measurement of the diffused layer's sheet resistance.

♦ *Phosphosilicate glass etching*

The PSG is removed in a hydrofluoric acid solution, time and temperature can vary. A correct removal changes the hydrophilic into a hydrophobic surface. Increases in emitter sheet resistance, as high as 10%, can be seen after this process

♦ *Front side coating*

To increase the optical performance of absorption in the silicon bulk, an Anti-Reflection Coating (ARC) is employed.

CVD techniques are normally used to create a coating with a thickness of tens of nanometres on the cell. This range of thickness decreases the reflection of the surface being an interference filter. A minimum of reflection for the a wavelength in the middle of the absorption range for silicon ($\lambda_{Si} \approx 660$ nm) is imposed and obtained using a known relation {Born and Wolf 1959}

$$t_{ARC} = \frac{\lambda_{Si}}{4 n_{ARC}(\lambda_{Si})}$$

Eq. 3—1

where the refractive index of the dielectric at the specified wavelength λ_{Si} is indicated by n_{ARC}.

This layer is also enriched with hydrogen during the deposition. This element, due to its small mass, can diffuse easily during subsequent high temperature steps. During this migration it can fixate to dangling bonds of the silicon interrupted crystal and therefore passivate their action. A study on the action of hydrogen on dislocation-rich material can be found in {Pernau, Hahn et al. 2001}.

This process is performed only on one side. On the contrary, all previous steps act symmetrically on both sides. Thus the coated side becomes the front side.

♦ *Metallisation*

Metal layer and contact formation is done in three steps; first a metal paste is printed on the cell through a screen. The paste is composed by metal particles embedded in a mixture of solvents and if necessary glass frits. Silver paste (Ag paste) is used to screen print the grid layout on the front-side, there the glass frits are needed for the local dissolution of the ARC. Aluminium paste (Al paste) and a mixture of aluminium and silver paste (AgAl paste) are printed on the back surface. On finished devices the first delivers a good contact with silicon while the second allows the soldering of the cell to metal ribbon for module production. The second step is drying this wet paste with a short low temperature process (<350 °C) and the third step, called in photovoltaic jargon "firing", is a sintering of pastes performed in an

equipment called Fast Firing Oven (FFO or RTP) at high temperature (T_{FFO}>700°C). Literature studies, {Schubert 2006} and {Huster 2005}, explain respectively how the Ag paste and the Al paste create a contact with the silicon and how, in the case of Al paste, a p$^+$ doped layer is grown by epitaxy. This new layer acts as a back surface field {Godlewski, Baraona et al. 1973}. The AgAl paste is also sintered and creates a contact with silicon, but does not generate any back surface field.
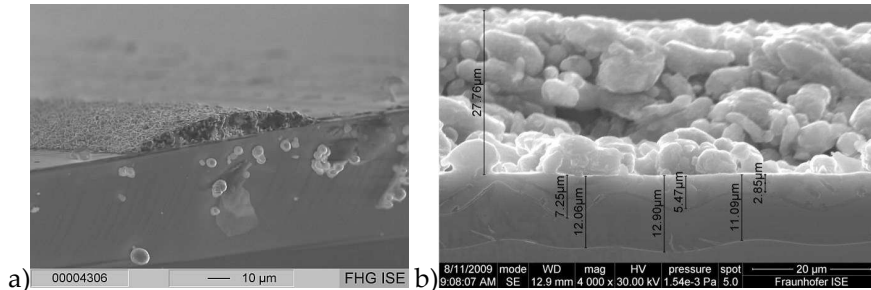

Fig. 3:5 a) Cross section of a front side screen printed finger. b) On the right a cross section of a back surface Al-BSF, the stratification is made possible by chemical etching (see 3.7.2). At the bottom of the image is the silicon, immediately on top, in negative relief, is the epitaxially grown p-type Silicon, the two other layers are composed of aluminium and have specific names, the one below is the eutectic layer and the other is the screen printed and sintered paste.

♦ *Lateral isolation*

The emitter on the front side is connected to the back side metallisation through the emitter diffused on the sides. This connection is detrimental for the cell since it increases the shunting activity, reducing considerably the current that can escape the solar cell under illumination.

Different implementations are used. One elegant solution is trenching the front surface in the vicinity of the edge. In this way the trench interrupts the emitter abruptly. This technique is implemented by means of laser machining. Other possibilities are the etching, cutting, or abrasion of a marginal part of the wafer.

3.3 Advanced process technology

The conventional processing has the advantage of a reduced set of processing steps. On the other hand this structure limits the maximum efficiency of the cell imposing surface recombination velocities in the order of 1000 cm/s down to 300 cm/s on the back. Up to this moment the wafer thickness was preventing the back surface to play an excessive role on the final efficiency (see 2.5). Another drawback of the conventional process is the mechanical stress which the interface between aluminium and silicon builds up during the metal paste sintering. The cell, in case of a thin substrate, warps under the stress and takes a typical bow shape {Kränzl, Schneider et al. 2004}. Albeit a solution has been proposed {Huster 2005}, this challenge remains addressed to the metal paste composition {Popovich, Janssen et al. 2009}.

The cells with reduced thickness (Fig. 2:15) benefit from a moderate surface recombination velocity (*S*). For this reason, concepts which adopt back surface passivation are an interesting approach for the efficiency increase. One candidate which was investigated previously is the Passivated Emitter and Rear Cell, or PERC. This proved itself at the laboratory scale able to achieve more than 20% efficiency {Blakers, Zhao et al. 1989}.

This advanced structure features on the front surface a metallization grid contacting the lowly recombining emitter below the anti-reflecting coating and on the back surface a flattened and passivated surface, where local contacts are made between a locally strongly doped area and a metal layer. A better perception of the structuring needed can be obtained from in Fig. 3:6

Several aspects have to be considered for the realisation of a PERC and they will be briefly detailed below.
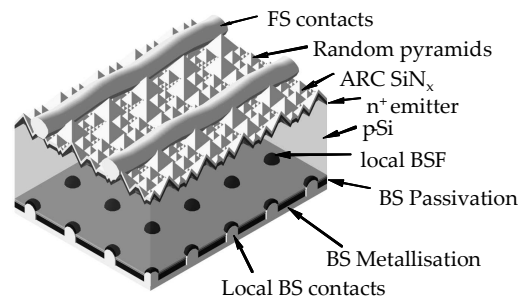

Fig. 3:6 A section of the targeted final structure, all the processing which are requisite to achieve this device will be detailed in the following.

A first aspect is the structuring of the surfaces on the base of their function. The front side, also called "sunny" side, is rough to enhance optical coupling. The back surface is flat to foster internal diffusive reflection and enables a higher potential for the passivation. These different functions make the device asymmetrical from front to back. This introduces a challenge of selectivity on the processing. This is solved with the advanced processing presented below. They are based on the selective removal of silicon on only one side of the wafer. This in turn creates the desired asymmetry of roughness. Both wet and dry implementations are evaluated.

A second aspect is the passivation for the back surface. The device concept needs a low surface recombination velocity to be performant. For this reason different dielectrics were explored in 3.6. Their evaluation has been performed in terms of passivation quality and integration with the metallization process.

A third aspect concentrates on the quality of the emitter on the front side. A normal emitter presents high saturation currents (J_{0e}), which in turn limits the potential of the solar cell. In this work one option for the decrease of J_{0e} was evaluated.

The fourth and last aspect is the local contacting which has to guarantee an electrical contact from the metallization to the cell and furthermore avoid the creation of strong local recombination areas.

The tendency is to improve and refit existing industrial technologies. This approach is interesting for industry since the initial investment is committed to an evolution of a previously existing production line. This reduces the amortization time.

In the following, the main achievements for modified processing steps will be described; they will be listed in a processing order, whenever this was possible.

3.4 Single side etching application, emitter removal and surface flattening

After a brief introduction, the work realised within this thesis will be described, two different procedures will be discussed in detail.

3.4.1 Importance of one sided etching

Beaucarne et al. {Beaucarne, Choulat et al. 2008} argue that a low roughness of the rear surface is an essential characteristic of high-efficiency cell concepts. This is further confirmed by a study on back surface flatness {Rentsch, Gautero et al. 2008} where this property is correlated to the optical light trapping (2.2.1) and the passivation quality.

This desired low roughness on the back surface is not present in conventionally processed solar cells. Process steps, such as wet chemical texturisation and junction diffusion, treat equally front and back surfaces: in other words the desired structuring of the front is also created on the back. Therefore, a junction and a rough surface will also be formed at the back, which reduces the internal reflection especially for mono-crystalline cells.

The two sequences proposed in the following interrupt the front to rear symmetry by removing silicon from one side of the substrate. The emitter will therefore be etched and, when the etching rate allows it, the rough optical structuring is entirely removed. The so prepared surface will therefore be suitable for the functions of a back surface.

The diffused junction itself could be used for back surface passivation purposes {Ghannam 1991}, though it introduces challenges to characterise imperfections of implementation {Honsberg, McIntosh et al. 1997; Breitenstein, Langenkamp et al. 2000; McIntosh, Boonprakaikaew et al. 2000}. This special passivation path will not be considered in this work; therefore the back surface emitter will always be removed.

The removal of the back surface emitter will sever the ohmic path at the edge of the cell between the cathode and the anode metallization. This avoids additional isolation processes (i.e. laser isolation on the solar cell front perimeter, as seen in 3.2) which eliminates edge shunting that affects the solar cell performances.

The flattening removes a non negligible part of silicon. Since geometrical features on the order of dozens of micrometers have to be eroded, it is significant to characterise the weight of removed silicon. The homogeneity of the etching (which is rarely an issue in inline processing) is evaluated by naked eye.

3.4.2   Wet back surface etching evaluation

The investigations at the **Fraunhofer ISE** were performed on industrially available devices, such as an inline chemical equipment from the company **SCHMID**. As sketched in the drawing Fig. 3:7, the chemical solution is brought in contact with the target surface by surface tension.
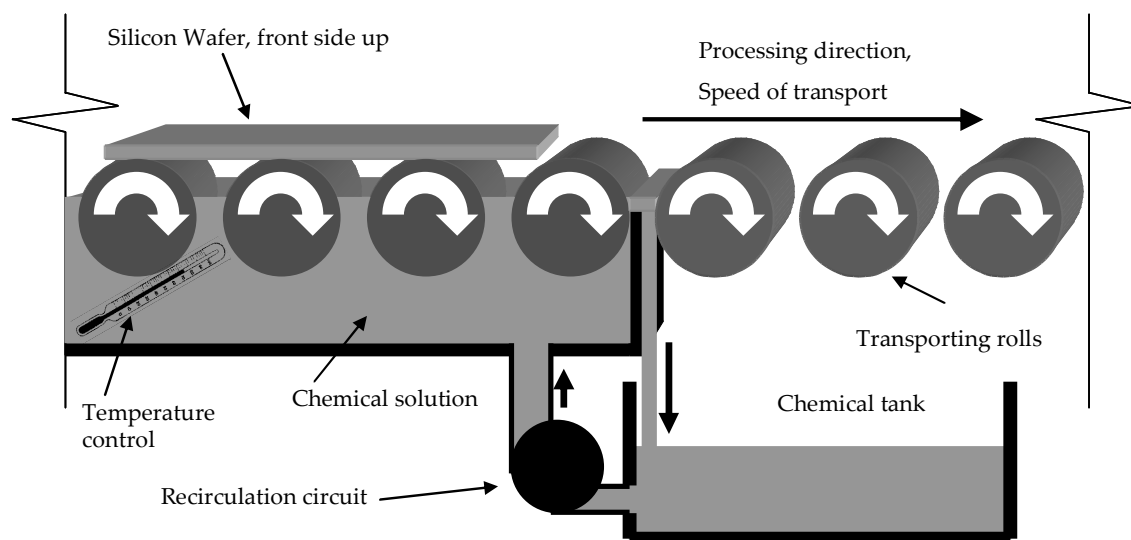
Fig. 3:7 Sketch of a representative part of the equipment configuration: the rolls, partially submerged, deliver the chemical solution to the exposed side of the wafer when the contact angle between liquid and roll surface is low. The temperature is controlled with a sensor in the bath (ironically sketched with a thermometer). The speed of the transport is controlled by the rotation speed of the rolls. The level of the bath is set by the pumping power of the recirculation circuit. The chemical tank is the reservoir of the chemical solution.

The chemical solution used is a well known silicon etching solution ($HF:HNO_3:H_2O$) {Robbins and Schwartz 1961}. This solution is based on a silicon oxidizer (HNO_3) and a silicon

oxide etcher (HF). Their concentrations are known to be concurrent on the action on the silicon. High concentrations of HNO_3 oxidise any open surface of silicon available, the HF is then the limiting factor and its diffusion is therefore the limiting factor. On the other hand, low concentrations of HNO_3 are more sensible to the criteria of SiO_2 formation. Crystal structure and electron availability are one example.

In the following four experiments are described. These help to understand how the equipment could implement the front to back isolation and the polishing on the targeted side.

♦ *Influences of equipment settings on etching rate*

From the first runs of the one side etching (1SE), knowledge about the most important settings was gained. This practical experiment needs to be further investigated for a systematic evaluation of the surface conditioning process. The most straightforward parameter that can be changed is the temperature. However, increasing the temperature can be deleterious as well since the vaporisation of the solution is also enhanced. This is dangerous for the working environment, and furthermore compromising for the front side. Consequently, its vapours[13] can also etch silicon and drastically affect the emitter thickness from its optimal value. Other parameters closer to the practical working principle are the revolving speed of the rolls, which influence the exposure time of the wafer surface; and the recirculation of the chemicals in the bath where an increase in the pumping speed leads to an increase of the chemical bath level (Fig. 3:30). A large experiment was undertaken to understand the impact of these settings. The following experimental realisations were used to investigate these effects in regard to their influence.

◊ *Temperature and recirculation*

The experiment used a 3 level full factorial design for two variables, adopting one sample per case. The material (p-type Cz-Si, $\rho = 1 \div 3$ Ω·cm, pseudo square, 156 mm side, 200 mm radius, 210 μm starting thickness) was treated in order to present the textured and diffused structure only on the back surface (Fig. 3:8). To attain this selectivity a diffusion barrier on the front was adopted.
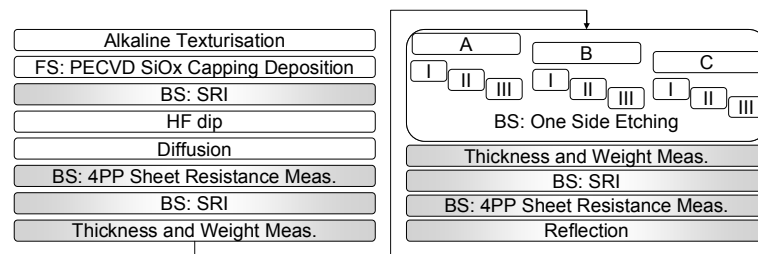
Fig. 3:8 Process performed on the material, detailed are also the characterisations used for the purpose of the batch. See Table 3—1 for details on the variations in the experiment.
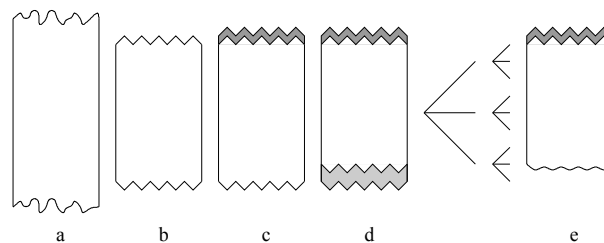
Fig. 3:9 Sketch of the sample through the processing, a: wafer as cut, b textured wafer, c: wafer capped on the front side, d wafer diffused only on one side, e: expected structure after the 9 combinations

---

[13] within which NO and HF can also be found, the first being an silicon oxidizer and the second a strong etcher for SiO2

The characterisation measured the sheet resistance by means of a 4PP and Sheet Resistance Imaging (SRI) (see Appendix A.a). Of interest is also the amount of silicon removed. These measurements are done before and after the 1SE processing; the reflection measurement of the treated surface is performed after the 1SE. One single value is calculated from the spectrum of reflections this is called weighted reflection.

The 9 combinations that were realised (Fig. 3:8) affect the monitored parameters. The data collected from the work was analysed in order to check whether a significant relation between process and measured values could be determined.

Table 3—1 Experimental combination realised, letters indicate different temperatures of the bath, and roman numbers represent the recirculation value.

Combination number	Temperature (°C)		
Recirculation (ℓ/min)	12	14	16
58	A I	B I	C I
60	A II	⁍ II	C II
62	A III	B III	C III

The most interesting result of the process is the etching rate. All samples are run through the equipment at the same speed (65 cm/min, the wafer stays in the etching section for 1 min and 10 s), therefore the etching rate can and is given as the amount of silicon removed, whereas the time information can be neglected. A polynomial second order surface that best fits the results takes into account one interaction of the first level, showing that there is an interaction between the two settings (Fig. 3:10). This fit cannot be tested for a "lack of fit" due to the low amount of samples, though by observing the residuals (Fig. 3:11), it can be deemed a good model in the range studied.
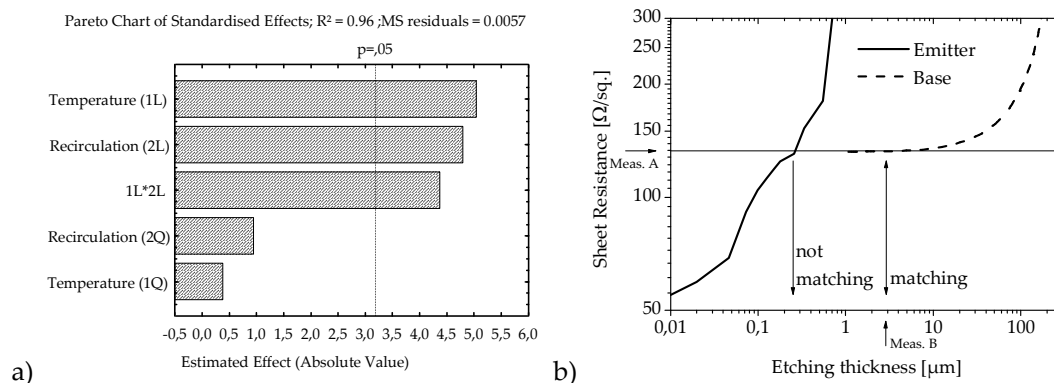
Fig. 3:10 The effects are ordered in this graph from the most to least significant. In this graph, 1 and 2 indicate respectively the temperature and the recirculation variation. The letter L and Q indicate the linear or the quadratic effect (See A.h.II for additional information regarding this and other graphs). b) The procedure to attest the emitter removal is sketched in this graph. The calculations are based on a 50 Ω/sq. emitter on a 300 μm thick silicon substrate with a resistivity of 4 Ω·cm. The sheet resistance value (Meas. A) could be measured on an etched emitter or on an etched base. Comparing the depth with the measured one (Meas. B) it is possible to prove the emitter removal.
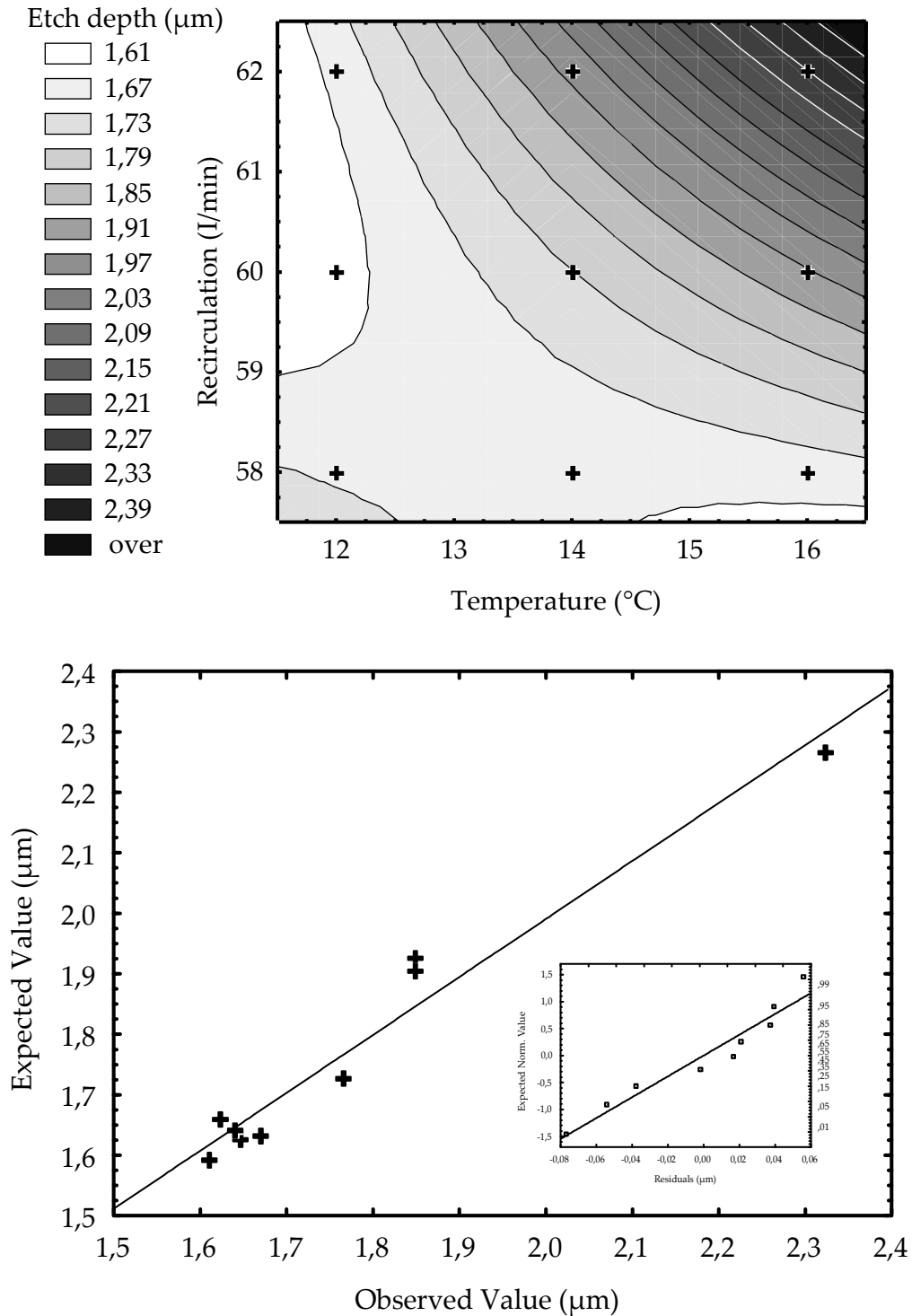
Fig. 3:11 Display of the regression fit: on the left is the surface that is represented by the regression and the points where measurements were performed; on the right is the deviation of the model from the observed values.

Once an understanding on how to influence the silicon removal was achieved, it is interesting to investigate how this value is related to the emitter etching on the whole surface and if a polishing effect can already be seen.

The emitter removal at the back is verified through two measurements, the first being the calculation of the average thickness of silicon removed. This can be obtained once the area of the treated surface and the density of the silicon wafer are known. This depth is then compared

with the known emitter depth for the specific diffusion process. This comparison is normally sufficient to state the complete removal. In case these are similar and raise doubts on the effective removal, the distribution of several values from a 4PP sheet resistance measurement on the etched surface can be used to calculate which amount of emitter attack[14] would be necessary to obtain that value (see Fig. 3:10 (b))

To state a simple example, assume the emitter profile is known and its maximum observed depth is 0.5 µm. From the profile and by using a well known mobility model in silicon for silicon {Masetti, Severi et al. 1983; Clugston and Basore 1997}, the total sheet resistance can be calculated. By using this sheet resistance, an attack on the emitter can be simulated.

On one hand, the silicon etched is calculated by weight difference and on the other hand the sheet resistance of the targeted surface also is measured. Based on the fact that a change in the emitter thickness of a few nanometres leads to a steep increase of the sheet resistance (well above the normal sheet resistances that can be measured on silicon bulk used in photovoltaics), a comparison between these methods can be performed.

In this experiment the diffusion step produced an emitter with a sheet resistance of 51±1 Ω/sq., and after the 1SE processing the measured value is found to be 176±2 Ω/sq.; this value would be measured on the same diffused emitter for a removal of around 30 nanometres. Since the minimum silicon removal observed is higher than this value, it follows that the emitter was successfully etched and the value of sheet resistance corresponds to the base resistivity.

In this experiment the emitter was entirely removed for all samples. Both of the following conditions were met: 1) higher average etching than emitter depth and 2) sheet resistance disagreement with an emitter attacking configuration. However the homogeneity of emitter removal is not confirmed. To investigate this aspect, the SRI technique can be used.

In the first analysis, the difference of SRI values before and after every process gave a large amount of data for every sample. The resolution of the measurement provides 4 pixels per mm^2. To gain an overview, the median and the value at respectively 15.9% and 84.1%[15] of the cumulative probability is reported. These values are consistent with a nought value, which means that all samples produced a signal after the etching that is consistent with the signal produced before the diffusion.

At the same time, since SRI is an imaging method, it was possible to observe a shift of the median linearly related to the change in reflectance (Fig. 3:12).
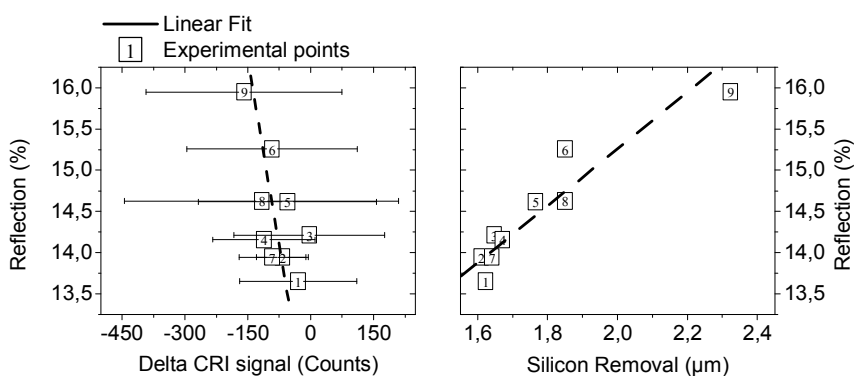
Fig. 3:12 Analysis of the experiment results. The number in the square indicates the combination, as of Table 3—1. On the right is the dependency of the reflection on the range of etching that could be produced. This graph indicates that much higher etching rates are needed

[14] An attack on the emitter is used here to indicate that parts have been removed from the emitter, but it has not been removed completely

[15] This procedure permits the exclusion of outliers; the two values at that cumulative probability correspond to the position of the standard deviation of all data of interest, excluding outliers.

if the target of maximum reflection (~35% wt) is targeted. On the left are the results of the differential SRI measurements. All experimental points give a result consistent with the value 0, which indicates complete removal of the previously diffused emitter. However, since the SRI method depends on optical properties of the surface, a significant influence could be determined. The observed departures from the baseline are still in a 1% range from the counts generated during the actual measurements.

The second analysis shows a linear change of weighted reflection due to the amount of silicon removed (Fig. 3:12): still, the value is far from the target value of a polished surface (35 %). The graph presents the measured value of reflection on the abscissa, while on the ordinate is the effect of the process. On the left is the shift of the SRI signal, and on the right are indicated the micrometres of silicon removed

◊ *Recirculation and speed*

A set of 100 wafers (p-type Cz-Si, ρ = 1÷3 Ω·cm, pseudo square, 156 mm side, 200 mm radius, 210 μm starting thickness) was processed following the scheme in Fig. 3:13 with all the steps needed to realise working solar cells. The diffusion process targeted an emitter sheet resistance of 70 Ω/sq.
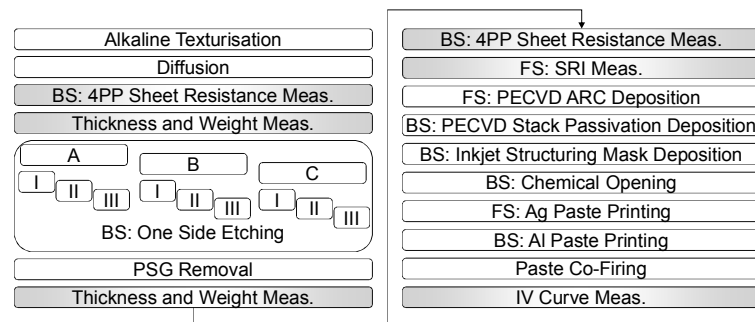
Fig. 3:13 Schematic of the processing used for the realisation of solar cells. The 1SE step had a combination of three recirculations (A = 57 ℓ/min, B = 60 ℓ/min and C = 63 ℓ/min) and three speeds (I = 57 cm/min, II = 65 cm/min and III = 72 cm/min), highlighted are the characterisation steps, stressing the differential characterisation of the 1SE process.

Of relevance for the investigation are:
- the loss in weight after a 1SE
- the change of the front side sheet resistance.

Furthermore the processing of these samples towards complete solar cell, featuring also a passivation layer at the back, can deliver information on the modification of the cell parameters as a response to the experimental part. This will be presented in the second part of the experiment.

First: Silicon etching

For this polishing step, the objective is to maximise the etch rate and minimize the damage to the front side emitter.
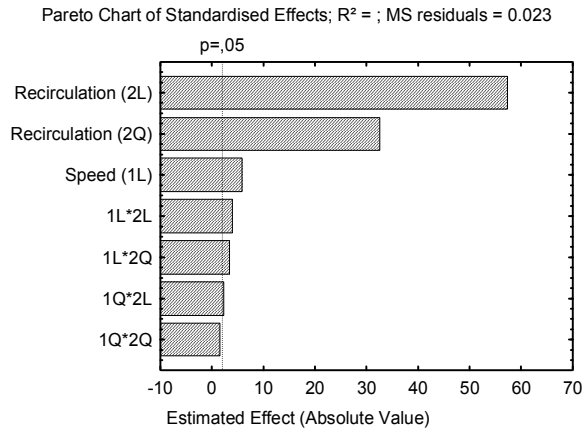
Fig. 3:14 Pareto chart of the effects; though the main role in the silicon etching is played by the recirculation, several other factors or interactions have significant effect. The full factorial design and the high number of repetitions allow the numerical evaluation of these effects to be trusted.

Fig. 3:15 Two SRI images offering a clear view of relative changes in emitter sheet resistance on two processed wafers; the difference between the two is the number of runs. On the right (wafer 7009) is the first wafer, which ran under certain processing parameters, and on the left (wafer 7008) is the last. This issue was l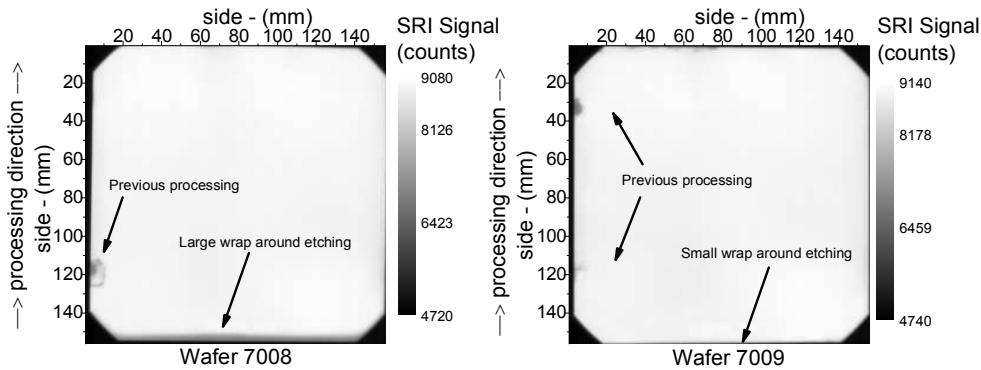ater solved and the large wrap around etching removed. The sensitivity to previous processing was stated with differential measurements pre and post 1SE.

By analysing the etching rate at the different equipment configuration the effects can be sorted (Fig. 3:14). The overall correlation is acceptable ($R^2 = 0.68$) and allows the interpretation of the statistical results. The recirculation has the strongest normalised effect. Nevertheless, speed is also significant for a change in the output. However, it can be safely stated that increasing in the bath level the silicon removed increases as well.

The variations are significant on the depending variable (silicon etched). Furthermore, it is possible to observe linear and quadratic dependency. The data can therefore be fitted with a high correlation value (see Fig. 3:16).

Much more illuminating is the graphical representation of the data, where the recirculation shows the biggest influence. Only at higher recirculation a slight influence of the speed can be seen.

As in the previous experiment, the emitter on the back surface was entirely removed for all samples. Both of the following conditions were met: 1) higher average etching than emitter depth and 2) sheet resistance disagreement with an emitter attacking configuration.

As characterisation for the front, thanks to the SRI technique, it was possible to map relative changes over the whole area of the wafer (Fig. 3:15). Evidence of etching of solution which wraps around the edges was identified. This issue became evident especially after consecutive long usage of the equipment, due to the wetting of transporting rolls (Fig. 3:7). This conundrum is therefore identified and minimized through a modification on the equipment. Albeit this

etching of the front side is measurable, it was not possible to detect a significant decrease in R_{shF}. Results from large wrap around of chemicals (as in the wafer 7008 in Fig. 3:15) were on average similar to small wrap around. This preemptive move is in any case necessary in sight of the necessary increase of recirculation which targets higher etching rates (Fig. 3:16).
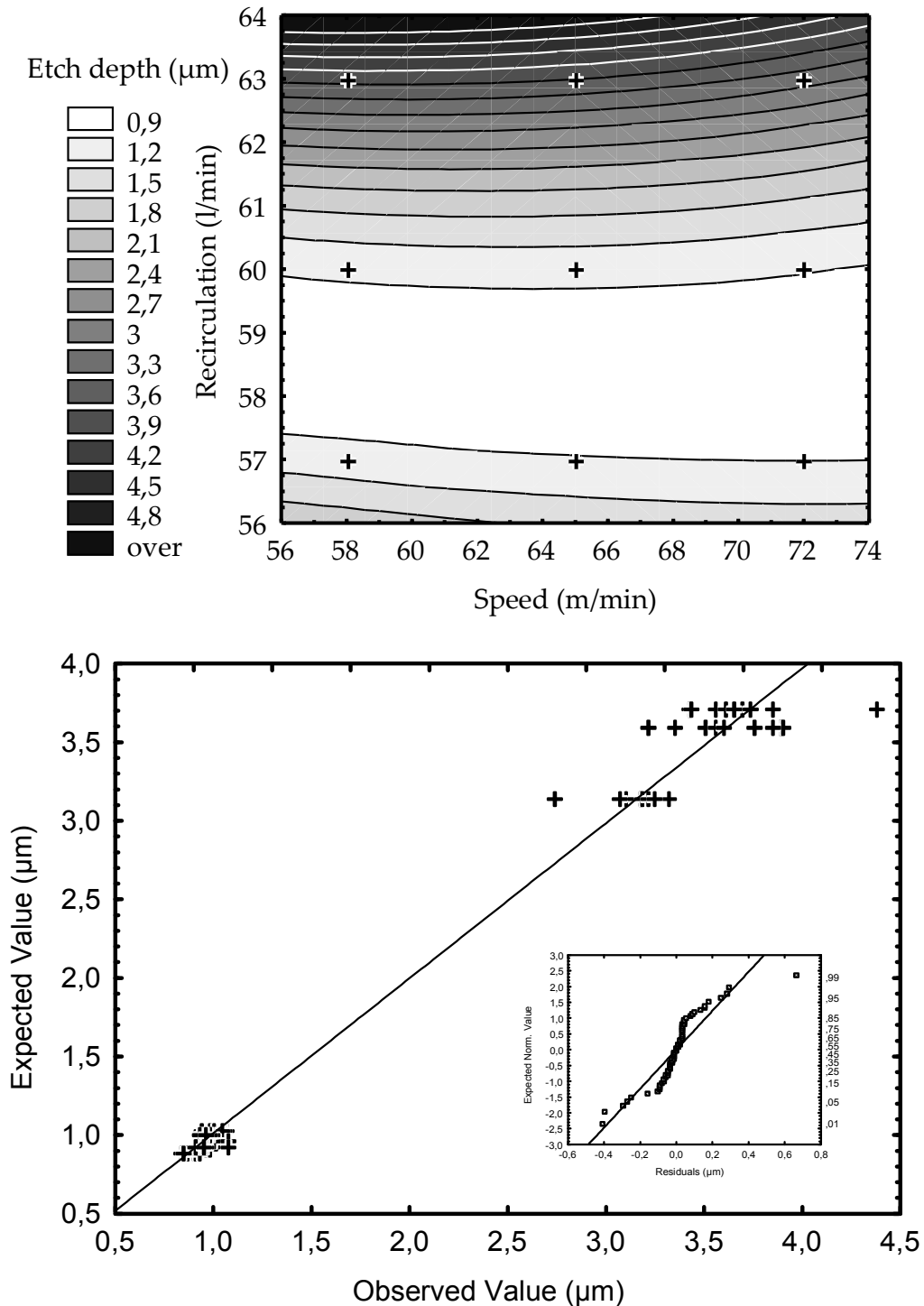

Fig. 3:16 Regression fit of the observed data presented as a contour plot. The gray scale indicates the amount of silicon etched in μm. On the right is the clustering of the produced data, samples prepared with a higher recirculation differentiated largely from the other combination.

Second: Solar cell characteristic

The silicon removal is a value of interest for the final cell characteristics. Its correlation to variation of cell parameters was investigated. The targeted parameters are:

- The V_{OC} for an indirect evaluation of the passivation quality,
- The J_{SC} for an evaluation of the light trapping improvement,
- The R_{shF} to verify the decoupling of the front emitter from the metallic contact of the rear surface.

Unfortunately the variation of silicon removal seems to be too small to directly show significant influence on solar cell parameters; V_{OC} and J_{SC} were unaffected by the setting variations, though the R_{shF} showed a significant increase in its value for higher amounts of silicon removed. This positive correlation guarantees that the wet single side etching processing delivers a homogeneous emitter on the front, which can be correctly contacted with a front side metallisation. This confirms that even the large wrap around detected is not affecting the solar cell performances.

♦ *The chemical solution*

Initial processing on the equipment resulted in low etching rates. To explore the capability of the chemicals employed, an experiment with complete immersion of the samples was performed.
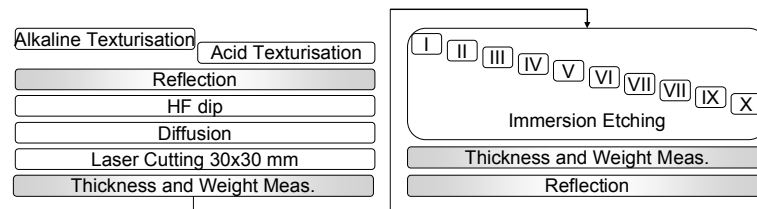
Fig. 3:17 Processing of the samples. The ten variations corresponds to the ten points in Fig. 3:18
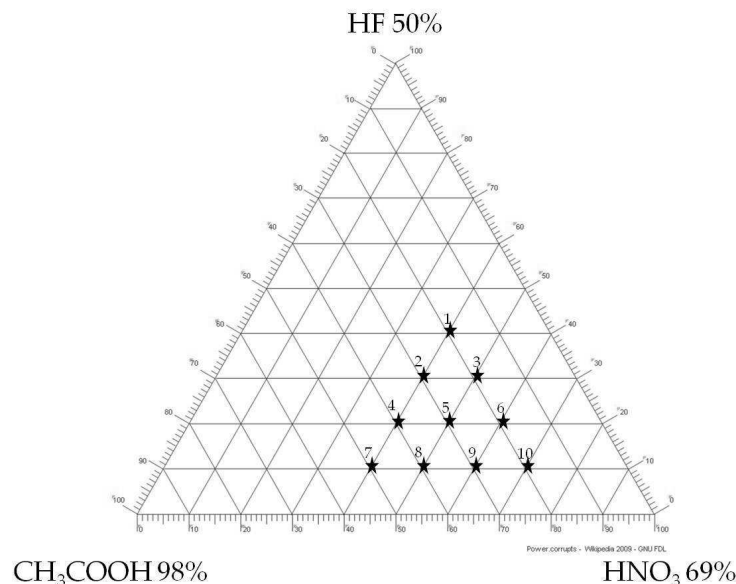
Fig. 3:18 Solutions used for the full immersion experiment, display of the investigation points on a ternary plot (empty ternary plot from Wikipedia 2009 GNU FDL).

The starting material (p-type Cz-Si, $\rho = 3 \div 6\ \Omega \cdot cm$, pseudo square, 156 mm side, 200 mm radius, 280 μm starting thickness and p-type mc-Si, $\rho = 0.5 \div 2\ \Omega \cdot cm$, full square, 156 mm side, 270 μm starting thickness) was processed to achieve a surface structure used in photovoltaic applications (Fig. 3:17) and then cut into several pieces of 30 mm x 30 mm; this allowed a larger

number of samples. There is sufficient surface to characterise by weight the etching rate and neglect edge effects. This area guarantees enough space to perform a reflection measurement on a spectrometer (see A.d).

In this experiment solutions are prepared from different ratios of the chemical formula ($HF:HNO_3:CH_3COOH: H_2O$). The first two chemicals, namely hydrofluoric acid and nitric acid, were already mentioned in previous experiments. The third chemical (acetic acid) helps to reduce the surface tension, hence to increase the surface wettability.

Each chemical is delivered mixed with a certain percentage of pure water which is clearly indicated on the containers. Mixing the chemicals to obtain the desired molecular weight will result in including a certain amount of water. This amount of water in the total mixture depends on the purity of the chemicals (indicated in Fig. 3:18).

This analysis also leads to another insight about the etching of silicon on structured front sides. The variation of material used, mono-crystalline and multi-crystalline silicon, presents two initial textures, respectively: regular pyramids, randomly distributed on the surface, and sharp peak and wide valley. As mentioned before (3.2), these two configurations have different reflection values.

The dependent variable is the difference of reflection before and after the chemical polishing; indicator of the regression quality is also reported. The results of the analyses presented below takes time and starting conditions in consideration as well as molecular weight. A multiregression model fits significantly ($p_{test} < 0.01$) with all the input variables used with a good correlation value $R = 0.92$. However, higher correlation values are achieved when considering only the three molecular weights of the chemicals. This shows that these three quantities have the greatest effect on the independent variable.

In Table 3—2 both the multiregression coefficient (indicated with B), and the normalised coefficient are reported. The first can be used to forecast the final reflection when the 5 input variables are specified (of course the validity range is limited to the explored space of combinations). Instead, the second gives an immediate picture of which variables have the strongest influence on the polishing action.

Table 3—2 List of the results from the multi-regression analysis. In the Beta column are the normalized coefficients, these indicate which parameter has more influence. In the B column are the coefficients which can be used for a prediction of the resulting weighted reflection value.

N=35	R= .92; Std error. of estimation: 2.2143					
	Normalised contribution					
	Beta	Std er. Beta	B	Std er. B	t(29)	p-value
Model Constant			-158.11	73.88	-2.14	0.041
Time (s)	0.20	0.07	0.14	0.05	2.86	0.008
Starting Reflection (%)	-0.69	0.07	-0.47	0.05	-9.68	0.000
HF	3.24	1.21	8.86	3.30	2.68	0.012
HNO3	3.10	1.42	11.69	5.35	2.18	0.037
CH3COOH	3.24	1.45	8.30	3.73	2.22	0.034

The characterisation of the processed samples concerned the weight of removed silicon and the reflection on the surface. The target weighted reflection is about 35%wt, the maximum achievable value on silicon.

A multi-regression was performed on the data set. It shows that the increase of reflection during the processing varies linearly with the molar weight of the chemicals in the solution, the time of immersion and the reflection of the surface structuring prior to the etching, the latter being the only one having a negative effect[16] (see Table 3—2). The investigation showed that

---

[16] The geometrical precision of the pyramids in the "random pyramid" structure guarantees low reflection values. This precision can be easily interrupted by etching, resulting in a fast increase in

starting from a lower reflection implies a steeper increase in reflection gain. The high correlation value is also proven by the residuals (Fig. 3:19)

On the same set of data, if a smooth surface is intended to have a high value of weighted reflection. It is observed by means of multi-regression that smoother surfaces are obtained with greater silicon removal. However, different solutions lead to smoother surfaces with different "smoothing rates" (strong correlation between silicon removal and smoothing but poor correlation between time and smoothing). In other words, different solution having the same etching rate can result in different smoothing rates.

The results showed that the concentrations used, which are a variation of the concentration used in the industrial equipment, resulted in a much higher etching rate in full immersion compared with the inline device configuration. The reason for this will be discussed in the conclusions.
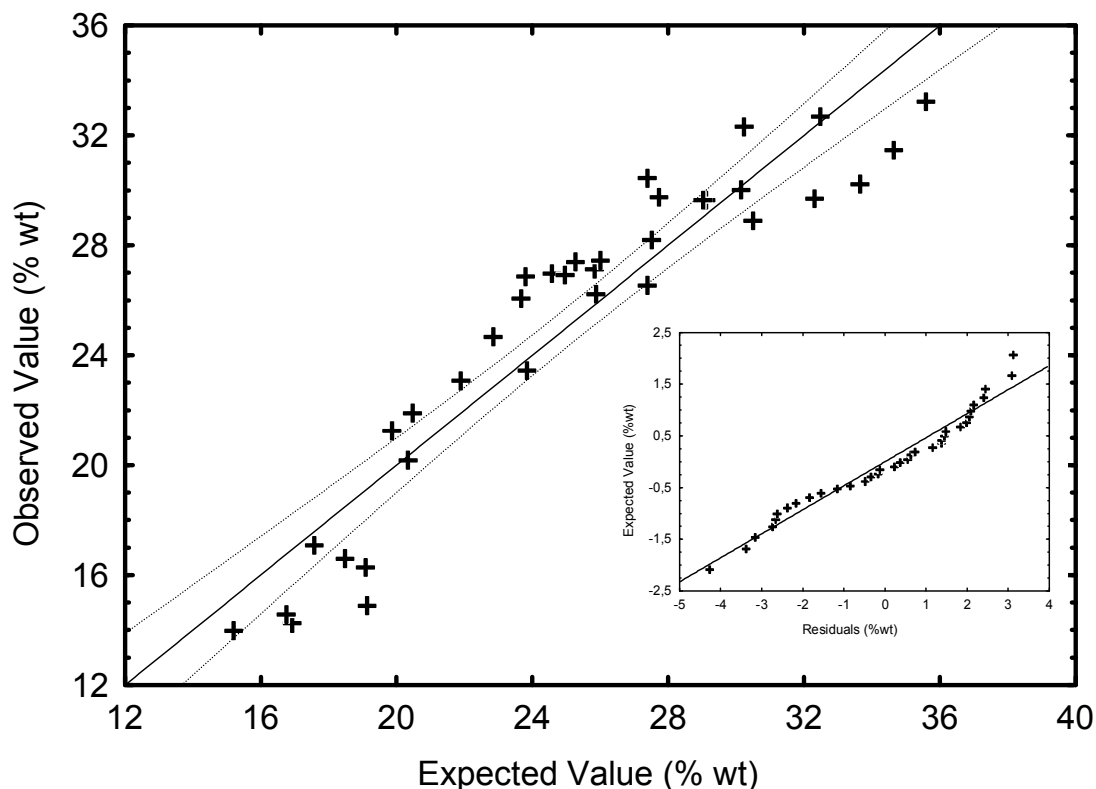
Fig. 3:19 Evaluation of the multi-regression on the data set. In the inset the alignment of the residuals on the line shows their normal distribution. The graph plots for each model value expected from the model for a certain parameter combination the measured (observed) value. The validity of the multiregression is therefore easily visualized.

A final observation was done on a wavelength of 1200 nm. This wavelength, and generally all the infrared part of the light spectrum, can travel the whole bulk of the sample without being absorbed. This is therefore an ideal candidate to evaluate internal reflection. Reflection values taken in the infrared part are also called escape reflectance. Albeit the high value implies a direct reflection from the measured surface, the transparency of a thin substrate of silicon at this wavelength allows a different interpretation. Indeed, the rays penetrated the bulk of the silicon and were reflected at the back. The reflectance measurement at this wavelength is therefore a

reflection. On the other hand, the isotropic texturing has to be profoundly modified to achieve an increase in reflection. Still it is worth mentioning that on average, higher reflections within the conditions of this experiment are realised on multi-crystalline materials.

quality value for the capability of internal reflection of the structure. Similar analyses have been previously performed for the optimization of highly efficient solar cells {McIntosh, Shaw et al. 2004}.

Fig. 3:20 Escape reflectance at 1200 nm. A convergence value of the two initial surface structures weighted reflection is seen with an increasing amount of removed material. The small sketches intend to give a first explanation.

In Fig. 3:20, all the measured reflections at 1200 nm are plotted versus the amount of silicon removed from the inspected substrate. In the picture three sketches have been inserted to a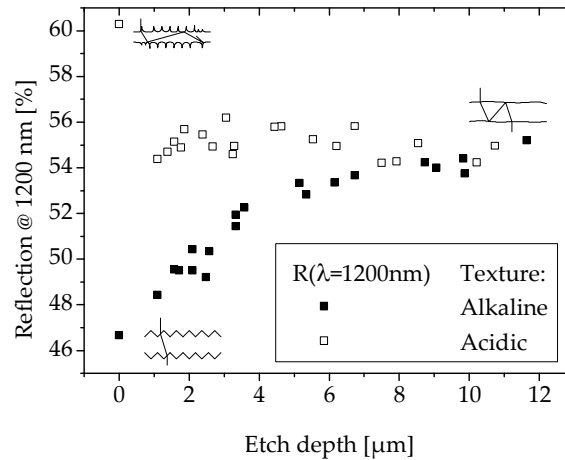llow a better comprehension of the resulting values measured. They correspond to the two initial states of the two surface textures (acidic and alkaline) and to the final polished state.

The acidic texture sketch shows that the random structure offers low coupling for rays travelling from the air environment above towards below. This explains the high value of escape reflectance.

The alkaline structure with its atom scale precision of facets angles guarantees a better exchange of rays between the air above and below. However, the value is not 0 since the measurement is done with diffused light, which has rays impinging on the surface in all directions.

The case of both sides polished, towards which both initial structures converge during silicon removal, is relatively convenient for light exchange since the structure result is almost symmetrical. Indeed, the low roughness still present is completely random and therefore contributes to the scattering of light in the bulk.

♦ *Doping range*

One additional consideration refers to the doping of the material to be etched. The chemical solution used, in certain concentration ratios, is also known for its selectivity towards differently doped silicon areas. With an experiment, we will elucidate whether effects linked to surface tension of the roll-wafer-air system shift the selectivity of the solution towards the doping.

The experiment will include a variation of substrate doping and of surface tension. The doping range is consistent with the usual resistivity of photovoltaic material. In addition, the surface tension configuration will be influenced by an additive, namely acetic acid.

Two sets of samples with resistances in the range of photovoltaic application (p-type mc-Si, measured average $\rho = 1.4\,\Omega\cdot$cm, full square, 156 mm side, 200 μm starting thickness and p-type mc-Si, measured average $\rho = 6.7\,\Omega\cdot$cm, full square, 156 mm side, 270 μm starting thickness) was textured and diffused on both sides, obtaining a rough surface and a sheet resistance of $64.6 \pm 0.6\,\Omega$/sq. at the surface. After this first preparation they were etched on one side (Fig. 3:21). Attention was paid in the measurement of the emitter removal, especially in the lowly doped material.

| Acid Texturisation |
| Reflection |
| Sheet Resistance Induct. Meas. |
| Cleaning |
| Oxidation |
| HF dip |
| Sheet Resistance Induct. Meas. |
| Diffusion |
| Sheet Resistance Induct. Meas. |

| Thickness and Weight Meas. |

Material A | Material B
I | II | I | II
BS: One Side Etching

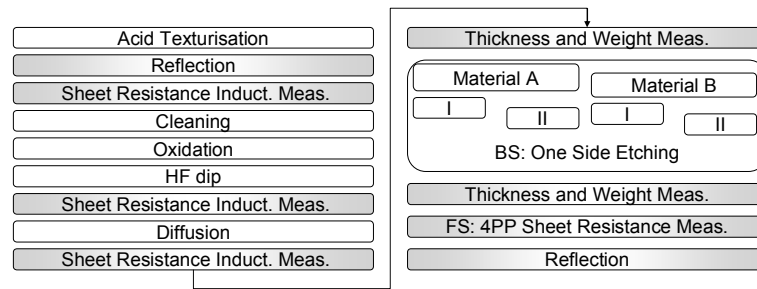| Thickness and Weight Meas. |
| FS: 4PP Sheet Resistance Meas. |
| Reflection |

Fig. 3:21 Process sequence for the creation of the samples, the PSG etching step was not carried out. The two materials (A and B) have different doping level. The setting I and II differ in the concentration of acetic acid.

The first group of each material is processed with the acidic etching solution (HNO_3:HF:H_2O). Then acetic acid is added (3.3 % wt) to the acidic etching solution and the remaining groups are processed. The processing speed is 1.2 m/min.

Pareto Chart of Standardised Effects; R^2 = 0.82; MS residuals = 0.0000189

p=,05

Additive (L)   8,344426

1*2   -1,22001

Doping (L)   ,7773031

0 1 2 3 4 5 6 7 8 9 10
Estimated Effect (Absolute Value)
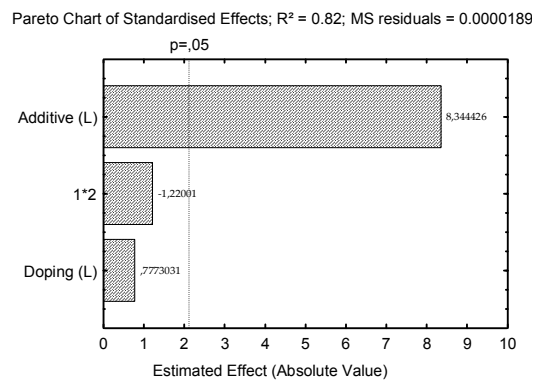
Fig. 3:22 Pareto chart indicating the acetic presence as the factor with the most influence. The interaction level is also considered (1*2).

Analysis showed that the doping of the bulk does not contribute to a different etching rate. However, a significant increase in etching rate is measured on the wafers etched where acetic acid was added to the bath. This confirms previous investigations {Robbins and Schwartz 1961}.

3.4.3 Dry Chemistry

Another possibility for removing silicon is offered by the plasma phase of specific gas mixtures. The equipment used for this implementation is an inline plasma etcher by **Roth & Rau**, where the wafer enters a vacuum chamber and runs under a shower of gas(es) in the plasma phase. This phase condition is attained by a microwave antenna close to the gas openings. The reacting gas is SF_6, oxygen can be present in addition {Hofmann 2008}. The setting is described as a chemical etching.

Previous internal experimental runs brought to evidence a recipe which removes silicon with a reasonably fast etching rate (>0.65 μm/min). Thus, variations around these settings are adopted in the following detailed experiments.

Fig. 3:23 Plot of the averages and their 95% confidence range, the difference in doping moves the amount of etched silicon within the confidences, while the additive is able to change the etching significantly. b) Good agreement could be found between the observed values and those predicted from the linear interpolation model.

♦ *Single sidedness*

As for the wet chemical etch, the evaluation of this processing step for photovoltaic applications passes through its compatibility with the comp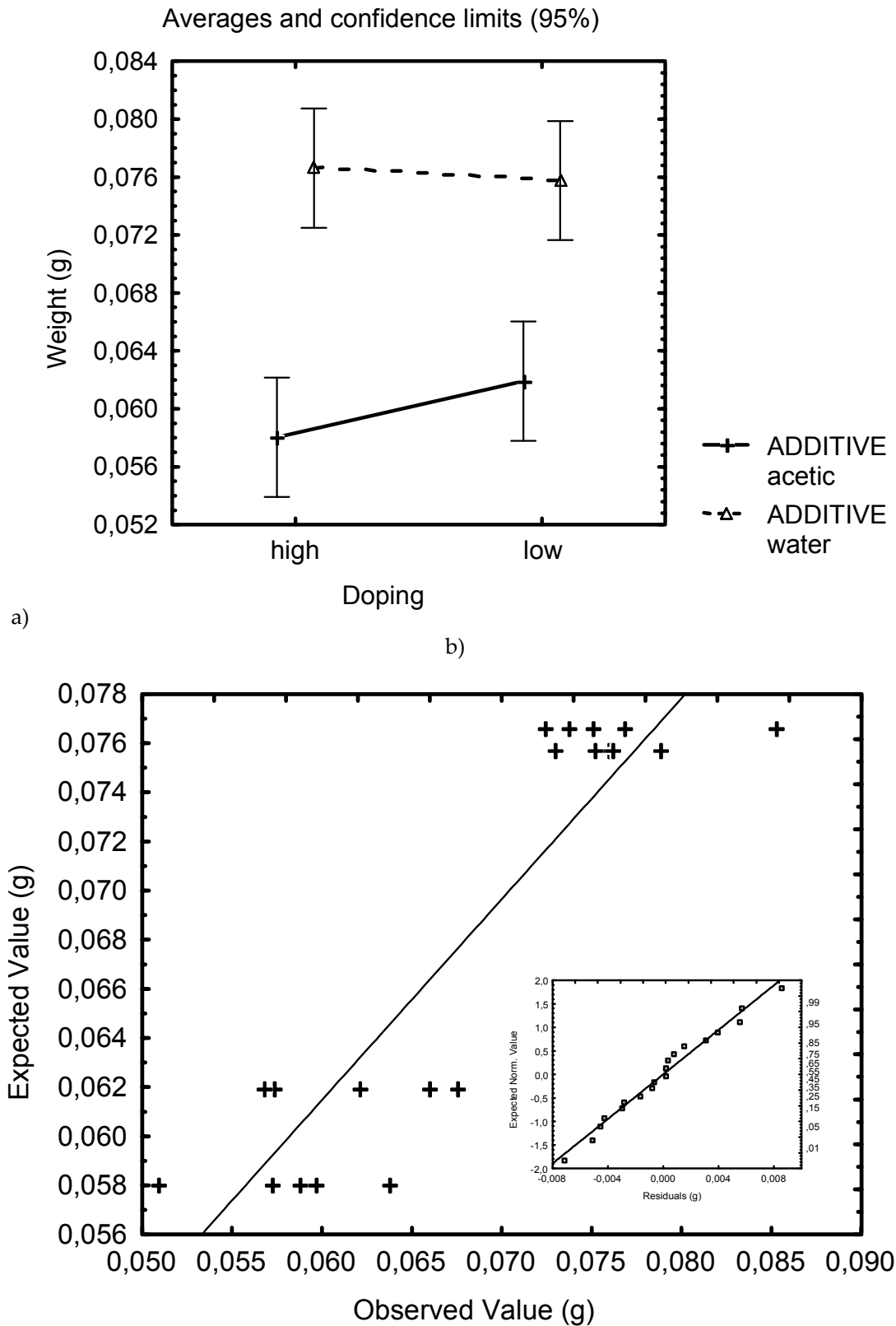lete solar cell fabrication process, the single sidedness is therefore paramount. This property is evaluated in this experiment.

When the sample are prepared for the etching variation (Fig. 3:24) they present on the side opposite to the polishing treatment (front side FS) a 70 nm thick SiN_x. After the polishing treatment the coating thicknesses on the edge and on the centre of the substrate depend on the amount of etching plasma phase wrapping around the target side. A thickness close to the original one suggests good single sidedness. The thickness measurements were performed by ellipsometry, which gives access to variation of thickness in the nanometres range with low error.

The material used for this experiment (p-type FZ-Si, $\rho = 1\,\Omega\cdot$cm, pseudo square, 125 mm side, diameter 150 mm, 250 μm starting thickness) has the front side capped with SiN_x up to a thickness of about 70 nm (Fig. 3:24). The etcher equipment implements the plasma phase of the gases above the carrier; for this reason, the coated surface (FS) will face the bottom.
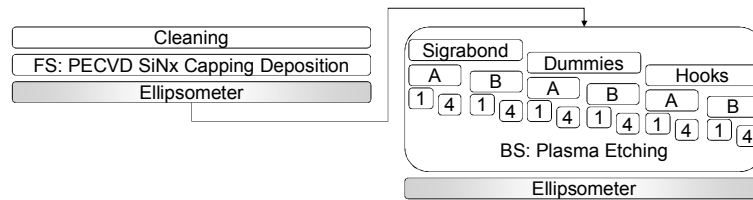

Fig. 3:24 Presented here are the process flow and experimental settings. The samples are laid on three different holders: plates of Sigrabond ®[17], a carbon fibre material out of which the inline plasma transport carriers are fabricated; silicon wafers (Dummies), a surface entirely covered by silicon substrates conditioned with a full immersion hot KOH treatment; and hooks, four aluminium hooks fixed to the carrier, whereby the fixation offers a large opening at the edges of the targeted side; the plasma phase can access the other side. The pressure in the chamber is varied (A: 0.08 mbar and B: 0.15 mbar). As indicated, the process is performed one or repeated four times.

The experimental design evaluated three different holding systems; two different chamber pressures and also the difference between a single run and multiple runs (four). The latter is an attempt to simulate more plasma sources, one after each other, to lengthen the total etching time. All remaining parameters are kept constant (Fig. 3:24).

Each factor was investigated for its variance on the measured thicknesses. This demonstrated that the greatest influence is given by the chuck configuration. The effect of repetitions and pressure configuration were not evident; the linear model, which is assumed for the interpretation, does not represent the speed of the etching on the SiN_x coated side, as the overall correlation was quite poor ($R^2 < 0.5$). The residuals of this linear regression model indicated that a process combination able to attack the coating exhibits a non linear etching rate; for this reason the measured thicknesses were weighted with a polynomial function (Eq. 3—2). In other words, an attack of small extent will have a bigger weight than an almost complete removal. After elaborating on the data (Eq. 3—2), with a coefficient $m = 4$, a linear interpretation is possible, and since the formulation is monotone for positive values, the obtained understanding can be directly translated to the original values.

---

[17] Sigrabond is a trademark of the **SGL Group**

$$t_{weight} = \left(\frac{t_{etch}}{\max\left(t_{etch}\right)} \right)^{m} \max\left(t_{etch}\right)$$

<div align="right">Eq. 3—2</div>

The linear interpolation of the treated data results in a R^2 value of 0.92, and permits the interpretation of the effects of the chamber pressure and the number of repetitions of the process; the first seems not to play a role while the second has a significant effect on the thickness results. By exploiting this independence from the pressure, the model gains access to two repetitions; hence, the lack of fit hypothesis can be, and is, tested successfully.
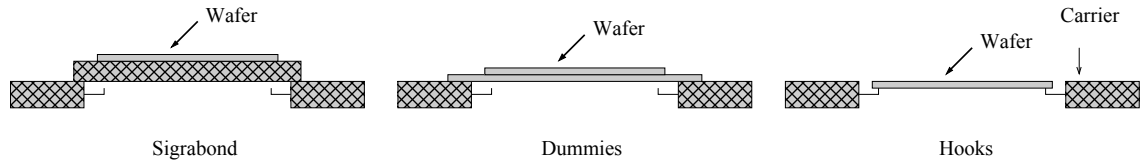
Fig. 3:25 Sketch of the three different wafer holding systems

The discrete combination of the experimental design was introduced in a specific order (Sigrabond, Dummies, and Hooks) in the model, since they cannot be easily numerically classified, any sorting would be valid, though this is the only order which engenders a linear model on the treated data, this means that if they differ in some value (i.e. opening to the coated side) this value is better represented by this given order.

From the sketch in Fig. 3:25 it is possible to evaluate why the sorting chosen is sensible. As it has been mentioned, there is no hard numbers to evaluate their difference. However, we can make a qualitative characterisation of the access of the plasma phase to the backside during the front side etching.
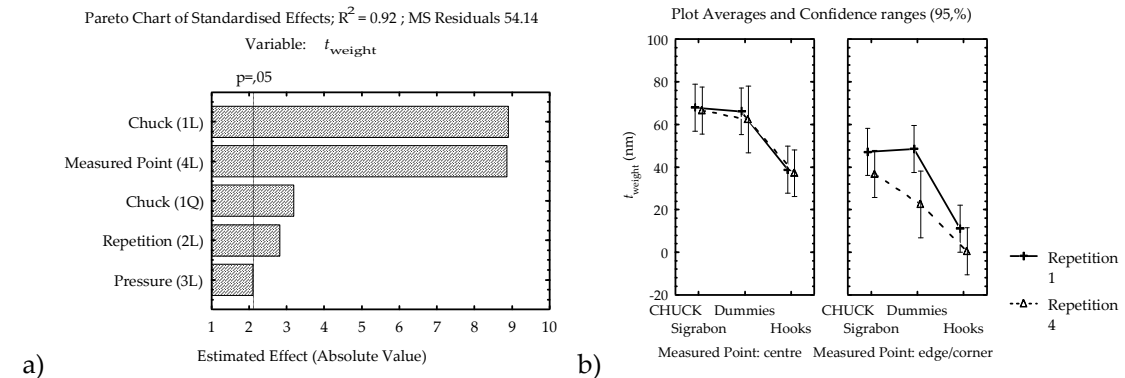
Fig. 3:26 a) A major role is played by the chuck and the measurement position; b) A graphic representation of the averages of the treated thickness, the linear model is not shown in this case since not all experimental settings can be numerically quantified.

The Hooks configuration, for example, presents openings on the side which are clear area of access for the plasma phase, and therefore etching can take place in abundance. The solution with dummies offers less access, however being their composing material also silicon, a warping of the dummies is not to exclude, especially because part of the dummies is covered and therefore not taking part to the reaction. Resulting positive or negative differences in temperature between etched and untreated areas could create enough stress to bend the thin dummies. Therefore these would offer less protection for the backside. Finally, the Sigrabond block has a configuration similar to the Dummies setting, although, due to its composition, warping is doubtful.

With this experiment it is demonstrated that the plasma etching system can be a good alternative for the silicon removal. However, the circumstances related to the holding mechanism explained above have to be taken in consideration for a new carrier design. Indeed, the parasitic etching of the unexposed side can be brought down to a few nanometres with proper holding systems. This allows the integration of the procedure within the solar cell processing. Furthermore it works in a vacuum environment, an advantage if preceding or following vacuum processes can be chained.

♦ *Flattening by SF6 plasma*

As previously mentioned, etching rates as high as 0.6 μm/min can be achieved; multiplying the number of plasma sources, for example by distributing them in a longer chamber or, as was performed in the following experiment, having the wafers travelling under the same source several times, the etching rate can further increase. This procedure distinguishes itself from the wet implementation thanks to this additional flexibility provided by process repetition.

It is interesting to investigate the level of achievable flatness when the pristine surface has texturing features in the micrometre range. An experimental setting (Fig. 3:27) with a full factorial design of the most important parameters is an answer to the question of plasma flattening.
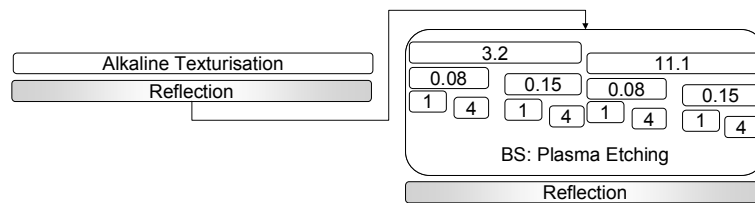
Fig. 3:27 Process flow, the main focus of the experiment concerns the conditioning of the surfaces. The variations refer, in the displayed order, to: the oxygen content (in %) of the total gas flux, the pressure in the chamber and the amount of time that the process was repeated.

Several samples (p-type Cz-Si, $\rho = 1\ \Omega \cdot cm$, pseudo square, 125 mm side, diameter 150 mm, 200 μm starting thickness) were processed to present an alkaline textured surface. By performing a process variation on those, we will attempt to determine the plasma etching effect on weighted reflection.
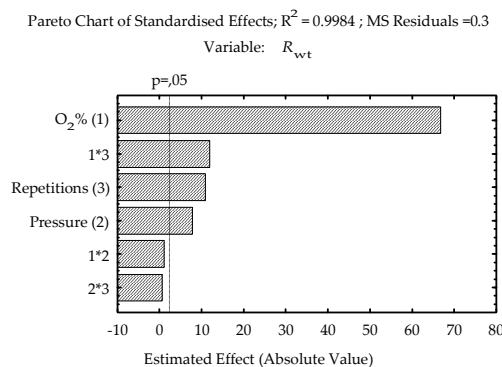
Fig. 3:28 The amount flux of oxygen in the chamber during the etching will affect the surface characteristic greatly.

All the samples have been measured for their weighted reflectance. The factorial design allows to identify linear correlations and interactions of independent variable (Fig. 3:29). One astonishing result is the significant and high effect of the oxygen in the chamber on the resulting weighted reflectance. A high availability of oxygen during the process enhances the formation

of residues on the silicon surface (i.e. SiO_xF_y). These residues perform a sub-masking {Hofmann 2008} and therefore hinder the flattening by creating additional roughness.

The effect of the pressure, albeit significant, was marginal. The explanation of its contribution can be seen in the reduced flow of the chemical species and therefore an increased time for the reaction. The work cannot guarantee that an exaggerate extrapolation of this result will result in an increased smoothing rate.

The range in which the variation took place is well represented by a plane, as the coefficient of correlation and the fits (Fig. 3:29) confirm. Albeit the long time required, the process can approach the maximum reflection well within the possibilities afforded by the equipment.
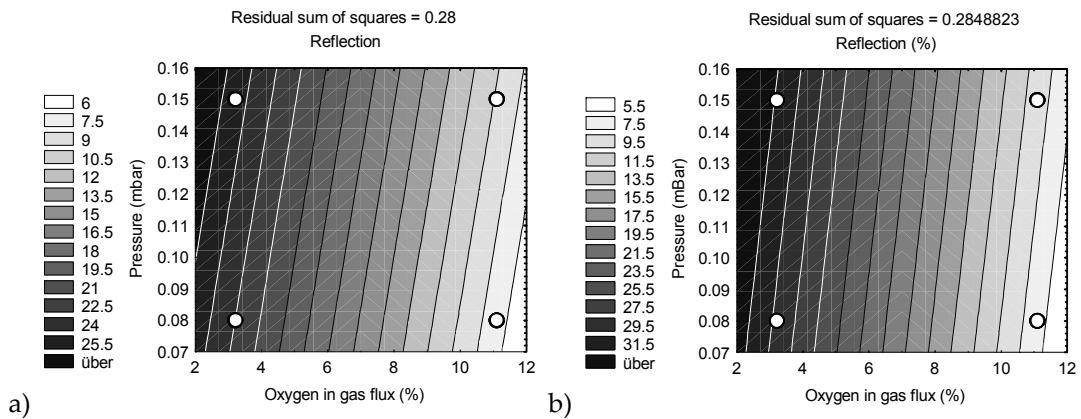
Fig. 3:29 Planes representing reflection, a) one time processing b) four time processing.

The linear regression show that higher pressures and lower oxygen content contribute to a quicker smoothing. Note that all samples processed with a high concentration of oxygen resulted in a weighted reflectance lower than the original. This is consequence of the additional roughness. The range in which the process is investigated is therefore capable of increasing and decreasing the original roughness of a silicon substrate.

3.4.4   Considerations on wet and dry etching

♦ *Conclusions on wet etching*

The process reveals itself as a good way to remove an emitter and to create a good ohmic isolation between front and rear. The advantage of this processing method over other edge isolation steps in a conventional line (see 3.2) lies in its placement; after the junction diffusion, a wet processing step follows. This additional wet step, aimed at back surface etching, would have low implementation cost thanks to refitting.

This equipment would also have an optimal placement to perform a flattening of the back surface. However, the observed etching rates lay below the requested values to achieve an effective polishing of texturing structures. The following consideration will delineate the physical limitations encountered by the process.

Based on the observations described above, a first interpretation of the high contribution of the recirculation on the etching rate can be made. In the setting detailed in Fig. 3:7, the etching capability strongly depends on the surface tension that the solution possesses with respect to the surface of the rotating roll. An increase in the solution bath level will increase the amount of liquid delivered to the wafer surface. An easy interpretation for this is the gravity force that the droplet has to counteract before sticking to the roll surface. This engineering consideration is sketched in Fig. 3:30.

Once the solution is brought to the wafer surface, the surface tension between solution and substrate limits the etching. In case a native oxide or when PSG is present, the solution wets the surface and the etching starts. Instead a freshly etched silicon surface does not wet itself on the rolls because of its high hydrophobicity. For this reason the process cannot be repeated. The

first step creates a hydrophobic surface and therefore the second step presents values of silicon removal resenting nought.
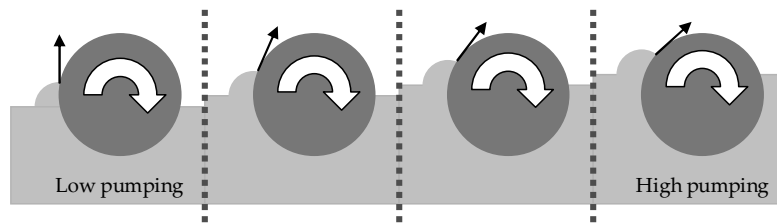

Fig. 3:30 Different recirculation pumping configurations. The amount of liquid that recirculates (imposed by a pump in the bath) will create different steady levels of the solution (in the picture), these in turn will create different configurations under which the surface tension can collect more or less liquid on the roll, decreasing the vertical component that has to compensate directly for gravity.

The liquid layer on the roll will then come into contact with the wafer surface, which can either float or swim in this liquid, depending on the hydrophobic character of the silicon surface. By increasing this level more chemicals are brought to the wafer surface. The etching would then take place more consistently. Hence, increasing the recirculation, the extension for polishing purposes is possible. On the other hand, this can compromise the single sidedness of the process and lead to wrap around of the chemical solution to the front surface.

♦ *Conclusions on dry etching*

The process can be used to realize proper surfaces for high efficiency silicon solar cells. The technological limitations can be overcome by a better holding system and a faster etching rate. These are both in sight with simple extensions to the system. Pressure can be set to high values to increase the polishing action, since the attack of the front due to wrap around is not influenced by this value in any of the configurations used.

♦ *Consideration on both procedures*

Two processes were evaluated to achieve the polishing of the back surface on equipments available on the market. One sided etching and high etching rates are a challenge for both types of equipment; indeed, they can achieve flatness when these constraints are removed. Slight modifications to the existing production tools (not suggested in this work) can lead to process a flat and emitter-less back surface structure.

3.5   Characterisation of the dead layer removal

The dead layer can be defined as all the volume, starting from the surface, where the phosphorus concentration exceeds the possible concentration of electrically active phosphorus, this value varies with the diffusion process, and is in a range around 1E+20 cm^{-3}

The high concentration of impurities in this region fosters recombination. The doping can also give rise to Auger recombination and free carrier absorption (FCA) phenomena {Clugston and Basore 1997}. Its substantial spatial extension, from surface towards the emitter bulk, prevents any dielectric to perform a passivation role of the surface. Within this section, an etching process will be evaluated for the removal of the dead layer.

The large range of processing speeds available on a plasma etcher, ranging from few centimetres per minute to hundreds, permits a wide spectrum of etching depths. By sufficiently increasing the speed, the thin dead layer, characteristic of one step diffusions, can also be removed. With this experiment a possible processing window for the emitter structuring will be analysed and compared to a pristine emitter.

The experiment made use of high quality materials (p-type FZ-Si, ρ = 1 $\Omega \cdot$cm, pseudo square, 125 mm side, diameter 150 mm, 250 μm starting thickness). These wafers were all diffused with

phosphorous; after this step, the substrates have an emitter with a sheet resistance of 61.8±0.3 Ω/sq. on both sides. The samples were divided into two groups, where the first is a reference group, where no plasma etching takes place; and the second incorporates variations in etching time (processing speed). After this step a SiN$_x$ ARC was deposited on all samples.
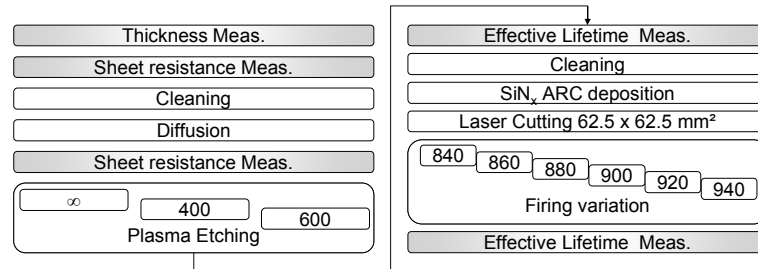
Fig. 3:31 Process sequence. The variation in the plasma etching is the displacement speed during the processing in cm/min, the group which is not processed is interpreted as a group which was processed at an infinite speed All the RTP temperatures of use in solar cell processing were implemented on the three plasma processing. These temperatures are written in degree Celsius on the sketch.

The second variation in the batch concerned the firing temperature, which was introduced in six levels. The samples were cut into smaller pieces to increase the amount of measurement points, without losing consistency. All combinations of etching speeds and firing temperatures were explored (Fig. 3:31).

The analysis takes into consideration the saturation current J_0 at the surfaces of the base, and since the base is always facing an emitter, the measured value will be J_{0e}. This value is chosen based on its sensitivity to the presence of a dead layer. The geometrical thickness of the etched layer was not measured because the value would not have given an insight into the working principle of the emitter.
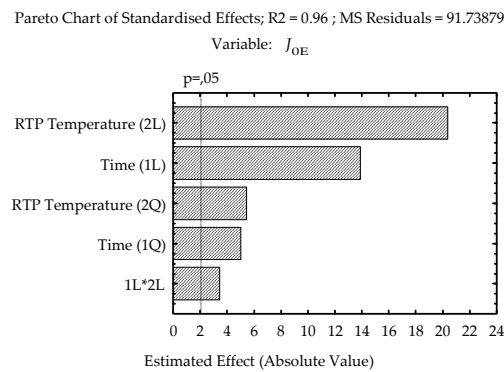
Fig. 3:32 Both RTP temperature and the etching time will have an influence on the resulting saturation current; interesting is also the effect of the linear interaction of the two.

The J_{0e} is extracted from the effective lifetime measurement performed on the samples after the firing. The procedure is called low level injection and is described in the literature {Fischer 2003} as being suitable on materials with high levels of doping, like in the case of photovoltaic materials. The results of the calculation are then used to gain an insight into the effect of the variations performed.

The plasma process is characterised by the inverse of the displacement speed, which is proportional to the time of etching. This makes possible to have one axis (etching time) where both the not processed samples and the other two plasma processing configurations can be plotted. The infinite speed indicated in Fig. 3:31 becomes 0 s of etching and the other two variations assume values well distributed on the ordinate axis (3.75 s and 2.4 s for 400 cm/s and 600 cm/s respectively).

Adapted Surface on Variable J_{OE}

a)

b)

Expected / Observed Values on Variable J_{0e}
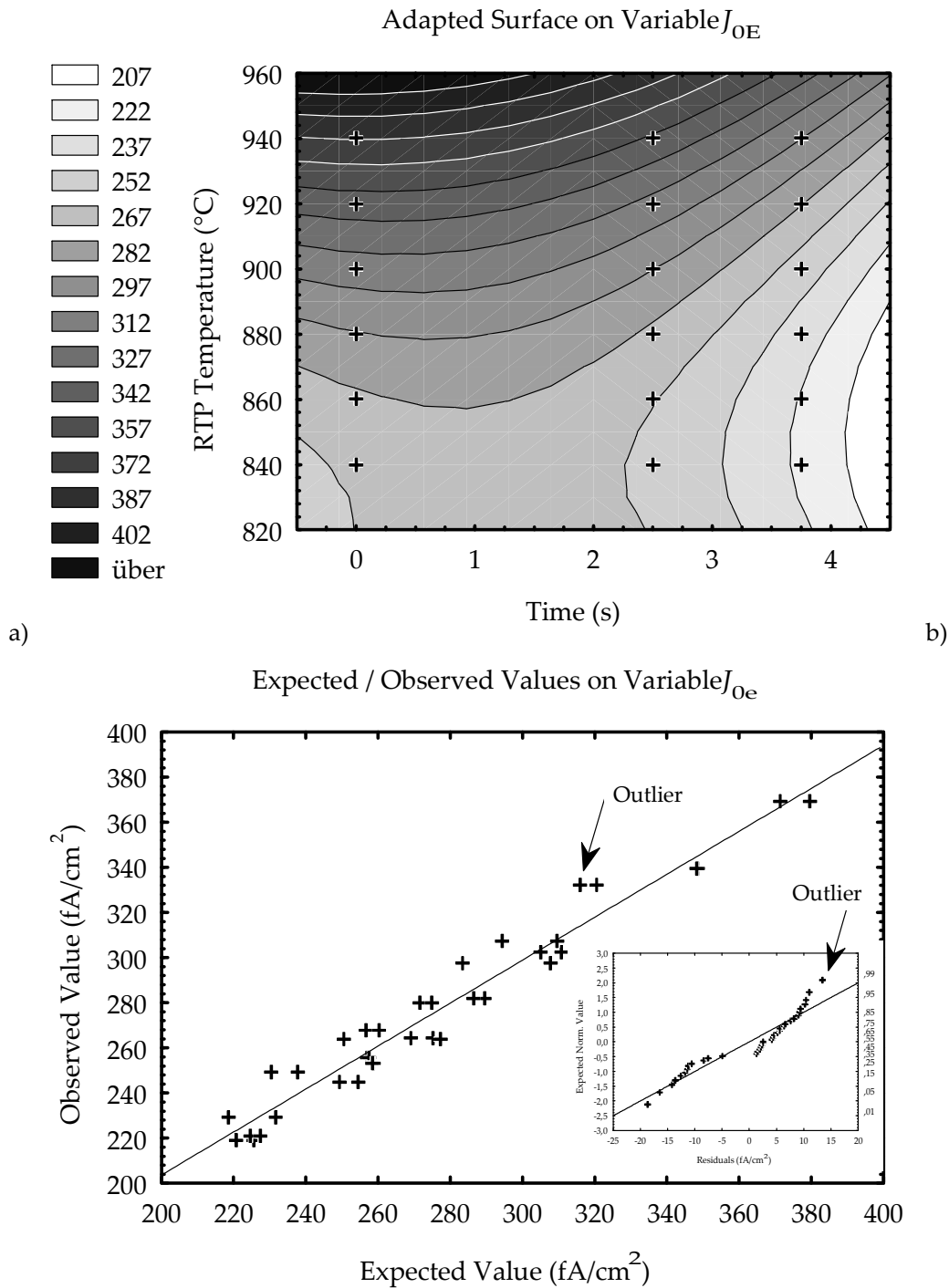
Fig. 3:33 The results of the saturation current were fitted with a linear model a), the combination of firing temperature and the inverse of the speed could describe the measured points, in b) the difference between the observed values and the values calculated from the model, one outlier was removed from the total of 36 measurement points to achieve a significant polynomial fit (indicated by the arrow). –Batch 090371–

Both the two variations have a significant effect, and also their linear combinations; a polynomial model was fitted to the results (Fig. 3:33), and it withstands the "lack of fit" test (see appendix B.a.I)

Starting from a speed of 600 cm/s and subsequently decreasing it, an improvement of the J_{0e} can be seen from the results; it is also possible to see that low temperatures (840°C and 820°C) have little influence on the characterised value, though in temperature regions more interesting

for solar cell processing the change is rapid. In any case, the plasma processing improves the saturation current, which is to expect when a significant amount of dead layer is removed.

3.6   Evaluation of industrially feasible passivation layers

As previously reported (2.5), the importance of a passivation layer for cells of low thickness is prominent.

Two kinds of passivation layers were developed and investigated during this work. Their difference is in the processing technique as well as in the passivating method. From the technical point of view, the first is a deposition of layers on the silicon substrate, whereas the second is an oxidation of the silicon surface at moderate temperature in wet conditions. The growth is followed by a plasma enhanced deposition of a stack of capping layers.

Both of these passivations are based on the decrease of the density of interface states and on the imposition of a field to separate in space the two recombining carrier types. The field is induced by the fixed charges in the dielectric.

3.6.1   Requirements for a complete plasma deposited passivation layer for industrial PERC concepts

The deposition of dielectrics by means of chemical vapour deposition techniques offers wide flexibility. In photovoltaic Plasma Enhanced chemical Vapour Deposition (PECVD) has the largest acceptance.

The investigation in the previous sections is closely related to the possibilities presented by industrial equipment. Inline industrial PECVD tools are available and well accepted by the industry and are natural candidates to deposit layers that could convey a benefit to the back surface.

The layers investigated were generated with a PECVD system installed in the pilot line laboratory PVTEC {Biro, Preu et al. 2006}. The equipment is an industrial tool from **Roth & Rau**, the SINA {Winderbaum, Romijn et al. 2006}. Inside the reaction chamber (deposition zone, see Fig. 3:34) plasma conditions are achieved ensuring vacuum, a high temperature and an electromagnetic field which ignites the plasma state. The presence of precursor gas, namely: silane, SiH_4; nitrous gas N_2O; ammonia, NH_3; and hydrogen, H_2; allows the formation of radicals which can deposit on the targeted substrate.
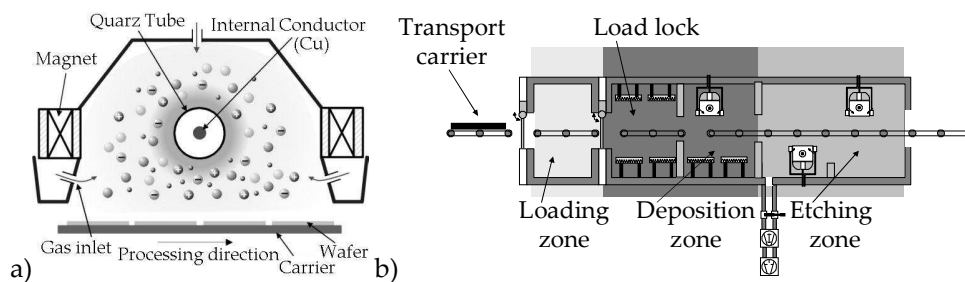
Fig. 3:34 a) scheme of a microwave, tube antenna plasma reactor chamber {Rentsch 2005}. b) scheme of the implementation, the equipment Sina, from Roth&Rau, can also be equipped with an etching system {Hofmann 2008}.

There exist several constraints for the realization of a passivation layer that could directly be implemented in a production line based on a screen print metallisation. The most stringent is the ability to withstand, after its deposition, the high temperature processing of the metallisation sintering without deteriorating its passivation ability. Previous works addressed the stability of SiN_x, including under high temperature processing **ANU** {Chen, Romijn et al. 2007} **IMEC** {de Wolf, Agostinelli et al. 2005} and **ECN** {Romijn, Soppe et al. 2005}. These works

are able to indicate parameters (i.e. refractive index, Si-N bonds) correlated with the passivation quality directly after the deposition and after the high temperature processing. The physical principle which allows the passivation behaviour at these two steps was identified as the donation of hydrogen to the surface. Hydrogen, in its atomic configuration, can terminate the dangling bonds found at the crystal interface.

An additional contribution given from high temperature steps to passivation quality is an increase of the positive charges present in the layer due to a restructuring of the silicon nitrogen bonds. The consequential increase of the electric field deprives the surface of majority (minority) carriers on p-type (n-type) material. This hinders recombination by decreasing the chances of two carriers to meet in space (see 2.2.2-SRH-Recombination at the surface).

A screening of the layer properties that can be deposited with the deposition system is then performed. In this way the capabilities of the inline PECVD will be better known.

♦ *Depositions*

The substrate used for the layer deposition (p-type FZ-Si, $\rho = 1\,\Omega\cdot$cm, pseudo square, 125 mm side, diameter 150 mm, 250 μm starting thickness) were processed following the scheme in Fig. 3:35.
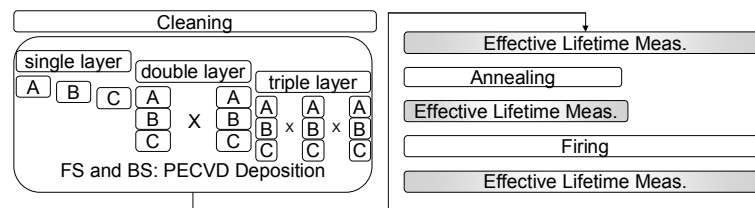
Fig. 3:35 The procedure investigated all possible combinations to identify the quality of the depositions performed on the industrial deposition equipment. The three combined layers are A: SiO_x, B: SiN_x, and C: a-Si. The deposition parameters were adjusted to achieve a thickness between 80 and 100 nm.

The screening variation explored different layers (amorphous silicon oxide SiO_x, amorphous silicon nitride SiN_x, and amorphous silicon a-Si) and their stacks, inspired from interesting results previously disclosed in the literature {Agostinelli, Choulat et al. 2006}. An annealing step was performed in an oven at 400 °C for 20 min in forming gas annealing (FGA) while the firing step was directly performed in an industrial sintering belt oven, indicated also as RTP throughout this work. The belt had a speed of 4.2 m/min and the peak set temperature was 800 °C.

A small introduction on the passivation principle of each single layer will be of interest for interpreting the result (for a complete overview see {Hofmann 2008}).

◊ *Amorphous silicon*

a-Si is a convenient passivation because of its ability to reduce the dangling bonds. This deposition takes place at low temperature and its bulk structure deforms quickly when the temperature increases. This reduces its ability to terminate the silicon crystal on which it is deposited. Recent development found in stacks the possibility to mend this temperature dependent degradation {Gatz, Plagwitz et al. 2008}.

◊ *Amorphous silicon oxide*

SiO_x is a deposited dielectric with optical characteristics similar to the thermally grown silicon oxide (SiO_2). Furthermore, also the passivation performance of SiO_2 can be reproduced when adequate settings are used {Sritharathikhun, Banerjee et al. 2007; Mueller, Schwertheim et al. 2008}.

◊ *Amorphous silicon nitride*

SiN_x is well known in the photovoltaic for its optical characteristics which find a perfect exploitation for the deposition on the cell front side. This layer finds also passivation use when its preparation contains high amounts of hydrogen, preferably in the ionized form, since this

element can easily bind with dangling bond and saturate them. This hydrogen effuses during high temperature steps. A fast increase of temperature can also lead to hydrogen blister formation.

♦ *Measurements*

This allowed candidates to be found that are able to withstand high temperature processing. The test consisted of an effective lifetime measurement on lifetime samples (appendix A.f.II and Figure A:4) after different post treatments (after the deposition of the layer, after a tempering, after a firing or the sequence of two of the latter).
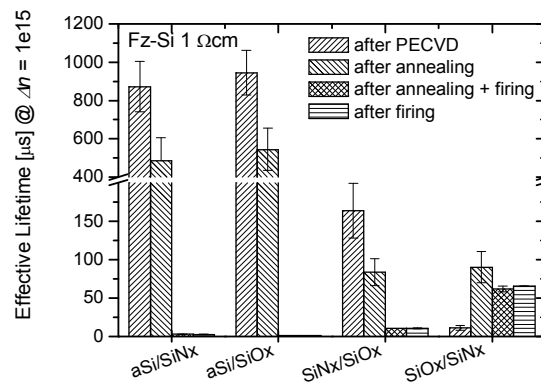
Fig. 3:36 Lifetime values of processed wafers. Here are presented double layer stack. The deposition order is equal to the labels presented The most interesting result of the screening test was the possibility to deposit layers that could still deliver a salient passivation to the surface of these heavily doped FZ wafers after the high temperature treatment. The level that came out of this first experiment encouraged more work in the staking of layers, as the development soon reached levels of effective lifetime above 1 ms.

The behaviour described in the paragraph "Depositions" was remarked also in this experiment for the single layer tests. Double layer results (shown in Fig. 3:36) are similar to triple layer stack, which are therefore of lesser interest. The behaviour of the a-Si layer does not change when capped and the SiN_x tends to blister also when capped.

Later more focus was given to interesting layers with several characterisation techniques to understand their passivation principles. One expectation was that the layers deposited could have positive charges. Indeed, as explained in the literature for the case of SiN_x, this would increase the effective lifetime by fostering a field effect passivation. This would result in an improved passivation without the need to decrease the density of interface traps. Therefore, dangling bonds at the surface would remain uncured.

3.6.2   Candidate PECVD layer

One of the most interesting candidates is a stack of a SiO_x and a SiN_x. Later experiments lead to an evolution of the SiO_x layer into a SiO_xN_y. Finally the establishment of a passivation based on a silicon rich oxynitride, in short SiriON, capped by a medium to high refractive index SiN_x, called CaTS as in "Capping on Top Surface" was achieved.

Because of the promising results and the need to understand the working principle for its correct employment at the solar cell level, more studies were performed. These are described in the following section.

An advantage of the amorphous layers is the large family of layers that can be generated with small changes in the deposition parameters. This was extensively used for the characterisation to relate the layer optical characteristics to the electrical properties.

♦ *Bottom layer*

The evaluated layer (SiriON) is not stoichiometric; therefore, a family of layers can be generated having similar optical properties. Within the variety of layers, a classification, based

on measurements performed on the resulting layer, is required. The value that better differentiates the layers is the refractive index at 632.8 nm.

Ellipsometry is used to obtain this value FINDME, the refractive index has a monotonic dependence on the gas ratio of different SiriON layers realised (see Fig. 3:37). The remaining parameters, like microwave antenna power, the vacuum level and the temperature are kept fixed.

In the literature, values of refractive index for the stoichiometric silicon oxynitride Si_2N_2O are reported as $n_{SI2N2O} = 1.83$, and other non–plasma implementations also result in a wide variety of refractive indices {Xu and Ching 1995}.
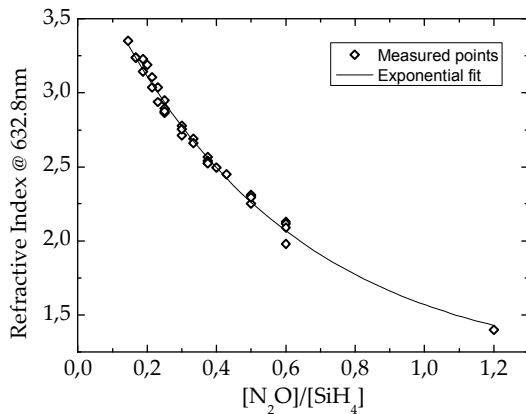
Fig. 3:37 The relation between the gas ratio and the refractive index, a more silicon-rich layer is grown with a higher amount of silane in the chamber. Furthermore, its refractive index gets closer to that of silicon ($n_{Si} = 3.9$). The line is an exponential fit that can be used as a guide to the eye.
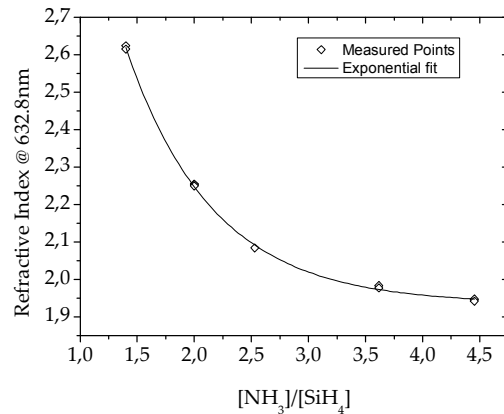
Fig. 3:38 The capping layer, deposited on a silicon substrate, was varied in order to achieve a different refractive index; also for this set of points an exponential fit is presented as a guide to the eye.

♦ *Second layer*

As with the first layer, also the capping layer (CaTS), depending on the deposition conditions, can generate a wealth of layers; the characteristic value to differentiate them is again the refractive index (Fig. 3:38). This window of refractive index in the specific deposition system is well documented from previous studies already mentioned (see 3.6.1).

Not all of the combinations will give rise to a working passivation, but this aspect will be discussed in the following.

3.6.3   Effective lifetime measurements on close to process samples

The superposition of the two layers is used to decrease the surface recombination velocity (SRV or *S*) while maintaining high temperature stability; in order to characterize the potential of the stacked layers, symmetrically deposited samples were prepared (see Fig. 3:39 and A.f.II).
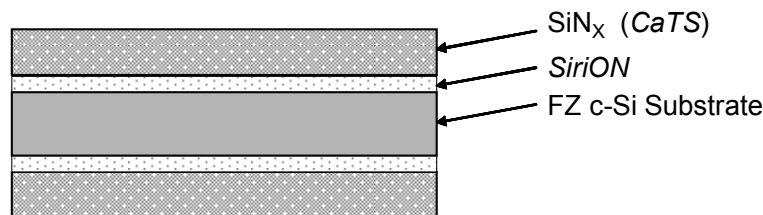
Fig. 3:39 Representative out of scale picture of a lifetime sample.

In the following, the measurements will have a specification as to whether they were taken after deposition or after the high temperature step; this step can be performed in a belt inline

oven (from **Centrotherm**) or in a single wafer RTP furnace (from **STEAG-RTP**)[18]. The first was used for the samples presented in Fig. 3:40a, the second instead has been used for all the other preparations.

a)   b)
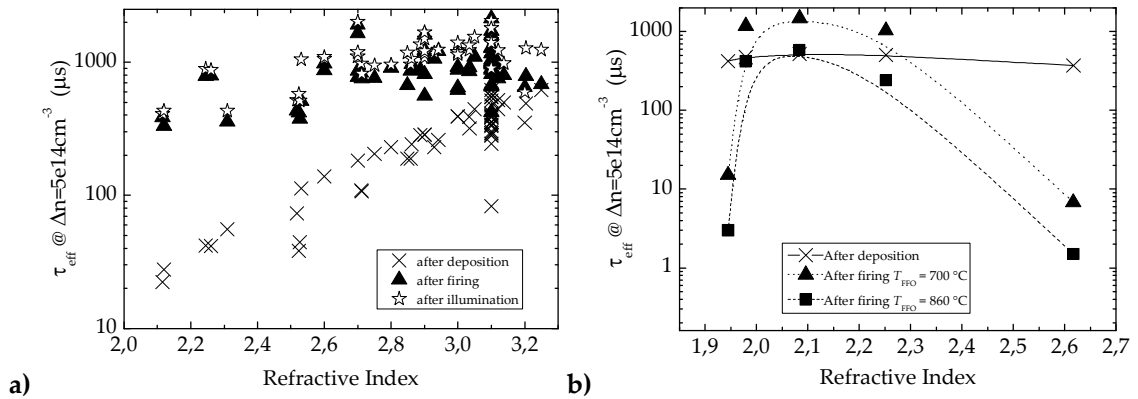
Fig. 3:40 Series of measured effective lifetime on p-Type FZ-Si (N_A= 1.5E+16 cm^{-3}). The firing was performed at T_{FFO} = 700 °C, on the left (a) the measurement of all SiriON deposition (~30 nm) made with the same CaTS (n_{CaTS} = 2.1, ~70 nm), are presented; in this graph, with different symbols the three stages of the processing are reported. As it can be interestingly noticed the level after the deposition step has a correlation with the refractive index. A satisfying level is attained throughout the range; one configuration (n_{SiriON} = 3.1) was preferred for investigation purposes. On the right (b) an experiment where the SiriON layer was kept fixed (n_{SiriON} = 3.1, ~30 nm), the CaTS layer (, ~70 nm) has a strong negative influence on the passivation effect only at its feasible extremes. On these samples the post-treatment was bypassed.

Bulk effective lifetime was measured on a series of samples where the refractive index was varied from 2 to 3.4 (Fig. 3:40). The CaTS used was kept constant in this variation. In a second run the SiriON layer was kept constant and the CaTS layer was varied. In this experiment it can be seen that a strong change of the passivation behaviour at the extremes of the possible refractive index can be seen.

From the characterisation of the deposition range an interesting composition of the stack (n_{SiriON} = 3.1, n_{CaTS} = 2.1) is defined, that will be used for the investigation of passivation conditioning (time, light and temperature). This combination was able to achieve an average surface recombination velocity on polished material as low as 3 cm/s.

In a later chapter, results will show that at the cell level another composition is preferred. Then it will be also suggested why such a divergence of results can be possible.

3.6.4   Time and illumination stability

The SiriON CaTS was also investigated for its stability in time. A slight decay of the passivation can be observed in the first hours, but it levels off after about a week, the level lowers in time but stays at the same order of magnitude.

---

[18]The first represents the real industrial high temperature condition while the second offers a higher reproducibility of the temperature profile. The second equipment offers the possibility to calibrate the temperature emissions at specific temperature on a dummy sample by means of thermocouples and a pyrometer, then with the calibrated pyrometer, which is pointed through the chamber walls to the sample, a precise temperature setting, which may also vary in time, can be reproduced.
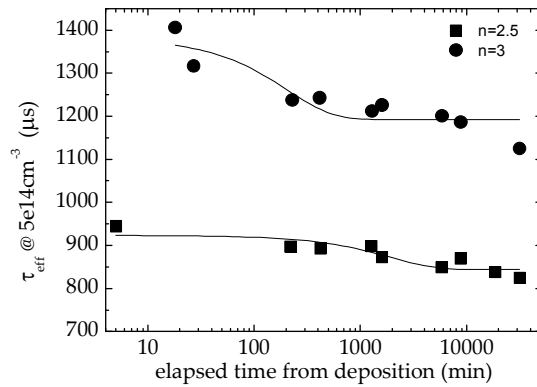
Fig. 3:41 Degradation of the effective lifetime in dark for two realisations of the passivation. The samples have a SiriON layer with the indicated refractive index on a silicon substrate (additional details: p-Type, FZ-Si, N_A= 1.5E+16 cm^{-3}, n_{CaTS} = 2.1, T_{FFO} = 700 °C).

From one measurement to the next, wafers are stored in the dark; this prevents any modification of the layer due to light absorption.

The absorption of light, even faintly[19], was investigated starting from two high temperature conditioning process and applying a wide range of refractive index, the results (Fig. 3:42) confirm that this lifetime increase is stronger at high n_{SiriON} and at lower firing temperatures.
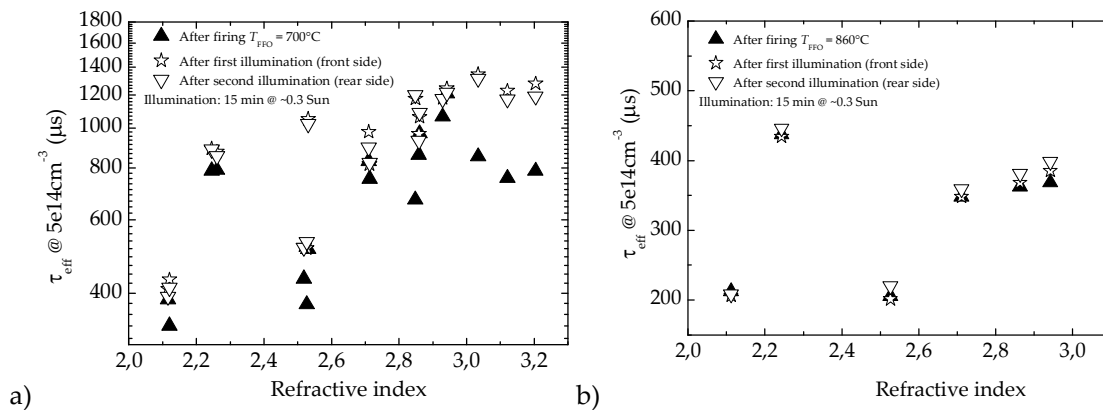
Fig. 3:42 Effective lifetime investigation on the illumination effect on p-Type FZ-Si (N_A= 1.5E+16 cm^{-3}) with a SiriON CaTS; values are reported after two different RTP treatments: a) 700 °C and 860 °C. After front illumination and after back illumination, each of which lasting 15 minutes, differences in measured lifetime can be seen. At the lower temperature, a first illumination results in a maximum. However, after a second exposure a decrease is observed. This lowering could be reported as time degradation.

An additional experiment was conducted to gain an insight on the spectrum of light that is taking part to the effect.

The experiment exploited the light absorption properties of silicon. For a wafer thickness of about 250 μm only long wavelengths, above 1000 nm reach the other not illuminated end. This part of light has energy only slightly higher than 1.2 eV. Furthermore, from ellipsometry measurements the optical bandgap of the two layers was extracted and measured to be higher than E_g (SiriON ≈ 2.2 eV, CaTS ≈ 2.8 eV). Additionally, from this same measurement, it is possible to notice that the stack does not absorb wavelengths longer than 800 nm.

Consequently, when the stack is deposited on both sides, only the coating facing the light source receives enough energy to create EHPs in its bulk, on the other hand the coating on the other side is unexcited. Although no photon excitation takes place, another kind of stimulus is

---

[19] The lamp used was a halogen lamp with a lumen intensity around 1/3 of the sun at the exposure distance.

consequence of illumination. EHPs are generated in the silicon bulk, and these flow to the surface where recombination occurs. This injection of carriers could contribute to the saturation of traps which have long lifetimes, more than minutes. Once these traps are filled, they contribute positively with their acquired charge to the already present field effect passivation. This would decrease the surface recombination velocity and in turn would explain the increase in effective lifetime.

The hypothesis under test is that the short wavelengths take part to the improvement of the passivation qualities of the layer. For the reason stated above, only illuminating separately the two sides, the best result can be obtained.

Samples with different heat post-treatment were illuminated on one side for 15 minutes and for 15 minutes on the opposite side. Accordingly, their τ_{eff} were measured at each step.

As it can be seen in Fig. 3:42 (a), the second illumination does not lead to an increase in τ_{eff}, this finding is a first suggestion that the illumination is enhancing the passivation effect through the injection of carrier at the surfaces.

In the case of higher temperature post-treatment the passivation benefits also from a second exposure. A possible argumentation is that the passivation layer needs more illumination time to saturate the traps.

♦ *Temperature stability*

In the previous pages it was already stated that the layers cure themselves during a high temperature step and, either by means of higher surface field or by decrease of the traps at the insulator semiconductor interface, increase the passivation.

The experiment on post treatment consisted in preparing a set of lifetime samples (Fig. 3:39) and firing those at different peak temperatures and perform a subsequent illumination (Fig. 3:43 a).

The τ_{eff} has a maximum around $T_{FFO} = 700$ °C. The trend is clearer after the illumination and does not depend strongly on n_{SiriON} (indicated in the graph).

a)   **b)**
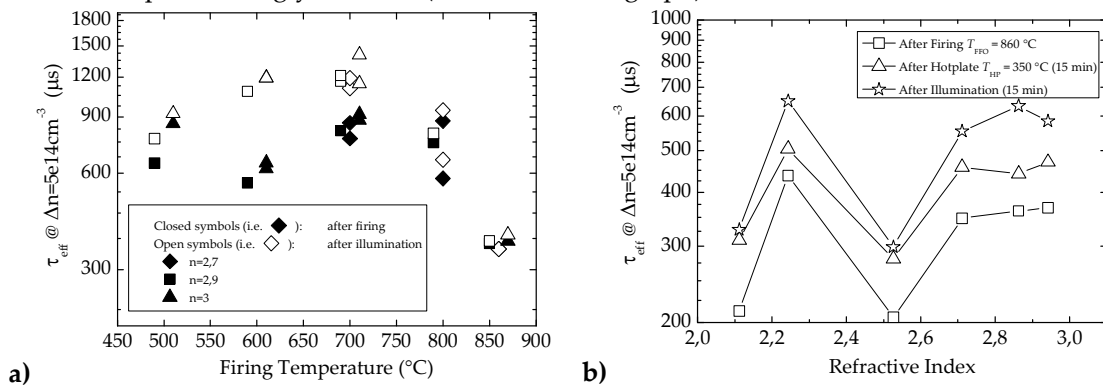
Fig. 3:43 Effective lifetime investigation of the maximal firing temperature T_{FFO} on p-Type FZ-Si (N_A= 1.5E+16 cm^{-3}) with a SiriON CaTS passivation; several refractive indices were again taken for this investigation. In picture a) the samples were fired at different temperatures (500 °C, 600 °C, 700 °C, 800 °C, 860 °C, each cluster of points represents one indicated temperature). In picture b) for different n_{SiriON} two sequential post treatments are included, the first being a tempering of the samples (350 °C in air for 15 minutes) and the second is an illumination on one side of 15 min.

A second post-treatment sequence included an annealing step on a hotplate and then the illumination step. Including this additional low temperature curing step the passivation changes the behaviour. The passivation at $T_{FFO} = 860$ °C reaches a higher passivation potential, although both lifetime samples, directly after the firing start from a similar level (300 µs).

3.6.5   Surface (photo)-voltage measurements

One interesting value which characterises the deposited dielectrics on a semiconductor substrate is the potential that builds up in the material to counterbalance the field generated by the charges in the dielectric. A complete explanation of the method and the instrument will be given in the appendix (A.c)

The measured value is the difference of surface voltage ψ_{surf} in dark and light conditions (Fig. 3:44) plus a correction due to the different mobility of holes and electrons (Dember voltage). The measurement is related to the amount of charges in the layer, especially when the charges induce an inversion in the semiconductor. In this case, instead of the normal exponential relations, a more docile inverse of the root leads the relation. This relation can be used without introducing huge errors in the calculation of the charges.
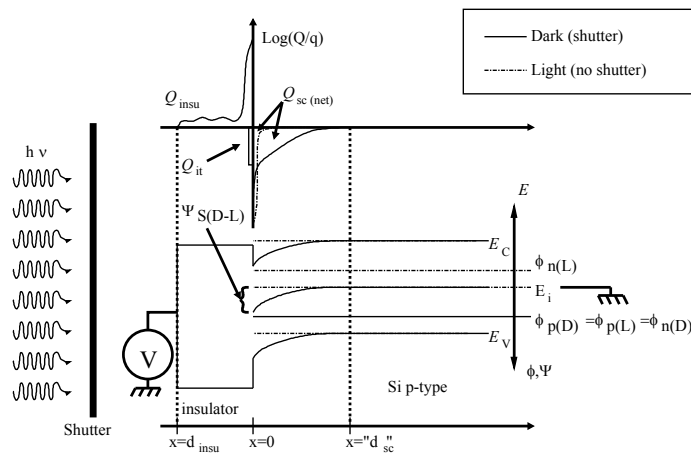
Fig. 3:44 Representation of the dark and the illuminated situation and the measurement principle. The dark, represented by full lines, represents a surface in weak to strong inversion, while as the shutter is removed and the light increases the amount of free carriers, the surface moves into a flat band, since a very small bending at the surface can already compensate for all the charges in the insulator.

In order to have a better understanding of the measurements and a cross checking of the results, samples with a deposition of a well established layer deposition, used normally as an ARC, and a sample with the SiriON CaTS were prepared. The samples were then chipped into several pieces and underwent different treatments, detailed in Table 3—3.

Table 3—3 The SPV and QSSPC measurements performed on SiriON CaTS allow an insight into the passivation mechanism. The SiNx possesses is characterised by a n_{ARC}= 2.1, as the CaTS layer in the stack. On the other hand, the SiriON layer has a refractive index n_{SiriON} = 3.2.

Sample label	Fired T_{FFO} = 700 °C	Illumination 30 min	ψ_{surf} (mV)	Q_{SC} (10E+11 cm²)	τ_{eff} (µs)[20]	S (cm/s)[20]
SiNx			734±5	-3.9±0.1	10	1621
SiN$_x$	X		760±5	-4.1±0.1	67	187
SiN$_x$	X	X	760±5	-4.1±0.1	74	168
SiriON CaTS			645±5	-3.48±0.05	214	53
SiriON CaTS	X		720±5	-3.76±0.05	1015	6
SiriON CaTS	X	X	755±5	-4.1±0.05	1167	5

To attain a better insight into the evolution, a graph of ψ_{surf} and S is presented in Fig. 3:45. An interpretation could be obtained by observing the curves presenting the S values as a function of the charges {Dauwe 2004} or as a function of the injection {Hofmann 2008}, the

---

[20] @ Δn = 5E+14 cm^{-3}

increase shown by the ψ_{surf} could alone justify the dramatic reduction in *S*. From other measurements, detailed in a future publication on the matter {Seiffe, Gautero et al. 2010}, we infer that the RTP step hardly has decreased the amount of traps at the interface. However these traps could be saturated by the charge storage which happens during illumination (the increase of ψ_{surf} testifies to the increase of charges in the dielectric).
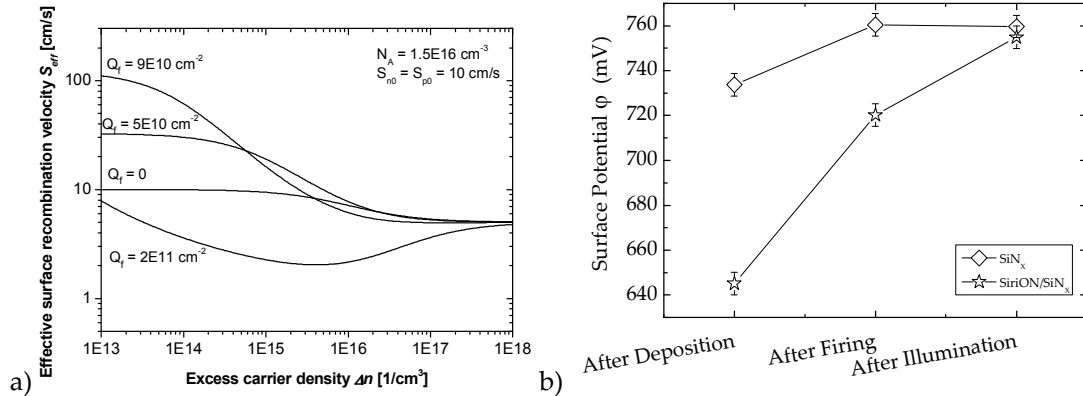
Fig. 3:45 a) Evolution of the surface recombination velocity as effect of the carrier injection and the fixed charges in the layer ($Q_{SC} \cong Q_f$) (from {Hofmann 2008}) b)Evolution of the surface potential in the post conditioning of the deposited layers. The increase in charges happens at the RTP step for both dielectrics, though the effect is much more pronounced with the SiriON CaTS.

3.6.6   Development of PECVD capping layers for thermal silicon oxide

There are two properties of an ideal passivation layer; first is the ability to isolate electrically the coated substrate surface from the metal layer, and second the ability to reduce the recombination activity at the surface of the silicon.

The first ability is challenged especially after high temperature steps. These are needed for the aluminium paste layer to sinter. One possible idea {Schultz, Hofmann et al. 2005; Gautero, Hofmann et al. 2009} is to prepare one layer in direct contact with the silicon, for example a grown silicon oxide (SiO_2), and capping it with high-temperature-resistant PECVD deposited nitrides.

The thermal growth of SiO_2 can become convenient if throughput is increased. The amount of wafers in a quartz boat can be increased when longer ovens are used; another approach is to decrease the loading time of the machine, with the option of an inline realisation {Biro, Mack et al. 2009}.

The adoption of PECVD capping is suggested by the high deposition rate that can be achieved with inline PECVD reactors (as the one presented in 3.6.1). Below a solution for a capping layer will be investigated. Furthermore, advantages from an intermediate buffer layer will be explored. The designed structure can have two or three dielectric layers (see Fig. 3:46).
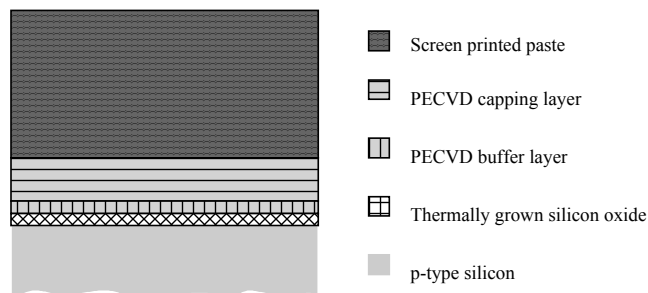
Fig. 3:46 Cross section of the designed passivation directly applied to the back surface of a solar cell (see the metal layer represented by screen printed Al paste).

A stack of these dielectric layers, each with the specified function, is prepared and analysed in this chapter; the choice of the SiO_2 is motivated by the low recombination that is obtained with a wet oxidation of the silicon surface, and the good understanding that was developed in previous years in the semiconductor industry {Nicollian and Brews 1982}. In the photovoltaic domain the adoption of SiO_2 as passivation for silicon solar cells lead to the development of many experiments, treatments, and models, which are well documented in the literature {Aberle, Glunz et al. 1992}.

This scheme will take the name of SiNTOx, a combination of silicon nitrides and a thermal oxide.

3.6.7 Capping layer

The deposited PECVD SiN_x takes on the task of being an isolator between the substrate and the aluminium paste layer. This ability is necessary for the entire stack to work properly, and for this reason is investigated first by means of conductivity tests.

The material (p-type Cz-Si, $\rho = 0.5 \div 3$ $\Omega \cdot$cm, pseudo square, 125 mm side, 165 mm diameter, 200 μm starting thickness) was etched in a bath of KOH to remove the damage. After this step, one side is deposited with the desired coating. The metallisation step covers both front and back surface with a glass frit-free screen-printed aluminium paste.

The samples go through a high temperature process, which sinters the paste. During this high temperature step, as is explained in 3.7.2, it is possible to create ohmic contacts if no alloying barrier is present. The objective of this batch is to evaluate the quality of the alloying barrier functionality of different depositions.

The variation performed involves the temperature and the ratio of the two gases used to deposit SiN_x, silane (SiH_4) and ammonia (NH_3); two different temperatures and three different ratios will be implemented.
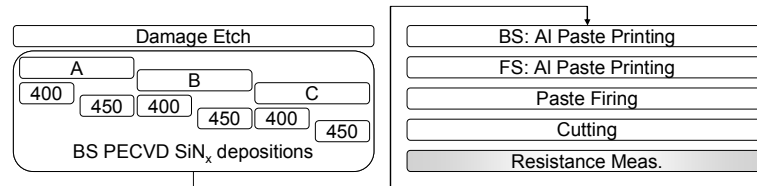
Fig. 3:47 The scheme that enables the characterisation of the layer density is composed of few processes.

The contacting between the aluminium layer and the silicon is random, and for this reason the samples were cut into several small pieces (ca. 2x2 cm²) so that for every deposition a large set of values could represent the target characteristic.

After taking the average and the standard deviations, it is possible to observe the average alloying barrier capability of the layers and therefore to classify them.
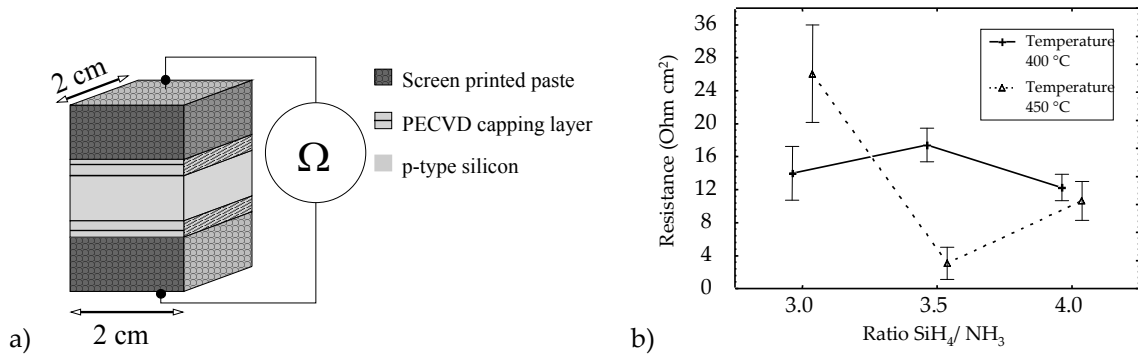
Fig. 3:48 a) Out of scale sketch of the 2x2 cm² sample for the resistance analysis. b) The obtained resistance values, scaled to the area considered are here depicted with 95% confidence interval. Noteworthy is to mention a reference term: a performant solar cell has a series resistance $R_s \cong 0.5\ \Omega \cdot cm^2$.

As can be seen from the low correlation coefficient, even though all variations are shown to be significant for making a difference in the layer, it is not possible to distinguish a clear trend.

The Pareto chart shows in this case one interesting result: the temperature does not play a role directly in the density of the layers. The other parameters, although imposing significant changes when varied, cannot create a polynomial model. Highly probable is the encountering of a surface which cannot be modelled with a simple design of experiment. The solution would be to reduce the range of investigation, or increase the number of steps in which every variable is sampled.
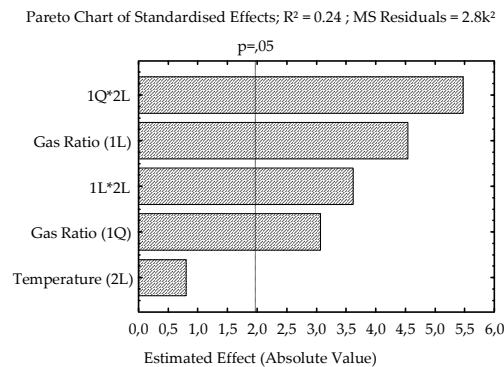
Fig. 3:49 Pareto chart of the deposition parameter effects on the average resistivity.

Since what we look for is also high stability, the chosen layer has to meet a low standard deviation. A high value with low variation is achieved in the configuration of 3.5 as gas ratio and 400 °C as processing temperature. This deposition also has the advantage that it makes use of a temperature far from the equipment limits.

3.6.8   SiNTOx Passivation

The focus shifts now to the preparation of a low recombination silicon to dielectric interface.

What will be achieved is a shift in the level of recombination speed. This can change due to deterioration of the passivation layer or because of shifts of charge quantity in the stack.

The experiment presented in the following is an attempt to show the potential of an industrial implementation of such a stack, so the roughness of texturised samples is reduced to minimum. The material (p-type FZ-Si, $\rho = 0.8 \div 1.2\ \Omega \cdot cm$, pseudo square, 125 mm side, 150 mm diameter, 200 μm starting thickness and p-type Cz-Si, $\rho = 1 \div 3\ \Omega \cdot cm$, pseudo square, 125 mm side, 150 mm diameter, 140 μm starting thickness) was first textured, resulting in a highly rough surface (random pyramids configuration). Subsequently, one side at a time, the substrate was wet chemically polished (see 3.4.2). The parameters were adjusted to achieve a removal of

silicon higher than 10 μm on each side. This produces a mirror-like surface (see Fig. 3:50). Subsequently the passivation has been prepared.

One of the most common methods to reduce the recombination activity at the silicon crystal boundary is to grow an oxide on the substrate. Much experience on the formation and on the characterisation of this oxide can be gained from the microelectronics {Nicollian and Brews 1982}, the application to solar cells was studied in depth by Aberle {Aberle, Glunz et al. 1992}.

The wet oxidation of the silicon surface was performed at 800°C. The parameters for the preparation of this thin oxide were explicitly kept constant for the following experiments.
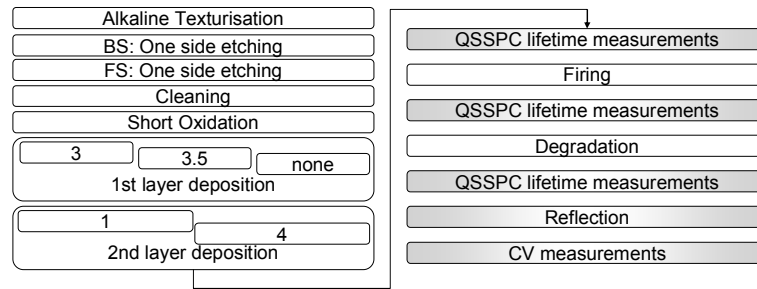
Fig. 3:50 Process for the creation of the samples, the depositions are performed on both sides. The numbers in the variation represent the gas ratio of the PECVD deposition. For the ´first layer the gas used were N_2O and SiH_4, instead for the second layer they were NH_3 and SiH_4.

After the short oxidation (its completing time is kept low to ensure its cost effectiveness), a sequence of capping layer is deposited (see Fig. 3:50), this introduces the possibility to investigate the influence of the layers on the underlying SiO_2.

The 1st layer is from the SiriON family, while the 2nd layer is a SiN_x. The ratio of the gas to grow them varies as described.

Finally the characterisation encircles the post-treatments.

♦ *Roughness*

Another field of intervention, which is here well taken care of, is the surface roughness of the silicon. A low level roughness eases the task of crystal termination for the dielectric layer. Moreover, in the case of a thick silicon oxide growth, a high roughness can result in cracks in the substrate due to increased stress in superficial valleys. Cracks, that propagate in the bulk are detrimental for the minority carrier lifetime {Cousins and Cotter 2006}. This effect is counteracted by preparing for the oxidation a low surface roughness; furthermore a thinner SiO_2 reduces the aforementioned stresses.

Reflection values are taken at 1200 nm. All samples have an unexpectedly low reflection and they share almost the same value (all in the range 34±1 %). This value is far from the desired 55 % of flat silicon to air interface (Fig. 3:20). Apart from the consistent roughness, another reason is the suboptimal thickness and refractive index of the dielectric layers. These layers can act as a good coupling medium between the silicon and the air.

♦ *Effective lifetime of SiNTOx*

As is it illustrated in its analytical detail (A.f.II), the lifetime can be directly correlated to the surface recombination velocity when a lifetime sample (similar to the implementation sketched in Figure A:4) is prepared. On this structure several measurements have taken place at different process steps. The effect of different stack combinations on the passivation quality will be investigated. These characterisations are: effective lifetime measurement, capacitance voltage, and reflection.

Both materials, FZ-Si and Cz-Si, present after the deposition an effective lifetime in the same range (Fig. 3:51). This indicates that the Cz-Si material, in the un-degraded state, has a sufficiently high bulk lifetime to show directly the influence of the surfaces. These have a common limitation in the low but not negligible roughness which increases the *S*.
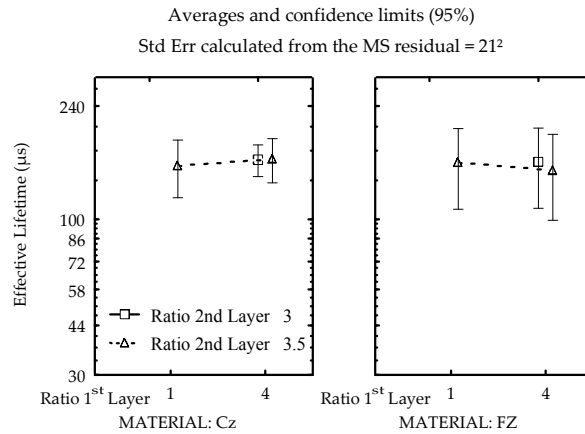
Fig. 3:51 Lifetime measured on as deposited wafers. On the left is the Cz-Si material and on the right is the FZ-Si material. Both were passivated with a wet thermally grown silicon oxide. This layer is then covered with a variation of SiriON (1st layer) and SiNx (2nd layer). The gas ratio used for the deposition of the 1st and 2nd layer is indicated in the graph in the ordinate and in the legend respectively.

The wafers are then fired in a RTP furnace. The measured effective lifetime remains on the same level, though the spread of the results increases.
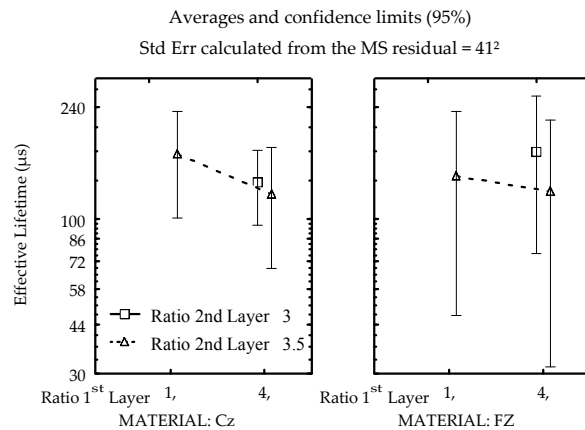
Fig. 3:52 Lifetime measured on fired wafers, the scale is kept in the same range as in Fig. 3:51. On the left is the Cz-Si material and on the right is the FZ-Si material. Both present a wet thermally grown silicon oxide. This layer is then covered with a variation of SiriON (1st layer) and SiNx (2nd layer). The gas ratio used for the deposition of the 1st and 2nd layer is indicated in the graph in the ordinate and in the legend respectively.

One of the materials chosen, due to oxygen contained in the bulk, can degrade if exposed to illumination for a long time. It is interesting to notice that τ_{eff} measurements unveil this shift towards lower values (see Fig. 3:52).
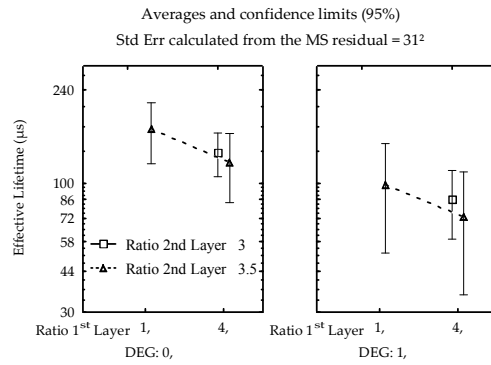
Fig. 3:53 Lifetime measured on fired wafers, a comparison between not-degraded and degraded state. It is positive to notice a strong influence from the degradation on the effective lifetime. The passivation, which remains unchanged during the degradation process, has an influence on the measurement which is lower than the bulk lifetime (see **Equation A—2**). In other words the decrease in bulk lifetime has a stronger effect than the surface recombination.

The samples present a surface roughness similar to processed solar cells, in this condition the effective lifetime results strongly limited by the surface. High purity material (FZ-Si) with bulk lifetime performs just as well as Cz-Si material, which is known for a lower bulk lifetime.

$$\frac{1}{\tau_{eff}} = \frac{1}{\tau_{bulk}} + \frac{2S}{W}$$

<div align="right">Eq. 3—3</div>

Exploiting the similarity of the effective lifetime calculation and the harmonic sum[10] (see Eq. 3—3), it is possible to explain the role of the passivation by "stick sum" (see Fig. 3:54). The assumption of this explanation is that the surface passivation of the layer is constant over material and degradation state.

The bars in Fig. 3:54 are scaled to the real average values for the measured lifetime and estimated for the rest. The first sum tells us directly about the influence of the surface. The large bulk lifetime of FZ-Si let the effect of the surface passivation. This number is then used for the approximate evaluation of the Cz-Si material.
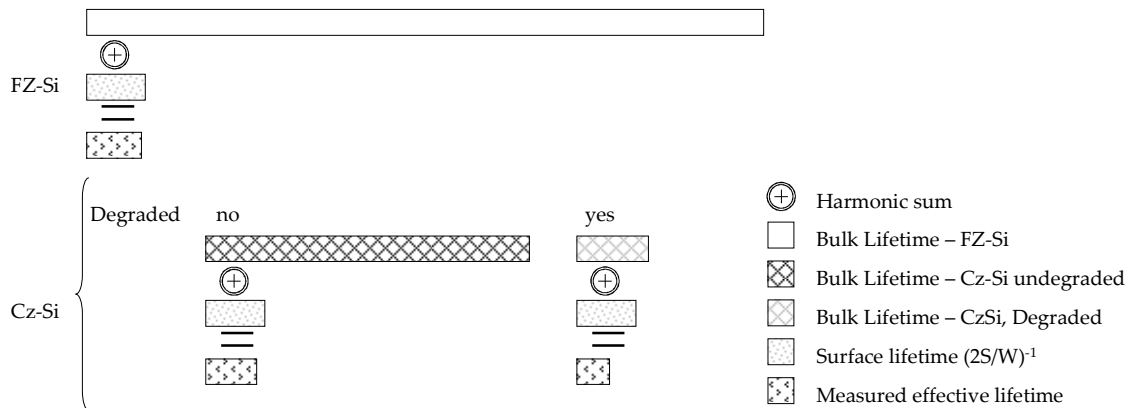
Fig. 3:54 Graphical representation of the harmonic sum. The harmonic sum is always the lower of each summand.

We can conclude that the surface passivation obtained is completely satisfying for the purpose of passivating Cz-Si material, especially after degradation. The effective lifetime measurements resulted in a surface recombination S of about 78 cm/s.

The combination that portrays itself as most suitable presents a capping layer which reproduced the optimal candidate of the previous investigation.

The first layer capping the SiO_2 seems to play a big role in the passivation mechanism especially after a high temperature process. The characterisation below will shed light on the mechanism.

♦ *Electrical characterisation of the SiNTOx stack*

In 2.2.2 an analytical approach is presented to explain how the surface states and Coulomb's law can influence the resulting S. The characteristics which influence this value the most are the density of interface states (D_{it}) and the amount of charges at the surface (indicated usually through its correspondent charge stored in the semiconductor Q_{SC}).

To underscore which parameter of the PECVD staked layer contributes to the surface passivation and to which level they do, analyses of the samples were performed by means of Capacitance Voltage (CV) sweeps (see Appendix A.b).

The CV measurement setting, which featured a mercury tip, could be performed directly on the samples without requiring additional metallisation steps. An additional advantage of this technique is a lower sensitivity to leakage, since the metallisation covers a small area, and therefore decreases the probability of intersecting a pinhole.
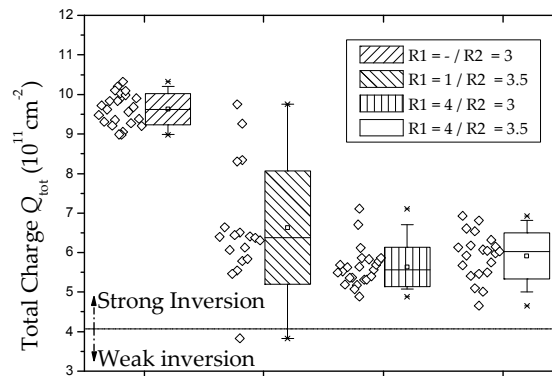
Fig. 3:55 Density of surface charge measured on four different passivation schemes. The measurement was repeated several times on different points on the same wafers. The legend reports the gas ratio used to deposit the 1st layer (R1) and the 2nd layer (R2) capping the SiO_2.

The measurements were performed on the three combinations presented previously and additionally on a configuration where the layer in the middle is removed.
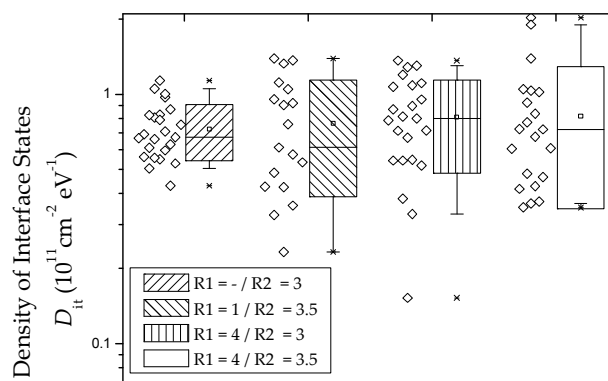
Fig. 3:56 Density of interface states of four different configurations, the level does not change with a change in capping layer.

The density of interface traps (D_{it}) is strictly related to the silicon to SiO_2 interface. All wafers characterised therefore show the same order of magnitude. This specific characteristic is independent to any change in the capping layer. Instead the charge measured in the dielectric is affected by the 1st layer. Its presence introduces a significantly lower amount of charges. This is

beneficial, since the layer does not impose an extremely strong inversion of type at the silicon surface. As it will be signalled from the model in Chapter 5, any conduction at the surface is to be avoided.

3.6.9 Comparison of the complete PECVD and PECVD capped thermally grown SiO₂ passivations

The complete PECVD passivation (SiriON CaTS) has the ability to reduce the *S* below 10 cm/s. The interest that this feature arises in PV motivates its investigation. This resulted in a complete empirical understanding and a modelling of the phenomena {Seiffe, Gautero et al. 2010}.

By means of SPV measurements it was demonstrated that the SiriON CaTS imposes a strong inversion layer in the silicon. Such an inversion can be conductive and deliver conductive channels for the minority carrier towards highly recombinative points. On the other hand, its implementation on n-type doped areas results in excellent passivation without imposing constraints at the solar cell level, since an accumulation region is created (see Chapter 5). These consequences will be partly seen in the pragmatic realisation of solar cells in Chapter 4.

Less prone to surface conductivity problems are passivations based on thermal oxide (SiNTOx). These have a low amount of charges of their own and can even be combined with other dielectrics to enhance functionalities.

A functional passivation based on the requirements was created. This is composed of a thin SiO₂ and a stack of nitrides. The adoption of certain PECVD deposition schemes also leads to advantages. These allows high level of passivation, even after RTP steps.

Below (Chapter 4) the implementation of these thermal oxide based passivations will deliver concrete and noteworthy results at the solar cell level.

3.7 Characterisation of the contact formation

The last component for the creation of the structure described in Fig. 3:6 is a metal to semiconductor contact. This allows the exchange of energy of the PERC structure to the world.

3.7.1 Theory

For a correct evaluation of the contact several aspects have to be detailed. In the following the three most important are gathered and explained, and references where higher detail can be found are also mentioned.

◊ *Spreading Resistance*

The small geometry of the local contact, compared with the width of the solar cell bulk, is the cause of a current crowding. Its effect translates into an increase of resistance in the bulk, in series with the contact resistance. The so-named spreading resistance effect depends on the contact radius *a*, the thickness of the sample *W*, and the conductivity of the sample bulk σ. The first proposed treatment {Cox and Strack 1967} is an empirical relationship

$$R_{\text{spread}} = \frac{1}{2\pi a\sigma}\arctan\left(\frac{2W}{a}\right)$$

Eq. 3—4

that describes the additional resistance term of one contact that depends on the geometry. The actual contact resistance is added to R_{spread}; with most of the semiconductor and metal combination, this latter component is not significant.

Later, Fischer in his dissertation {Fischer 2003} used the expression (Eq. 3—4) to describe the situation of locally contacted solar cells by adding an extension

$$R_{\text{spread-F}} = \frac{1}{2\pi a\sigma} \arctan\left(\frac{2W}{a}\right) L_{\text{p}}^{2} + \frac{W}{\sigma}\left(1 - e^{-\frac{L_{\text{p}}}{W}}\right)$$

<div align="right">Eq. 3—5</div>

that takes into account that the contacts have a surrounding area which square root is equal to L_{p}. This length is large in comparison to the thickness W; an example is offered by the drawing A in Fig. 3:57. In the literature the extreme of this condition ($W \gg L_{\text{p}}$), when additionally the radius a is small compared to the thickness W, is called the small scale limit. Since pitch and radius of the contact are given, it is possible to define the coverage fraction f as the ratio of the contact area and the area interested by the contact (which is a function (u()) of the pitch and on the distribution of the contacts).

$$f = \frac{a}{u\left(L_{\text{p}}, \left|\begin{matrix} \text{contacts} \\ \text{distribution} \end{matrix}\right|\right)}$$

<div align="right">Eq. 3—6</div>

A useful term for the analyses of the back surface is the coverage fraction (f). It indicates the ratio between the surface dedicated to the transport of majority carrier (metal contact) and the total area. This ratio depends on the radius a, the pitch L_{p} and the contact distribution scheme (i.e. contacts on the corners of adjacent triangle or adjacent squares, see Fig. 3:57 (b)).
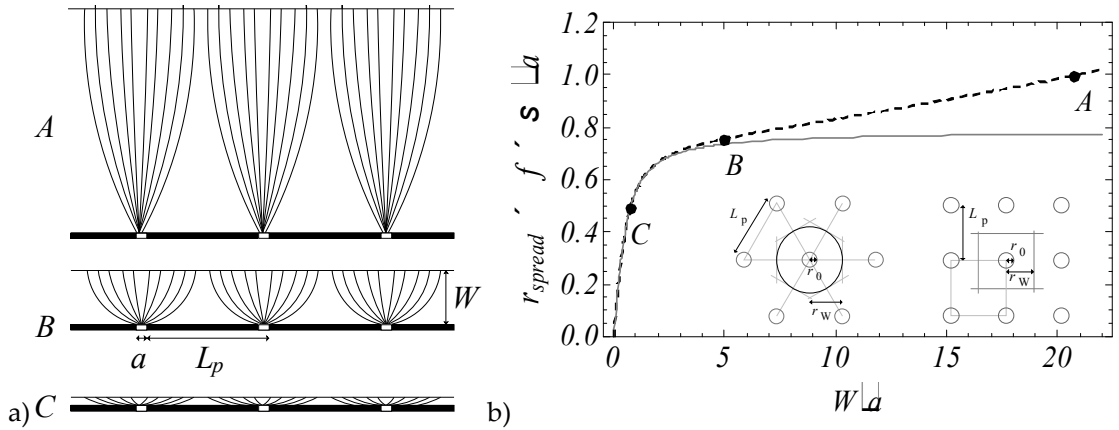
Fig. 3:57 a) Different geometrical configurations of local contacts (white rectangles) at the back surface (thick line) and the current flow (lines) towards the front surface (thin horizontal line). In the drawings the thickness W, the contact radius a and the pitch between contacts L_{p} are indicated. b) The normalised spreading resistance is presented in the dashed black line. Furthermore, the three situations (A, B, and C in a) are highlighted. The back surface can be either filled with contacts on every corner of adjacent equilateral triangles (full lines) or on every corner of adjacent squares (dashed lines). In light gray a mere Cox and Strack formulation weighted by the harmonic sum[21] of the contacts' resistance is indicated.

Current technology faces cell thickness to contact radius ratios between drawing B and drawing C, as represented in Fig. 3:57. Extreme cases below C were investigated {Kray and McIntosh 2009}, and it was shown experimentally that the model no longer holds, as the resistance does not tend to zero in the case of small thickness. The model predicts this decrease in resistance because it does not consider the lateral conductivity needed for transport of generated carriers; more about this will be described in a near future publication {Saint-Cast, Wolf et al. 2010}.

---

[21] With harmonic sum it is indicated the sum of the inverse of the elements taken in consideration.

◊ *Contact Resistance*

The interface which is created is governed by barrier mechanisms {Sze and Ng 2006}; unfortunately a large divergence from this theory is found, and there are two reasons for this: a lowering of the silicon to metal barrier due to image force, and an high amount of interface states within the barrier. The former effects reduce the amount of potential needed to overcome the barrier and the latter introduces electric paths below the maximum barrier height. For example, aluminium deposited on silicon has good contacts already after low temperature annealing (well below Al melting temperature or Al-Si alloying eutectic temperature). This is due to the formation of interface states {Bardeen 1947}. In the next paragraph, reasons will be given to disapprove this configuration. Therefore, other mechanisms of transport have to be used.

From an earlier study {Yu 1970}, it is stated that an increase of surface doping can lead to higher probabilities of carrier tunnelling through the barrier (case of field emission in Fig. 3:58). The increased surface doping will foster field emission even in case of image force; on the other hand, a high number of interface states will conceal the effect of surface doping.

This field emission configuration leads to pseudo-ohmic behaviour of the contact and it is convenient for the contacting application.
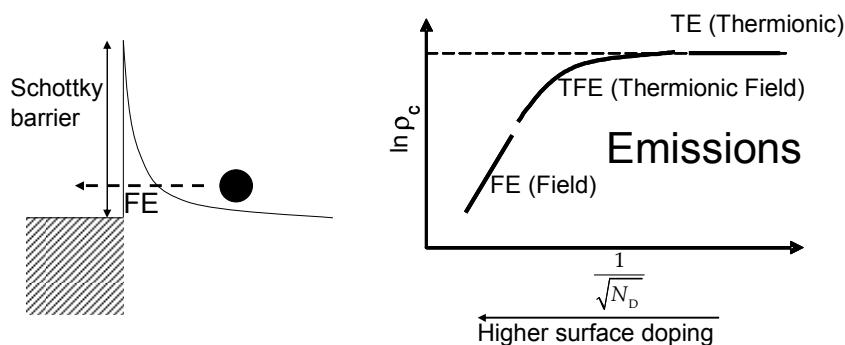
Fig. 3:58 A schematic description of the favourable emission for low contact resistance is depicted here, after Yu {Yu 1970}.

While it would be possible to use highly doped substrates, it is in practice avoided to prevent a bulk completely dominated by Auger recombination even at low injection. A more feasible alternative is to dope locally the bulk in the region surrounding the interface to the metal; high Auger recombination is then limited to part of the surface (corresponding to the coverage fraction f).

Glunz characterises the field emission effect by evaluating the amount of current which is needed to saturate this conduction channel and to force conduction also in the aluminium–silicon Schottky diode {Glunz, Nekarda et al. 2007}. This characterisation method allows a qualitative evaluation of the contact resistance. From this work it results that the contribution of the contact is marginal in most cases. The bigger part of the contact resistance consists of the spreading resistance.

◊ *Surface recombination velocity at the contacts*

Degrading the surface recombination velocity at the contact (S_{met}) to high values by increasing the number of interface states below the maximum barrier height is one possibility to have a good contact resistance. The loss introduced by this treatment results, on the whole back surface, in an increased S; hence a loss in efficiency. Even worse would be the case of back surface passivation by a floating junction as described below (Chapter 5); there, the lateral conductivity of the junction would allow rapid displacement of carriers to the metal to silicon highly recombining regions.

More convenient is a built-in field from the surface towards the bulk, realised by means of local doping around the contact area. This can decrease the contact resistance fostering

tunnelling transport, and can introduce a high-low junction {Godlewski, Baraona et al. 1973}, which, creating a small space charge region, decouples the geometric metal to semiconductor interface from the base to contact recombination interface, moving it towards the bulk {Dauwe 2004} (Fig. 3:59).
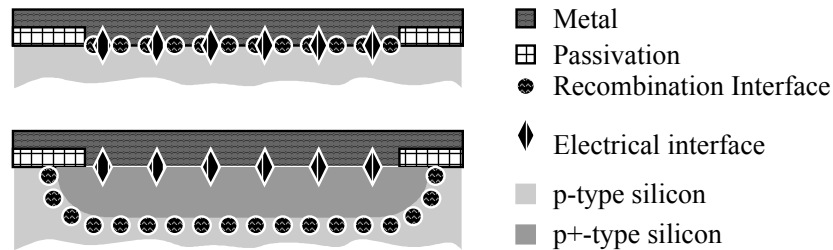
Fig. 3:59 Sketch of the decoupling introduced by a doped area. The recombination interface and the electrical interface are distributed differently in space and can be optimized independently.

Recent studies have lead to accurate modelling {Altermatt, Steingrube et al. 2009} of the aluminium doping effect on the passivation level, taking also into account the decreased lifetime of an aluminium doped region.

♦ *Implementation*

Two methods were evaluated for the realisation of contact structures for highly efficient solar cells. The first takes inspiration from the conventional implementation by confining geometrically the alloying area to defined windows through an alloying barrier. The second method exploits the alloying barrier during the high temperature process on the whole surface to avoid alloying. After the sintering of the aluminium layer the procedure locally heats the aluminium, the barrier, and the silicon by means of a laser. The melt re-crystallizes and creates a contact {Nekarda, Stumpp et al. 2009}. This second method is a modification of the Laser Fired Contact {Schneiderlöchner, Grohe et al. 2005}. Note that in this first implementation the aluminium layer is brought to the surface by evaporation. This is, for this reason, denser and therefore a reduced thickness, compared to the screen printed approach, delivers the same conductivity.
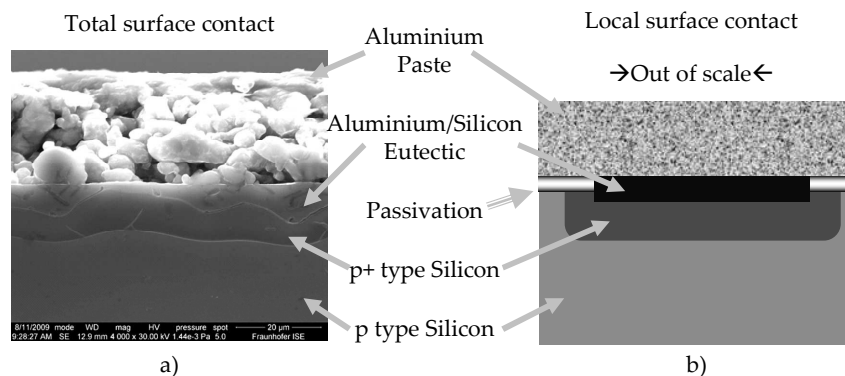
Fig. 3:60 a) Cross section of a fired aluminium paste to silicon interface, created with a conventional process flow b) sketch of an ideal local contact.

The alloying barrier is chosen to be functional, thus, it introduces a passivation effect on the surface which it covers. For this reason the alloying barrier is also a passivation layer.

Based on the contact theory it is possible to sketch an idea of the targeted structure (Fig. 3:60). Of paramount importance is the p+ area close to the metallic interface.

3.7.2 Sintered local contact

One possibility to create local contacts is to exploit the sintering action which takes place during the high temperature step (FFO). The feasibility of this approach was demonstrated previously on PERC type structures {Agostinelli, Szlufcick et al. 2005}.

The necessary steps for the creation of the contact structure on the back surface of a solar cell were extracted from the advanced PERC device processing and applied to a silicon substrate. The contact structure is reproduced as a consequence on one surface of the silicon wafer (Fig. 3:62). The starting material (p-type mc-Si, $\rho = 0.5 \div 2\,\Omega\cdot$cm, full square, 125 mm side, 200 µm starting thickness) is treated to remove the saw damage; the target surface is then coated with the best PECVD SiN_x passivation investigated in 3.6.7. This acts as alloying barrier. At this stage the samples are split into three groups, "Flat", "Hollow", and "LFC"; each representing a different technique to realize a contact (Fig. 3:61).

The opening procedure, which is adopted for both the Flat and Hollow cases, is a chemical etching of the PECVD deposited passivation dielectric. The etching was made selective with the help of a wax mask deposited on the dielectric by means of an inkjet (similar use of the technique was previously employed {Alemán, Bay et al. 2008; Specht, Biro et al. 2008}.

Additionally for the Hollow case, the interface is further structured with a hollowing procedure, resulting in a cavity surrounded by the passivation; this latter structure is achieved by etching the exposed silicon to a chemical etching by means of diluted hot KOH before screen print. The LFC case, instead, does not receive any treatment before the paste deposition.
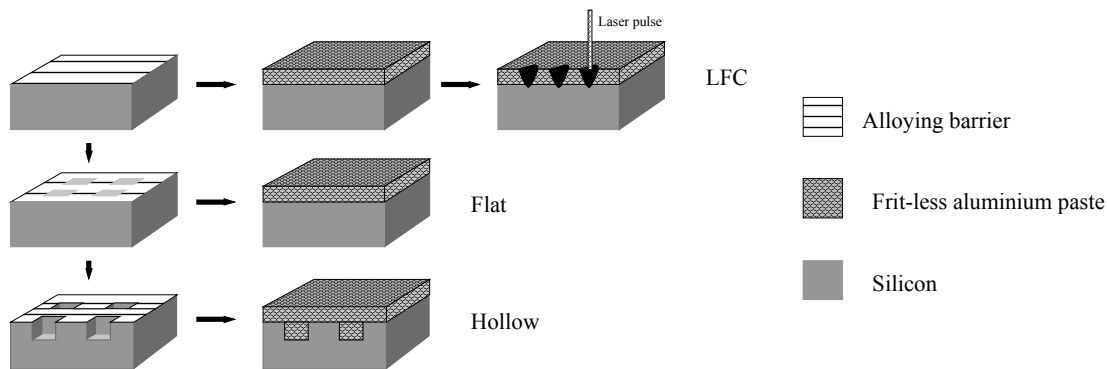
Fig. 3:61 sketch of the different contacts configurations explored in the experiment.

All samples are deposited with aluminium paste and exposed to a high temperature process (indicated as firing or RTP). In two cases, flat and hollow, a sintering of aluminium particles and silicon takes place.
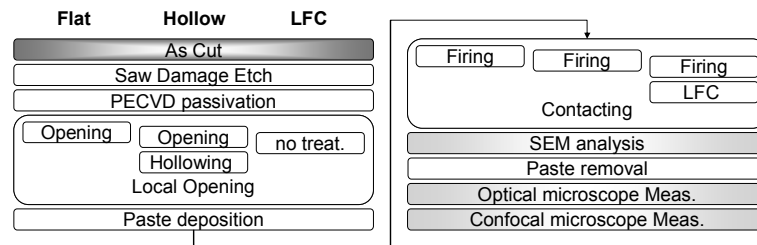
Fig. 3:62 Process sequence for the samples characterised, the three groups: left (Flat), centre (Hollow) and right (LFC) differ for the contacting technique; the amount of paste deposited is reported and mentioned in cases where it introduces particular behaviours.

Optical characterisation was chosen as observation tool. It was performed by means of: optical microscope, confocal microscope, and scanning electron microscope (SEM). Images were taken to measure the contact area and the depth with the sample laying on the chuck and the

lens perpendicularly on top of it (see Fig. 3:63 a) &b) for optical microscope and SEM pictures, in Fig. 3:64 a cross section realised by means of confocal microscope is presented). The details of case LFC will be presented in 3.7.3.
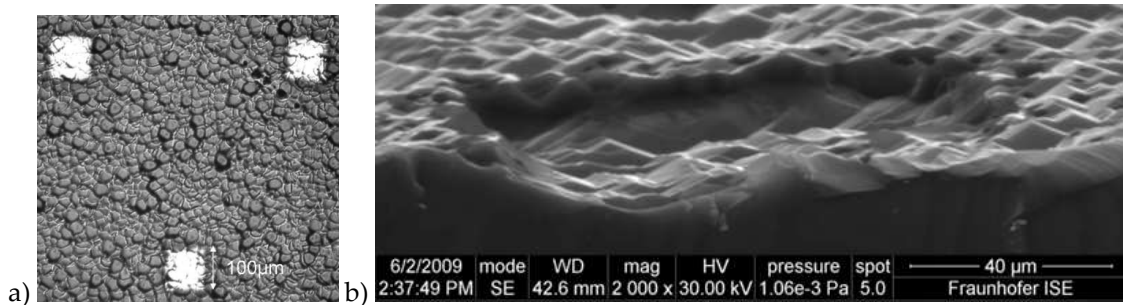
Fig. 3:63 a) Openings on the silicon surface, in white is the silicon and in light grey is the passivation, Flat configuration b) Tilted view of a hollow in the silicon at a fresh cut, Hollow configuration.

For the case of "Flat" several measurement are reported in Fig. 3:64 b). These relate the opening performed to the processing stage at which is observed. The values represent the opening area of: the mask design, the printed wax mask, the resulting windows in the passivation after chemical etching, and finally the openings after the sintering. These measurements were performed for three different mask designs, all the processes resulting in a stepwise increase in the area. The presence of this increase has to be taken into account during the design phase; the final total metal coverage f depends on a careful design.

After the processing and the chemical etching of aluminium, the sintered local contacts present a slightly larger opening (Fig. 3:64) especially in the hollow case. Additionally, in both cases, a depth greater than 25 µm is measured.
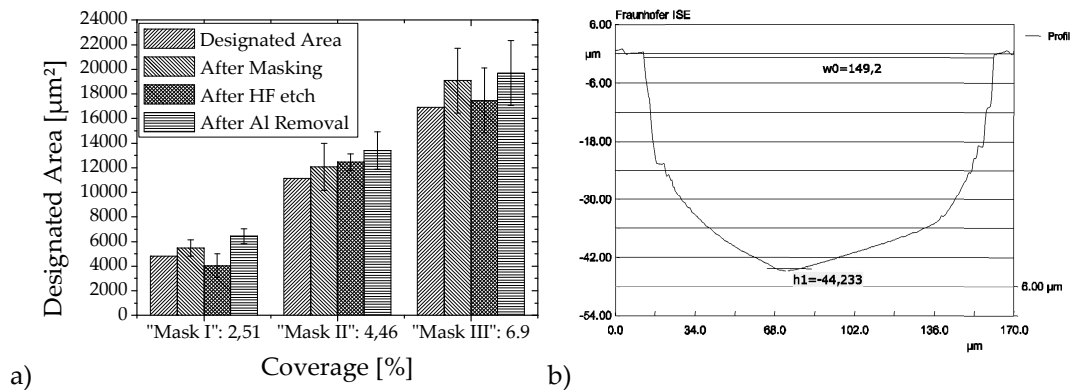
Fig. 3:64 a) The area of the contacts is verified at each stage of the processing (Flat), since the coverage is a critical parameter. This graph gives hints on how the masks have to be designed to achieve specific coverage. b) The depth profile of a contact measured by means of confocal microscope after the etching of the metallic part.

After etching the samples in a hot HCl solution, the metallic part of the contact can be removed, making it possible to characterise any modification of the contact area. This is found to have increased for both Flat and Hollow (Fig. 3:64 a). In addition, the morphology of the residual silicon interface can be measured with the help of the confocal microscope. The fingerprint of the metal to silicon interface is found deep in the substrate. Depths greater than 25 µm on average were observed. A typical depth profile is reported (Fig. 3:64 b).

During the high temperature step the alloying removed a large quantity of silicon; this digging procedure has unfavourable crystallographic planes, which present themselves in the final metal to silicon interface as precise planes. This characteristic was observed on the mc-Si

substrate (Fig. 3:65), the randomness of the grain orientation, however leaves little room for a direct optical analysis of these preferred directions[22], in the literature {Uruena, John et al. 2009} the mentioned hardest plane to etch is the (111).
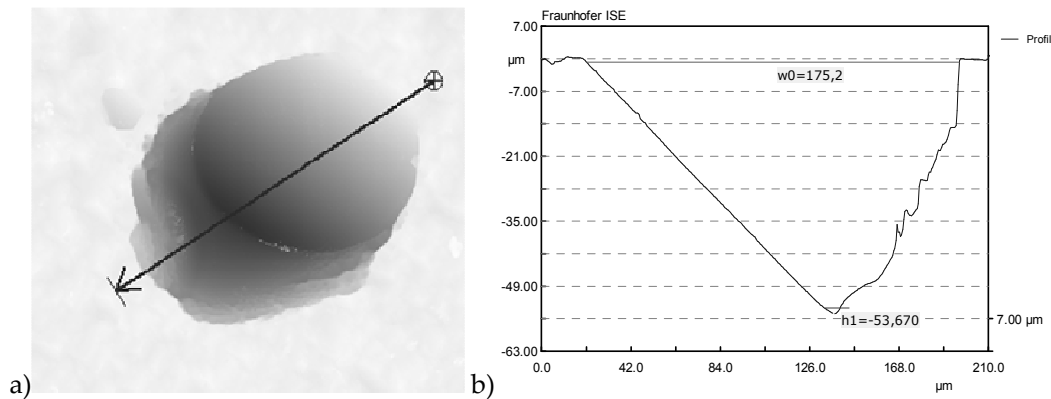
Fig. 3:65 a) Gray scale relief image, the arrow indicates the line on which the depth measurement takes place. b) Optically measured profile, the etching plane and its precision can be easily recognized. Hollow configuration with 7.9 g/cm².

Further information of the contact formation is available by imaging the contact cross section; great care has to be taken to guarantee that all different material layers are cut along the same cross sectioning plane and that they remain present after the polishing. These are necessary requisites for the correct interpretations of the cross sections {Grasso, Gautero et al. 2010}.

While the technique was performed to the best practice possible, rarely is the cross section exactly along the middle of the contact. Hence, the depth and lateral dimensions cannot be directly compared to the previous characterisation, performed with a top view. Dimensional values measured on these cross sections indicate that the cut is close to the maximum diameter of the contact.
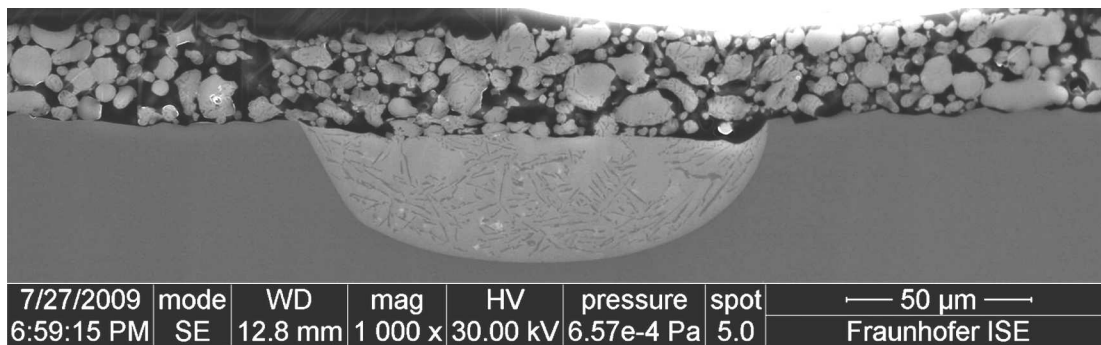
Fig. 3:66 Example of cross section. This image was taken on a Hollow configuration where 6.2 mg/cm² of paste was deposited. The light gray features in the contact and in the particles of the paste matrix are lamellas. This was confirmed with further processing (Stain Etching SE). Lamellas can be found farther than the edges of the contact, a significant and fast transport of silicon towards those areas happens during firing.

An additional set of information is gathered from the imaging when a selective etching of the doped areas is performed {Runyan 1975}. As demonstrated from a previous work {Huster and Schubert 2005}, a higher aluminium doping concentration is found at the interface between the bulk silicon and the aluminium doped silicon layer. This monotonically decreasing Al

---

[22] Characterisation methods to measure the grain orientation are available. Their application is planned as next sound step of the analysis.

concentration towards the surface is a consequence of the temperature dependence of the aluminium segregation coefficient in silicon

This aluminium doping profile, sketched in Fig. 3:67 a), relaxes the selectivity requirements for the etching solution, but the actual minimum value of doping that allows etching does not contribute to the measurement of the maximum depth of the doped area. Measurements on the etched area are translated into measurements of the location where doping is found.
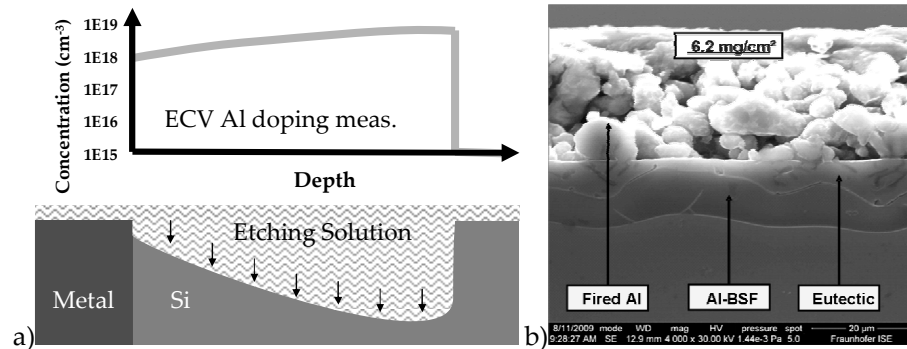
Fig. 3:67 a) Sketch of the staining procedure, b) effects on a total BSF sample, the different areas are now in sight thanks to the relief effect of the etched area.

The etching procedure, which is usually also named stain etching[23] (SE), was calibrated on a part of the experiment samples where an uninterrupted opening of several millimetres was present through the alloying barrier. The large opening configuration allows the same formation conditions of a conventional Al-BSF; during the cooling phase of the RTP, the epitaxial layer of Al doped silicon grows on the substrate. The SE procedure is applied and this doped silicon can be distinguished from the eutectic layer (Fig. 3:67 b), the depth of the doped area is also in the range found in the literature for similar processing conditions.

The SE will lead to an etching of doped areas in the local contact configuration as well, allowing the desired geometrical characterisation of the aluminium doped areas {Popovich, Janssen et al. 2009}.
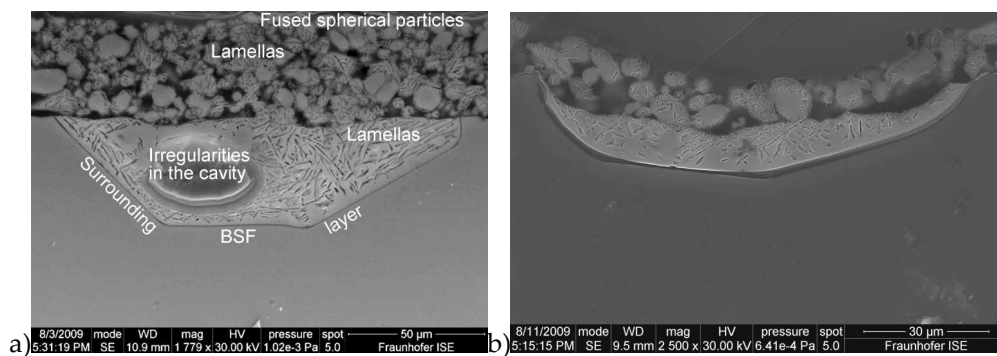
Fig. 3:68 a) Example of a contact formed on a Hollow configuration, details on the features that can be seen are highlighted, the amount of paste printed is 7.9 mg/cm² b) Hollow configuration with reduced amount of paste (4.7 mg/cm²), the doping area is inhomogeneous and in some areas absent; this observation was also possible on other contact configurations of the same kind.

The results are illustrated with images from the SEM (Fig. 3:68 and Fig. 3:69). The features of importance are highlighted in one picture (Fig. 3:68 a) as a guideline. Many of these features are

---

[23] This procedure is commonly used with dyes that are sensitive to specific properties and give colour to the surfaces possessing them; in our case we are not colouring the surface of interest, but simply putting it in negative relief by corroding it.

predicted from an existing alloying model {Huster 2005}. However, the following list will introduce more clarity.

The first feature, fused spherical particles in the paste matrix, testifies to the interchange of materials during the high temperature step, as explained in the literature.

Second, lamellas formed in the particles during the cooling down period. These are composed of the Al-doped silicon expulsed from the Al-Si melt. This silicon was not in the vicinity of the silicon substrate and therefore could not contribute to epitaxial growth.

Third, a cavity filled with eutectic mixture, the volume of the dug silicon is filled with the by-product of the melt. Material analysis on this area, performed by means of Energy-dispersive X-ray Spectroscopy (EDX), reveals a high quantity of aluminium and, to a lesser extent, silicon. These findings indicate this mass is a eutectic region.

Fourth, lamellas in the eutectic region, though they exist in the vicinity to the substrate, this expulsed silicon can not diffuse[24] towards the substrate, therefore crystallizes in elongated shapes in the middle of the eutectic solid.

Fifth, a thin etched region in contact with the silicon substrate is observed. The doping level of this region, detected by stain-etching, can create a built-in field at the surface, hence it can be called BSF region.

Finally, sixth, some irregularities which are not expected, like voids.
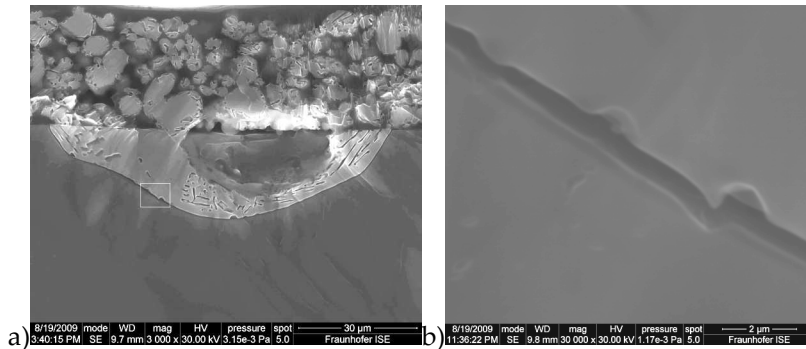
Fig. 3:69 a) Example of contact formed on a Flat configuration, the features repeat as in the image Fig. 3:68 but less accentuated b) a detail taken at the white square of the image a); a thin surrounding BSF can be seen.

Lamellas are distributed in a random manner in the particles and in the contact centre. A closer observation unveils a region, in the proximity of the thin BSF layer, where these Si crystals are not present; this goes in agreement to a small capability of transport of silicon in the melt. Unfortunately this diffusion is too slow to allow the epitaxial deposition of all the exceeding silicon on the substrate. Factors such as cooling time or maximum amount of silicon dissolved in the eutectic melt can play a role in the formation of a better local BSF (LBSF).

Based on previous models of aluminium and silicon alloy with no geometrical constraints, using the information gathered with these observations on the samples, and interpreting the information shared by the photovoltaic community on the matter {Beaucarne, Choulat et al. 2008; Uruena, John et al. 2009} it is possible to resume the ideas in a contact formation model (Fig. 3:70). The aluminium silicon phase diagram is helpful to understand how the observed sintered contact is achieved.

---

[24] The transport mechanism of the individual silicon atoms in the melt is assumed to be diffusion. Gravity could play a role only when the two components of the melt are not soluble and differ strongly in density. This is unfortunately not the case, silicon and aluminium share the same mass density in their liquid phase. Furthermore, silicon aggregate solidifies instantaneously due to the solidification temperature of silicon. This quick solidification hinders the presence of silicon onto the bulk surface.
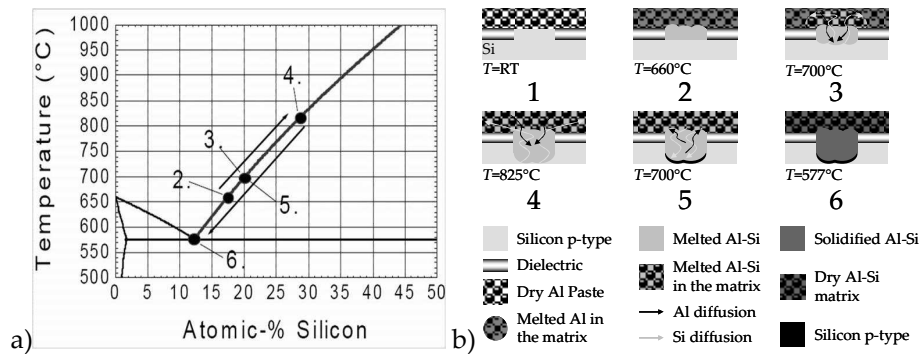
Fig. 3:70 a) Model steps as they can be found on the phase diagram (phase diagram sketch from {Huster 2005}), b) sketch for a modelling of the contact formation sequence, as it results from the consideration of this work.

The model (Fig. 3:70) explains specifically the evolution of the system at the starting interface between silicon and aluminium; this geometrical surface is indicated by a white line in step 1. The system is described using the phase diagram of silicon in aluminium.

The processing starts with step 1 (Fig. 3:70), room temperature and silicon-free aluminium above silicon (RT, 0% Si). A steep increase in temperature leads the aluminium to melt (660 °C, 0% Si), furthermore, with this temperature at the interface, within a growing volume, the aluminium starts to incorporate silicon. As seen on the phase diagram, the situation moves from the ordinate towards point 2 on the phase diagram (660 °C, 17% Si). This volume contains liquid Al-Si alloy, and expands farther in the aluminium matrix and in the unprotected substrate. By increasing the temperature further, the alloying process can drive more silicon in the melt. Stepping from point 3 to 4, it is possible to observe that the only source of silicon is the substrate through the opening; for this reason, the digging can reach several tens of micrometres. Further heating results in an increasing percentage of silicon in the melt, which is distributed equally thanks to diffusion.

During the cooling down step, the mechanism of silicon transport is able to contribute to an epitaxial growth to a small extent (the LBSF is few micrometres, as seen in Fig. 3:69 and Fig. 3:70). However, this transport is not fast enough to bring all the excessive silicon back to feed the epitaxial growth on the substrate. The result is that this almost immobile silicon expelled in the Al-Si melt curdles into several clusters, which, as already mentioned, are called lamellas in the literature.

The average distance of the lamellas depends on the diffusion velocity of silicon.

The final configuration will have a thin LBSF, and a large part of the silicon at the contact will be replaced by an Al-Si eutectic layer filled with lamellas.

A consequence of the layout of a model is to exploit this understanding and modify the processing in order to achieve the desired structure. A first indication from this model consists of reducing both max temperature and cooling speed to enable the flight of doped silicon towards the silicon substrate to enhance the epitaxial growth.

At **IMEC** the control of silicon absorbed during the alloying with the aluminium is obtained by reducing the metal accessible through the alloying barrier. The depth of the contacts is kept well below the thickness of the cell[25] thanks to a great accuracy of the deposited aluminium thickness (i.e. deposition by evaporation)

3.7.3 Laser Fired Contacts

The Laser Fired Contact technique (LFC) was introduced with the purpose to investigate a cost effective procedure to allow for contacting for highly efficient solar cells {Preu 2000; Schneiderlöchner, Preu et al. 2002}. This first implementation exploited as doping source an

---

[25] Private communication with Joachim John and Guy Beaucarne.

evaporated layer of aluminium on the back surface. This continuous metallic layer can connect the locally fired contacts with each other.

A first adapted laser process has been developed in parallel work based on advanced electrical characterization. It was then possible to successfully replace the evaporated aluminium with a screen-printed and sintered layer of aluminium paste.

The advanced electrical characterization {Nekarda, Stumpp et al. 2009} made use of advanced electrical characterisation to find a suitable window for the implementation of the process on screen-printed metallisation. A further analysis, which can show the laser fabricated structure at the micrometre scale, is the cross sectioning and the subsequent stain etch {Grasso, Gautero et al. 2010}. This latter technique will be detailed below.
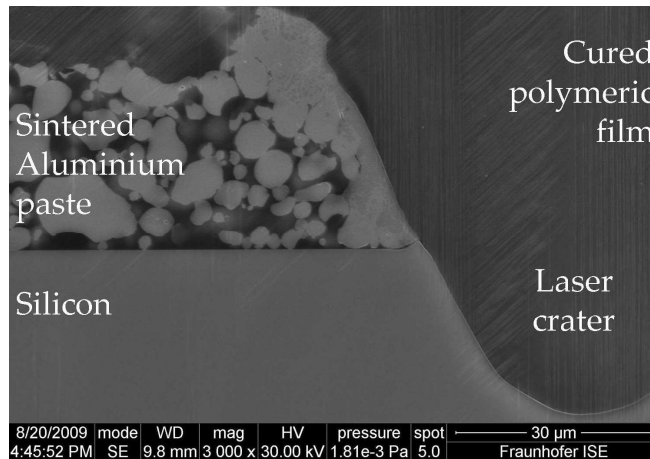
Fig. 3:71 Cross section of a LFC, the polymeric paste fills the crater left from the laser processing.

The samples (p-type FZ-Si, $\rho = 0.8 \div 1.2\,\Omega\cdot cm$, pseudo square, 125 mm side, 210 μm starting thickness) were entirely coated by means of PECVD on both sides with a passivation layer (SiriON CaTS); subsequently, a screen print step deposited a layer of aluminium paste (ca. 6 mg/cm²) on both sides, and afterwards an RTP process sintered the paste. At this point the LFC points were performed at their state of the art.

The sample is preventively coated with a heat curable polymeric paste. After the curing the sample is ready for any cutting procedure, preventing any break away of aluminium paste during the mechanical stress. The samples are cut in order to meet a cross section of the realised LFC (Fig. 3:60). As it can be seen in the SEM picture, the polymeric coating reveals itself to be of great help for the study of the contact; we understand that the crater, already evident from a top view, deepens in the silicon substrate. Traces of melted and recrystallised matter are found on the edges of the crater, on top of the sintered metallic paste.

Further information can be gathered from such an imaging technique when the SE technique is applied to the local LFC contact. Again the polymeric coverage turns helpful when setting the limit of the sample before the staining. It is therefore possible to measure the distance between the previous border of the sample and the end of the etched region, as this defines the thickness of the LBSF.
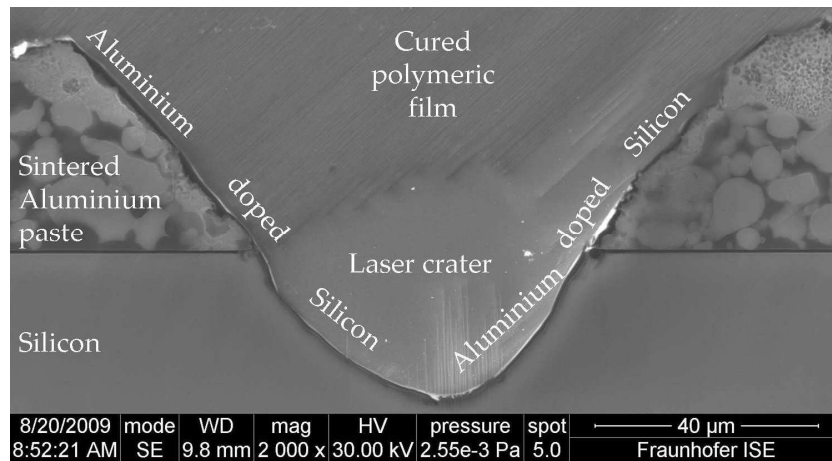
Fig. 3:72 Stained cross section of a LFC point. The SE unveils a thin doped layer all around the contact. This is indicated as "Aluminium doped Silicon". Furthermore, it attests that the recrystallized material on top of the screen printed aluminium is composed partly of doped silicon. However, the picture presents a sponge like texture of crystallised aluminium. This is probably due to the fast recrystallisa time, which hinder the formation of long lamellas.

This thickness is well below a micrometer, though the electrical characterisation indicates that the performance of such contacts, evaluated through the term $I_{0b,LFC}$, is lower than a recombination limited only by the maximum speed of carrier movement (thermal velocity v_{therm}). This is a positive indication of passivation on the contact surface. Furthermore, the sample thickness used also avoided any strong contribution from diffusion limited minority carrier transport. This means that all generated carriers diffuse in the whole bulk and the carrier distribution can almost be approximated with straight lines.

The material found on top of the sintered aluminium paste is also detected as doped silicon from the SE technique; this information guarantees the presence of a melted phase between aluminium and silicon.

Based on the electrical and the optical characterisation it is observed that a local BSF with a small thickness is already sufficient to deliver acceptable contact and passivation. This result was also put forth by simulations {Haase, Müller et al. 2010}. These demonstrate that even a thin, lowly aluminium-doped silicon layer can be implemented in PERC structures with good results.

3.7.4 Conclusions

Local contacts on the back surface of solar cells can be realised with two techniques, both of them can guarantee a good contact with the base. An optical study demonstrated that the thickness of the Al-BSF is low. However, studies and further experimental work demonstrated that this number is not of great influence on the final performance of a PERC structure {Haase, Müller et al. 2010} if the coverage fraction is kept low.

When the passivation is realised by means of a floating junction, much higher requirements on the contact structure are demanded (see Chapter 5).

Chapter 4   Considerations on realisation and characterisation of solar cells

Target of this chapter is the creation of PERC-like structures. After a brief summary on existing schemes, the attention will move to newly introduced specific production flows that integrate the advanced processing described above (Chapter 3). Experiments on the complete solar cell processing were conducted in order to identify which method would be successful and deserved more attention. Of uttermost interest is the profitability of the final product. Therefore, in the first experiments (from 4.2 to 4.4) the material cost was brought down by reducing the thickness. Instead for the experiments detailed in 4.5 and 4.6 the convenience of integrating more advanced plasma based processes was explored. The section on the cells ends with a series of analysis which unveils the ideal potential of the thin cells realized (see 4.7). At the end of the chapter considerations on integration of high efficiency solar cell in modules are presented (4.8). A process is realised and tested. All the challenges for the implementation of the highly efficient cell structure and their integration in solar modules will then be faced.

4.1   Industrializing a passivated emitter and rear cell concept

More efficient solar cells foster their introduction in the energy market. The study of a new technique to increase the ratio of power generated versus the production cost is therefore of lively interest. The implementation of highly efficient solar cell structures has already been demonstrated at the laboratory scale. The nowadays concern is to use the acquired knowledge to create and to evaluate advanced processing of high throughput which are able to realise highly efficient solar cell structures. Therefore, the PERC structure presented in Chapter 3 (see Fig. 3:6) will be the theme of this and the following sections. Below a short review of the existing works on the subject and an exploration of the possibilities will be presented.

4.1.1   Existing concepts

First attempts for the production of an industrially practical both side passivated cell were intrinsic to bifacial cell concepts. Indeed, the passivation scheme was an induced emitter on both sides, realisation was demonstrated on large cells {Jaeger, Roth et al. 1992}. Another approach based the passivation on a diffused and contacted emitter acting as an additional cathode also on the back side {Warabisako, Matsukuma et al. 1993}. These two implementations reduced the saturation current of the bare metal contact. The gain obtained compared to conventional solar cells of those times was considerable.

Already before these implementations, the passivation by means of a thermally grown silicon oxide was mature enough for application at the lab scale. This paved the way for the realisation of high efficiency structures. Efficiencies over 20% were recorded in several labs

working on PERC like structures {Blakers, Zhao et al. 1989}. However these latter cell concepts were far too elaborated for the time. Technologies available to the industry were not cost effective. The knowledge of the structure was there, though the technology transfer process needed more time.

Many studies on the structure have been performed since. They concerned cheaper passivation procedures and faster metallization technologies. These were proposed to reduce complexity.

With a first publication in 2005, **IMEC** presented an industrialization of a back surface passivation {Agostinelli, Choulat et al. 2005; Agostinelli, Szlufcick et al. 2005}. This process exploits a passivation layer based on deposition technique. Furthermore, it adopts a screen printed metallisation technique. This is an already well established technology for conventional cells.

Figure 1. Integral process sequence for the production of i-PERC solar cells. The process, while making use of screen printed metallisation, is nevertheless suitable for ultrathin substrates and has been successfully tested on cells as thin as 90µm.
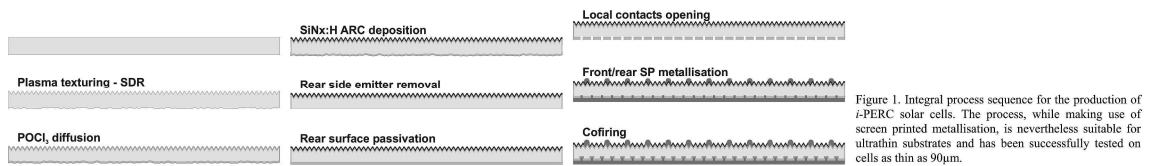
Fig. 4:1 Process flow listing and sketch of the processes on the silicon substrate. (from {Agostinelli, Choulat et al. 2005})

4.1.2   Roadmap for the development

On this regard, also the **Fraunhofer ISE** proposed several approaches. Noteworthy is the work from Hofmann {Hofmann 2008}. In this work passivation procedures have been further studied and developed.

In the time period of this work two process flows have been explored in the **Fraunhofer ISE** lab. These are both compared with a conventional processing sequence in the diagram of Fig. 4:2. They offer the possibility to break the front to back symmetry (see 3.3 and especially 3.4.2) and produce a flat back surface. Alternative "A" is a prior back surface conditioning, which is performed by applying single sided chemical and diffusion barriers {Biro, Mack et al. 2009}. Alternative "B" features a processing able to perform a silicon etching selectively on one side after the texturisation and junction diffusion.
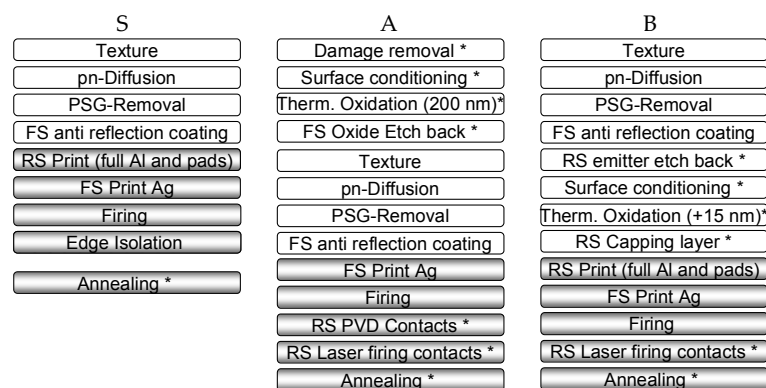
Fig. 4:2 Process sequences for the conventional Al-BSF fabrication (S) and for the fabrication of rear surface passivated solar cells (A and B) (from {Biro, Mack et al. 2009}). A small asterisk in A and B indicates additional steps with respect to S. Back-end processing (metallization) is indicated in gray boxes. In process (B) in the right hand column the emitter etch back and the surface conditioning can be coupled in a single step.

The experience necessary to realise within an industrial environment what is called a PERC type cell (Fig. 3:6) was gathered from the experiments described above. The scheme chosen for the processing detailed described below is the Alternative "B".

4.1.3 Solar cells from thin substrate

Previous work on PERC structures demonstrated its high efficiency potential. Additionally, this realisation demonstrated on a thin substrate high efficiency also with reduced thickness {Kray, Dicker et al. 2001; Kray, Kampwerth et al. 2004}. Thinner substrates are a ploy to reduce cost. The silicon needed for the solar cell alone can cost as much as 28% of the whole production cost {del Canizo, del Coso et al. 2009}. Based on these considerations, efforts were made to demonstrate that thin high-efficiency solar cells can be produced on industry-close equipment.

This target was comprised in a European project. A German company and the **Fraunhofer ISE** laboratory worked together on it. In practical terms, one thousand and five hundred thin wafers (p-type Cz-Si, $\rho = 2\,\Omega \cdot cm$, pseudo square, 125 mm side, 150 mm radius, 140 μm starting thickness) received a front side processing at **Deutsche Cell GmbH,** Freiberg, Germany; the front-end processing steps are: alkaline texturing, $POCl_3$ diffusion, phosphorus silicate glass removal and anti-reflecting coating (ARC) deposition on the front.

The thin wafers were processed with the company modus operandi. The production line managed to achieve a high yield (96 %) on this unusually thin substrate. On the same day the production line was used for the frontend processing of conventional thickness substrates (~210 μm). These thicker precursors were then finished with aluminium coverage (Al-BSF). The resulting average efficiency of 17.4 % testifies to the state of the art of the front-end processing and set the efficiency level that improved implementations have to catch up with.

The initial fabrication of the thin precursors reduces the thickness further down to 130±5 μm. All steps to process further these precursors were conducted at Fraunhofer ISE, within the pilot-line in the PV-TEC laboratory (PV-TEC) {Biro, Preu et al. 2006; Preu, Biro et al. 2006}.

On this large batch of wafers, sets of different emitters were diffused. An emitter resulting in a 70 Ω/sq. sheet resistance was diffused for the first of the three experiments described below. This first experiment focuses on the technical challenges of the high efficiency concept (see 4.2). For the other two experiments (4.3 and 4.4) a sheet resistance of 85 Ω/sq. characterised the front side emitter. This increased sheet resistance introduces a potential for larger short circuit current (the positive effect on J_{SC} was demonstrated) and a smaller saturation current (J_{0e}), these advantages are useful to show if limitations from the rear passivation emerges.

A solar cell with such a low thickness can have a large benefit for values of back S_{eff} below D_n/L_{Dn} as explained above (2.5). Efforts focused on two passivations: first a functional stack, based on thin thermally grown silicon oxide and a PECVD capping (3.6.6), and second a family of all-PECVD deposition of dielectric (4.4). The results of the latter are affected by inversion channel shunting (Chapter 5). Other phenomena which decrease the performances are common to both approaches. A detailed study on these (next subsection 4.7) will shed light on mechanisms which limits the full potential.

4.1.4 Plasma techniques for the implementation of PERC structures

In Chapter 3 an alternative to the wet chemical polishing was presented. This dry technique was able to reach high etching rates and smooth surfaces. The profitability of this technique could be enhanced if the vacuum needed in the etching chamber is shared by other contiguous processes on the cell. Indeed, the use of Chemical Vapour vacuum reactors for the realisation of a solar cell was presented with direct examples of feasibility for each technique {Rentsch, Seiffe et al. 2008}.

The plasma enhanced processes used will be the ones described in 3.4.3 and 3.5. They can be sequential, sharing the same vacuum region.

Two experimental settings will be investigated (4.5 and 4.6) for their impact and their effects on the fabrication and characteristics of solar cells. In the first experiment, the two mentioned plasma enhanced processes will be added to a conventional flow. In the second experiment, in addition to the procedure described in the first experiment, a passivation will be deposited on the polished back surface by means of PECVD. The second approach wants to give a basic view of the possibility of a PERC solar cell fabrication in vacuum; it comprehends the back polishing and passivation deposition. However a complete integration, an "only plasma" implementation, requires less vacuum interruptions, thus, for example, avoiding intermediate wet processing steps.

The thickness of the wafers employed ranges between 170 μm and 210 μm. This thickness is just slightly lower than the standards of the industry.

4.2 Back surface passivation with a functional stack

The functional stack SiNTOx described above (3.6.6) was used below to implement a PERC structure. This stack presents on the silicon rear surface a thin silicon oxide thermally grown in wet conditions. This interface dielectric is then capped with a SiriON layer and a SiN_x layer.

4.2.1 The optimized process sequence

The fruitful settings which resulted from several preparation experiments were selected to design an optimized process flow. This is depicted in Fig. 4:4. This process is described in more detail below.

After front-end processing, the emitter on the wafers rear surface is wet chemically removed using the inline equipment (3.4.2). As mentioned above, this process exposes only the rear surface to a silicon etchant (nitric acid (HNO_3), hydrofluoric acid (HF) and DI water (H_2O)). With a subsequent short hot dip in Potassium hydroxide (KOH) and deionised water H_2O a smoother surface is prepared. The masking activity of the ARC is important to this second etching step as it prevents parasitic etching of the front structure {Wolf, Mack et al. 2009}, namely the texture and the emitter.

Prior to a short wet oxidation step, the samples undergo a surface cleaning using a modified RCA clean {Kern and Puotinen 1970; Lemke, Furtwängler et al. 2007}; it includes an SC1 step (ammonium hydroxide (NH_4OH), hydrogen peroxide (H_2O_2) and H_2O) and an SC2 step (hydrochloric acid (HCl), H_2O_2 and H_2O), both followed by a full immersion in diluted HF acid. This is based on a batch approach which makes use of carriers able to host up to 100 wafers.
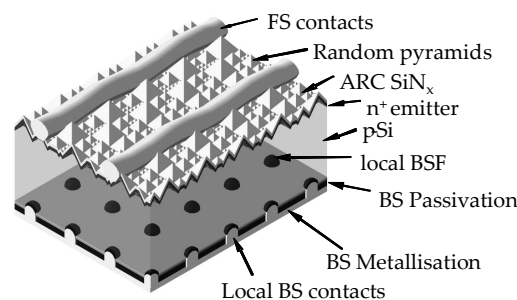
Fig. 4:3 On this sketch the front-side with its two-step metallization and the rear surface structure with its application of a passivation stack and the LFC can be seen.

The silicon oxidation takes place in an industrial furnace, able to host as many as 200 wafers at a time; once again the masking of the ARC is crucial to prevent strong influences on the emitter profile {Wolf, Mack et al. 2009} and to allow the formation of a thin thermal oxide only

at the wafer rear side, where silicon is directly exposed. Subsequently a stack of capping dielectric layers was deposited using an inline PECVD system. This dielectric stack is composed of a hydrogenated amorphous silicon rich oxynitride (a-SiO$_x$N$_y$:H or SiriON {Seiffe, Weiss et al. 2008}) layer and a dense hydrogenated amorphous silicon nitride (a-SiN$_x$:H, in short: SiN$_x$), this combination is only few tens of nanometres thicker than the one presented in 3.6.6. The bottom PECVD layer is meant to act as a charge compensator, while the topmost act as a well reflecting layer for long wavelength radiation. Furthermore this second capping layer protects the layers beneath from any screen print paste reaction occurring at high temperatures (alloying barrier, see 3.6.7).

Alkaline Texturisation	BS: Al Paste Printing
Diffusion 70 Ω/sq.	FS: Ag Paste Printing
PSG Removal	Paste Co-Firing
FS: ARC Deposition	Laser Fired Contact (LFC)
BS: One Side Etching	Sintering
Cleaning	Light Induced Plating
Short Thermal Oxidation	IV Curve Meas.
BS: PECVD Stack Passivation Deposition	
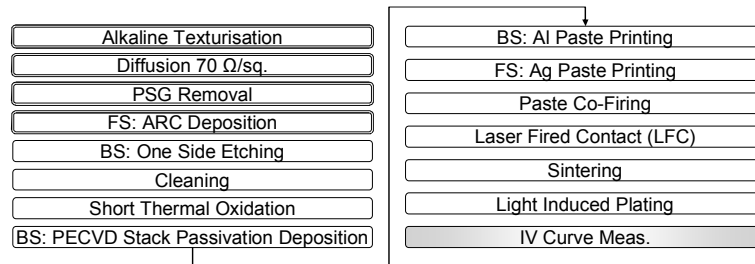
Fig. 4:4 Process sequence for the creation of high efficiency silicon solar thin cell. Boxes with a double line are the fabrication steps realised at Deutsche Cell, potential cleaning steps are omitted. The characterisation used as process control is here not included.

During the passivation steps it is possible to perform a first process control. This consists in the measurement of effective lifetime of the samples so far processed (Table 4—1).

The metal pastes are applied with an adapted screen printing procedure. The adaption reduces the stress on the substrate and therefore diminishes breakage. This step, without the proper settings, severely influences the yield. Small screen openings of 90 µm width were used without evident problems of finger interruption on the front side. The rear surface instead was entirely covered with a low amount of aluminium paste (~ 6 g/cm^2).

Using the experience gained in respect of the combination of front side paste and the thickness of the cells, a known firing profile on an industrial inline implementation of a RTP was used.

The rear local contacts were prepared using a modification of a technique known as laser fired contact (LFC) {Schneiderlöchner, Grohe et al. 2005}. The modification consists of a different metallic layer. While previous investigations focussed on evaporated aluminium, in this work the metallic layer is a screen-printed and sintered aluminium paste.

Contacting the cell with a laser pulse on a screen-printed and fired aluminium layer required the understanding of the process parameters influencing the contact quality. Several contact tests lead to the optimal process window, more details on which are published elsewhere {Hofmann, Erath et al. 2008; Nekarda, Gautero et al. 2009}. The tool used has a high throughput rate. Therefore this step is a promising candidate for successful implementation in a production line

To settle the damage introduced by the sudden and local heating by the laser a short annealing step with a low temperature followed. The equipment was an inline belt furnace; inside the chamber a nitrogen environment was created, in these settings the wafers were exposed to a temperature of 300 °C for 1 minute.

The final step, consisting of light-induced plating (LIP), takes place on an inline system. This step is necessary to reinforce the conductance of the screen-printed fingers. Silver is plated onto the front side grid exploiting the photovoltaic effect {Mette 2007}. This metallization equipment needed some adjustments to correctly handle thin cells.

This approach is mainly characterised by passivation composed of silicon nitride and thermal oxide, and the metallization is entirely based on screen print. The process will therefore hereinafter be referred to as SiNTO SP (Silicon Nitride, Thermal Oxide, and Screen Print).

4.2.2 Passivation quality and process control

In order to control the status of the passivation along further processing, lifetimes were measured on four wafers before metallization. The measurements were performed after wet thermal oxidation (TO)[26], after the PECVD, and after a Forming Gas Annealing (FGA). This latter step simulates the annealing carried out before the silver plating (Table 4—1). Such an annealing guarantees an optimal environment for the additional saturation of silicon dangling bonds. However, it is underscored that the samples are not undergoing an "Alneal"[27]. Therefore the dissociation of hydrogen molecules to form ions is not fostered. The results show a strong improvement, especially after the PECVD deposition, when hydrogen is suspected to fixate at the interface.

Table 4—1. Process control on effective lifetime a) and Implied-Voc b), both of which were monitored on four wafers. The average values, after the TO and after the PECVD deposition process, are presented; these control cells also underwent a FGA in order to evaluate the full potential of the passivation.

a)

effective lifetime (μs) @ $\Delta n = 5 \cdot 10^{14}$ cm^{-3}			
Sample	TO	PECVD	FGA
Average -4-	17	62	68
Stdev	3	5	5

b)

Implied V_{OC} (mV) @ illumination = 1 Sun			
Sample	TO	PECVD	FGA
Average -4-	616	645	648
Stdev	4	2	2

After metallization, a group of cells was monitored for their open-circuit voltage (V_{OC}) and, when possible, for their 1-Sun-illuminated Current density versus Voltage measurement (JV1Sun). An example of one cell is provided in Table 4—2. The V_{OC} does not reach the level forecasted by the implied Open-Circuit Voltage (Implied-V_{OC}) {Cuevas and Sinton 1997} values presented in Table 4—1, and the damage after the firing is not fully cured.

Table 4—2. Monitoring of the V_{OC} during the processing. The small disagreement in V_{OC} between the SunsVoc tool and the JV1Sun might be the result of a small spectral mismatch {Roth, Hohl-Ebinger et al. 2008}.

	V_{OC} (V)	pFF	FF	η (%)	R_{shF} ($\Omega \cdot$cm^2)
FFO (SunsVoc)	0.629	0.834			5220
Annealing (SunsVoc)	0.630	0.828			7170
Annealing (JV1Sun)	0.633		0.76	17.8	
2nd Annealing (JV1Sun)	0.633		0.75	17.8	

4.2.3 Reflectance and metallisation

The thickness of the front side ARC during the chemical treatment was only reduced by a few nanometres on the wafer edges. The monitoring was performed by reflection measurements. On these regions the increase in weighted reflectance (and the consequent decrease in absorption) was around 0.4% absolute. This absorption loss was partly offset by the subsequent deposition of nitrides. This ARC thickening took place as a parasitic wrap around while the rear surface stack was prepared. An absolute decrease of 0.3% in weighted reflectance was measured afterwards; the total loss is now within measurement deviations.

---

[26] The passivation performance of the SiO$_2$ is limited since post treatments like annealing are omitted.

[27] This process is performed during an FGA with a layer which presents bulk aluminium covering the surface.

The low thickness of the substrate requires the implementation of light trapping concepts. Indeed, wavelengths as short as 800 nm can reach the back surface and trespass it. The implemented structure acts in two ways against the trespassing and therefore against optical loss: first the dielectrics, with their refractive indices lower than n_{Si}, ensure a smaller cone of escape for the rays colliding with the back surface interface, second the asymmetry of the front side texture and the low roughness of the back surface allows a randomization of the rays in the bulk. These improvements increase the optical path of impinging rays. Therefore, they increase the chance of absorption. This structuring performs better than a conventional back surface on thick wafers. A comparison is done by fitting the spectral reflection measurement to the two bounces model implemented in PC1D {Basore 1993}. This procedure was previously used to evaluate other high efficiency concepts {Hermle 2008}. The results of the comparison are presented with two reference terms: the first is an optimal implementation: a 2x2 cm^2 PERC solar cell realised in the **Fraunhofer ISE** clean room, the second is instead a conventional structure. For convenience also the thickness is indicated.

Table 4—3 Fitting of reflection data with the two bounces Basore model

Structure	Reflection 1st	Reflection 2nd
Clean room high efficiency cell structure (PERC structure, ~230 μm thick)	95 %	97 %
SiNTO SP (this work, PERC structure, ~120 μm thick)	87 %	92 %
Conventional solar cell (Al-BSF, ~200 μm thick)	51 %	65 %
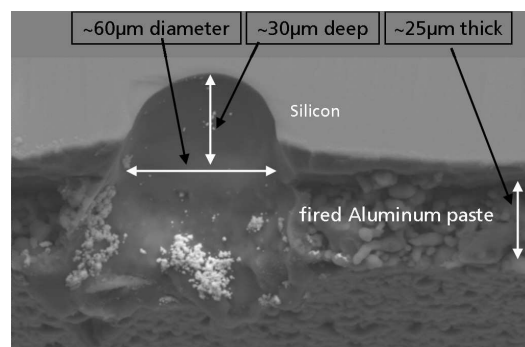
Fig. 4:5 A cross section of the wafer is shown here. The image portraits a fresh cut of a solar cell. The sample is slightly tilted and the rear surface of the printed aluminium can be seen on the bottom of the picture. Above that, the printed and fired aluminium paste cross section can be seen, topped by the even silicon surface, and the LFC point. It cannot be concluded on the basis of this image whether the cavity that can be seen was filled with doped silicon or eutectic alloy of aluminium and silicon before the breakage. This information was then provided by the detailed study of the LFC contact presented in 3.7.3, which showed that the cavity is actually empty and silicon is exposed to air without passivation. Furthermore, the ohmic contact between the silicon bulk and the aluminium is supported by lateral metallic bridges from the screen-printed aluminium to the inner side of the cavity.

The front metallization was investigated by means of voltage drop on the metallic grid. The well known Corescan technique {van der Heide, Bultman et al. 2001} was used. This tool measures the voltage drop from the two wide lines (busbars) to a point on the front surface of the cell. The method performs a mapping of the voltage drop. The probe, a thin needle, measures the voltage while scraping the surface. The solar cell is afterwards damaged beyond use.

Analysis by means of scanning electron microscopy (SEM) indicated a growth of silver on top of the fingers of around 5 μm. This leads to a decrease in series resistance, increasing the fill factor (*FF*) by up to 10 % absolute. This gain is compromised only by a 2 % absolute decrease in short-circuit current density (*J*SC).

The amount of aluminium paste on the rear surface is no more related to the formation of a back surface field since no alloying is taking place (see 3.7.3), meaning that a lower amount of metal paste can be printed. Sheet resistance measurements were performed {Van der Pauw 1958} to ensure that the conductance of this printed layer was within acceptable ranges after firing {Gautero, Rentsch et al. 2008}.
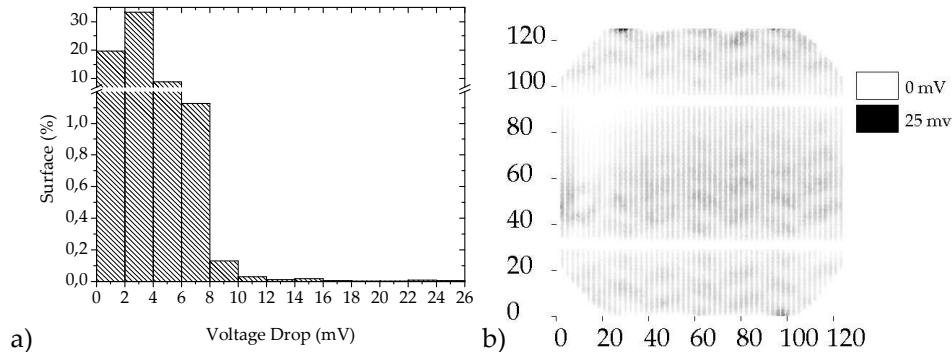
Fig. 4:6 a) Histogram of the voltage drops from the busbar to the measured point, notice the gap in the scale used b) A voltage drop mapping, issued by the Corescan tool, indicating a low homogeneous level on the whole surface. The quality of the firing process results in average values within an acceptable range. A zero voltage drop is a white point while darker points represent higher voltage drops, with completely black points representing 25 mV.

The LFC process was optimized for a large surface contact and a minimal damage. In Fig. 4:5 a SEM picture provides the geometrical data on such a metal contact configuration.

4.2.4   Solar cell results

Average results of solar cells processed with the optimized sequence in PV-TEC, are presented in Table 4—4 together with the best cell of the experiment and stabilization from the light induced degradation effect. The efficiency histogram (Fig. 4:8 a) has a small spread of results. This demonstrates the reproducibility of the process. Entirely realized in the pilot line of PV-TEC, the process implementation can be easily transferred to industry.

Table 4—4. Average values of the 24 cells group and best cell results. The material (2 Ω cm, p-type Cz-Si) is 120 μm thick.

	V_{OC}	J_{SC}	V_{mpp}	J_{mpp}	FF	η
Measurements on 24 solar cells:	**(mV)**	**(mA/cm²)**	**(mV)**	**(mA/cm²)**	**-**	**(%)**
Median	636	37.0	520	34.4	0.76	17.8
Average±Stdev	632±7	37.0±0.2	514±13	34.2±0.5	0.75±0.02	17.6±0.7
Best cell	638	37.3	521	34.9	0.766	18.2
Stabilized	636	37.3	520	34. 8	0.762	18.1
Stabilized – CalLab	635	37.3	521	34.6	0.760	18.0

Fig. 4:7 a) shows that six experiments were started simultaneously, at which stage the different options for the passivation of the rear were evaluated.

As mentioned above, over a time period of several months, groups of thin silicon wafers were processed to investigate which forethoughts are necessary to obtain the best sequence. The yield of every experiment improved following a learning curve (Fig. 4:7 a), and assuming this work as a first proof of concept, the trend confirms feasibility.

a)

b)
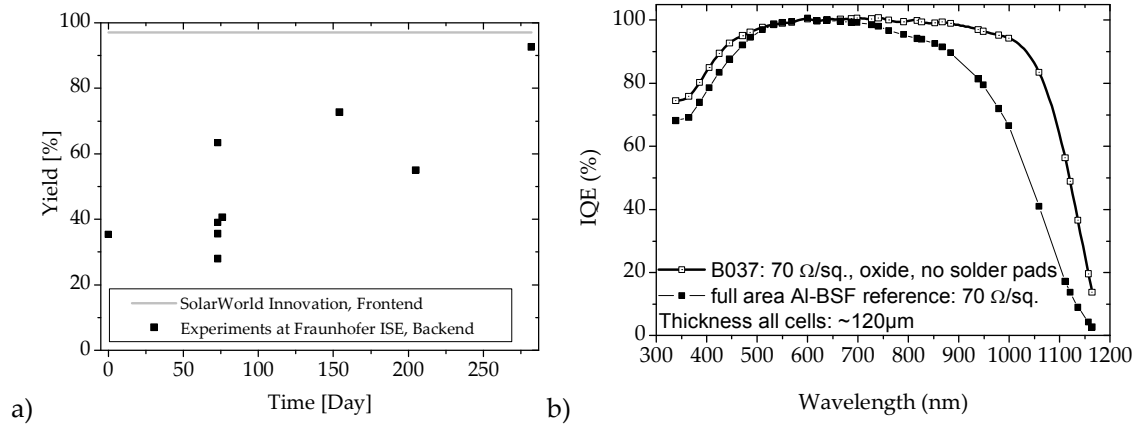
Fig. 4:7 a) As with every activity {Ritter and Schooler 2002}, the efficiency increases with time. A yield exceeding 90% was achieved within this work. b) Comparison between two thin solar cells with different rear surface structures: The SiNTO SP cell benefits from the passivated rear, increasing its efficiency of long wavelength collection. On the other hand, the Al-BSF structure on the thin cell suffers from a reduced amount of aluminium, which was required for the pragmatic realization of the thin cell.

One solar cell from this process was compared with a conventional industrial solar cell. This latter features full aluminium coverage on the rear surface, this in turn creates a back surface field (Al-BSF). Both cells had a thickness of about 120 μm. The comparison, performed by measurements of internal quantum efficiency (Fig. 4:7 b), highlights the difference of the internal quantum efficiency. The gain of the SiNTO SP implementation over the Al-BSF is more evident in the long wavelength region.

The full area Al-BSF reference has a reduced amount of printed aluminium paste which decreases the aluminium-doped Back Surface Field Al-BSF. On the other hand reducing the amount of paste decreases the wafer bowing {Huster 2005} and allows the realisation of the solar cell. Bowing results from uncompensated expansions between the thin substrate and the metallic layer.

a)

b)
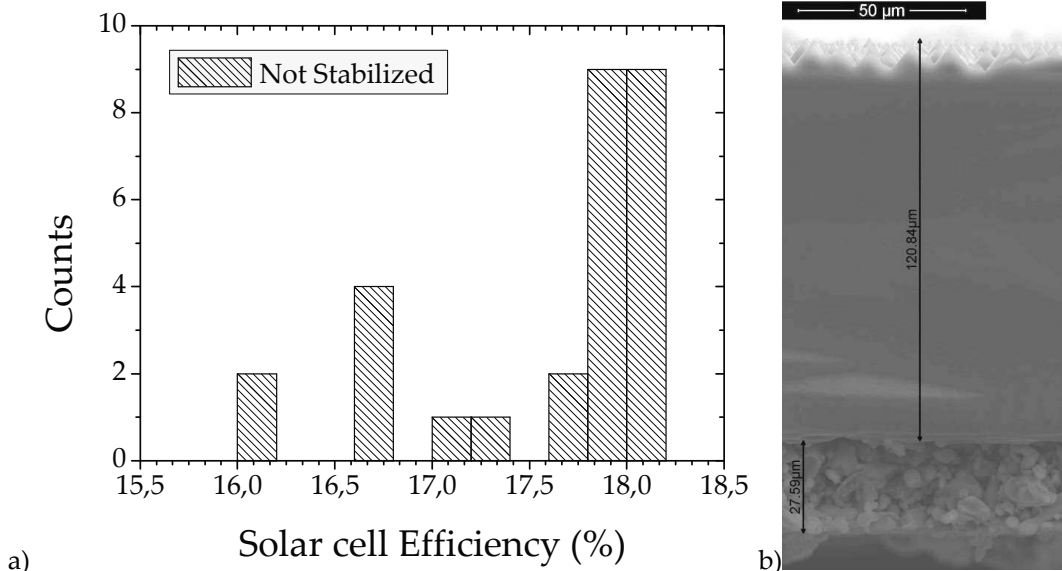
Fig. 4:8 a) The efficiency of the group was distributed mostly around the 18% efficiency level. The solar cells present here their efficiency in a non-stabilized state. b) A picture of a complete section of the cell was taken with an SEM. On the basis of this image it can concluded that the features such as texture and metal layers begin to play a significant role on the total geometry of the cell at the thickness used in this work.

An SEM image of a functional solar cell is presented in Fig. 4:8 b); the surface to volume ratio is approximately doubled from that of a standard cell.

The degradation effect is caused by impinging light {Herguth, A et al. 2008}. The energy caused by photon fosters the association of the Boron Oxygen complex. Once associated, a trap level in the energy gap appears and gives rise to recombination sites which decrease lifetime and therefore diffusion length. The low substrate thickness used in this work, as mentioned in the literature {Münzer, Holdermann et al. 1999}, diminishes the influence of this diffusion length decay. Such a thin solar cell is affected less than the currently common product thickness. This intrinsic property of thin cells allows the use of heavily doped base material, having benefits in both open circuit voltage, as a result of a higher built in voltage, and fill factor, thanks to a reduction of the spreading resistance effect.

4.3   Influence of a lowly doped emitter

Additional solar cells were fabricated according to the process sequence shown in Fig. 4:9. These cells have an emitter sheet resistance of 85 Ω/sq. The main benefit of such a lowly doped front emitter is an improved response to shorter wavelengths (blue response) of the final solar cell. This advantage comes from reduced Auger recombination in the bulk of the emitter. Carriers generated by direct absorption in the first few nanometres by penetrating photons of high energy can be collected effectively.
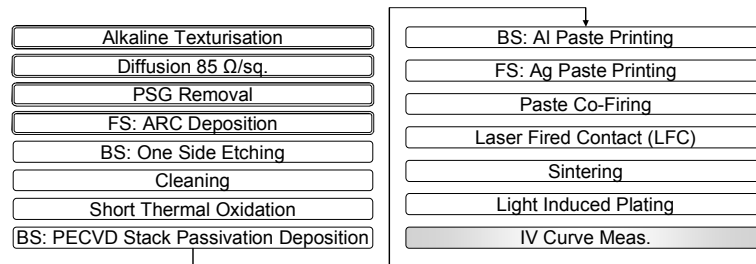
Fig. 4:9 Process sequence for the creation of a high efficiency thin silicon solar cell. Boxes with a double line are the fabrication steps conducted at Deutsche Cell. The characterisation used as process control is omitted.

Compared to the experiment above, where a 70 Ω/sq. was used, the aforementioned improvement of efficiency for short wavelengths is confirmed by IQE measurements (see Fig. 4:10).

In contrast to the implementation reported previously, contacting problems were encountered in respect of this lowly doped emitter at the front metallization. After the step "co-firing" Fig. 4:9 it is possible to make measurements on the cell exploiting its photovoltaic principle. Oddly, during these measurements an exceptionally low fill factor is observed (see Table 4—10 in 4.7). A drastic increase in Fill Factor (*FF*) took place during the front side light-induced plating. A detailed investigation will be given below (4.7).
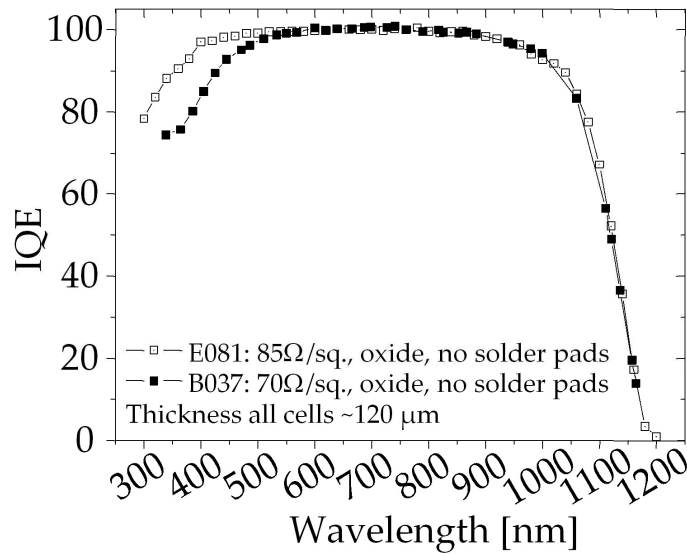
Fig. 4:10 This comparison shows the advantage of an enhanced internal reflection and a low recombination velocity on the rear surface of the SiNTO SP structure in the long wavelengths. In the blue part (short wavelengths) a lowly doped emitter at the front proves its advantage in effectiveness of photon collection.

The final average solar cell results and the best cell of this batch (labelled E081) are presented in Table 4—5. Note that the measurement of the best cell was taken at ISE CalLab with the most recent standard up-to-date {IEC 2008}. Furthermore, this cell is measured after light induced degradation (LID, more detail about it in 4.7).

Table 4—5. Solar cell results (Cz-Si, p-type, 2 Ω cm) with a lowly doped front emitter (sheet resistivity of 85 Ω/sq.). AD stands for "After LID[28]", and the degradation lasted 12 h.

	V_{OC}	J_{SC}	FF	η
24 solar cells	**mV**	**mA/cm²**	**%**	
Average ± Stdev	**642±3**	**37.2±0.4**	**75±2**	**17.8±0.6**
E081 AD CalLab	**639±2**	**37.7±0.8**	**74.7±0.5**	**18.0±0.4**

These fabricated cells presented in their finished state a low fill factor, even after the plating of the front side metallisation grid. This aspect is therefore analysed in detail in 4.7.

4.4 Back surface passivation with complete PECVD dielectric stack

A set of the thin precursors from **Deutsche Cell** was further processed implementing a rear passivation based on a dielectric stack grown by means of PECVD. This passivation is described in detail in 3.6.1. An additional group was processed applying only a single layer passivation composed of a thin silicon nitride deposited with a gas ratio (NH_3/SiH_4) of 2.53.

Except for the oxidation step, the overall fabrication procedure (Fig. 4:11), is identical to what was presented for SiNTO SP. During this processing a set of SiNTO SP solar cells were fabricated sharing the common processing steps, which ensures the quality of the processing.

---

[28] This acronym refers to Light Induced Degradation (not to be confused with LIP).
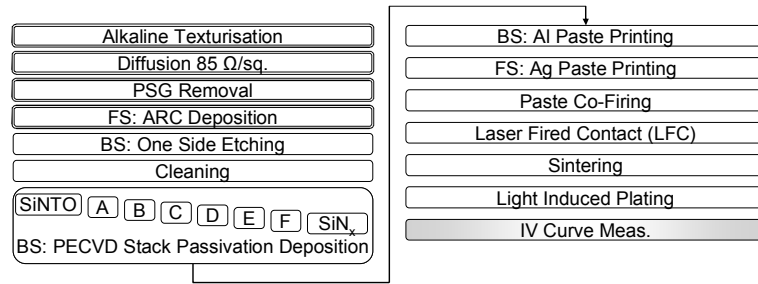
Fig. 4:11 The process is slightly simplified. As compared to the reference SiNTO SP, one step, the oxidation is entirely removed.

4.4.1 Passivations used

The experiment evaluated a full factorial design with combinations of three SiriON configurations and two CaTS deposition settings. This explored the space of solution described in 3.6.1. The characterisation was performed at different levels, both during the processing and on the finished cells.

Table 4—6 Performed variation of passivation in the experiment

Name of the combination	SiriON, gas ratio / n_{SiriON}:	None	0.5 / 2.25	0.21 / 3.2	0.02 / ~3.6
	3.5 / 2.05			SiNTOx[29]	
CaTS gas ratio / n_{CaTS}:	2.53 / 2.1		A	B	C
	3.62 / 2.05		D	E	F
	2.53 / 2.1	SiNx			

Effective lifetime was measured straight after the deposition of the PECVD layers on the back surface. The SiNTO SP group was measured as a reference. This characterisation, performed as a process control, shows a trend expected from the layer variation. This trend was previously observed on lifetime samples (Fig. 3:40). After deposition, the S value ranges from 1000 cm/s down to 10 cm/s.

4.4.2 Metallization

SunsVoc curves were measured after the metallization process but before the laser fired contact (LFC) process. The V_{OC} is positively related in a logarithmic manner to the effective lifetime at the injection level corresponding to 1 Sun {Kerr 2002}. To gain more insight into the values measured numerical calculations were performed with the PC1D tool[30]. It can be seen that samples with a $V_{OC} < 580$ mV have a recombination on the back surface only limited by carrier diffusion through the bulk (Fig. 4:12), this represents a S above thermal velocity v_{therm}.

Detailed optical investigation revealed the cause in the drop of group B, C, E, and F. The damage is permanent and is a severe blistering of the passivation layer (Fig. 4:14). Blistering creates discontinuities in the passivation layer. These gaps expose silicon directly to air and foster local recombination, if the coverage of the blister is high enough (which in view of their occurrence is the case) the effective surface recombination velocity degrades to high values.

---

[29] The PECVD layers are a capping to the thin thermally grown SiO2.

[30] Detail of the simulation: $W = 130$ μm, $\tau bulk = 100$ μs, $J0e = 100$ fA/cm², $\rho = 2.2$ Ω·cm, 2 front diffusions: erfc $\rho sheet = 120$ Ω/sq., Gaussian $\rho sheet = 290$ Ω/sq.; the shadowing from the fingers was taken into account through the reflection.

Blistering occurred during the paste co-firing. It is found at the edges of the truncated pyramids, where sharp discontinuities of the surface can be observed. In this case we suspect that the surface roughness was not low enough to guarantee a safe high temperature processing.

The optical analysis also revealed occasional local alloying, although this mechanism is not able to deliver the surface passivation necessary for such thin cells. Furthermore it is highly improbable that this contact formation will respect the strict requirements that the inversion layer imposes of contacts.

The cells tainted by blistering (groups B, C, E, and F) were not processed any further. Their status compromises any investigation related to passivation behaviour.

4.4.3 Laser fired contacts

Finishing the electrical contact with the cells is an LFC process. As described in 3.7.3, it is needed to create a contact with the base.

The challenges for this step are two. The first is specific to the instrument and basically an implementation issue. The laser adopted to melt the thick layer of aluminium is used in a multi-pulse configuration {Nekarda, Stumpp et al. 2009}. An excessive repetition digs the substrate from one side to the other and leads to detrimental effects. The second issue relates to the passivation layer and its working principle. As described in 3.6.1, the layer induces an inversion layer on the surface. Models (Chapter 5) state the complete isolation of the inversion layer from points of lower level injection to be beneficial for a better performance of the passivation. The characterisation of the isolation correlates with the final performance of the solar cell. Therefore the method chosen for this task is the measurement of the External Quantum Efficiency at a certain wavelength. This method, explained in the literature {Dauwe 2004}, is not able to quantify the resistivity of the path towards a lower level injection point, though it can be used to make comparisons between different realisations.
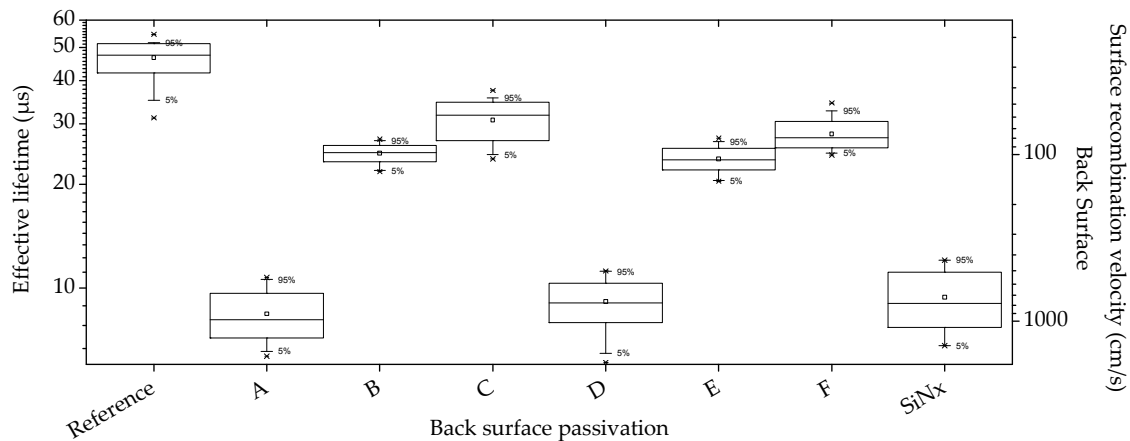
Fig. 4:12 The effective lifetime measurements were performed at an injection of 5E+14. More than one order of magnitude less than the doping (N_A = 7.22E+15) guarantees the low-level injection (lli). The surface recombination velocity was calculated {Cuevas and Macdonald 2004} on the basis of the following values: τ_{bulk} = 100 μs, J_{0e} = 100 fA/cm². These are based on the assumption that the SiNTO passivation (named Reference in the graph) results in an almost perfect passivation of the solar cell (this assumption is supported by the measurements reported in Table 4—1[31]). The combinations of the gas ratio are explained in Table 4—6.

---

[31] A maximum value $\tau_{eff} \cong 64$ μs was obtained with different passivations. A corresponding value of S is obtained imposing the assumed bulk lifetime and the saturation current of the emitter.
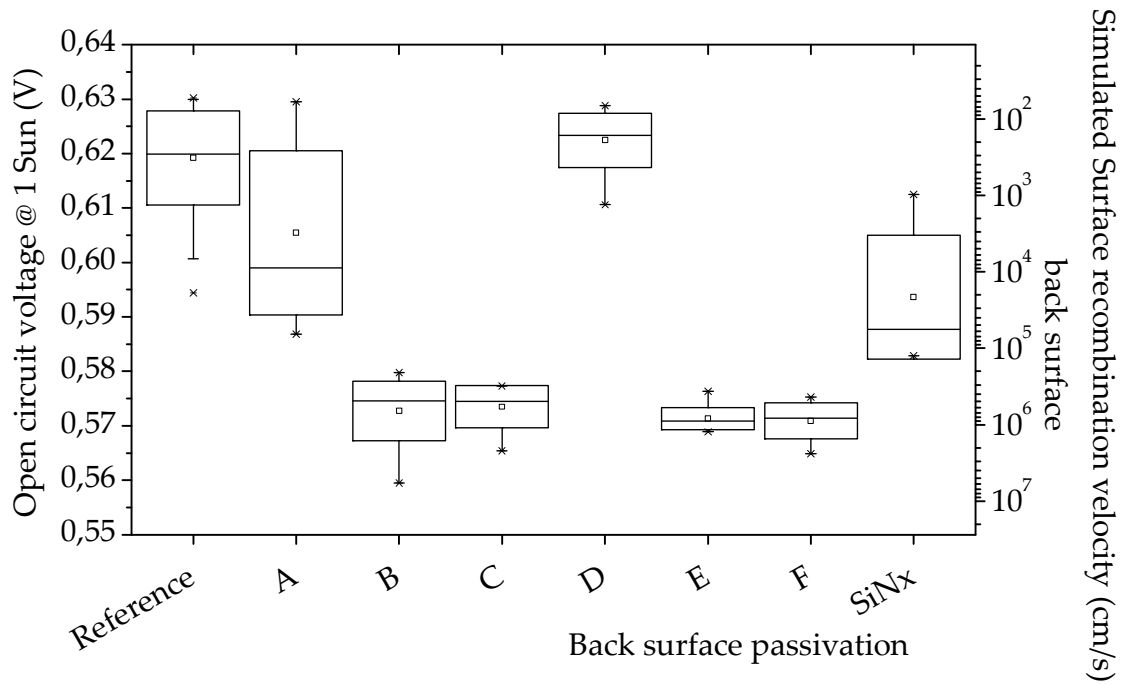
Fig. 4:13 The values of V_{OC} are now completely turned around, the variation of more interest after the passivation deposition was severely damaged by the high temperature step. Group A and group D show still some interesting candidate for a complete cell. The right hand scale is reported from simulated data[30]. Notice that S higher than the thermal velocity does not have physical sense.
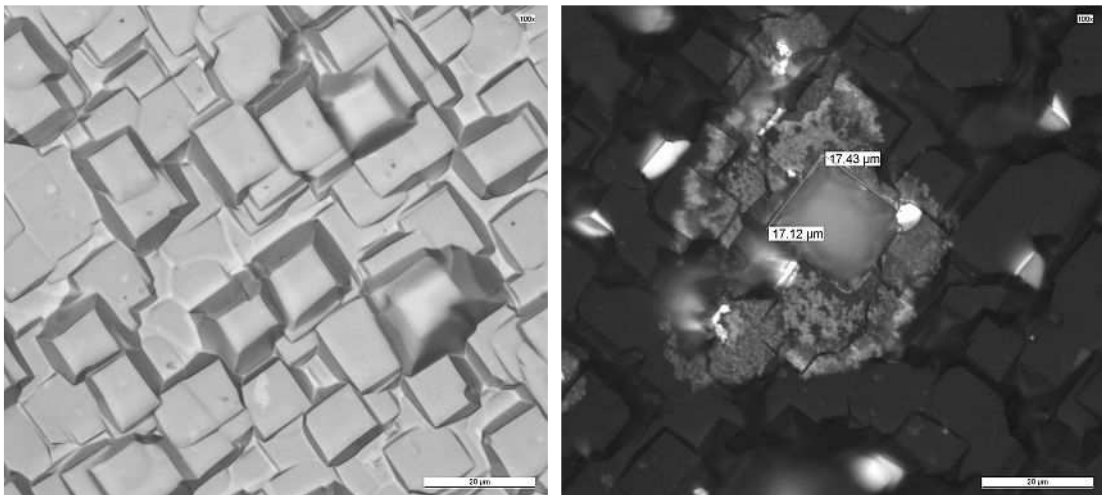
Fig. 4:14 A 100X zoom on the back surface of solar cells after the removal of the sintered aluminium, on the left of passivation "A" and on the right a passivation "F". On the right the white spots are regions in which the passivation is no more present. It is easy to correlate their presence with sharp edges of truncated pyramid. Furthermore, in the middle of the image, we can see a point where an alloying has taken place (The surface was lavishly covered with similar features). Although small, the typical fingerprint of an inverted pyramid can be seen and measured. This confirms the local alloying between silicon and aluminium {Uruena, John et al. 2009}.
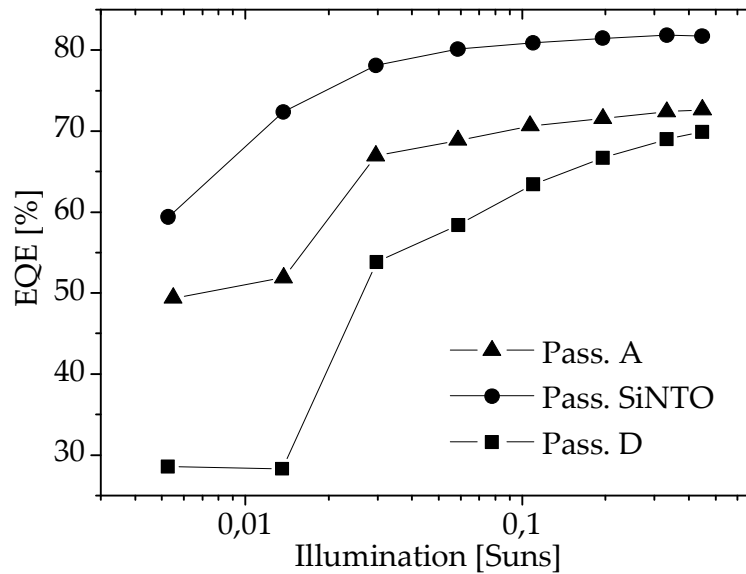
Fig. 4:15 Measurements of EQE at 999.3 nm of different passivations. Shown are measurements of a cell for each passivation. The pitch is the same for all three cells. Its bias dependency of EQE was not evaluated.

In Fig. 4:15 are reported the measurements of the External Quantum Efficiency (EQE). These measurements are extracted from the best approach. The Silicon Nitride case, since similar to passivation A (and D), received the same optimized parameters.

It was noticed that the passivation itself influences the optimal LFC configuration. It is interesting to observe the lowest injection level; there the passivations differentiate the most from each other. An interpretation, based on the model presented in Chapter 5, is that a passivation based on a higher field effect (i.e. Pass. A or Pass. D) needs more current to saturate the shunt resistance R_{shB}. For passivation A and D note that at very low level of injection the EQE is low. Only when an adequate amount of injection is provided then the passivation will raise the splitting of the Fermi levels; then the EQE increases slowly.

From Fig. 4:15 we can also deduce that the SiNTO passivation is also based on the inversion of the back surface, since a loss of current is present in the low bias region.

In order to investigate the effects of the back surface contacts distance, two different pitches were performed, 500 μm and 600 μm. In the following the best results of each group are presented (Table 4—7). Unfortunately the number of cells successfully processed up to this point does not allow a meaningful statistical representation.

In the case of SiNTO and the SiN$_x$ a higher pitch raises both V_{OC} and J_{SC}, while the FF decreases. The relation is different for the two SiriON CaTS cases. Furthermore, for the group D a lower FF was measured. More consideration and characterisation are conducted in 4.7.

Table 4—7 Best results from each group

Passivation on back surface	Pitch	V_{OC}	J_{SC}	FF	η
	(μm)	(mV)	(mA/cm²)	(%)	(%)
SiNTOx	500	631	36.9	76	17.7
SiNTOx	600	634	37.5	75	17.8
Pass. A	500	617	36.1	77	17.1
Pass. A	600	617	36.7	75	16.9
Pass. D	500	624	37.0	71	16.3
Pass. D	600	625	37.0	71	16.4
SiN$_x$	500	603	35.3	77	16.3
SiN$_x$	600	614	35.8	74	16.3

We can conclude that a passivation of the back surface is present in all of the observed cases since open circuit voltages, though not as high as in the SiNTOx case, are all above the previously simulated lower limit of ~ 580 mV that represents the worst case, i.e. an infinitely high S. The short circuit current shows a good long wavelength mirroring effect for all cases. A hypothesis is that the PECVD SiriON CaTS used, and especially the Pass D, are delivering a surface recombination velocity at least in the same order of magnitude of the SiNTOx case. However, the lower FF reflects another imperfection of the structure. The case of silicon nitride (SiN_x) passivation is not affected by the FF problem, though its S can be evaluated in the range of 1E+3÷1E+4 cm/s (Fig. 4:13).

None of the electrical issues, like high R_s or low R_{shF}, contributed to the reduced FF, this conclusion egresses from the observation of the values of respectively low pFF - FF and high R_{shF} (measured from a fit on the JVDark). However, on those few cells which indeed presented low R_{shF} a specific laser edge isolation process was performed. Nevertheless, the low FF issue was not solved. More information on this issue will be given in the analyses section (4.7)

4.5 Improvements to conventional processing by Plasma processing

The substrates (p-type Cz-Si, $\rho = 2\,\Omega\cdot$cm, pseudo square, 125 mm side, 150 mm radius, 200 μm starting thickness) were textured and diffused (Fig. 4:16), once the PSG was removed the batch was split in three sets, the subsequent dead layer removal step was performed on two of them with different carrier speed (A = 600 cm/s and B = 500 cm/s, they correspond to an etching time of 2.5 s and 3 s respectively), additionally, on these two sets, the back surface was treated in plasma, the parasitic emitter is removed and the surface is polished. The rest of the processing was performed with conventional steps common to all groups, made exception of an edge isolation step. This is performed only on the reference set by means of laser.
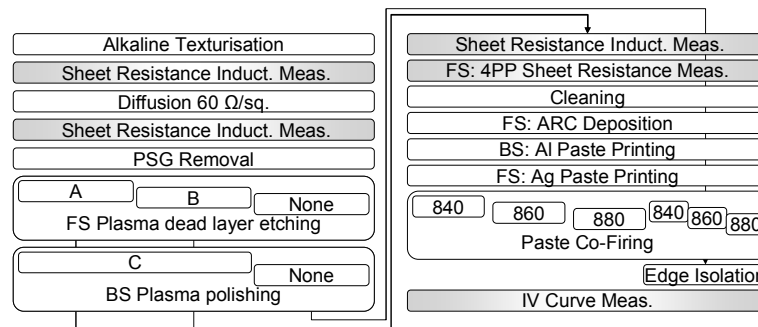
Fig. 4:16 Process flow. Notice the possible coupling of the plasma processing in one single PECVD equipment. The samples can be processed without leaving the vacuum when each processing has a given chamber. The sheet resistance characterisation steps are included. Two dead layer removal process settings (processing speed A = 600 cm/s and B = 500 cm/s, both at 0.08 mbar of pressure and 400 sccm of SF_6 gas, the peak power is 3.5 kW) and one back surface polishing (C = 4 times at a speed of 10 cm/s, at 0.2 mbar of pressure and 400 sccm of SF_6 gas, the peak power is 3.5 kW) were compared to the reference process (None = no dead layer removal and no back surface polishing).

As process control, several measurements of sheet resistance were performed, this characterisation controls the evolution of the emitter through its sheet resistance; two methods are available: a contact-less inductive measurement of eddy currents in the conducting layer(s) and 4 needles (4PP) contacting the layer under test imposing a current and measuring the voltage drop and the resistance thereof (Appendix A.a). The inductive method is preferred to control the emitter diffusion process while the 4PP method is better suited to analyse the consequent change in sheet resistance due to the dead layer removal.

The inductive method indeed can not track the change of the emitter thickness during the plasma treatment. The polishing of the backside decreases the thickness of the base, changing its sheet resistance. Hence, the model on which the emitter sheet resistance calculation is based does not correspond to reality anymore. Thus, a better suited method is the 4PP, this classical method is unaffected by the sample thickness.

The diffused emitter, before the PSG etching, is measured with the inductive method. This results in a sheet resistance of 64 ± 0.2 Ω/sq. on average. After the PSG removal this same value measured with the 4PP method is 56.7 ± 0.9 Ω/sq. on a pristine emitter. This slight disagreement is due to the surface texturisation, this difference is expected and was already documented {Spitz, Belledin et al. 2007}.

The plasma processed emitter showed a higher sheet resistance (Fig. 4:17) compared with the reference. From these values an approximate evaluation of the silicon removed can be calculated. The relation between the emitter sheet resistance and the amount of silicon removal (added on the right scale of Fig. 4:17) can be calculated when few necessary information are provided. These are: the diffused phosphorus profile, which is measured by SIMS technique; a model for the mobility of carriers {Masetti, Severi et al. 1983; Clugston and Basore 1997}; and a reasonable assumption detailing the maximum amount of doping ions in silicon {Solmi, Parisini et al. 1996}. Based on this data a good linear approximation of the more complex relation can be found in the region of interest (57 to 88 Ω/sq.).

Any small variation of etching depth can severely influence the resulting sheet resistance, this explains the large measurement spread observed. A severe consequence is a spatially aleatory surface concentration of phosphorus, which makes the metallisation prone to isolate from the emitter {Grote, Hermle et al. 2008} or create shunt paths if the diffused domain is shallow.
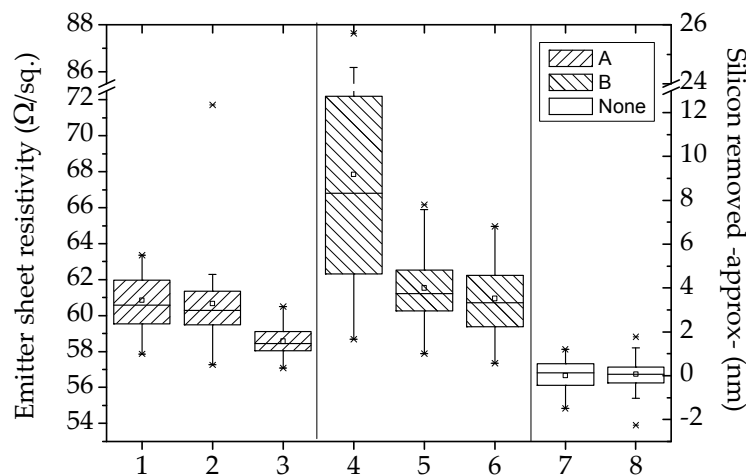
Fig. 4:17 The resulting emitter sheet resistance after the dead layer removal for the process A and the process B, as a reference two values from pristine emitter is shown. Every box and whiskers represent 25 measurement points uniformly spread on the surface of one wafer. The statistic is built on the base of these 25 points.

The rest of the batch processing was performed according to standard procedure and only routine characterisation was performed. The solar cell results were investigated for significant effects from the process variation performed. It was possible to observe a correlation (see Pareto diagrams Fig. 4:18) for V_{OC} and J_{SC}. Below these relations will be presented in detail.
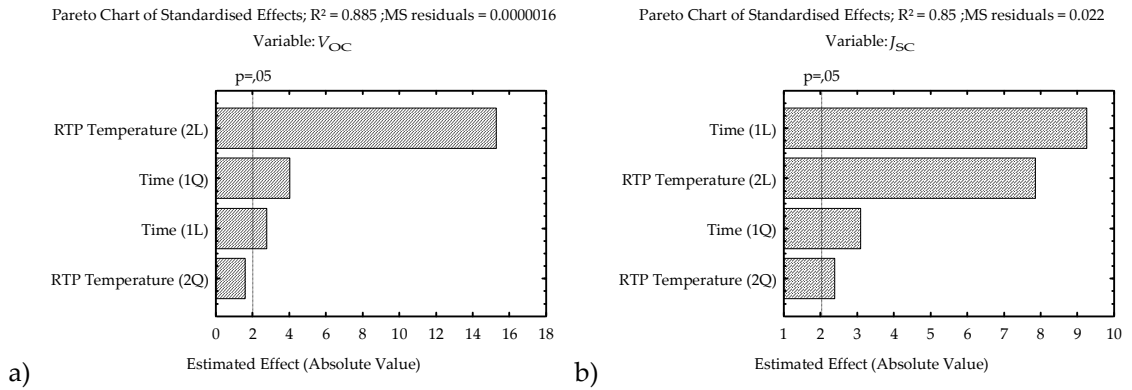
Fig. 4:18 Pareto diagram for V_{OC} (a) and J_{SC} (b), the first shows that a strong linear dependency on the RTP temperature outbalances the contribution from the plasma processing, which in any case is still significant. On the other hand, for the photovoltaic current generation (J_{SC}), the plasma process has the greatest effect in a linear (positive) fashion.

The J_{SC} can be fitted with a quadratic polynomial model and thus obtaining a good coefficient of correlation. It is possible to see that the exposure to the plasma gives a significant increase of this specific cell parameter. The reason for the current improvement lays in the removal of the highly recombinative dead layer. The part of the short wavelength which would be absorbed but not converted in the dead layer is now available for conversion. This is also demonstrated from the analysis of the IQE (Fig. 4:21), which shows a better blue response for the solar cells for process A. The improved blue response depends mainly on the conditioning of the first tens of nanometres. This increase, compared with the reference wafers, leads to a higher current.

a)

b)

Expected / Observed Values on Variable: J_{SC}
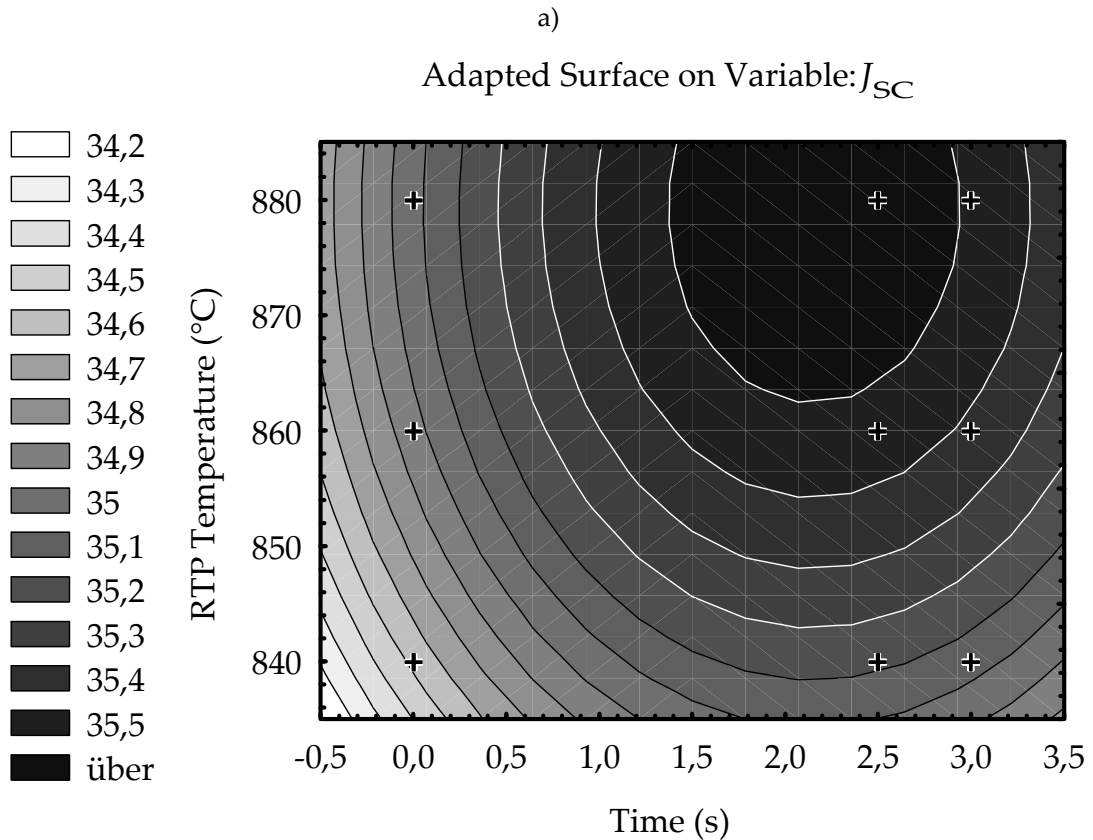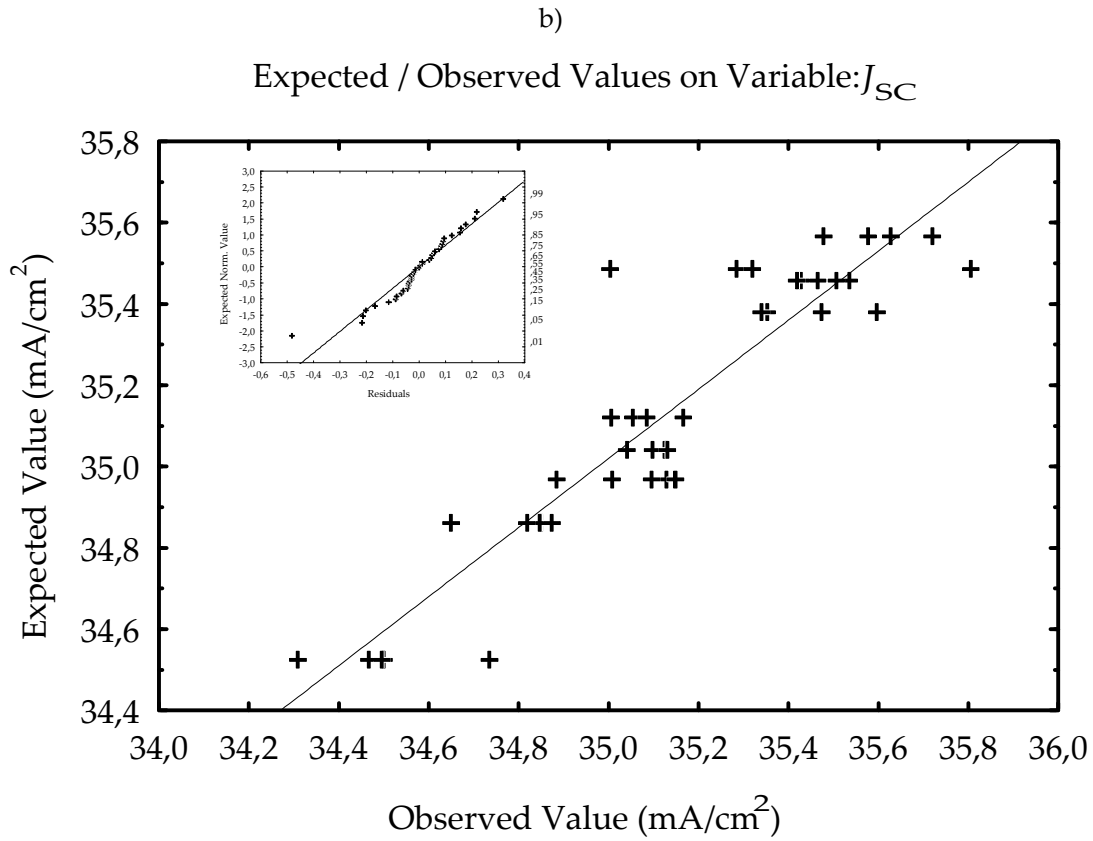
Fig. 4:19 a) The quadratic surface fitted on the results and b) the verification of the model. There, one outlier results to be a reference wafer affected by non ideality problems.

a)

Adapted Surface on Variable: V_{OC}

b)

Expected / Observed Value; Variable V_{OC}
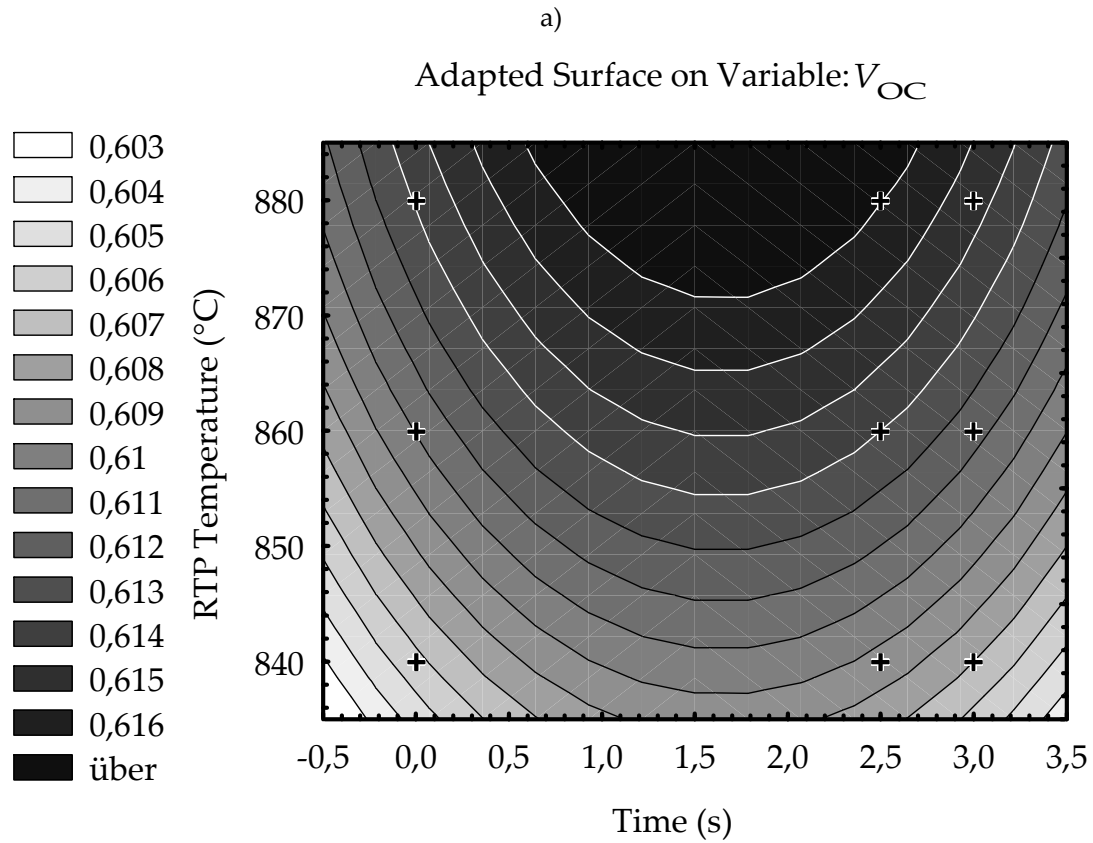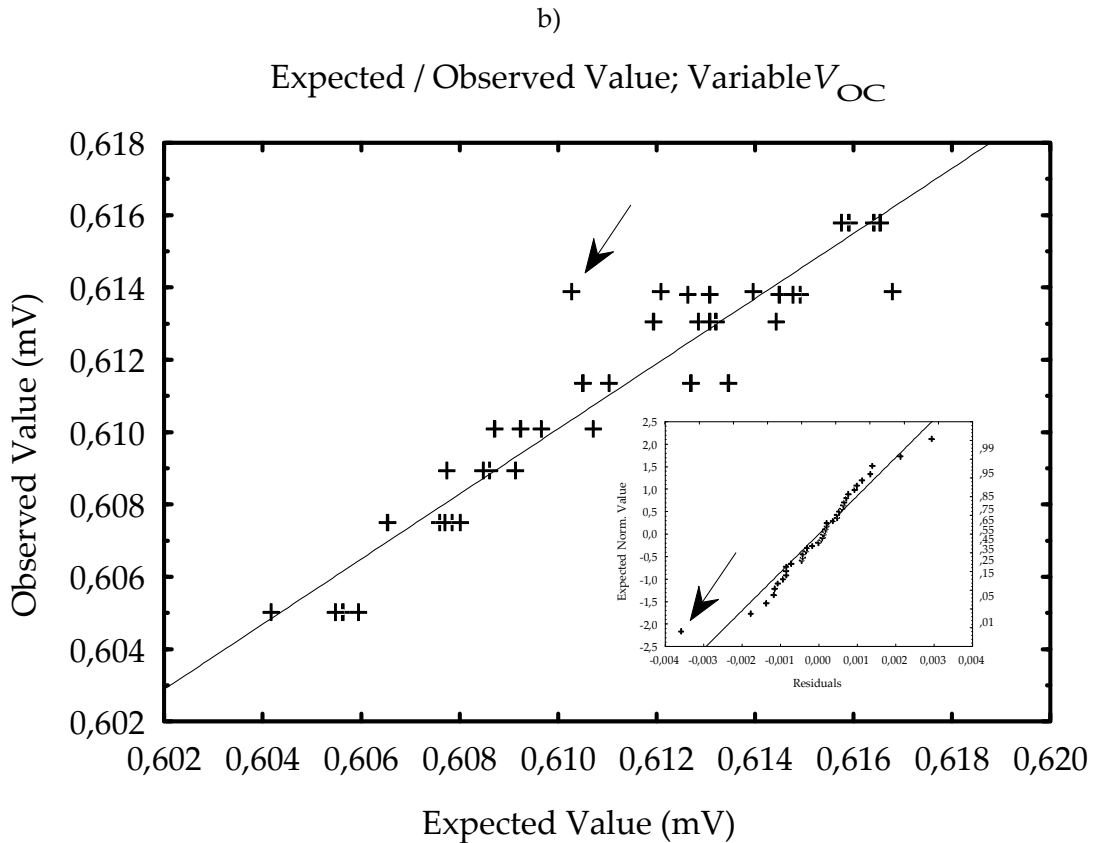
Fig. 4:20 a) The quadratic surface fitted on the V_{OC} results. The gray scale indicates the value of V_{OC}. b) The verification of the model. Here an outlier is highlighted and is the same as in Fig. 4:20.

The V_{OC} is influenced positively by the firing temperature. This is an antithesis of the finding in 3.5, which forecasts a decreasing J_{0e} with increasing temperature. The observed increase is though explained as the improvement of the Al-BSF on the back of the solar cell. Recent experiments {Huster 2005; Rauer, Schmiga et al. 2009} detail two consequences of high temperature firing, the first and more important is a higher aluminium doping concentration in the region closer to the base bulk, and the second is a thickening of the aluminium doped region. We expect these two phenomena to take place also in this experiment. A higher doping concentration close to the base increases the built in voltage of the high low junction formation and therefore decreases its equivalent saturation current.

Indeed, the thickness of the cell allows the passivation of the back surface to play a role on the resulting device open circuit voltage. This limitation also motivates the small, though significant, increase of open circuit voltage for the plasma processed wafers.

Another antithesis to the previous finding (see 3.5) is the better V_{OC} for a shorter plasma etching time. The reduced attack leaves an emitter almost as thick as the original (Fig. 4:17). Although the removal of the dead layer is not optimal, a thicker emitter prevents a shallow SCR. A shallow SCR is mostly undesired. Indeed, contamination can take place during subsequent high temperature steps. For example a firing step exposes the emitter to the diffusion of metals and other impurities in the bulk {Haase, Müller et al. 2010},

Although these impurities are almost innocuous in the thicker reference emitter and for wafers of the process A, they could be harmful for process B. Another confirmation of this tendency is that impurities assumed in the SCR between the emitter and the base decrease the open circuit voltage, but do not affect the short circuit current {Robinson, Aberle et al. 1994}, as it is observed in this experiment. This can be seen comparing the two polynomial fit of figure Fig. 4:19 and Fig. 4:20.

Experiments based on clean room technology have been performed at the same time in other institutes {Altermatt, Steingrube et al. 2009}. These confirm the tendency of an improvement due to the dead layer removal. However due to the different metallization scheme applied, which allows the contact of a low surface doping emitter, other tendencies are observed. From a straight comparison, we could argue that the dead layer in this work is not removed. On the other had, present industrial contacting technology is not capable of stable ohmic contacts on low surface concentration {Hörteis 2009}.
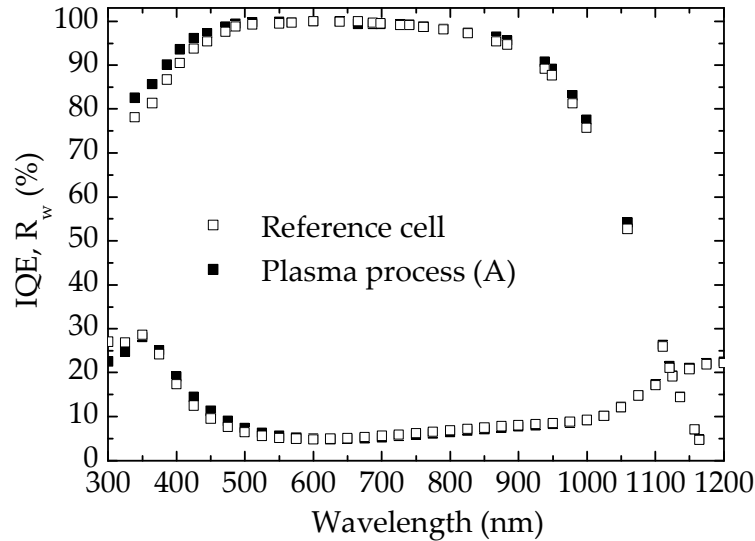
Fig. 4:21 IQE response of a reference wafer and a plasma processed wafer (variation A), the RTP peak temperature is the same for both cells and is 880 °C.

Looking at the outliers from other cell characteristic surface models it is possible to acknowledge that in several cases the shallower emitter leads to an increased FF_0 to pFF difference ($FF_0 - pFF$). This difference indicates the dissimilarity of the device from an ideal diode. Deviations from the ideal diode present higher local ideality factors in the low injection region (low bias). The common interpretation is a contamination of the SCR {McIntosh, Altermatt et al. 2000}. Therefore, here a further proof for the diffusion of impurities is underscored.

An occasional increase in pFF to FF difference ($pFF - FF$), which indicates directly a series resistive loss, spurs observations similar to the previous. The experiment setting gives only an increased contact resistance as an explanation of this aleatory divergence.

These two phenomena are aleatory. This contributes to the reduction of the correlation of these values, or the solar cell efficiency, to the processing variations.

As it was underlined, dead layer removal processing has a positive and significant influence on the V_{OC}, as well as on the J_{SC}. Indeed, when cells are realised without the metallization problems mentioned, higher efficiencies can be reached with the plasma processed wafers (see Table 4—8). Indeed the best solar cell of the batch belonged to a plasma processed group.

Table 4—8 Average solar cell results

	V_{OC} (V)	J_{SC} (mA/cm²)	FF (%)	η (%)
Process A	0.612	35.44	76.62	16.62
Process B	0.613	35.47	77.64	16.88
Reference	0.610	34.81	78.34	16.62
Best cell (Process B)	0.617	35.80	77.42	17.10

Therefore the process has the potential to positively influence the solar cell efficiency. Striving to increase the stability of the process can result in a significant gain.

a)

b)
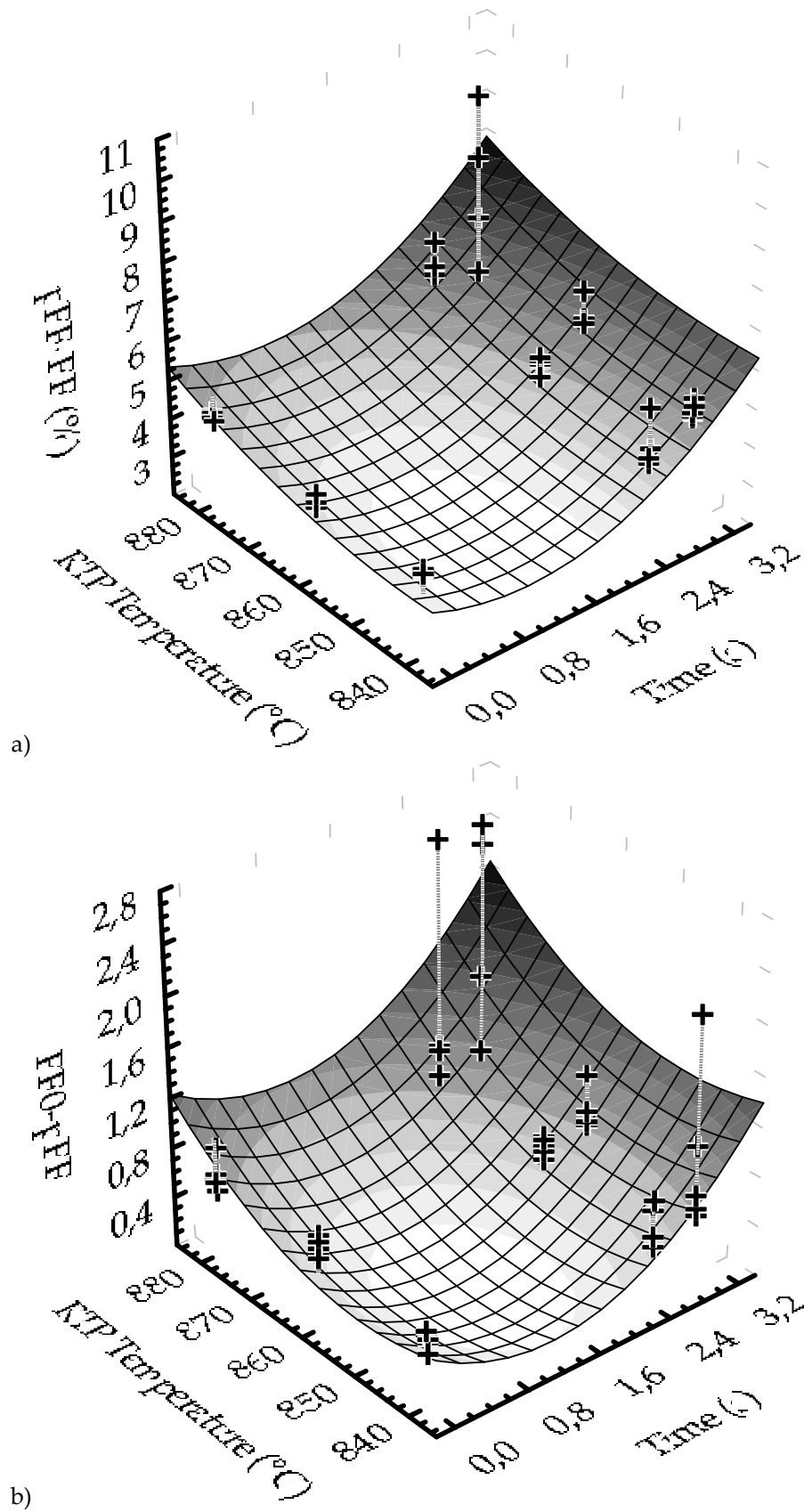
Fig. 4:22 a) It is possible to notice the larger spread of the *pFF - FF* for the plasma processed wafer. b) Also for the *FF0 - pFF* a larger spread is to be found in the processed wafers. It can also be noted that in the reference group the temperature contributes to an increase of this spread. The second degree polynomial surfaces are given as guide to the eye.

4.6 Plasma processing and PERC structures

The material (p-type Cz-Si, $\rho = 6\ \Omega\cdot$cm, pseudo square, 156 mm side, 205 mm radius, 200 µm starting thickness) followed a processing similar to what was already described (compare Fig. 4:16 with Fig. 4:23) until the backside passivation depositions (BS: SiriON CaTS Dep.), the plasma etch processing parameters are identical. The front side was deposited with a SiN$_x$ ARC on all cells while the back surface passivation (SiriON CaTS) is applied only to the plasma etched wafers. Further processing steps, as a contacting technique (LFC, sintering and LIP), are then performed on the two plasma etched subgroups
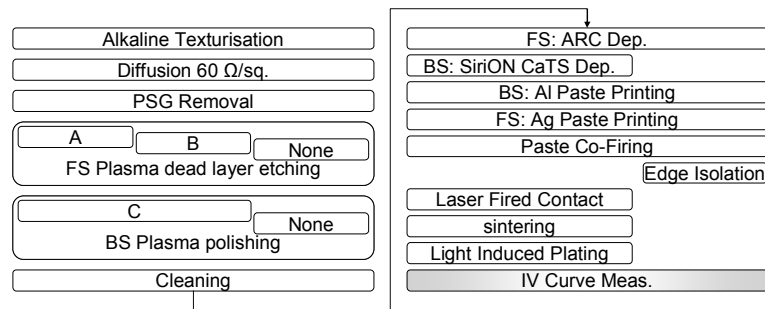
Fig. 4:23 The process flow shows the increased amount of steps to finalize a PERC solar cell. A complete plasma line implementation would try to decrease the number of steps in atmospheric pressure. Additional alternatives are becoming available in these days, for example vacuum metallization techniques {Nekarda, Reinwand et al. 2009}.

Unfortunately, due to issues during the processing independent from the plasma processes, the ohmic contacts from the metallisation to the cell are highly resistive; the *FF* is therefore low for all groups.

Table 4—9 Results from the batch. Though processed in parallel with the other samples, the reference in this comparison had technical problems of realisation. The *FF* is affected by processing issues independent from the focus of the here presented experiment, for this reason they have been omitted.

Process	V_{OC} (mV)	J_{SC} (mA/cm²)
A	606±6	35.9±0.5
B	610±5	36.0±0.3
Reference	602±2	35.5±0.1

Few considerations on the base material are due before interpreting the results. The high resistivity of the base limits the open circuit voltage by imposing a smaller built-in voltage; this is one of the reasons for such low performances of the reference group. The PERC processed wafers exhibit higher V_{OC} and higher J_{SC}, consistently with the previous results.

Albeit small, the increases shown in Table 4—9 confirm that the process can improve the wafer potential, especially when the sequence B is chosen. This etching time reveals to be an optimum compromise to allow contacting and avoid severe contamination of the SCR.

4.7 Analysis of Fill Factor losses

The control of the processes unveils the effects of the processing on the realised structure. However, more often than not, additional characterisation on the finished solar cell can help to understand which are the issues that are hindering the complete potential (in this case conversion efficiency) of the device.

The aim of this work is to improve our understanding of the remaining loss factors and process limitations exhibited in the thin cells of the experiment detailed in 4.3 and 4.4. The method that we propose suggests a procedural analysis to understand which technical

difficulties are hindering the state of the art implementation of PERC structures in the industrial production.

The efficiency presented in the previous experiments, coupled with the thin substrate on which they were achieved, allows a reduction of the production cost when expressing this unit on money per power (i.e. €/W) {del Canizo, del Coso et al. 2009}. Nevertheless the good results obtained in the previous experiments (4.3) are still affected by minor losses. Eliminating these losses the solar cells would present a *FF* of about 78%. An immediate boost of 0.6% absolute efficiency would be observed.

Quantifying the losses on fill factor (*FF*) is done conducting analyses of all possible causes where a loss could be individuated. The approach is helpful for several reasons: first it will be easier to understand where more effort has to be invested for increases in cell efficiency, second it will show exactly what can be the maximum achievable level once improvements are undertaken, third and last, this method can be partly used to identify losses also in a production line.

To get a complete overview of the *FF*, two other values will be introduced: the *pFF*, indicating the potential of the cell without series resistance and the FF_0 which indicates the *FF* of a cell with only ideal recombination mechanism. A detailed explanation of these two quantities can be found in the Appendix (A.h).

4.7.1 Measurements and results

The cells on which the measurements were done present a backside passivation composed by a functional layer (SiNTOx) and a lowly doped emitter with a sheet resistance of 85 Ω/sq.

The investigated losses are presented in an order geometrically similar to a solar cell cross section. In conventional solar cells, *FF* losses are normally imputed to the front metallization. In order to face the easiest interpretation before unnecessarily entering in more complicated analysis, the front side metallization will be the first to be investigated. Second will be the mechanism of recombination saturation presented by the defects in the bulk. These SRH saturation mechanisms have an effect on the *FF* when the injection level overwhelm the amount of impurities or defect, a complete treatment of this is given in {Robinson, Aberle et al. 1994}. Third and fourth investigated aspect are related to the PERC structure, the third evaluates how severe is the influence of the point contact scheme on the whole series resistance while the fourth evaluates the effects of the passivation on the low injection regime. Finally the fifth analyses confronts the reality of the cell with the imperfection of the interruption of the planar symmetry. These investigations are presented below.

First: Front metallization: influence of plating on contact resistance

One cell was monitored throughout the process steps (see Fig. 4:9). The values shown were measured by means of SunsVoc before the laser contacting procedure (LFC), due to high R_s, and by a JV1Sun after LFC.

The measured results are used to show the drastic increase in *FF* (Table 4—10). The plating process can decrease the resistance of the front side grid thickening the silver finger which in turn increases the *FF*. Still the jump of more than 10% observed in this work cannot be explained by a simple reduction in lateral conductivity of the fingers.

Table 4—10 List of V_{OC} and *FF* values along the process. The high-temperature firing step is indicated as FFO and "Laser-Fired Contacts" realisation as LFC.

Cell status	V_{OC}	*pFF*	*FF*	η
	mV	**%**		
FFO (SunsVoc)	629	83.7		
LFC (JV1Sun)	630		64.0	15.1
Sintering (JV1Sun)	638		64.7	15.5
LIP (JV1Sun)	643		75.2	18.3

The same screen-printed grid, used for the front metallization of cells with an emitter of higher surface doping concentration, presented a *FF* above 70% straight after the firing step. This evidence moves therefore the focus on a possible change in contact resistance.

By using the transfer length measurement (TLM) method {Berger 1972} the contact resistance was analysed on two cells structure. One cell presented solely the screen-printed front grid composed of Ag paste. The other cell instead had additionally silver plating. The results are shown in Table 4—11. A significant decrease in contact resistance explains the better fill factor obtained after plating.

Table 4—11. Contact measurements using the TLM, performed on sister samples, before and after LIP.

	After sintering	After LIP	Units
Specific contact resistance	80±10	1.4±0.4	mΩ cm²
Contact resistance	5.7±0.2	0.28±0.07	Ω

The decrease in contact resistance due to additional plating of screen-printed front side grids was already observed and explained {Pysch, Mette et al. 2009}. The improvement is delivered by an increase in the interconnection of Ag crystallites and the screen-printed grid through the plated silver.

Crystallites are a by-product of the reaction between the paste and the highly doped silicon surface at high temperature {Schubert 2006}. A normal screen-printed metal finger presents on the sides a vast area with a reduced amount of paste. This does not hinder the formation of silver crystallites, but their connection is jeopardized. For this reason, coating an additional metal layer, for example by plating, can be profitable.

To study the effect of a further increase of the fingers' conductivity, an over-plating test on a 70 Ω/sq. emitter was performed. The standard plating time was increased by a factor of 1.40 and 1.75. In both attempts, no significant increase in *FF* could be measured, whereas increasing losses in J_{SC} due to a broadening of the fingers affected the overall efficiency.

Later in this work, on the occasion of a dedicated investigation of the rear side contacting resistance, a calculation of the contribution of the front on the *FF* will be presented and commented.

Second: Influence of LID[32] and bulk impurities on *pFF*

The first analysis demonstrated already potential for improvement. The following investigation instead will measure the effect of the light induced formation of boron oxygen (BO) complexes in p-type material. Their formation creates a trap level in the bandgap which is convenient for SRH recombination. The installation of this recombination degrades the cell and is fostered by illumination. Thus, the phenomenon is also known as light induced degradation (LID).

LID acts upon strongly boron doped p-type bulk. This material is common in the photovoltaic as starting material. Few solutions have been proposed to counteract this

---

[32] This acronym refers to Light Induced Degradation (not to be confused with LIP).

phenomenon with processing techniques. Furthermore it is known that its presence can influence the final *FF* of a cell {Schmidt, Cuevas et al. 2001}.

The influence of LID had been observed over a period of 12 h on a solar cell with high R_{shF} values and an 85 Ω/sq. emitter. The monitored cell parameters were the Open-Circuit Voltage (*V*OC), the pseudo Fill Factor (*pFF*) and the ideal maximum value of Fill Factor (*FF*0). The first and the second are directly measured on the SunsVoc curves, the latter is calculated (Equation A—5).

The experiment started after 15-minutes of heating at moderate temperature (250°C). A first measurement in this un-degraded state is performed. After this moment the measurement is repeated at regular intervals. In between those measurements, the sample is kept in the dark or is exposed to light, in this second case the interval of exposure is accounted with a precision of minutes (see Fig. 4:24). The data is then plotted on a XY graph, the x-axis reports the integrated exposure time, and y axis represents *V*OC measured at each total exposure time (Fig. 4:25). The degradation effect is clearly visible, and can be successfully fitted with an exponential decay of the first order.
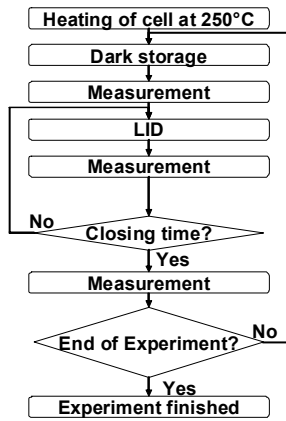
Fig. 4:24 The flow chart explains the procedure followed to track the LID during its evolution. "Closing time" means the actual laboratory closing time, before storage in dark a second redundant measurement was performed.
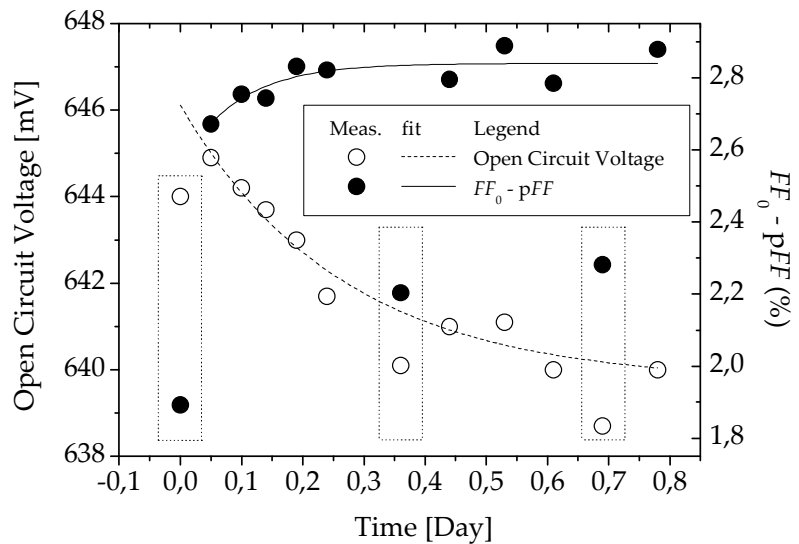
Fig. 4:25 Degradation curve of a thin cell. The points report the *V*OC measured as a function of net illumination time. Excluded from the analysis are the measurements performed straight after the storage in the dark (enclosed in dotted rectangle). These systematically deviate strongly from the exponential behaviour. A hypothesis is that they represent another metastable defect.

Based on the LID graph (Fig. 4:25) of the thin cell and its fitting curve, we can accurately calculate the degradation constant and determine the time after which the degradation reaches saturation.

$$V_{OC}(t) = V_{loss} \cdot e^{\left(-t / \tau_{DEG} \right)} + V_{OC0} \qquad \text{Eq. 4—1}$$

From the first-order exponential decay fit (Eq. 4—1) all parameters are obtained. Indicated as V_{loss} is the amount of *V*OC loss caused by the LID, the *V*OC of the completed degraded state is indicated as V_{OC0}, and the time constant of this decaying process and is indicated as τ_{DEG}:

The values in respect of the thin silicon cell, implemented by the described processes, are provided in Table 4—12, which also includes exemplary values of a thicker PERC type cell.

Although the fit accuracy is high (R^2=0.97) the error on the values is quite big, especially on the time constant. The consequence is an approximate prediction of the time for an LID of 90%. Here this time ranges between less than 12 h and almost 20 h.

The integration in Table 4—12 of a slightly different bulk resistance shows that this thin cell, with a resistivity of 2 Ω cm (N_A ~ 7E+15 cm^{-3}), scores much less V_{loss} (the comparison material resistivity is 1.5 Ω cm (N_A ~ 1E+16 cm^{-3})). Models in the literature predict a positive correlation between doping and degradation rates {Schmidt, Aberle et al. 1997; Rein, Rehrl et al. 2001}. However, from the comparison we confirm a previously observed tendency on thin CZ-silicon solar cells {Münzer, Holdermann et al. 1999}. Also there, divergence was remarked from the predicted correlation of LID and bulk boron doping level.

It should be noted that the measurements at the calibrated laboratory (Table 4—5) were made after a 12 h LID. The cell had a loss in V_{oc} that was much lower than what we had predicted in the model as characteristic total loss V_{loss} in Table 4—12. Because of its exponential decay, this implies that the cell was already partly degraded before the LID[33].

Table 4—12. Summary of the fitting algorithm results of the data in Fig. 4:25, also including a comparison with a thicker PERC type cell.

	W = 120 μm ρ = 2 Ω·cm	W = 200 μm ρ = 1.5 Ω·cm	unit
V_{loss}	6.4±0.5	8.9±0.2	mV
V_{OC0}	639.7±0.5	627.0±0.1	mV
τ_{DEG}	0.26±0.07	0.23±0.01	Day

The FF_0 does not change through the degradation. This is due to the low sensitivity of the formula for few mV changes on the V_{OC}. Instead, the pFF decreases slightly along the LID progress. This suggests that the role of a non-ideality of the diode, monitored by the difference between the FF_0 and the pFF, becomes stronger during the evolution of LID. The extent of this decrease is pFF 0.3% and is obtained from an exponential fit on the FF_0 - pFF data presented in Fig. 4:25. This loss is remarkably small. Indeed this is a consequence of the low sensitivity of the cells towards the boron oxygen complex activation. Different was the case presented in the literature, where thicker cells (400 μm) were used {Schmidt, Cuevas et al. 2001}, there the loss was expected to be as high as 2%.

In the following, plots of the local ideally factor (m_{loc}) will be presented (Fig. 4:26). Indeed a local deviation of m_{loc} at high injection levels is consequence of the LID. Since these graphs are of interest for a lower injection level range (>500 mV), the influence of the degradation on these plots is low if not absent. Confirmations to this sentence were calculated with the help of a simulator tool[34] {Cuevas, Sinton et al. 2008}. Several thickness and defect density were found to act only above high injection levels (1 Sun and more than 600 mV).

The repeatable deviation from the degradation trend (exponential decay) highlighted in Fig. 4:25 could be imputable to another metastable defect in the bulk. This metastable defect imposes a low, injection-independent lifetime, lower than the one due to BO complexes, in the injection range of interest (between pFF and V_{OC}). This results in a lower V_{OC}. However, its independence from injection creates a more ideal device and in turn allows a higher pFF. This increase in pFF is not to be regarded as a positive gain since the loss in V_{OC} is larger.

Third: Back Surface Contacting: Influence of rear contact structuring on *FF*

The rear surface contacting scheme and its consequences on *FF* are now investigated in more detail, first by measuring the current density versus voltage under a 1 Sun illumination

---

[33] The last process is LIP, during which the cell undergoes a long and intense light exposure.

[34] Input parameters similar to the ones declared in footnote 30. Oxygen concentration is 1E+18 cm^{-3} and the `tau_d enhancement` = 4.

(JV1Sun), then by measuring the current density versus voltage in the dark (JVDark) and finally by measuring the V_{oc} as a function of the illumination level (SunsVoc). The latter has the characteristic of tracing pseudo JVDark and a pseudo JV1Sun curve where the series resistance is not taken into account.

The first characterisation gives a direct evaluation of the *FF* while the second and the third ones will give an insight into the conduction/recombination mechanisms that are taking place in the cell at different voltages or illumination biases.

It must be aforementioned that the PERC structure has intrinsic limits of *FF*. This is due to the limited total area of a local contact point structure. For an empirical study of the influence of the rear side contacts density on the series resistance, an analysis of a change in distance between the back surface local contact points was performed. This distance will hereinafter be referred to as pitch L_P.

We present in a summary (Table 4—13) the result from the JV1Sun curves. Before the measurements, the three solar cells, having each a different pitch, underwent a complete LID and an additional edge isolation on the front to exclude any resistive shunting at the edges (fitted $R_{shF} > 1E+4\ \Omega\cdot cm^2$).

Table 4—13. The cells presented here were fabricated at the same time through every stage of the process. The only difference in their implementation is the pitch, the V_{oc} dependency on the pitch is easy to recognize.

Cell Nb.	Pitch	V_{oc}	J_{sc}	FF	Eta
	μm	mV	mA/cm²	%	%
A018	400	629	36.7	76.3	17.6
A021	500	631	36.9	75.4	17.6
A027	600	635	37.5	74.3	17.7

The resistive path from the bulk towards the contact was calculated using Eq. 3—5, the spreading resistance effect results as the main contributor to the rear contact resistance {Nekarda, Gautero et al. 2009}. The values are reported in Table 4—14, column R_{sRear}. In the same table the total series resistance was calculated by a fit to the JVDark measurement data (Table 4—13). Finally the front contribution was calculated as the difference between R_s and R_{sRear}.

Table 4—14. This table shows the series resistance fitted from the JVDark and the calculation results of the resistive path towards a contact.

	Measured		Calculated	
Pitch	pFF - FF	R_s	R_{sRear}	R_s - R_{sRear}
μm	%		mΩ cm²	
400	3.7	540	184	356
500	5.2	610	287	323
600	6.2	830	413	417

Analysis based on of the data presented in Table 4—14 allows to calculate the *FF* of a cell where rear contacts do not contribute to resistive losses, such a value is *FF* ≈ 77.5%. The front metallisation is contributing for all pitches more than the 50% to the resistive loss, this contribution needs to and can be reduced. A first point where improvement is necessary is now identified.

JVDark curves and SunsVoc curves were measured on the set of solar cells with different pitch, the curves are then compared (Fig. 4:26 a). The current density of JVDark was normalized to light intensity using the respective J_{sc} of every cell.
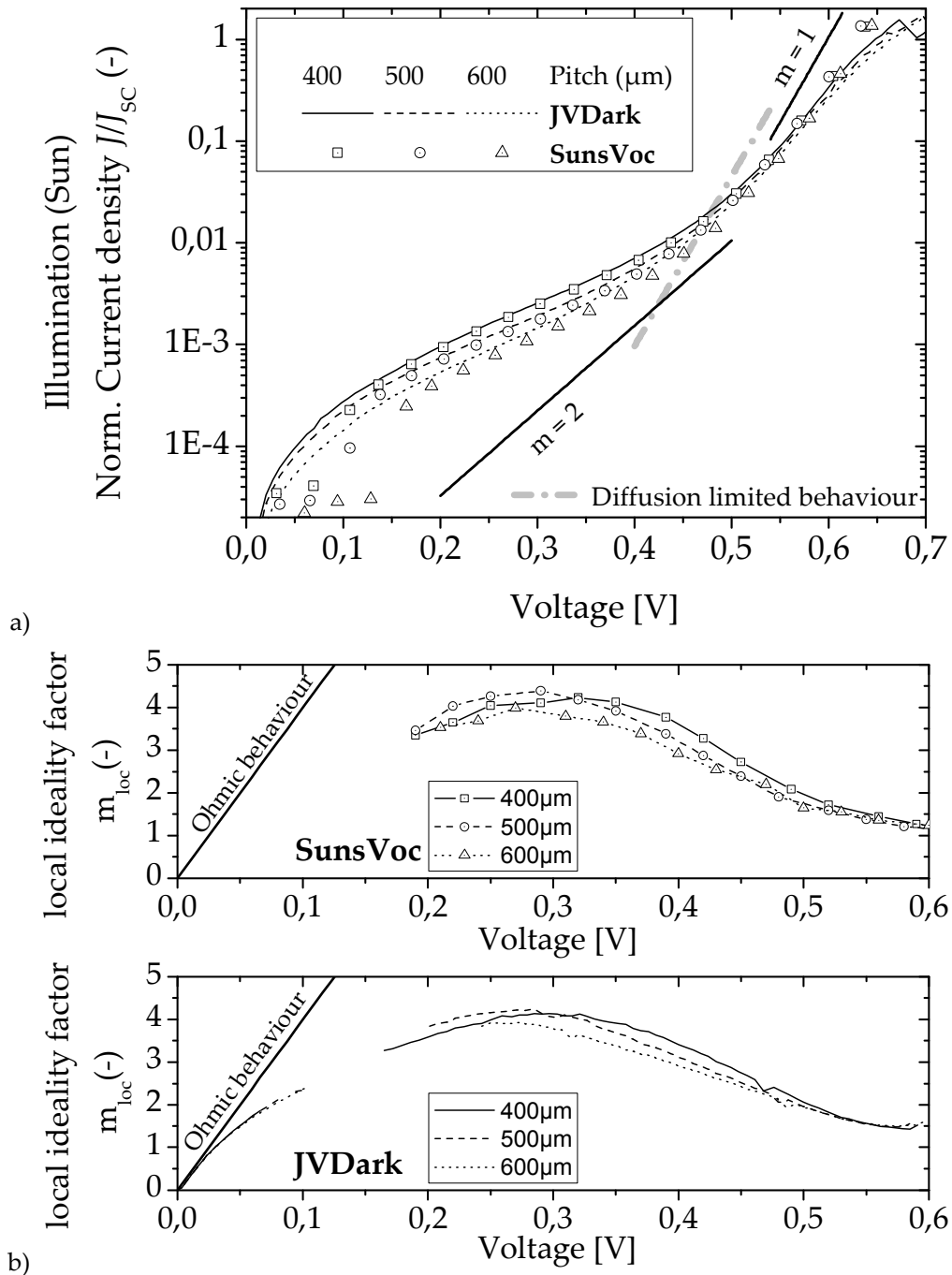
Fig. 4:26 a) The legend details the point and line style in a table manner. The SunsVoc curve either overlaps or is below the JVDark curve for every pitch in the low voltage bias, below Maximum Power Point (V_{mpp}), and for higher bias, the series resistance reduces the slope of the JVDark curve. Continuous lines indicate the typical slopes that a two diode model uses to fit the JVDark curve. The point dash line indicates the saturation current of a diffusion limited solar cell (V_{OC} = 580 mV). b) The m_{loc} curve was calculated on the basis of both SunsVoc (above) and JVDark (below) measurements. The SunsVoc curve was taken from the average of several measurements to increase S/N. The JVDark curve shows a gap between 0.1 V and ~0.2V because of impedance coupling problems. The continuous black line represents the ohmic behaviour. The deviation from this line, confirmed for all of the three measurements, shows the presence of another mechanism of current conduction. We clearly see the shift of the peak in agreement with the pitch variation which supports the hypothesis that RLRC has a correlation with rear contacts.

The JVDark and SunsVoc curves overlap for voltages below 0.55 V, which means that series resistance effects are not strong until this voltage bias in the JVDark; this information was

translated to an observation of the low effect of the series resistance on *FF* in the illuminated case (JV1Sun) in the paper presented by {Gautero, Hoffmann et al. 2009}. However, this observation is not entirely correct: the shifts in voltage due to resistive paths are seen before V_{OC} in the JV1Sun curve; these are negative and influence the *FF*. On the contrary, in the JVDark curve shifts are always positive. From the observed data it is qualitatively concluded that R_s is low. Although, the quantitative information cannot be obtained for each bias.

Fourth: Back Surface Passivation: Influence of rear contact structuring on *pFF*

A higher pitch increases the area coated with a passivation and therefore decreases the effective surface recombination velocity (*S*), hence reduces J_{01} and increases V_{OC}. The consequences of the pitch change are evident in Table 4—13. On Fig. 4:26 a) this shift is less visible, yet present in the range of $0.6 \div 0.7$ V and especially on the SunsVoc curve.

The pitch-dependant shift of current density (illumination response) at low-voltage bias on the JVDark (SunsVoc) curve is not explained.

In Table 4—15 a list of the FF_0, *pFF*, and *FF* is presented. Noteworthy is the correlation of the different pitches on the *pFF* - *FF* difference. Indeed is the shunt resistance high ($R_{shF} > 1E+4 \, \Omega \, cm^2$) and therefore the high FF_0 - *pFF* difference results from the presence of non-idealities, namely loss mechanisms which impact at low bias regimes. However, its extent is consistently larger than what we saw from the previous investigation on bulk effects.

Table 4—15. The difference between the ideal FF_0, the *pFF* and the *FF*.

Pitch	FF_0	*pFF*	FF_0 - *pFF*	*FF*	*pFF*- *FF*
μm	(%)				
∞	83.3	83.7	-0.4[35]	--	--
400	83.3	80.0	3.3	76.3	3.7
500	83.4	80.6	2.8	75.4	5.2
600	83.5	80.5	3.0	74.3	6.2

A deviation from the ideal behaviour of injection independent lifetime, and a unity ideality factor ($m_{const} = 1$) could be represented by strong dependency of the *S* on the injection level. To explore this hypothesis the SunsVoc curve will be used. From this curve it is possible to calculate the effective lifetime towards injection rate by means of few calculations {Sinton and Cuevas 2000; Kerr 2002}. In these calculations important parameters are the silicon wafer thickness and the J_{SC}. This indirect measurement has the advantage that there are no artefacts as for low injection rate[36].

Proportional to the inverse of this effective lifetime is the *S* plus two terms, which we will consider constant because of the low injection spectrum of our measurements ($\Delta n < 1E+13 \, cm^{-3}$). This velocity can therefore be calculated (see Eq. 4—2, from Eq. 14 in {Cuevas and Macdonald 2004}) to check its development.

$$S_{eff} = \frac{1}{2}\left(\frac{W}{\tau_{eff}} - \frac{W}{\tau_{bulk}} - J_{0e} \frac{N_A + \Delta n}{q n_i^2} \right)$$
$$= \frac{1}{2}\left(\frac{W}{\tau_{eff}} - k_1 - k_2 \right)$$

Eq. 4—2

In the equation the wafer thickness is $W \, (= 120 \, \mu m)$, the bulk lifetime contribution is $\tau_{bulk} \, (= 100 \, \mu s)$ and the front-side emitter is modelled with its saturation current

---

[35] This incongruous measurement could not be repeated, reported is the value observed.

[36] What is tracked is the open-circuit voltage for all light intensities measured, which tells us about the distance between the quasi Fermi levels. Once we know the doping, we can calculate the injection as it changes in time, as light does, the light can be qualified as injection when normalised to the term J_{sc}.

J_{0e} (= 100 fA/cm²). These two terms are equal for the three cells. Therefore, for the comparison they can be treated as constants (k_1 and k_2). Furthermore, in the low injection regime, the influence from the emitter is constant and the bulk lifetime is limited by constant Auger and radiative recombination limits.

The trend can be seen in Fig. 4:27, to guide the eye a power law function $f(\Delta n) \propto \Delta n^{-0.85}$ is shown, comparing this graph to previous consideration on the matter {Fischer 2003}, we can say that the dependence is not strong.
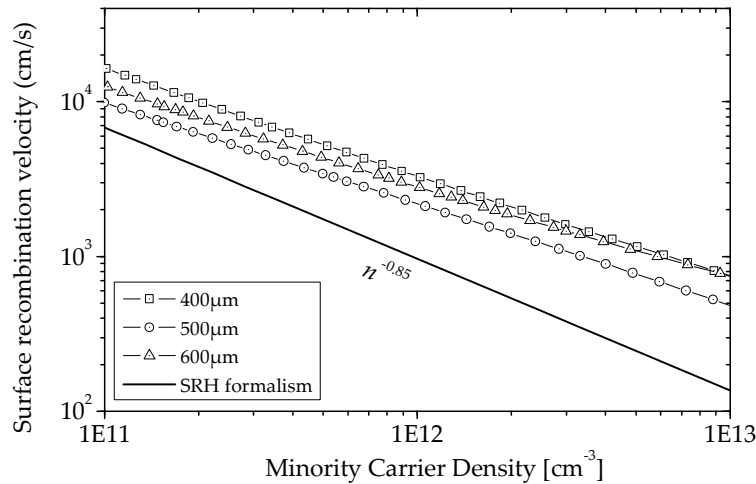
Fig. 4:27 The graph shows curves proportional to the measured surface recombination velocity plus the two constant terms. The *S* does not depend on the injection level more than in SRH formalism.

Besides, we must acknowledge that even if the *S* rises to the thermal velocity limit all of a sudden, its effect would not explain the curve seen in Fig. 4:26 a). This statement can be better understood with a comparison to recombination saturation effects {Robinson, Aberle et al. 1994}. From these studies it can be seen that *S* varies as consequence of interaction between capture cross sections and carrier population. Important to observe is the minimum and the maximum behaviour, the first let the carrier diffusion limit the recombination at the back, while the second imposes a substantially smaller rate of surface recombination. Both cases share an ideality of 1 for a diode representing their behaviour at low injection. In these thin cells the minimum attainable V_{OC} was calculated and the corresponding saturation current is shown in Fig. 4:26 a). Indeed the curves trespass this limit in the whole low injection range, this therefore excludes any influence of the backside passivation and contacting scheme on the pitch dependent shifts observed.

Another analysis of the JVDark and SunsVoc curves that could tell us more about the solar cells' behaviour derives from the calculation (Eq. 4—3, from Eq. 2—42)

$$m_{\text{loc}} \;=\; \frac{1}{V_{\text{T}}} \cdot \frac{\partial V}{\partial \log(J)} \qquad\qquad \text{Eq. 4—3}$$

which gives us the local ideality factor m_{loc}, its derivation is presented in 2.4.2. This calculation (Fig. 4:26 b) is performed on both JVDark and SunsVoc.

The slope of the m_{loc} curve distinguishes ohmic conductance from exponential conductance, the former is shown as a line with a fixed slope of $1/V_{\text{th}}$ while the exponential behaviour is shown as a flat line, and its level corresponds to the ideality factor of the diode which is conducing current.

The graph presented in Fig. 4:26 b) shows that the initial rising deviates from the $1/V_{\text{th}}$ which characterises ohmic conduction, and grows towards a peak. The peak shifts amongst different implementations.

Similar peaks, namely called humps, were explained to be the consequence of spatially located recombination points {McIntosh 2001}, or recombination points with a resistive path limiting their activity {Hernando, Guitérrez et al. 1998}; in the literature these are called resistance-limited recombination centres (RLRC). The quoted literature gives also indication on method to interpret the m_{loc} curve; for example the crossing point between the ohmic behaviour and the calculated curve, named m_H[37], is a good estimator of the type of recombination which is affecting the cell.

Another parameter that can be qualitatively read is the limiting resistance value. The higher this resistance is the lower injection is needed to saturate it. The peak, which indicates this recombination shutdown, moves towards lower injections (Fig. 4:28 b). When resistance is written, it means that the recombination is limited by the abundance of majority carrier.

In the three cases the diode has an ideality factor slightly above one (Fig. 4:26 b); moreover the higher the pitch, the more the peak will move to the left. This correlation between limiting resistance R_H and pitch purports on where the majority carrier transport is limited.

Although the low statistical value of the analysis could be argued, the mentioned correlation could be a first indicant that RLRC are located in coincidence with rear contacts. A statistical approach on a larger number of cells can give more insight on this first assumption here formulated. Anyway, since the three samples used are best cells of their category, their measurements are not likely to be compromised by random causes. Therefore additional hypotheses will be offered as an interpretation and tested on the specimens.
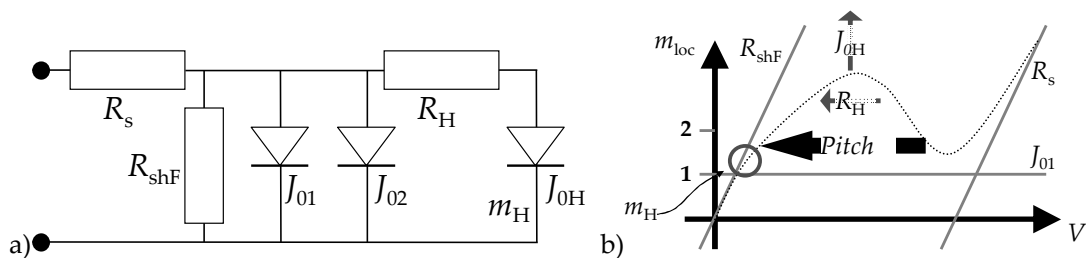
Fig. 4:28 Here the Two-diode model is depicted including an extension that provides the contribution of the RLRC through the implementation of R_H and J_{0H} and the ideality factor of the diode m_H.

The *pFF* observed on finished cells (around 80%, see Table 4—15) is lower than the *pFF* before the LFC process (around 84% see Table 4—10); Table 4—15 shows the comparative data. This could be another indication of the RLRC effect introduced by the rear side contacts.

Presently, argumentations were given that testify to the existence of RLRC and that those are correlated somehow to the pitch. However, a clear picture of where these mechanisms are found is not given. Below, with the help of an additional image, a satisfactory explanation will be laid out.

First of all, it shall be reminded that the cell structure presents craters in the bulk at every contact (Fig. 4:29). These allow a good contact, and furthermore, a thin Al-BSF avoids the drift of the local surface recombination up to the thermal velocity. Indeed, this concave surface is most likely the strongest point of recombination at the depth of 78 μm, injected carriers are likely to recombine there as soon as they get in their vicinity. Notwithstanding these points account for less than 2% of the whole surface, therefore before recombining there carriers have to find their way there.

---

[37] The H stands for Hernando, the scientist who first presented this modelling.
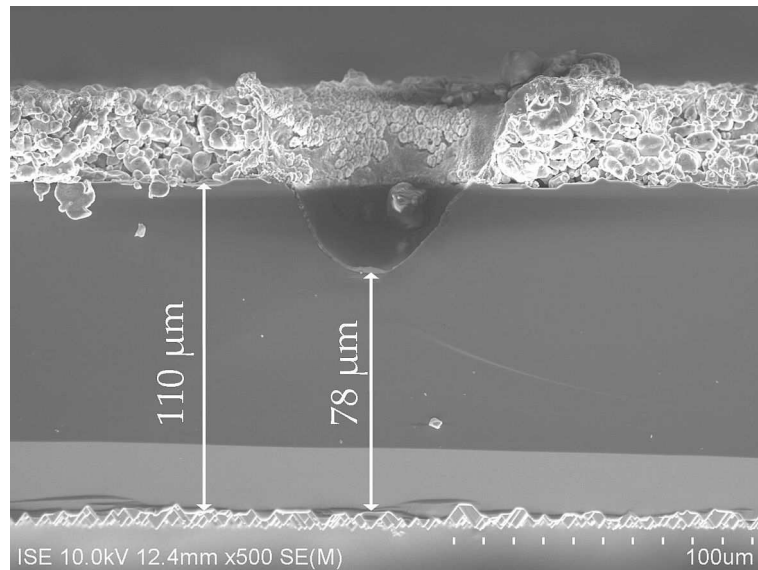
Fig. 4:29 Cross section of a broken SiNTO SP cell, highlighted here is the distance of the crater bottom to the emitter region on the front.

Minority carriers who recombine in the base are supplied by bias/injection. Limiting the observation to the JVDark, there the injection is provided by majority carriers travelling through the emitter by drift and through the base by diffusion. This being the case, these majority carriers see a resistive path (emitter) limiting their flux. In the case of three different pitches but a same (highly resistive) emitter, we could expect this recombination path to have all the requirements to fit the description of a RLRC.

This loss mechanism can have an influence in the range of 1÷1.6% on the *pFF*. This estimation is spurred from the comparison to state of the art conventional solar cells based on the same front-side structure.

Fifth: Edges: Influence of lateral areas on *FF*

To evaluate the effect of areas far from electrical contact, located at the edges, the cells were measured for their characteristics with a masked illumination. From the side, 3 mm were excluded, and both JVDark curves and SunsVoc curves were measured. Subsequently 3 mm from the side of the solar cells were removed, and then the cells were measured again in the same way (JVDark and SunsVoc). A list of the results are presented in Table 4—16.

Before presenting considerations on the solar cell results, few remarks are necessary: first, a masked solar cell can still benefit from the fingers which, even though shaded, act still as conducting path. Second, a solar cell with its edges removed has a slightly increased amount of front metallization with respect to the surface, though this was not observed in an increase of the difference between *pFF* and *FF*.

The values of the *pFF* improve after the edge removal. This effect does not happen on the masked solar cell. We conclude that there was a removal of shunting paths on the edge. Indeed, higher shunt resistance values were achieved.

Although the *pFF* increases, its gap towards the FF_0 is still valuable (>2 %) and presents a dependency on the pitch. Again this supports the existence of pitch-dependent RLRC.

We can conclude that the edges play a role in the *FF* loss through a shunting mechanism. A second point of improvement was found, the tolerance accepted in a first stage (R_{shF}>1E+4 Ω cm²) is not enough to guarantee high *pFF*.

It is pointed out that the SunsVoc curves of the solar cells after the edge removal have the same pitch dependent behaviour as shown in Fig. 4:26 b), which means that the edge removal reduced but not eliminated the problem.

Table 4—16. Solar Cells results. The size of the full cell is 148.3 cm², the size of the mask is 135.69 cm², and the size of the same solar cell, after the edge removal, is 135.2 cm². All the measurements were done anew, to guarantee a short time between the measurements, resulting in a small deviation from the data presented in Table 4—13.

Pitch/label	V_{OC}	J_{SC}	FF	pFF - FF	pFF	FF_0-pFF	FF_0	η
	(mV)	(mA/cm²)	(%)	(%)	(%)	(%)	(%)	(%)
400 µm								
Complete	**628**	**36.3**	**76.9**	**3.1**	**80.0**	**3.2**	**83.2**	**17.5**
Mask	**626**	**36.4**	**77.4**	**2.5**	**79.9**	**3.3**	**83.2**	**17.6**
Edge off	**628**	**36.8**	**77.3**	**3.3**	**80.6**	**2.6**	**83.2**	**17.9**
500 µm								
Complete	**630**	**36.7**	**75.7**	**4.9**	**80.6**	**2.7**	**83.3**	**17.5**
Mask	**628**	**36.7**	**76.6**	**3.5**	**80.1**	**3.1**	**83.2**	**17.6**
Edge off	**631**	**37.2**	**76.0**	**4.9**	**80.9**	**2.4**	**83.3**	**17.8**
600 µm								
Complete	**634**	**37.2**	**74.2**	**6.3**	**80.5**	**2.9**	**83.4**	**17.5**
Mask	**632**	**37.2**	**75.7**	**4.7**	**80.4**	**2.9**	**83.3**	**17.8**
Edge off	**635**	**37.7**	**75.2**	**6**	**81.2**	**2.2**	**83.4**	**18.0**

Part of the data in Table 4—16 is reported as a graph in Fig. 4:30, there the trends are easier to recognize. The first observation is the increase in *FF* for both masked and edge off case. For the masked case, the gain is a consequence of lower resistive loss. This is attributed to the increased ratio of metallization[38] versus the amount current density, since less area is illuminated. This phenomenon is no more present when the edges are cut; nevertheless a gain in *FF* is obtained through the decreased influence of non idealities and low R_{shF}. The dependence of the non ideality on the pitch is well put in evidence by the graph. Below, there will be another example of non ideality in a different cell configuration (see 4.7.2); this will bring further evidences of the phenomenon.
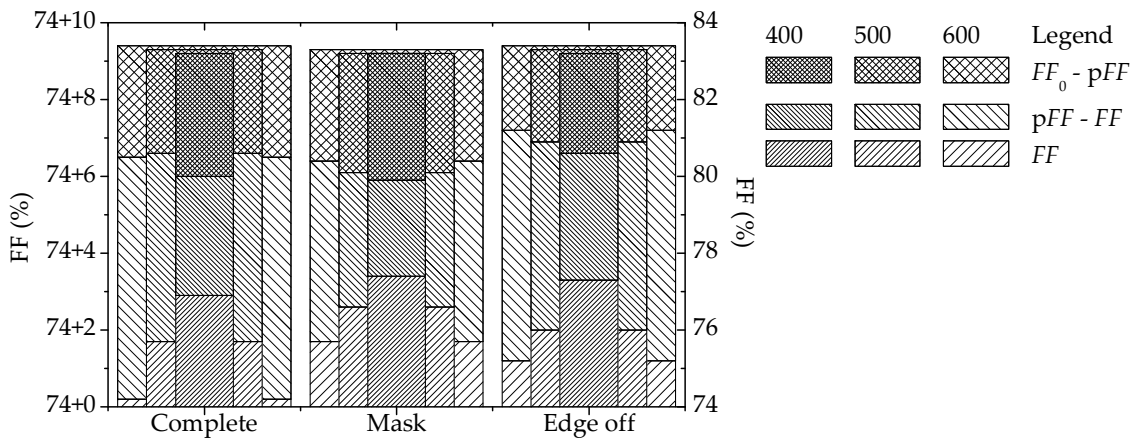
Fig. 4:30 Breaking down of the *FF* limitation.

4.7.2   PECVD Passivated solar cells

As it was reported (Table 4—7), also in the case of a back surface passivated with complete-PECVD passivation a strong limitation in *FF* occurred.

---

[38] The cell presents a redundant line on the edge, which is completely shadowed by the mask, this additional finger can compensate for eventual finger bottlenecks and deliver a more homogeneous voltage on the cell front surface.

Since these cells share all the issues analysed hitherto for the SiNTO SP case, in the following only the problems related to the backside will be presented. The JVDark curve was measured on the cells and compared to the one of the reference group of the batch.
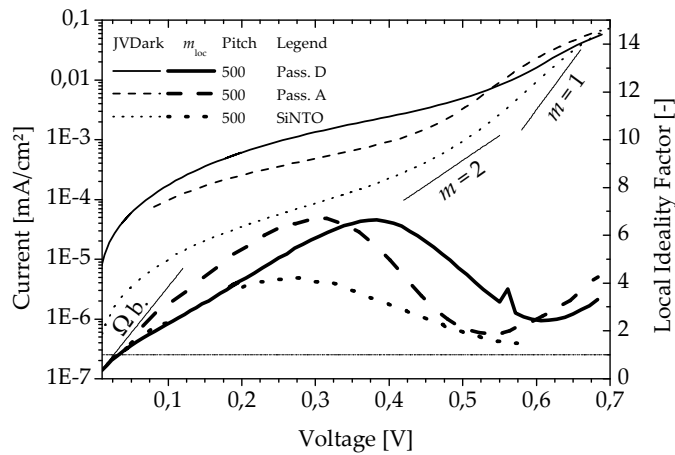
Fig. 4:31 JVDark and m_{loc} curves of the completely PECVD passivated and SiNTOx passivated cells. The behaviour of the curves from the different passivation lies on different levels. However, their behaviour can be likened.

The comparison diagram (Fig. 4:31), in which also the m_{loc} curve is plotted, shows that also this second group of cells, with fully-PECVD passivated cells has large non idealities. The non ideality which figures here can be likened to the RLRC which happens with the SiNTO SP cells.

The hypothesis is that the contact formation procedure is influenced by the passivation layer, and can therefore change the size of the crater or its depth. This test was performed breaking one sample from each group of passivations. From this a fresh cut was obtained. This cross section intersected several LFC points. Below, two representative images, one for each passivation, are reported (see Fig. 4:32 and Fig. 4:33).
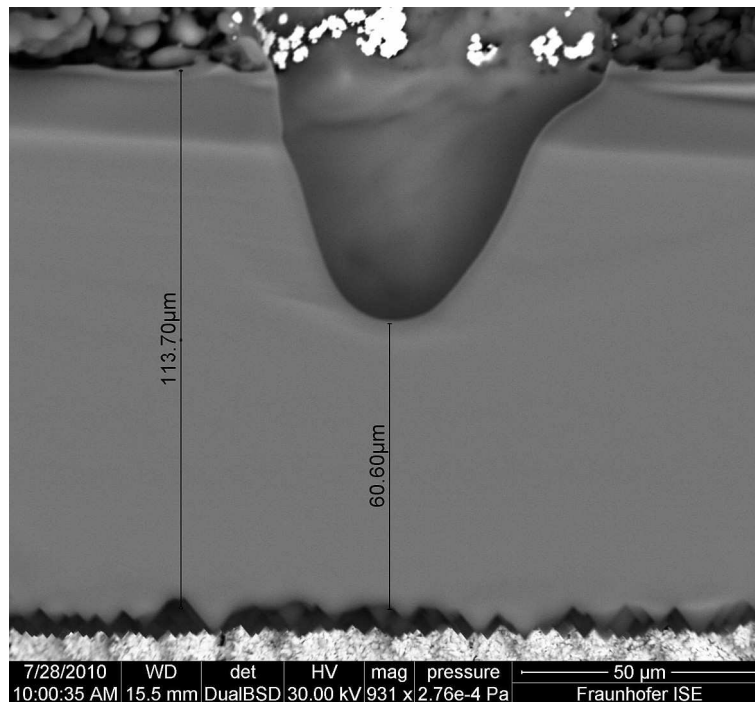
Fig. 4:32 Cross section of the solar cell adopting passivation B in correspondence of a LFC point. The solar cell is sunny face down. The measurements show a high penetration of the laser.

The images can be compared to a similar measurement performed on SiNTOx passivated cells (see Fig. 4:5).
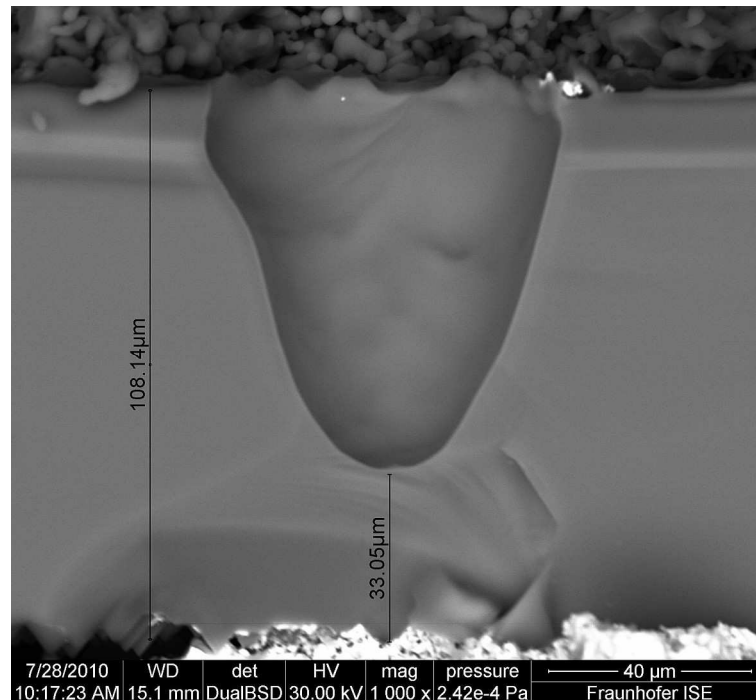
Fig. 4:33 Image similar to Fig. 4:32, although adopting passivation D. The measurements show an even higher penetration of the laser. Also in this picture the solar cell is sunny face down

As mentioned above and shortly recapitulated in Fig. 4:28 b), the resistance limiting the recombination is influencing the peak position while a higher J_{0H} increases the peak height. More detailed analysis (McIntosh) showed that also an increase J_{0H} can slightly move the peak.

A deeper crater imposes a larger local saturation current, for this reason this can lead to a higher J_{0H}. It can be noted that higher penetration corresponds to the lower *FF*. This supports the hypothesis that RLRC are located in correspondence of the crater. Furthermore, by looking at the peak position we can conclude that if the pitch is similar between SiNTOx and the SiriON CaTS the limiting resistance is similar. An interpretation of this fact is that the emitter is representing the resistive limitation for the local recombination points.

Conclusions

The identification of the bulk influence on *FF* had the only goal to understand if it represented a strong limitation. Using better material is already a priority of device fabrication.

The processing improvements concern the metallization technique of the front on lowly doped emitters, this matter can actually deliver up to 1 % absolute gain in *FF*. Furthermore, a gain of up to 1.5 % could be obtained from a better conceived rear contacting technique.

Effects on the edges are also a strong limitation, withal, to the author definitive alternative is unknown to avoid the problem aside from the complete removal.

4.8   Alternative solution for the soldering pads

The solar cells built within this work present a continuous layer of aluminium on the back surface. This back surface metallisation cannot be easily soldered. Therefore, it hinders the integration of such devices in modules. On the other hand, by reducing the aluminium coverage in favour of soldering pads, a decrease of performances (especially with thin solar cells.) is

expected (see Fig. 4:34). To maintain high performance and to allow a flexible integration in classical solar modules, an investigation into alternative soldering options was conducted.

The so called "Solder Pads" are areas on the back surface where the cell can be soldered to ribbons (tabs) and therefore can have an ohmic contact to other cells when encapsulated in a module. With a screen printing technique pads are implemented with AgAl paste as described briefly in 3.2.

Adhesion issues between the substrate and this AgAl paste impose deposition schemes as described in the illustration A and B in Fig. 4:35. These implementations limit the BSF areas in standard industrial implementation. In the case of PERC cells, they increase the metal coverage on the cell. Actually, such AgAl paste contains glass-frits which are also present in Ag front side paste. In that compound they are meant to etch the ARC coating to let the silver in contact with the silicon surface {Schubert 2006}. In the AgAl mixture, they dissolve the back surface passivation, since it is also based on Si-N bonds. Additionally its composition is not suitable for Al BSF formation. Local increase of surface recombination velocity is therefore expected where the paste is printed. For this reason the S_{eff} of the entire back surface increases as well.

In a direct comparison between 120 μm thick PERC cells with and without soldering pads (Fig. 4:34) the significant drop of open circuit voltage is directly passed to the solar cell efficiency.
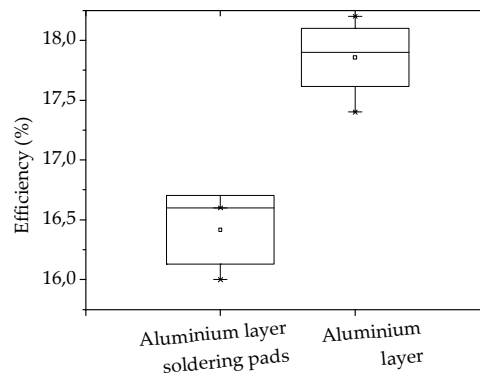
Fig. 4:34 Box-Wiskers plot representing the solar cell efficiency of two groups. In addition to the processes performed on the group on the right, the group on the left was screen printed with AgAl paste to form soldering pads. The difference between the two efficiency levels is significant. From these results we observe these pads compromising almost entirely the effort of PERC structuring on silicon wafers. The results are a comparison of cells realised during the experiment showed in 4.2.

The contacting scheme C of Fig. 4:35 would allow a larger BSF area and therefore a better passivation at the backside.

Samples were prepared to test the ideal configuration. Since it is a proof of concept approach the final quality of the cell is not a critical result. For this reason a conventional processing on low quality material (p-type mc-Si, $\rho = 0.2 \div 0.5\,\Omega\cdot cm$, full square, 156 mm side, 200 mm radius, 210 μm starting thickness) was performed.

Paste producers delivered to our laboratory prototypes that could have been good candidates to implement the scheme C of Fig. 4:35. These were classified in type 1 and type 2, the first had a procedure for its application totally similar to commercial AgAl pastes, the second instead needed a different procedure (see Fig. 4:36).

Aside from the soldering pads, transfer length method (TLM) structures were printed; though on such high-sheet conductivity material (Al) meaningful measurements were doubtful. Their implementation was anyway unproblematic and they represented a pre-emptive move in case of incurrent limiting factors. Finally, they stayed unused for this part of the experiment.

Pastes of type 2 are not intended to undergo the normal co-firing sequence (Fig. 4:36), instead their application was meant after the complete solar cell process. Except pastes of type

2, which were both printed and dried after firing, all the others fell literally off during the processing.
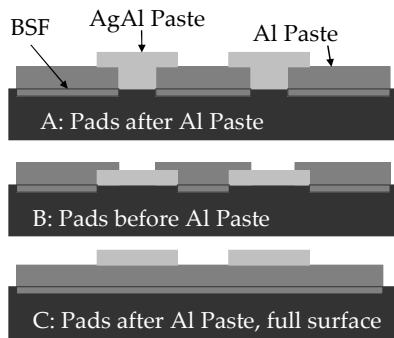
Fig. 4:35 In this picture an out of scale sketch of the back surface metallisation is presented, the three diagrams show the metallised back surface turned up. The metallisation schemes allow an effective soldering of the solar cell. Variant A and B represent normal industrial implementation.
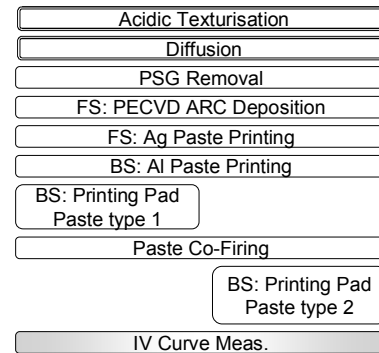
Fig. 4:36 Conventional processing for the realisation of a standard solar cell (Fig. 3:3), double lined boxes represent steps performed in an industrial line. The Printing box takes into account also the drying of the paste. Precautions were taken during the printing of the paste containing copper.

Of interest is the ohmic contact that the printed paste can create with the aluminium layer. The impact evaluation of this resistance was done directly on the realised solar cell. The series resistance was obtained from the two diode model fit on the JV1Sun. This resulted in a slight resistance increase after the printing and drying of the two candidates, the series resistance increased within a maximum of 4%, which is not enough to affect significantly the *FF*.

The investigation resulted in the establishment of a route for the solderability of completely aluminium covered back surfaces. The required additional step is characterised by processing settings that are safe to incorporate in the cell fabrication, for example, the curing temperature of the paste is well below 200 °C.

4.8.1   Integration in a module

As was mentioned in 4.8, the pastes of type 2 deliver a good contact between the Al layer and the topmost part of the printed pad. These results were satisfying and brought motivations for a soldering test and further characterisation (Fig. 4:37 a).

Tin plated copper ribbons (tabs) are soldered to the soldering pads bringing them in contact and increasing the temperature up to 300 °C; a solder joint will then be created. Different soldering configurations and solder pastes were tested. The soldering test requires strength of adhesion between solder pads and tabs to attain a certain level while the tab is ripped from the wafer.

During this test only one paste resulted positive. The paste was able to present a reaction force to pulling able to satisfy the minimal requisite of 2 N (Fig. 4:37 b), the soldering parameters were therefore accepted and used to produce a mini-module[39] with 3 cells in series. The stability in time of the mini-module is investigated below.

---

[39] A mini-module consists of a few cells, compared to a commercial one. The goal is to show feasibility with a reduced set of cells.

a)

b)
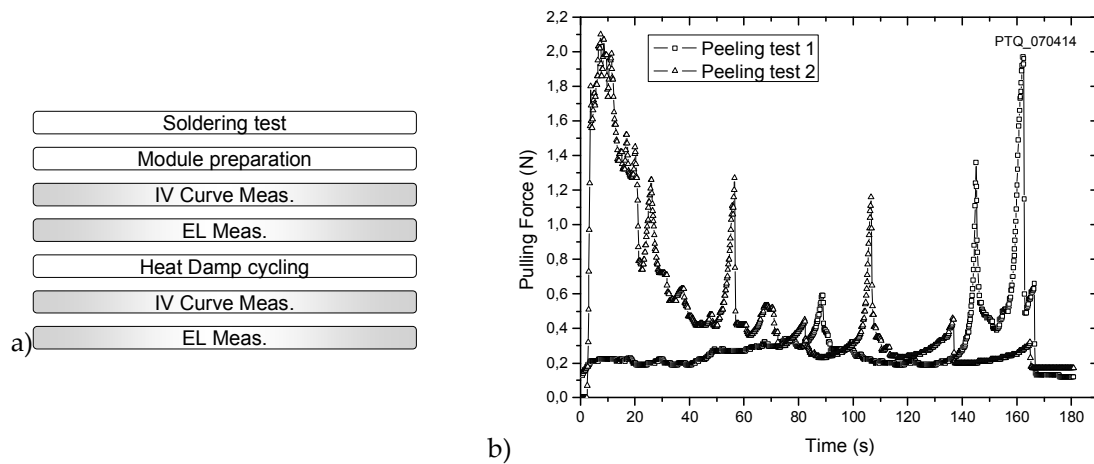
Fig. 4:37 a) Characterisation scheme of the realised module. b) Tearing force for the soldered tabs. The pulling force reaches 2 N.

The cells were selected to have a similar current under short circuit condition, due to the low availability a perfect match was not found (see Table 4—17).

Table 4—17 Characteristics of the three cells used to build the module

V_{OC}	J_{SC}	FF	η
(V)	(mA/cm²)	(%)	(%)
0,605	32,5	69,0	13,5
0,601	32,4	72,6	14,2
0,599	31,8	72,4	13,8

The mini-module was then measured (see Table 4—18), on its low *FF* two comments need to be mentioned:

1. From one cell to the other, in this string configuration, the increase of the electrical path of the current shows as resistive losses, this lead to a loss in *FF*, this loss is common to every module and it is proportional to the number of cells encapsulated.

2. The mini-module is a replica of its bigger brothers. As them, it has terminals electrically connected to the inner string of devices. These terminals represent also a resistive path. Since modules are implemented by series of solar cells, the level of the current is the same as the one of one single cell. Therefore, the loss on these terminals, which see always the same current independently from the number of cells, is a fixed voltage drop. This voltage drop has an effect on the efficiency which is inversely proportional to the number of cells in the module. This also results in a *FF* loss, in our case this loss is almost at its maximum.

For the stability of this new metallisation technique to be confirmed, the mini-module undergoes a Damp Heat test[40]. JV1Sun curves were taken before and after the test. Furthermore, electroluminescence images were acquired (Fig. 4:38).

---

[40] The Damp Heat test is performed in a climatic chamber. In this chamber the temperature and the humidity are kept to a constant level for 1000 h. The levels are respectively 85°C and 85%.
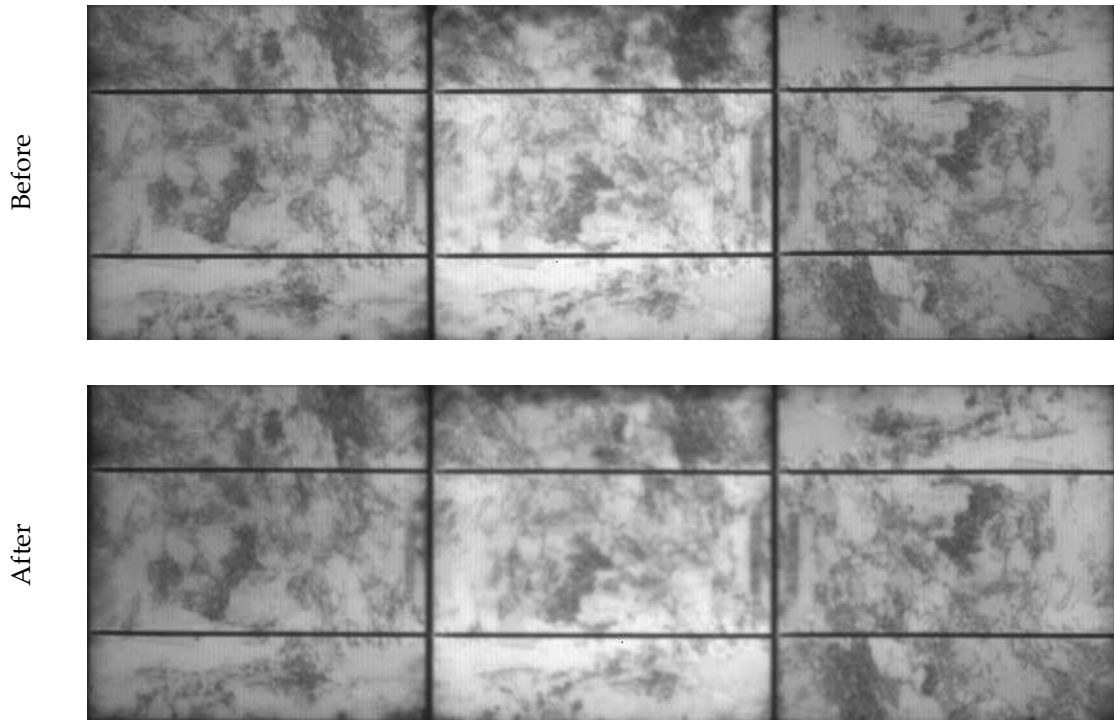
Fig. 4:38 Using Electroluminescence measured before a) and after b) the Damp Heat test. The difference of the aligned images does not put in evidence the copper paste structure that were printed on top of the aluminium (i.e. 4 mm wide pads, 4 TLM structure on the edge of the cell.), which indicates that the metal could not diffuse through the paste and contaminate the silicon bulk.

The IV measurements do not show any substantial difference, all the variations are within the uncertainty. One effect which finds justifications from a naked eye analyses is a reduction in current. Dirty traces were found on the module from the test (dried water drops).

Table 4—18 Measurements were taken under the IEC 60904 standard.

Label			Unit	Deviation
Open-circuit voltage	1,803	1,8	V	-0,17%
Short-circuit current	7,92	7,89	A	-0,38%
Maximum output voltage	1,278	1,28	V	0,16%
Maximum output current	7,04	7,08	A	0,57%
Maximum output power	8,99	9,08	W	1,00%
Fill Factor	62,9	63,8	%	1,43%
Aperture efficiency	12,3	12,4	%	1,00%
Measurement uncertainty for the power value: ±		5	%	

The test is therefore positive; one of the pastes can effectively work as a surface for soldering on aluminium covered backsides.

The candidate paste composition has a high amount of copper; therefore special attention has to be taken to prevent contamination[41]. Although this possibility of contamination, the EL image did not show any evident degradation after the heat damp test, especially, observing where the copper paste was printed, no trace could be found.

A complete coverage of the back surface with aluminium does not present a problem for the solderability; the presented procedure allows a stable and durable use of the cell.

---

[41] Copper is a highly diffusive contaminant for silicon.

Chapter 5   Attempted modelling of inversion layers shunting in PERC structures

The practical work presented above left open questions regarding the effect of positively charged passivating layers. On acceptor doped material they induce an inversion of type at the surface. Phenomena as the quantum efficiency dependency on bias light (see Fig. 4:15) or the reduced V_{OC} in the case of PECVD passivated cells (see Table 4—7) are typically observed when this inversion layer is present. In this chapter the existing models as well as a newly developed model are described. These models purport an understanding of the effects induced by the weak or strong inversion of the rear surface exploiting the interrelation of this region with floating junction configurations. Following this reasoning, the new approach targets a more quantitative analysis, closer to the working principle of a solar cell. Existing models are gathered in section 5.1 together with characterisation techniques. In section 5.2, within an experiment, we suggest that a current model based on solely geometrical inhomogeneities of passivation is not proper to explain the phenomena taking place. On this basis, the novel work is then detailed (in section 5.3). The attempted goals of this model are to propose a better discernment of the issue and an improved accuracy for the characterization. This in turn will improve the knowledge of design rules for solar cells presenting a floating junction on the rear surface. This structure is better known as passivated emitter and rear floating (PERF).

5.1   Analytical modelling

The phenomena linked to an inverted surface unfolded in several aspects of a solar cell. Two examples of observations are found in the literature. The first is related to measurements on a lifetime sample. This characterization method obtains information on lifetime probing the conductivity under injection. This measured conductivity is altered by the presence of a superficial inverted layer. Therefore an apparent lifetime is evaluated. The second instead unveils the issues of p-type silicon solar cell structures (i.e. PERC) relying on positively charged dielectric layers for back surface passivation purposes. In these cells minority carriers are supposedly captured by the inverted layer on the back surface. Additionally, these are supposed to recombine there. Below we present a summary of the models devised from these observations to take them into account.

5.1.1   Inversion layer effect on effective lifetime measurements

The described presence of an inversion layer and the consequent misinterpretation of lifetime measurements is already correctly modelled in the literature {Fischer 2003}. In his work, Fischer calculated the excessive increase of conductance of illuminated samples. These

observations were then extended to the measurements performed on a QSSPC instrument (see Appendix A.f.I). Indeed this behaviour appears in this measurement as an increase of lifetime in the low injection regime (the sample is more conductive as it is expected to be).

A similar effect, which also leads to a false lifetime interpretation, is provoked by the depletion region modulation (DRM). When stepping from dark to illuminated condition, the extension of the depleted region changes, and in turn changes the thickness of the conducting base {Neuhaus, Cousins et al. 2003}. Again a shift in conductance is observed. Considerations of these effects have been exploited for interpretation of results {Cousins, Neuhaus et al. 2004}.

These theories are helpful when using specific lifetime measurement techniques which increase S/N. Indeed, it was noticed that DRM cannot explain all effects, neither the consideration of trap levels {Cornagliotti, Kang et al. 2008}. More elaborated theories were then called for.
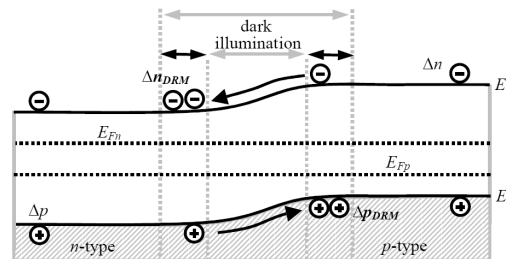
Fig. 1: Energy band diagram of an illuminated *p-n* junction at V_{oc} conditions. Excess carrier densities Δn_{DRM} and Δp_{DRM} build up at the edges of the depletion region, in addition to the excess carrier densities Δn and Δp of the quasi-neutral regions.

Fig. 5:1 The effect of the depletion region modulation is seen as additional mobile carriers that are added in case on injection (from {Neuhaus, Cousins et al. 2003})

5.1.2 Inverted surfaces in solar cell structures

The concept of inversed layers at the surface exists since the 70's as a method for passivation of back surfaces of concentrator cells. Later a simulation has been proposed {Ghannam 1991} for solar cells without concentration. The simulation is based on the large signal model for pnp/npn {Ebers and Moll 1954}. The suggestion from these simulations was gladly accepted and went under the name of floating junction passivation (FJP). Cells with this type of structure were then named passivated emitter and rear floating (PERF) cells.

Several implementations based on the diffusion of junction on the back side have been reported {Lölgen, Leguijt et al. 1994}. Implementations are still found in recent literature {Cousins, Mason et al. 2006}. The original description was also encircling the case of charges inducing a field strong enough to invert the surface. Indeed the presence of an inverted region implies a junction {Dauwe 2004}. The passivation of silicon surface using an inversion layer induced by surface charges had been successfully applied to mc-Si solar cell with improved front side structure {Morikawa, Niinobe et al. 2010; Niinobe, Morikawa et al. 2010}.

The difficulties encountered in the realisation of high efficiency concepts needed a higher degree of details in the Ghannam model. This was implemented taking in consideration the illuminated case {Wenham, Robinson et al. 1994}.
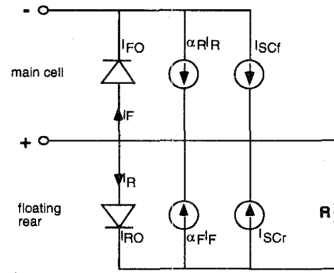
Figure 3: Ebers-Moll equivalent circuit for an illuminated PERF cell with shunted floating junction.

Fig. 5:2 Model presented by Wenham, the limitation of this model resides in the unpredictability of the component that creates the photogenerated current addressed towards the back, in the schematics this component is indicated with I_{SCr} (from {Wenham, Robinson et al. 1994}).

The claim of this model (see Fig. 5:2) is to assign to both sides of the cell (front side emitter and rear side collector) a characteristic saturation current and an injection depending on the opposite voltage and another depending on the illumination. This model is stable for the dark, since all injection depends on the potential at the extremes of the sandwiched base and distributes with the known rules (continuity equation). However, for the illuminated case, assumptions on the partition of the photogenerated light must be taken, since the generation profile is not specified. The mend applied was to fix the injection towards the back to a certain percentage of the whole photogenerated current (10 %). Although this simplification can be qualified as arbitrary, the model prediction was shown to reproduce correctly the behaviour of the solar cell device. Reduction of *FF* as well as a loss in *J*sc and *V*oc were explained through a shunt resistance at the back side junction (indicated with R in Fig. 5:2, in this work indicated as R_{shB}). Any current flowing through this resistance is indeed of detrimental effect.

This resistance (R_{shB}) is therefore located between the inverted region at the surface and a bulk potential. Local metal contacts on the back surface of the cell are indeed at the bulk potential and represent an abrupt interruption of the inversion layer. These interface perimeter can be interpreted with a good confidence as the location of this resistive path.

♦ *Numerical modelling*

The analytical model suggested by Wenham is not rigorous enough to understand which parts of the cells are tainted upon the shunting. Therefore, a group of scientists gathered their ideas few years later and presented numerical simulations of the phenomena. {Altermatt, Heiser et al. 1996}. The simulation was specifically addressed for high efficiency concepts. Furthermore, it has a section in which the potential of the different cell concepts are compared.

Later, Dauwe proposes the use of the `PC1D` tool as a middle way between the model of Wenham and the complete Altermatt's numerical approach. He manages to simulate the dependence of the External Quantum Efficiency on the shunt resistance of the rear floating junction. He states with this model that this resistance is critical for the solar cell performances.

♦ *Characterisation procedures*

The implementations of PERF structures have often reported a loss in *FF* {Aberle, Robinson et al. 1993}. The reason was identified in this loss of current through the back surface shunting resistance R_{shB}. Therefore, methods have been suggested for the characterisation of the loss mechanisms. These elaborated interpretations stem from the schematic of Fig. 5:2. The first approach proposes an analysis on the JVDark curve and a consequent calculation of the local ideality factor {McIntosh and Honsberg 1999}. The second uses instead illumination conditions {McIntosh, Boonprakaikaew et al. 2000}. This second method requires the cell to have conversion capabilities on both sides. This method therefore restricts itself to a specific cell concept. One example is the double sided buried contact cell (DSBC).

On the DSBC concept, a direct analysis of the current loss can be conducted by imaging techniques {Breitenstein, Langenkamp et al. 2000}. An interesting result is the fast propagation

of a local defect to a whole area between electrodes. This suggests that the phenomenon is intrinsically not robust[42].

5.2 Direct observation of the shunting phenomena on a designed structure

The effects of a low R_{shB} on the effective lifetime are of interest to understand when this component becomes a thread for the photovoltaic device. Therefore solar cell-like structures were prepared to expose clearly the effect. A photoluminescence technique was used to show two dimensional relative differences of effective lifetime.

BS: PECVD SiOx Capping Deposition	BS: Opening etching
Diffusion	Wet mask stripping
Sheet resistance Meas.	FS SiN$_x$ ARC deposition
HF dip	BS: Al Paste Printing
BS: PECVD Stack Passivation Deposition	Paste Co-Firing
BS: InkJet masking	LFC
	PL imaging
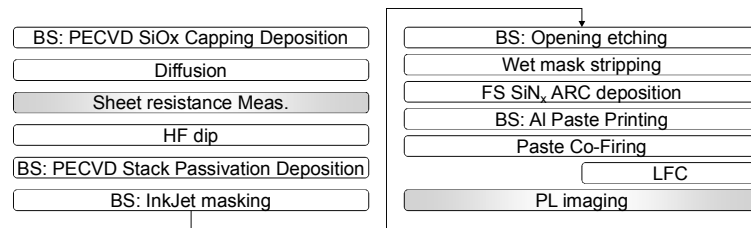
Fig. 5:3 Process to create the samples for the validation of the model.

The material (p-type FZ-Si, $\rho = 1\,\Omega\cdot$cm, pseudo square, 125 mm side, diameter 150 mm, 210 µm starting thickness) was processed (Fig. 5:3) to achieve a structure presenting a passivated emitter on the front and differently contacted areas on the back surface (See the detailed sketch in Fig. 5:4).
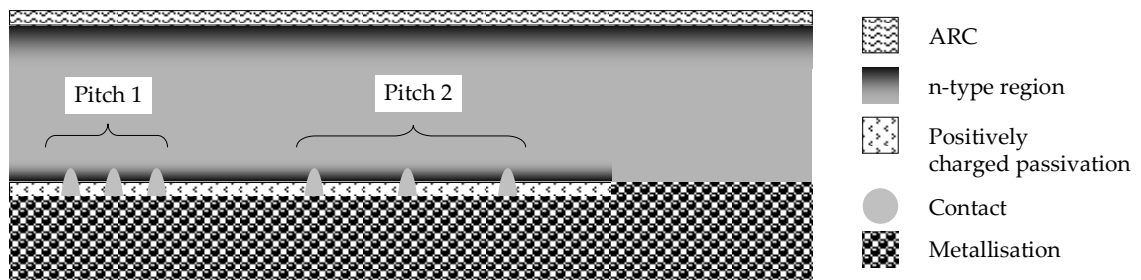
Fig. 5:4 Sample configuration, the samples contained areas presenting different contacting techniques. On the right side of the sample is represented an Al-BSF area with the metal directly in contact with the bulk silicon. On the left are instead the local contacting schemes, these can have different pitch and different creation techniques. The drawing is out of scale to enhance particular details.

The contribution of the shunted inverted region for every pitch present on the wafer rear surface can be extracted from a comparison between the photoluminescence signal on only passivated areas and passivated and contacted area (see appendix A.f.III). Also the Al-BSF areas have been investigated. Still, the scaling factor Y_{PL} is a priori unknown.

$$S_{\mathrm{invShunt}} = Y_{\mathrm{PL}} W \left(\frac{1}{\tau_{\mathrm{eff}}\big|_{\mathrm{contacts}}} - \frac{1}{\tau_{\mathrm{eff}}\big|_{\mathrm{passivation}}} \right) \qquad \text{Eq. 5−1}$$

In Fig. 5:5 an example of a measurement is proposed. Several samples have been prepared in a similar manner. Therefore, the reproducibility of the Al-BSF was exploited to normalise the

---

[42] A phenomenon would be called robust if the outcomes vary significantly only upon a strong variation of the input parameters.

wafers to a fixed value ($S = 1000$ cm/s for Al-BSF passivated surfaces[43]). This approach furthermore allowed scaling the intensity to surface recombination velocities.
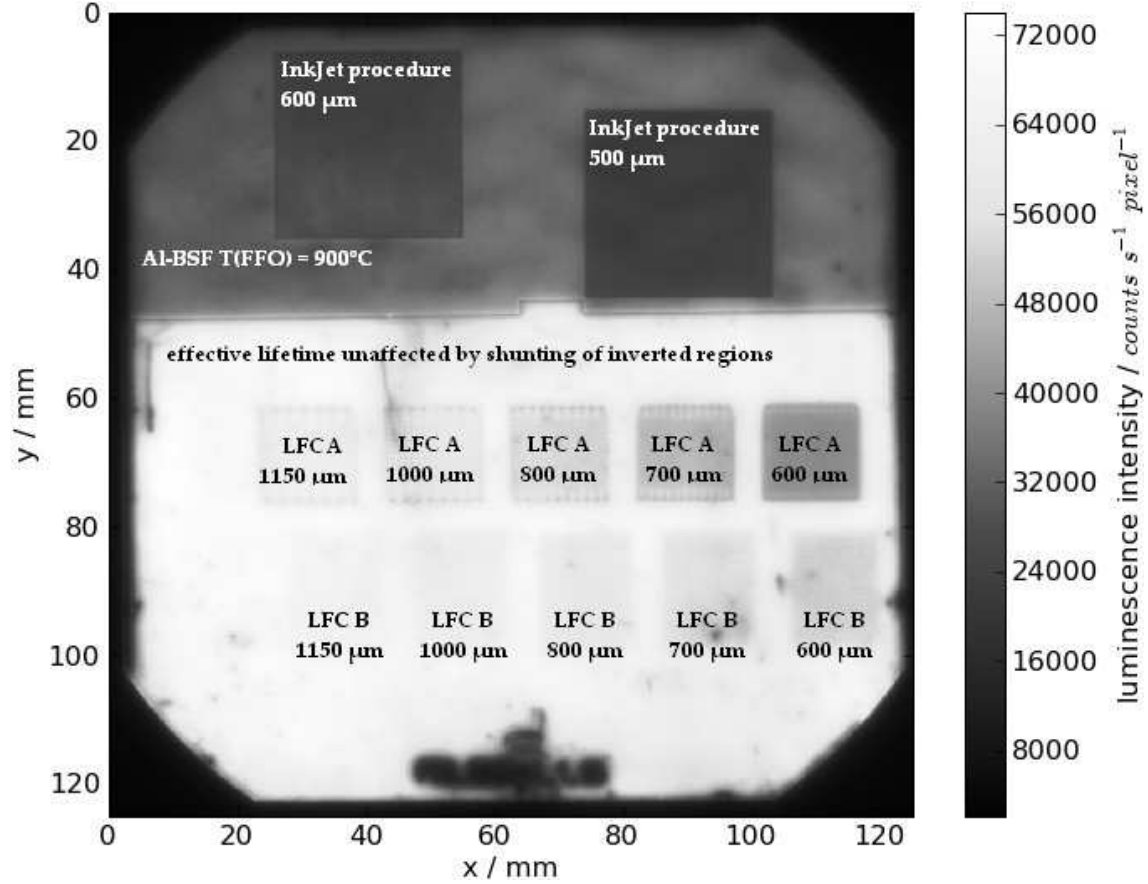
Fig. 5:5 Example of photoluminescence measurements performed on the samples

The gathered information can be now tested. Our hypothesis is that the surface recombination velocity is not only influenced by the strong difference between a passivated area and a metallized area (at the contact). Indeed, a further effect is present. This effect is as well expected to deteriorate the performances by increasing the coverage fraction.

A complete study on recombining local metal contacts distributed over passivated areas can be found in the literature {Fischer 2003}. This leads to the calculation of an effective surface recombination velocity for the passivated and contacted region. The geometry is defined by the thickness of the sample (W), the half pitch distance (r_{HP}), and the radius of the contact (r_0). From these last two the coverage fraction f is calculated.

The electrical parameters are the recombination velocity at the metal contact S_{met} and the recombination on the passivated area. These parameters are normalised to the diffusion constant of the material (D_n) and multiplied by the material thickness ($s_i = S_i W / D_n$).

$$s_{invShunt} = \frac{s_{pass}}{1-f} + \left(\frac{r_{HP}}{W\sqrt{\pi f}} \arctan\left(\frac{W}{r_{HP}} \sqrt{\frac{\pi}{f}} \right) - \exp\left(-\frac{W}{2r_{HP}} \right) + \frac{1}{fs_{met}} \right) \qquad \text{Eq. 5−2}$$

The passivation contribution of the positively charged dielectric (S_{pass}) has been already removed (Eq. 5−1), therefore in this case $S_{pass} = 0$. The radius of each contact configuration has

---

[43] This value of surface recombination is an arbitrary assumption. Although, it is in an acceptable range for this type of back surface field.

been measured and an average value is inserted. The S_{met} is varied to find an agreement being the only degree of freedom left.
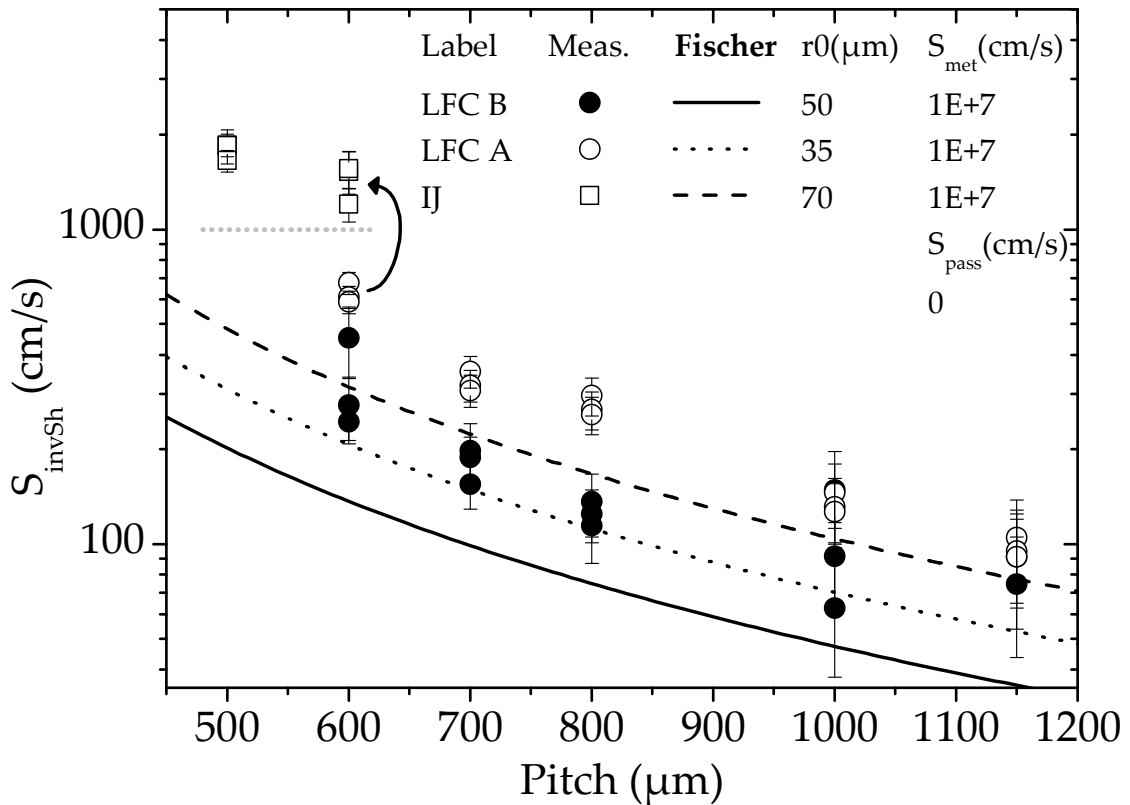
Fig. 5:6 Measured and simulated result. The simulated curves are not intersecting the observed points.

This model is tested on the extracted surface recombination velocity for each contact configuration (a maximum of three points per pitch and technique is represented with the respective measurement error in Fig. 5:6). The values have been normalised taking as reference the Al-BSF passivation effect ($S_{AlBSF} = 1000$ cm/s). The values were taken from three different realisations. The agreement between measured points of the same pitch and technique is substantial, albeit based on a simple normalisation.

Fig. 5:6 presents many interesting points of view. First: large differences are observed between the model and the measured points. Note that the surface recombination velocity of the metal contact was set to the highest physically possible value (v_{therm}). Second: the position of the points, as explained above, depends on the supposed S of the Al-BSF. By lowering this assumed S the points would shift down. However, this would not help to find a validation for the Fischer model since the distance between the measured sets is larger than the calculated one. Third: for convenience, the S_{AlBSF} level is indicated by a gray dotted line. An arrow underscores a configuration observed by comparing all the techniques: IJ, LFC, and Al-BSF. In this pitch configuration (600 µm) a metal coverage of less than 2 % can be very close to the level of complete coverage. Although, the passivated area has twice as much lifetime then the Al-BSF part (see Fig. 5:5). Furthermore, we can say that the IJ case is the technologically closest to the Al-BSF. Indeed, both profit of the high temperature step to dope the silicon (see 3.7.2). Nevertheless, the high percentage of passivation coverage let recombination happen copiously. The author concludes from this experiment that the effect of shunting, which was designed to be remarkable in this experiment, leads a surface to foster even more recombination than a Back Surface Field. By quoting the existing models, the shunted inverted area is an effective drain for the electron. Although, there is little knowledge on how a supposedly known shunting path will affect the passivation. Below the basis of this approach will be described.

5.3 Newly developed analytical interpretation of the back side floating junction passivation

The models and characterisation mentioned above emerged as explanations to the observed fill factor losses in practical solar cell realisations. Below the same motivation will lead to the creation of a multi-dimensional analytical model which explains the main mechanism of the floating junction passivation in a close-to-design environment. In order to find valid boundary conditions to the analytical model developed in this chapter an algorithm, that has to be computed numerically, was employed.

5.3.1 Sheet conductivity dependence on the amount of charges and illumination

The inversion layer, in its weak or strong condition, is conductinve. Although, it is isolated from the substrate's bulk by the depletion region (Fig. 5:7) and therefore creates a two dimensional channel where carriers can move. This conductance depends on the amount of carriers and their position. Therefore a simplified conductance calculation will be proposed and evaluated for different configurations of dielectric charges Q_f and injection. The latter can a be consequence of both bias and illumination.
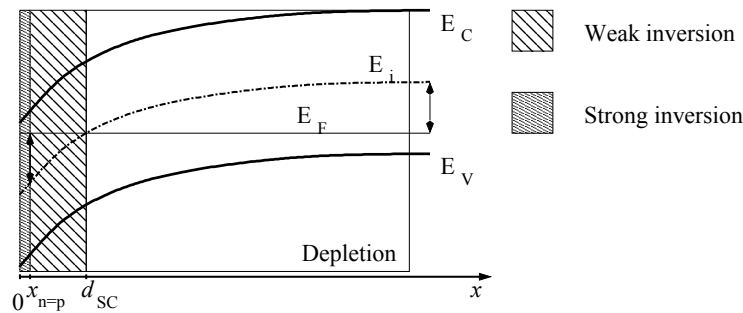
Fig. 5:7 A typical band bending situation. From the relations presented above (2.2.3) it is known that the surface can be classified under the above mentioned 4 situations (accumulation, depletion, weak inversion, and strong inversion) depending on the charge configuration on the surface. Additionally, also regions in the bulk are classified by these definitions. The layers belonging to an inversion are isolated from the bulk of the substrate by the depletion region. In turn they can have a conductance of their own. The natural two dimensional confinement of the surface allows the concept of sheet conductance (or either its inverse, the sheet resistance) as the more intuitive to characterise this electrical conductivity.

In order to allow the use of simple analytical expressions, few assumptions will be taken. The first and most severe concerns the model assumed valid for the calculation of the carrier mobility. The model assumes scattering as the limitation to mobility. Scattering depends on doping concentration. However, we impute the mobile carrier as additional sources of scattering. The expressions used for the carrier mobility calculation are common to the one implemented in in the software PC1D {Clugston and Basore 1997}. Published coefficients {Kray 2004} have been adopted.

As it was previously shown (see Fig. 2:8 and Fig. 2:9), the surface potential increases/decreases with respect to the Fermi level and the quasi-Fermi levels as consequence of external amount of charges (Q_f) and mobile carrier injection (Δn). This implies a band bending (in Fig. 5:7 an example of positive Q_f and negligible Δn on a p-type material). For the present work we are interested in all mobile carriers in an inverted layer.

In order to find these we need to know the position of the Fermi level with respect to the intrinsic energy level. From this quantity it will be possible to calculate the density of carriers which are mobile and contribute to transport. Furthermore, as specified before, we assume that

they participate to scattering phenomena. Therefore, from their density it will be possible to evaluate their mobility.

A procedure to obtain the desired quantities was already detailed {Dauwe 2004}. However the main steps are here recapitulated.

The first information that is needed is the surface potential ψ_{surf}. This information is obtained from the knowledge of the doping of the sustrate N_A, the amount of fixed charges in the dielectric Q_f and the injection level Δn (see Fig. 2:8).

With the same procedure used to calculate the electric field at the surface {Schroder 2001; Sze and Ng 2006}, it is possible to evaluate the electric field at any point in the bulk depth. Moreover using the relation between field and potential, it is possible to obtain a function P giving the position d of a certain potential ψ_d when the surface potential ψ_{surf} and the expression of the field are known for all depths.

The mobility is normally calculated using spatial considerations on the carriers involved in transport. The boundaries of the integration are the substrate's surface and the onset of the weak inversion.

$$\sigma \;=\; \int_0^{x_{n=p}} q n(t)\mu(t)\mathrm{d}t \qquad \text{Eq. 5—3}$$

The freedom of adopting this formulation (Eq. 5—3) is in this case not given. For this reason the integration domain has to be substituted with a domain in potential. Eq. 5—3 is substituted with the expressions found in Eq. 2—32.

$$
\begin{aligned}
\sigma \;&=\; q \int_0^{x_{n=p}} n_{\mathrm{p}}\mu_n \frac{\mathrm{d}t}{\mathrm{d}\tilde{\psi}}\mathrm{d}\tilde{\psi} \\[2mm]
&=\; q \int_{\psi_{\mathrm{Surf}}}^{\psi_{n=p}} n_{\mathrm{p}}\left(\tilde{\psi}\right)\mu_n\left(\tilde{\psi}\right)P'(\tilde{\psi})\mathrm{d}\tilde{\psi} \qquad \text{Eq. 5—4} \\[2mm]
&=\; q \int_{\psi_{\mathrm{Surf}}}^{\psi_{n=p}} n_{\mathrm{p}}\left(\tilde{\psi}\right)\mu_n\left(\tilde{\psi}\right)\frac{-1}{\mathcal{E}(\tilde{\psi})}\mathrm{d}\tilde{\psi}
\end{aligned}
$$

The boundaries of this integration are set as the inset of the weak inversion all the way to the potential of the surface.

When the potential of the surface is lower than the inset of the weak inversion the layer disappears and no conductivity shall be calculated. Noteworthy is to mention that the potential at the inset of weak inversion corresponds to the distance of the Fermi level from the intrinsic layer (see Fig. 5:7)

Using these boundaries it is possible to observe the dependency of the sheet resistance of the inversion layer on two different values. The first is the doping level of the bulk and the second is the amount of fixed charges in the dielectric bulk and injection (see Fig. 5:8). This latter is of highest interest for the model below.

Noteworthy in the graph is the increase of sheet resistance of the layer in case of high injection. By increasing the injection the bands flatten and the inversion vanishes. This phenomenon will be referred as pinching of the channel below.

Note that this conductance has little to do with the DRM effect and has been calculated with a different method than that Dauwe uses for his calculation of apparent lifetime (see appendix 6.2A.f.II).
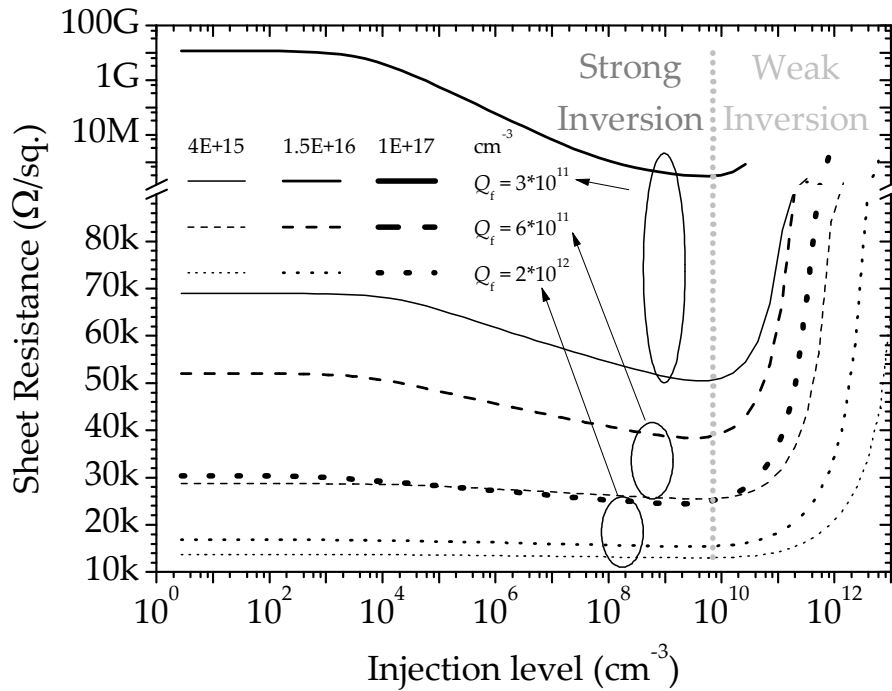
Fig. 5:8 Sheet resistance of the inverted layer, the calculations are done for the same doping levels employed in Fig. 2:8 and Fig. 2:9, namely: 4E+15 cm^{-3} (3.5 $\Omega\cdot$cm), 1.5E+16 cm^{-3} (1 $\Omega\cdot$cm), and 1E+17 cm^{-3} (0.2 $\Omega\cdot$cm). The picture shows the low sensibility of strongly doped material to the presence of external charges. Indeed, two of the three curves related to a bulk with a 0.2 $\Omega\cdot$cm resistivity result in an infinite resistance, since any inversion layer could be created. The circles entangle curves where a same amount of external charges excites the system. This is intended as a guide for the reader. The steep increase on the right part represents a pinching of the conducting channel, by reaching a depletion condition at the surface the channel disappears. Indeed, the bending of the bands decreases as a consequence of high injection. To underscore this effect the graph is approximatively divided in strong and weak inversion. The dotted gray line is almost in correspondence of the threshold of all combination shown in the graph.

5.3.2 Assignment of the injected carrier to each side of the solar cell

The electrical excitation that the injection in the solar cell is imposing on the inverted layer is of interest for this study. This quantity is obtained as the current that the base can impose on the back surface. The base is interpreted as the part of the substrate where electric fields are absent. Therefore this region is found in between the depletion region of the front and of the back.

Considering the regions in schematics, the base will be at zero potential, while the collector and the emitter will be both forward biased.
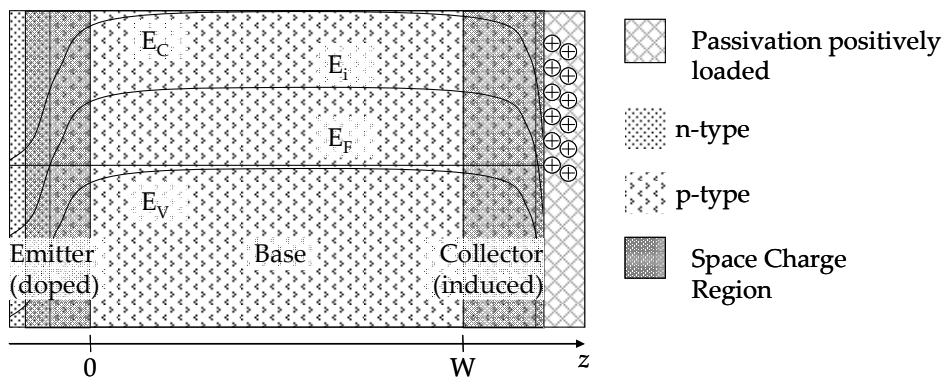
Fig. 5:9 Section of the solar cell along its thickness (z axis). The area taken in consideration corresponds to a small field (light bending of the bands). Note the change of axis in comparison to 5.3.1

Also in this case few assumptions are needed to allow an analytical treatement. The first is a completely equipotential front, which, thanks to the highly conductive emitters, typical of solar cells, is always satisfied. The second is a constant thickness, for example any roughness on the front and on the back cannot be modelled. The third is a constant generation profile over the entire depth of the solar cell. This configuration of deep infrared monochromatic light, albeit far from the reality, is a simplification worth pursuing for a better understanding of the phenomena. The fourth condition concerns the absence of impurities. Indeed, few recombinations of the SRH type are present in high quality material. This makes this assumption nonarbitrary. The fifth excludes any other type of recombination (i.e. Auger, radiative). This is partly met by limiting the analysis to lli. The sixth assumption is that the substrate extends in all directions, except z, presenting the same characteristics. This ensures the possibility of a problem solution in one dimension.
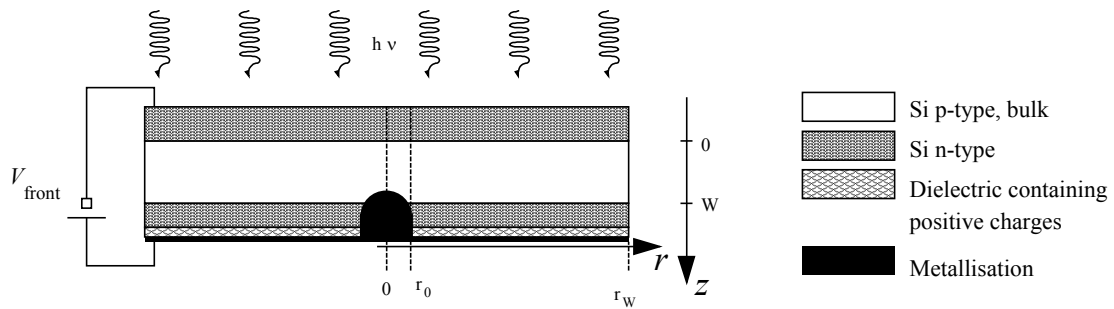
Fig. 5:10 Cross section of the system taken into consideration.

With these assumptions the differential equation derived from the continuity equation (Eq. 2—25) has an analytical solution[44].

$$\frac{\mathrm{d}^2\, n_{\mathrm{p}}(z)}{\mathrm{d}z^2} = \frac{n_{\mathrm{p}}(z) - n_{\mathrm{p}0}}{D_{\mathrm{n}}\tau_{\mathrm{n}}} - \frac{G_{\mathrm{l}}}{D_{\mathrm{n}}} \qquad \text{Eq. 5—5}$$

The solution comes with two coefficients which need to be determined with the help of the boundary conditions.

$$n_{\mathrm{p}}(z) = A \sinh\left(\frac{z}{L_{\mathrm{n}}}\right) + B \cosh\left(\frac{z}{L_{\mathrm{n}}}\right) + n_{\mathrm{p}0} + G_{\mathrm{l}}\tau_{\mathrm{n}} \qquad \text{Eq. 5—6}$$

The solution finds its parametrisation and boundary condition in the imposition of the forward voltage bias on both emitter and collector and a fixed saturation current on the front side.

The front side voltage will be indicated with V_{front}, while the voltage of the back junction will be indicated as $V[r]$. The first potential becomes one input of our calculation while the second will be consequence of the system, and in turn one of the important results. The degree of freedom (in r) indicates deliberately that this potential is not equal in one of the geometrical extensions that will be described below (see 5.3.3).

---

[44] Taking a deep infrared light, it superfluous to specify a exponential decay of the intensity. Absorption is therefore considered homogeneous on the whole bulk.

$$n(z) = \underbrace{\frac{n_i^2}{p_{p0}}}_{\text{Doping}} + \underbrace{G_1 \tau_n}_{\text{Illumination}} +$$

$$+ \underbrace{\frac{\left(\frac{n_i^2}{p_{p0}}\left(e^{\left(\frac{V_{\text{front}}}{V_{\text{th}}}\right)} - 1\right) - G_1 \tau_n\right)\sinh\left(\frac{W-z}{L_n}\right)}{\sinh\left(\frac{W}{L_n}\right)}}_{\text{Injection from voltage bias at the front junction and illumination}}$$

Eq. 5—7

$$+ \underbrace{\frac{\left(\left(\frac{n_i^2}{p_{p0}}\left(e^{\left(\frac{V[r]}{V_{\text{th}}}\right)} - 1\right) - G_1 \tau_n\right)\sinh\left(\frac{z}{L_n}\right)\right)}{\sinh\left(\frac{W}{L_n}\right)}}_{\text{Injection from voltage bias at the rear junction and illumination}}$$

From this expression it is possible to know which current the bulk will impose on the effective back surface thanks to the derivation of the density expression found.

$$\left.\frac{dn(z)}{dz}\right|_{z=W} = \underbrace{\frac{\left(1 - e^{\frac{V_{\text{front}}}{V_{\text{th}}}}\right)\frac{n_i^2}{p_{p0}} + G_1 \tau_{\text{bulk}}}{L_n \sinh\left(\frac{W}{L_n}\right)}}_{\text{Diffusion from the front to the rear}} +$$

$$+ \underbrace{\frac{\left(\left(e^{\frac{V[r]}{V_{\text{th}}}} - 1\right)\frac{n_i^2}{p_{p0}} - G_1 \tau_{\text{bulk}}\right)\cosh\left(\frac{W}{L_n}\right)}{L_n \sinh\left(\frac{W}{L_n}\right)}}_{\text{Diffusion from the rear to the front}}$$

Eq. 5—8

$$\Rightarrow$$

$$\left. qD_n \frac{dn(z)}{dz}\right|_{z=W} = J_{\text{nbW}}\left(V_{\text{front}}, G_1, V(r)\right)$$

The equations lead to an almost linear dependence of the carrier density on the distance, this is represented in Fig. 5:11.

Before entering the details of the modelling, the various curves in Fig. 5:11 will be commented, this will be useful to understand the goals of the model. As it was mentioned before, a monochromatic light is assumed. This underscores the difference between the dark and illuminated case. Notice that the current sign can be seen on the slope of the Δn curve.

The first curve is the dark condition where both junctions are forward biased (*a*). In this case the front is slightly more forwards biased. The current flows from the base to the emitter. Assuming the collector floating (except for a shunt resistance as in Fig. 5:2 R = R_{shB}), the injected EHPs at the back are either consumed by a net recombination or they split or both. In the first case, as it was seen in the REF, recombination depends on *V[r]*. Indeed the potential at the back

is linked to the injection through the law of the junction, in lli the potential $V[r]$ can be linked to the injection in the base (Eq. 5−9 from {Dauwe 2004}).
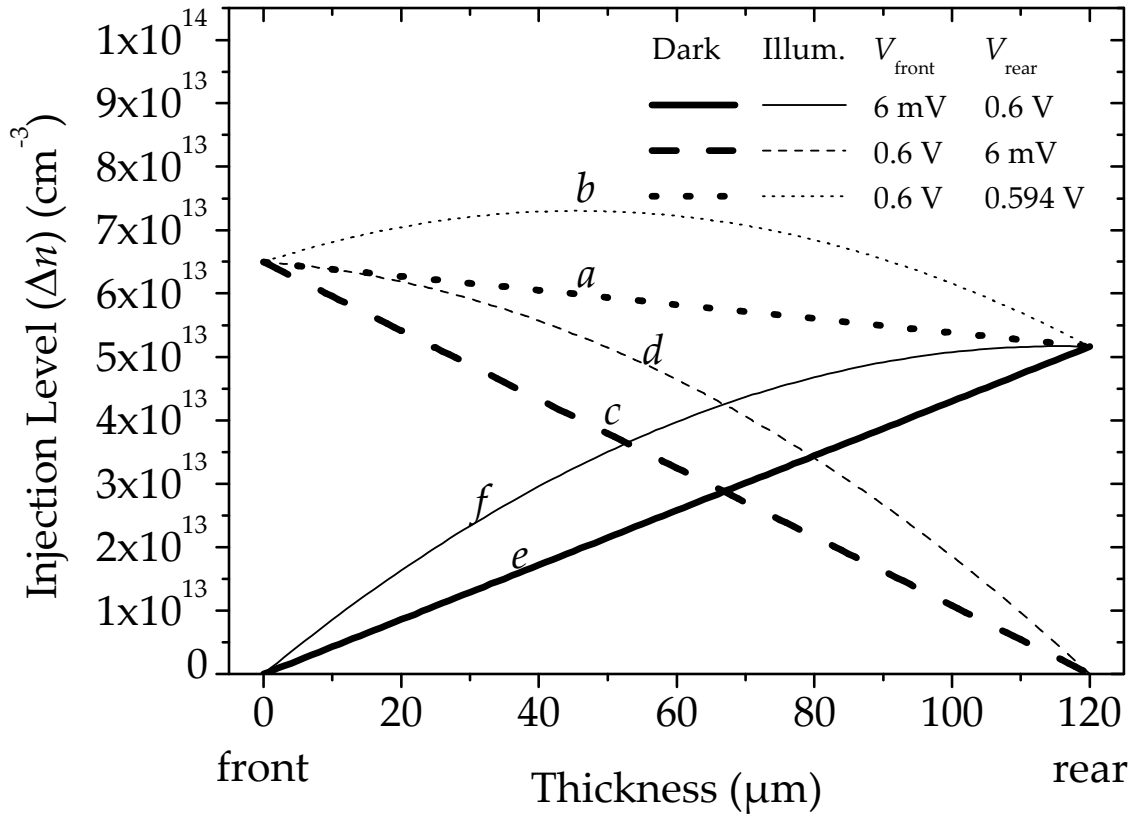
Fig. 5:11 Graph indicating the carrier density in the bulk. The letters will then be used to comment the picture in detail. The slope of the curves on the extreme right is obtained from Eq. 5−8. This quantity is proportional to the amount of current that is injected from the base to the inversion layer (collector). Notice the difference between dark and illuminated condition. The slope increases because of additional carrier diffusion. Moreover the amount of carriers at both ends is strictly related to the imposed potential through the law of the junction.

$$\Delta n\big|_{z=W} \quad = \quad \frac{n_i^2}{N_{dop}}\left(e^{\frac{V[r]}{V_{th}}} -1 \right) \qquad \text{Eq. 5−9}$$

In the second case, the electron is transported through R_{shB} to a lower potential, where it can recombine with another available hole. In all cases the collector will bias itself to attain equilibrium. When light excites the bulk (*b*), both emitter and collector receive an additional amount of EHP. This amount is able to change the sign of the current. The situation is typical of a solar cell. The collector receives an additional amount of EHPs. If its surface recombination velocity does not attain a stable equilibrium of injection and recombination, it will auto increase its potential.

The situation of *c* is a worst case situation. The collector needs a very low $V[r]$ to induce a high current in R_{shB}. Such a low potential imposes a current through the emitter strictly related to the thickness of the cell. Such a situation can present itself also when light shines (*d*). The direct consequence can be seen at the curve slope at the front. Although, first is useful to represent V_{OC} at the front in illuminated condition as a zero slope. Case *d* represents a forward bias above V_{OC}, therefore the device is a utiliser. On the other hand, case *b* is still below this voltage and represents a cell of higher potential.

Case *e* even though mathematically possible does not represent a feasible condition. The absence of injection cannot create an autobias condition. Instead in illumination condition, the autobias can raise the back potential. Furthermore, if, as in the graph the surface does neither recombine nor transport carriers away, all carriers are pushed to diffuse towards the front, fostering the J_{SC} to reach maximum levels.

From these considerations, it can be deduced that monochromatic light is a worst case scenario. The carriers can easily spatially diffuse to the collector. The advantages of a separation in space of net generation and net recombination, taken into account by Wenham by supposing a mere 10% of light exciting the back, are not granted.

One limit of this analytical expression is the insensibility of the physical limit of carrier mobility. This limit, represented by the thermal velocity, will be verified a posteriori on the calculated values of surface recombination velocity.

5.3.3   Potential and current flow in the inverted annulus region

The inversion layer is now characterized by a sheet resistance and a biasing current. Once its geometrical extensions are defined, it should be possible to gain knowledge of all the potential and current present in every point.

The geometry of the system reflects a PERC type structure. The bulk is locally contacted and the surface between these contacts is passivated. Furthermore we specify the distribution of the contact to lie on the corners of adjacent equilateral triangles with the same side length (see Fig. 5:12).

This configuration allows a first safe assumption, which is in fact an approximation. The area around a contact, which repeats symmetrically per every contact, will be assumed circular instead of hexagonal. The radius of this circle will be assumed to be the half of the distance between two contacts. Another geometrical constraint is the radius of the contact. This is taken from practical realisation and fixed to 30 µm. After these definitions, the model will take in consideration a plane ring.
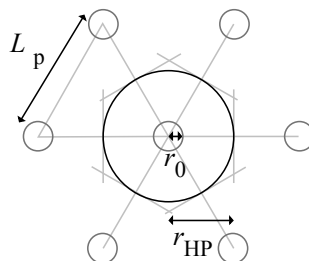
Fig. 5:12 The region belonging to each contact results similar to a circle or radius equal to the half of the pitch. The treatment calls an inverted annulus region or ring the area between the circle of the contact circle and the circular inverted region that the contact influences directly.

The ring is excited by the current bias of the base and will build up a potential while electrons are transported. This potential will be named $V[r]$. The law of the junction forces this potential to be exactly the same potential biasing the back junction (collector). It was seen above (Eq. 5—8) that the rear potential $V[r]$ and the biasing current are related in the bulk. The additional electrical condition imposed by the resistive path in the ring will therefore be met under the condition of agreement with the potential and current in the bulk.

The mathematical description of the problem will shed light on the last paragraph. The first relation will concern the increase in rear voltage for every dr in the ring. This equation, taking an assumption of negligible current crowding, has only one dimension in force of the ring circular symmetry.

$$dV(r) = \frac{\rho_{\text{Sheet}}}{2r\pi} I_\varrho(r) dr \qquad \text{Eq. 5-10}$$

The increase is proportional to the product of the sheet resistance of the layer and the amount of current flowing from the exterior ring through the dr ring. For the rest of the model a fixed sheet resistance for all the injection levels will be taken. The value introduced will be the minimum of the curve traceable once the details on the substrate and on the dielectric are known (see 5.3.1 and Fig. 5:8). This will guarantee a simplification of the expression and a safe overestimation of conductance effects[45].

The condition on the current in the ring recalls Eq. 5-8, the current gathered in a dr of the ring is a result of the front bias, the injection level and of the voltage characteristic of the dr ring.

$$dI_\varrho(r) = 2r\pi \cdot \left(-J_{\text{nbW}}\left(V_{\text{front}}, G_1, V(r)\right) + J_s\left(S_{\text{it}}, S_{\text{SCR}}, V(r)\right)\right) dr \qquad \text{Eq. 5-11}$$

The term J_s represents any possible current loss due to a recombining surface (S_{it}) or any recombination taking place in the space charge region (S_{SC}). All currents of electrons that recombine before taking part to the transport in the ring are excluded by this term. Additionally, its dependence on the injection, especially important for the case of SCR recombinations, is introduced through the local potential $V[r]$ (see also Eq. 2-20).
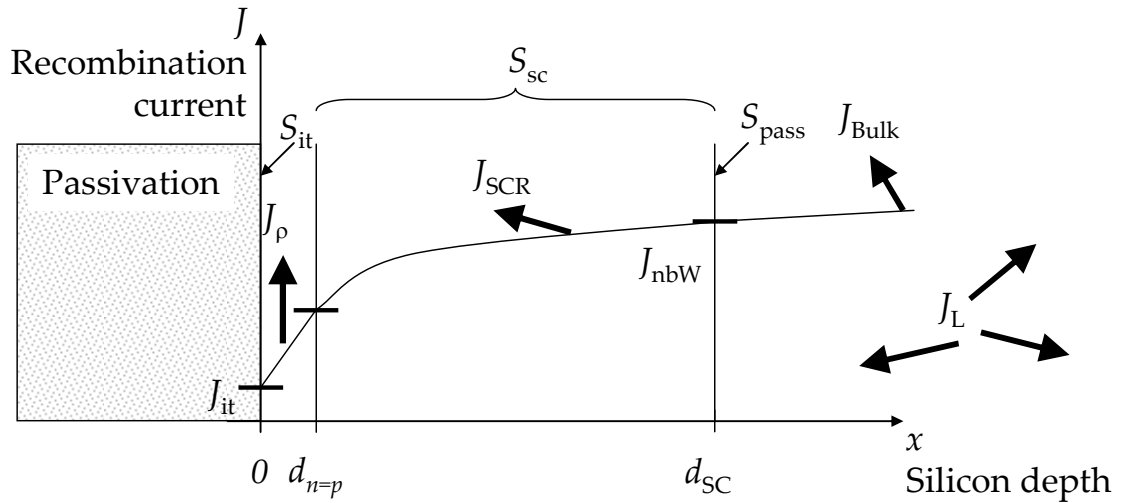
Fig. 5:13 Sketch similar to Fig. 2:7. Here the additional current J_ρ figures as the part of the current which is entering the channel. The total amount of carrier injected is represented by J_{nbW}. The arrows represent flows of electrons.

The signs in the equation follow from the conventional definitions of the bias of the cell. Since electrons diffuse from the bulk towards the ring, the current is conventionally interpreted as negative. On the contrary "disappearing" electrons, due to recombination, are modelled with a positive current.

---

[45] The increase of sheet resistance for high injection level will contribute to a self pinching of the channel. This is a beneficial effect since the working point of the region is moved to higher potentials.
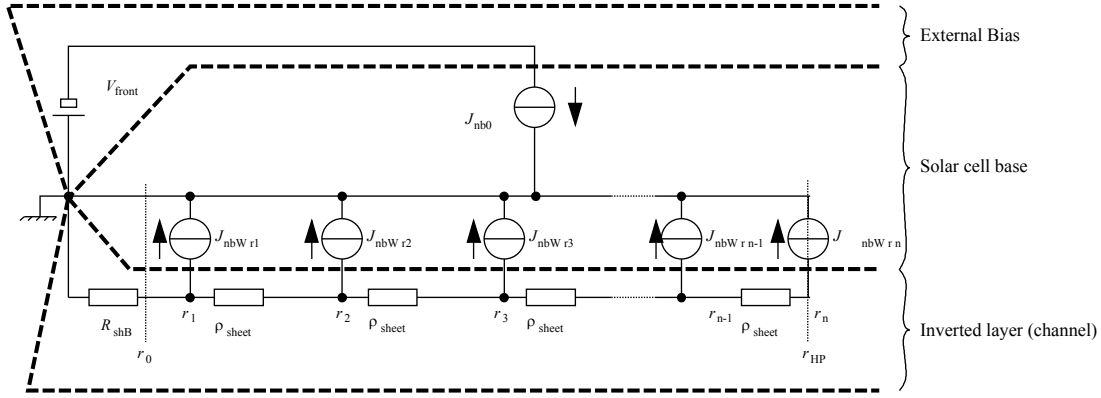
Fig. 5:14 Schematics valid for a p-type cell with an inverted back surface. The biasing current in every r_i point is obtained with Eq. 5—8. This sketch helps to understand the nature of the scattered parameters. The mathematical description used in the text will follow the description in this graph. J_{nb0} represents the current that diffuses towards the front. Instead $J_{nbW\,r\_}$ represents the flow of electrons diffusing towards the back surface for each point r_i. The carrier distribution starts at $r = r_{HP}$, which is the middle point between two contacts. These electrons will flow to a point of lower potential (the cathode of the solar cell, connected to ground) which is represented by the local contact of radius r_0. The arrows in the picture indicate current flow, electron flow is therefore reverse. The picture presents as well the input voltage V_{front} and the lumped parameter resistance R_{shB}.

The two equations (Eq. 5—10 and Eq. 5—11) can be solved in one second order differential equation (the expression can be found in current or in voltage).

$$V''(r) + \frac{V'(r)}{r} = \rho_{\text{Sheet}}\left(-J_{\text{nbW}}\left(V_{\text{front}}, G_1, V(r)\right) + J_S\left(S_{\text{it}}, S_{\text{SCR}}, V(r)\right)\right) \qquad \text{Eq. 5—12}$$

This problem definition took inspiration from a similar treatise {Chen and Dimitrov 2007} used for the characterisation of ultrashallow junctions. However, in their thinking the local relation between current and potential were defined linearly. The solution of the obtained second order equation was a superposition of Bessel functions. In this specific case (Eq. 5—12), the introduction of an exponential dependency (Eq. 5—11) results in a differential equation without known direct solutions.

Noteworthy is to mention that the current injected from the base is not constant over the distance r. This special case would allow an easier treatment. Indeed it would be possible to define a single equivalent resistance for the whole system. The study of the equivalent resistance of a ring under constant current bias was of interest for a particular cell structure and is therefore documented {Hall and Soltys 1980}.

5.3.4 Scaling rules and passivation effects

The further description of the system will profit from the adoption of scaling rules. First will be the normalization of the voltage to the thermal voltage, for second the thickness of the base will be normalised to the diffusion length of the substrate and third a current will be defined as depending from the substrate characteristic and thickness.

$$v(r) = \frac{V(r)}{V_{\text{th}}} \qquad w = \frac{W}{L_{\text{Dn}}} \qquad U_{\text{brec}} = \frac{qD_n}{L_{\text{Dn}}\sinh(w)} \qquad \text{Eq. 5—13}$$

A good approximation for the behaviour of a passivation based on a floating junction is represented by a diode {Dauwe 2004}. Therefore, the model will implement an ideal diode of saturation current J_{0c} instead of the more complete J_s expression of Eq. 5—11.

$$J_S\left(S_{it}, S_{SC}R, V\left(r\right)\right) = J_{0c}\left(e^{v(r)} - 1\right) \qquad \text{Eq. 5-14}$$

5.3.5 Rigorous definition of the problem: boundary conditions and solution

Inserting the expression of the biasing current on the ring, we can obtain an equation which describes the system.

$$v''\left(r\right) + \frac{v'\left(r\right)}{r} = K_2 e^{v(r)} + K_1 \qquad \text{Eq. 5-15}$$

The expression can be summarized factorizing every term with respect to the rear potential $V[r]$. The collected terms are called K_1 and K_2. These terms depend on the input to the system (material doping (D_n), amount of external charges (ρ_{sheet}), diffusion length (L_{Dn}), illumination (G_L), and front side biasing (V_{front})).

$$\frac{K_1}{\rho_{sheet}} = -J_{0c} + U_{brec}\left(G_l \tau_{bulk}\left(1 - \cosh\left(w\right)\right) + n_{p0}\left(1 - e^{v_{front}} - \cosh\left(w\right)\right)\right)$$

$$\frac{K_2}{\rho_{sheet}} = J_{0c} + U_{brec} n_{p0} \cosh\left(w\right) \qquad \text{Eq. 5-16}$$

The boundary conditions are strictly related to the resistive path towards the metal contact. Indeed, this contact region has a potential equal to zero. It is the cathode of the cell which imposes this condition.

$$v\left(r_0\right) \cdot V_{th} = I_{\varrho tot}\left(r_0\right) \cdot R_{shB} \qquad a)$$

$$v'\left(r_0\right) \cdot V_{th} = I_{\varrho tot}\left(r_0\right) \cdot \frac{\rho_{Sheet}}{2r\pi} \qquad b) \qquad \text{Eq. 5-17}$$

The inverted region is electrically connected to the metal contact by a lumped resistance (R_{shB}) (Eq. 5-18 a). This lumped resistance and the sheet resistance assumed for the whole ring imposes conditions on the voltage value and on the voltage derivative at the innermost circumference. The current flowing from the ring towards the metal contact will create a drop of voltage proportional to the resistance R_{shB}. Furthermore, the slope of the voltage in r_0 will be equal to the product of the current value and the sheet resistance of the inverted layer (Eq. 5-18 b).

One convenient relation between the boundary conditions is the total current extracted by the ring from the base. This term, defined as the integral of J_ρ along the distance r, starting from the outermost circumference to the metal contact, is named $I_{\varrho TOT}$. Both absolute value and derivative of $V[r]$ are expressed in terms of $I_{\varrho TOT}$ (see Eq. 5-17).

♦ *Fourier series*

The goal of proposing design rules for PERF structures has to take into account that dozens of thousands of local contacts can be present on the back of a solar cell. An adequate approach to look for a solution is to impose periodicity of the solution. Applying Fourier series would originate all the possible solutions, to the cost of an increased complexity of the solution of the differential equation (Eq. 5-15). For this reason a different approach will be chosen.

♦ *Definition of a particular solution*

Any value of $I_{\varrho TOT}$ will lead to the respective solution for $V[r]$. However, it is given by design that the outermost circumference neighbours with an exact same reproduction of the studied

region. This vicinity imposes symmetry conditions. Therefore, the potential must have a derivative equal to zero (Eq. 5—18 c).

$$v'\left(r_{HP}\right)\cdot V_{th} \;=\; 0 \qquad\qquad c)$$

<div align="right">Eq. 5—18</div>

The solution is included in the set of solutions that a Fourier series would propose. Nevertheless it is not excluded that a rigourous Fourier series would give different results.

♦ *Analytical solution*

The problem as it is set, and to the best knowledge of the author, does not have a solution (an attempt to find an analytical solution through some approximation is presented in the appendix B.b). The advantage of an analytical solution is worth some sound simplification. A treatment in this regard in under preparation.

5.4   Solving numerically the equation

The Eq. 5—15 can be solved numerically. This gives an insight on the rear potential curve $V[r]$ and the consequent distribution of the current. From these two values the effective surface recombination velocity can be calculated. This value is helpful to evaluate the passivation of the rear and compare it with other structures.

However, on the ring we find for each circumference different values of potential $V[r]$ and different current densities. For this reason it is necessary to average the contributions. The average term of minority carriers is an adequate term, as supported from a work of recent publication {Saint-Cast, Wolf et al. 2010} and can be calculated as the integral of Eq. 5—9 on the ring, normalised by the area of the ring. For the current the $I_{\varrho TOT}$ can be used when also normalised to the ring surface.

$$S = \frac{J_{invTOT}}{q\left\langle \Delta n\big|_{x=d_{SCR}} \right\rangle}$$

<div align="right">Eq. 5—19</div>

The average S is obtained from the definition of surface recombination velocity (Eq. 5—19).

As it was mentioned above, the results are valid only if the S value is below the limit of thermal velocity (v_{therm}). Even when this first condition is satisfied, regions of the annulus can present local values of S above v_{therm}. This happens because generation occurs also at the back surface. This makes the calculations less trustworthy for quantitative analyses on real solar cells. However, this imprecision of the model could be neglected for a first interpretation of the results. Later, suggestions on how to mend this issue will be given.

In Fig. 5:15, three bias conditions under constant illumination at long wavelength ($\lambda_m = 1100$ nm) are presented. Each imposes on the annulus a different current bias.

Before reporting the small differences between the three bias situations, common features will be detailed.

The first observation is on the reduction of S in correspondence of high values of lumped resistance R_{shB}. Indeed, in these settings, a high potential $V[r]$ is obtained even for low amount of current escaping the back ($I_{\varrho TOT}$). Furthermore, increasing the distance between two contacts the innermost circumferences will receive more current. This could saturate the channel before the half pitch distance is reached (see Fig. 2:12).

The condition of saturation is found at a certain distance from the center. At the corresponding circumference the potential in dark is almost equal to the potential of the front side V_{front}. In the illuminated case the voltage has a higher saturation voltage (V_{ocRear}) which depends on the passivation quality (evinced by J_s). This condition is beneficial for the cell, especially if the corresponding radius is small compared to the half pitch (r_{HP}). Indeed, the benefit comes from the increased area subject to a higher band splitting.
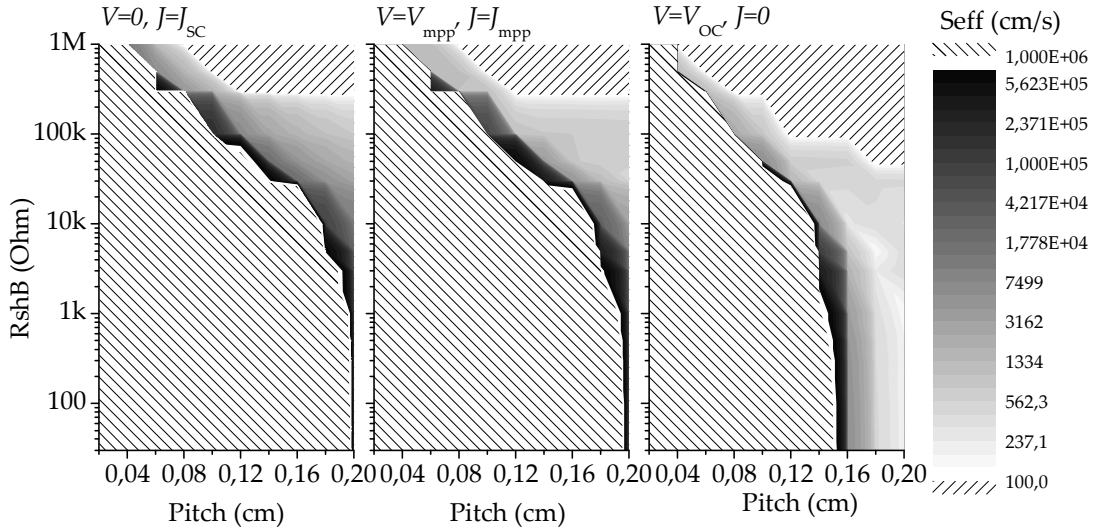
Fig. 5:15 The results of the simulation. The details are: $N_A = 1.5E+16$, $J_{0c} = 0$, ρ_{sheet} 50 kΩ and thickness $W = 120$ μm. Illumination: monochromatic source ($\lambda_m = 1100$ nm) with intensity able to generate 40 mA. The solar cell does not take into account any resistive loss on the front side cell. The areas indicated below 100 cm/s reported absence recombination, therefore in those cases any potential effect of a passivation will be seen in full. Areas above the thermal limit v_{therm} have been neglected. These regions are behaving like perfect electron sinks.
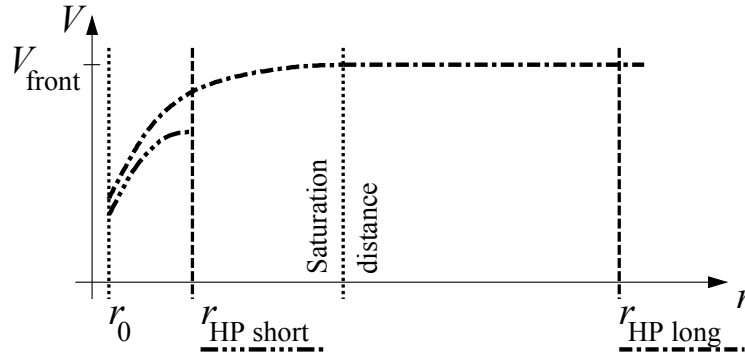
Fig. 5:16 Voltage distribution for a short half pitch distance and a long half pitch distance. The length adjective referes to the saturation distance which depends on the resistivity of the channel and the bias of the solar cell. Notice that although under the same illumination condition a small r_{HP} delivers a lower potential along the annulus.

In terms of S (see Eq. 2—22), albeit the average minority carrier density increases when larger areas of the ring reach saturation condition, a limit is attained. In dark this limit is V_{front}, instead in illumination it results as V_{ocRear}. On the other hand, the term of current is constant. This is the reason of a slower decrease of S for low channel shunting and high pitches.

After these remarks we can observe the difference between the illuminated front bias conditions proposed (see Fig. 5:16).

For short circuit conditions the potential at the front is lower than any potential building at the back side. For this reason only additional injection (by illumination) can bias the annulus in current (see Fig. 5:11). However, the positive interaction of large R_{shB} and large r_{HP} values can indeed result in saturation and even make this happening very close to r_0. This leads to low S.

In the case of maximum power point conditions the two junctions are disputing on the current, especially if the generation is constant through the bulk[46]. Therefore already a greater

---

[46] This is the case in the drawings of Fig. 5:15

part of the current can bias the back, lower values of R_{shB} and r_{HP} can lead to satisfying passivation.

The open circuit condition shifts all the generated current towards the inverted region (the model does not take into account bulk recombination). The splitting of the quasi-Fermi levels is at its maximum and therefore a larger set of conditions offers low recombination velocities.

The two graphs of J_{SC} and MPP resemble from close. Instead, the V_{OC} condition offers a larger area of low S. This is an explanation of the reduced FF in combination with low R_{shB} or small r_{HP}.

Although a numerical approach, this method allows a view on the main parameters and how they exactly take part to the recombination. However, these conclusions above were achieved also previously {Altermatt, Heiser et al. 1996}. Nevertheless, in this case they are related a to design variable, and can therefore predict what will be the behaviour of a floating junction passivated cell.

The inquired quantitativeness will be addressed in a later publication.

In the outlook a suggested approach will provide acceptable assumptions towards a more quantitative approach.

5.5 Outlook on inversion channel modelling

The need for a tool able to help the characterisation and the design of PERF structures is present, especially in view of the high level passivation that can be achieved with nitride layers.

The model proposed here is still under evaluation. However a large set of questions can be already answered. The compromising of the passivation with decreasing distance between local contacts is now related to both the shunting but also the coverage fraction.

Further literature would help to get the model closer to reality. Works on surface inversion layers, dating already few decades, can give a significative enrichment to the proposed model {Kingston and Neustadter 1955; Chen and Muller 1974}. Unfortunately, these sources have been available in a later phase of the development, and have not been implemented yet.

Further work on the validation could clarify the role of lateral diffusion in the bulk. The treated model excludes any lateral diffusion, on the other extreme a concept of immediate diffusion could also be implemented easily. In this case the problem would implement a "diffusing" plane between the bulk and the inversion layer which distribute uniformly the currents from the base in the floating junction. This hypothesis would be strongly valid when the diffusion length (L_{Dn}) is much longer than the pitch.
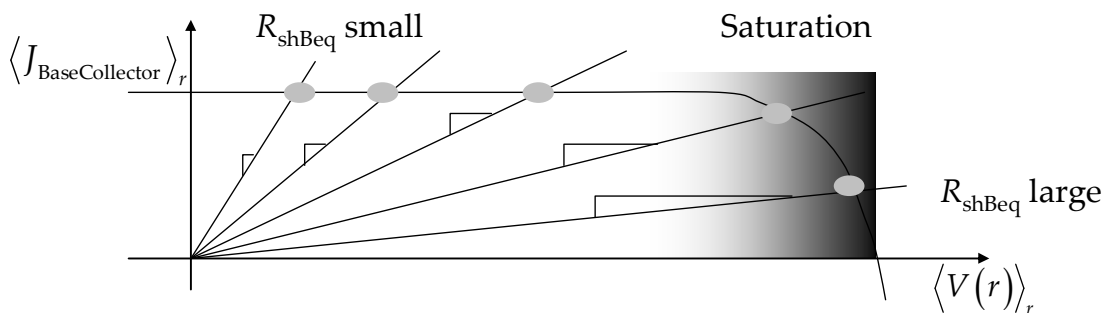
Fig. 5:17 Working points for different settings of R_{shB} equivalent. The higher its value, the closer will be the back surface in saturation.

This high diffusivity assumes a constant current entering the channel. Therefore an equivalent resistance can be calculated from the known system specification on resistive paths with a known procedure {Hall and Soltys 1980}. Then the relation between the current from the base and the average level of injection is traced in a JV graph. The working point of the system

will be the meeting point between this JV curve and the slope represented by the calculated equivalent resistance. This point will also show if the saturation is acceptable (see Fig. 5:17).

Indeed even in this case, the concept of saturation is useful, since it would help to understand when the back surface has benefits from the surface type inversion.

Chapter 6   Conclusion and outlook

*Quantitative and qualitative results are summarized in this last chapter.
This gives a complete view of the achievements. A few considerations on the
scope of the results are given to correctly assess the role of the findings.
Furthermore, based on the work performed, outlooks are offered towards the
possible future development of highly efficient industrial solar cells.*

6.1   Conclusions

The evaluation of advanced processing steps and the understanding of their performances required expertise to merge them in the complete solar processing. The achievements of the technological survey are recapitulated here.

First is the progress on the techniques to accomplish single side structuring. The interruption of the front to back symmetry, typical of the early processing stages, is a necessary preliminary investigation for the advanced processing.

Wet techniques were evaluated for this purpose. The chemical etching delivered a thorough and reproducible emitter removal already with just a few micrometres of silicon removed. This was achieved in little time thanks to etching rates as high as 3 μm/min. Methods to increase the etching rate up to the level of flattening were extrapolated from the experimental results.

Dry alternatives for the emitter removal and rear surface flattening proved also capable of attaining the desired levels. The etching rate (0.6 μm/min) is about 5 times smaller than that of the wet procedure. However, in the range of the experiments mirrorlike surfaces were attained increasing the number of plasma source sections.

Furthermore the dry etching was evaluated for the improvement of the emitter perfomances by the removing of the dead layer, a detrimental emitter diffusion by-product. The emitter saturation current decreased as a consequence of the process. The lowering was measured as 80 % of the saturation current of the pristine emitter.

A second investigation concerned two stacks of dielectric layers: SiriON CaTS and SiNTOx. These have been optimized for a reduced surface recombination velocity. Best results, expressed in terms of surface recombination velocity, were 3.3 cm/s for a SiriON CaTS stack on polished surfaces and 78 cm/s for a SiNTOx stack on close-to-solar-process surface roughness. Additionally, both layers were exposed to procedures typical of the conventional solar cell processing. This allowed the establishment of two candidates, completely compatible with widespread metallisation techniques.

A third part focussed on the actual mechanisms behind the formation of the contact. A model on the local sintering resulted from the interpretation of the observed details. This new knowledge was an advantage in the comparison of a laser fired contact and the sintered one.

The techniques developed were integrated in complete solar cell processes. The compatibility was well cared for through the detailed study of viable process flows.

In one case, a further constraint of reduced substrate thickness was added to the implementation. Finally, the fabrication of thin (120 μm) large area (125x125 mm²) Cz-Si solar cells applying a LFC-PERC structure resulted in stabilized top efficiencies of 18.0%.

The fabrication included both grown and deposited passivations. The thermal oxidation of the rear surface resulted in the highest efficiency. On the other hand, explored passivation based on a PECVD technique performed at a close level compared to the SiNTOx approach. However, a better understanding of the contact formation could fill the performance distance.

All process steps were performed using industrial or industrially applicable processes. The stress inside the finished device was at a very low level. Consequently, the bowing typical of thin substrates was absent. The presence of bowing is detrimental for production yields and would further complicate the handling of thin substrates.

The realised PERC structure, while achieving high levels of results, presented significant power losses. Therefore it was analysed in detail. The study represents a first step towards the minimization of losses in *FF*.

The result of the analysis explored both common and uncommon loss mechanisms in solar cells. The *FF* losses identification was performed in steps. First the series resistance was analysed in detail and it was discovered to be not optimal. Then the presence of non-ideality of the diode was indicated. In this regard, highly active recombination points corresponding to the rear contacts were proposed as a possible explanation for a *pFF* loss. Finally a loss from the edge region due to non-idealities was identified and quantified.

These first analyses are an interpretation of the *FF* loss and suggest methods to improve the cell concept. The front side metallization could be improved using thinner fingers, or even reduce the first metallization step to a seed layer printing step and adopt the silver plating to build up the bulk of the metal fingers. Advanced front side metallization techniques are available {Mette 2007}. In particular, aereosol printing was revealed to be adequate for the industrial application {Hörteis 2009}. Aside from the reduced *FF* loss, this metallization can decrease the necessary amount of metallised area on the front, and in turn increase the current density.

The effort on the promising techniques of plasma processing resulted in a better insight into the implementation issues as well as a noteworthy result of 0.2% absolute efficiency increase with respect to conventionally processed cells. Best cell results suggest an even higher increase potential of 0.5% absolute.

Further coupling to other processes convertible to CVD or PVD techniques in vacuum could result in convenient and elegant production lines. The vacuum condition would ensure a more controllable and clean environment for the fabrication. Concrete ideas for the industrial realisation were presented recently {Rentsch, Seiffe et al. 2008}. As demonstrated previously in 3.4.3 at the paragraph "Single sidedness" great care has to be invested in the design of transportation carriers for the (simultaneous) processing of both sides.

Finally, from the experiences gathered with the processing of passivation based on field effect, the core issue of channel shunting has been faced from a design point of view. An attempt to model the behaviour and explain the limiting factors with the help of sound assumptions has been proposed. A numerical approach is used to compile the model results. Considerations on the results are the first approach to the issue from a design point of view. Possible paths for the complete analytical description are given. The validation of the effect is then presented as a disagreement between the measurements and the existing theory.

As a final consideration, the work performed and reported proposes advanced structuring techniques to transfer the technology of "high efficiency" concepts to high throughput processing. Highly efficient solar cells were realized on thin substrates and in large number. This testifies to the feasibility of such approaches for the industry. One challenging issue of passivation based on type inversion has been modelled. The model needs further work for

approaching validation. However, the qualitative results agree with the phenomena observed at the cell level.

6.2   Outlook

The realisation of highly efficient solar cell awakes a growing interest. Indeed, between the obtained 18% and the theoretical maximum (see 2.5) there is plenty of potential. The critical issue is though the increase in process complexity and, in turn, process cost. Below a few ideas for extensions of the technology transfer work will be delineated

As commented in 2.2.1 and then later confirmed on realised cells in 4.2.3, the reflectance of the back surface influences the light harvesting capability. The realised schemes were optimized for a good reflectance. However, room for improvement can be found in the effective scattering of the light in the solar cell. For example, adopting advanced light trapping concepts, for example photonic crystal structures {Janz, Voisin et al. 2009}, on the rear side, light can be diffused in the substrate in directions almost parallel to the surface, avoiding the escape of a specific set of wavelength (IR) from the front escape cone (Fig. 2:5).

The exploration of the contact formation, although not entirely developed, answered questions concerning the formation of the contact. The model proposed can be used to understand how the limitations can be avoided. The same argument is valid for the LFC implementation. The characterisation performed in this work is a key observation for the development of improved contacts. Further dedicated studies on the contact formation will improve and stabilize the performance of this vital structure in the solar cell.

During the analysis (see 4.7.1) it was possible to note a strong negative impact of the edges on the cell ideality. Work should be addressed to the study of a dedicated structure for the edges. The purpose of this would be to reduce non-ideal effects and furthermore to make the cell less prone to shunting problems.

The introduced model was presented with the only purpose to shed light on the significant limitation of the floating junction passivation technique. The same treatise can be used for the characterisation of the contacts-inversion region interface in the same way existing models are used for similar challenging characterisations (see separation of S_{met} and S_{pass} with the Fischer model, an example of its limitation in this case is shown in 5.2). Consequent application will enable the correct design and proper characterisation of solar cell structures based on this principle.

Appendix A Measurements systems

To obtain an insight into the realized structures all available characterisations need to be used; in this appendix quick comments on the principles and references towards proper treatments are given.

The photovoltaic research benefits from the experience thas has maturated since its beginning in the 1950 on the characterisation of semiconductor for electronics and microelectronics components.

Some of the following tools are taken as they are from the semiconductor research; some others were developed from scratch to meet special needs of the photovoltaic community. In the following this difference will not be depicted, although it may be interesting for semiconductor history enthusiasts.

A.a   *Resistance measurements techniques*

A.a.I   Four Points Probe 4PP

The four points probe method makes use of 4 metallic needles, with the tips arranged on a line, to create a force and sense system on a surface.

A current is forced through the external needles while the innermost needles are used to sense the voltage drop between the two points, since the distance between the needle tips is known and since the current that is flowing has to be the same, a value of a sheet resistance, the unit of which is Ω/sq., can be calculated.

A.a.II   Inductive sheet resistance measurement

The generation of eddy currents in conductive layers by induction needs some power from the inducing part. When the inducing part is always the same and the conducting layer is changed, a change of power needed will be observed, a calibration of the shift will give the possibility of establishing a measurement method for the sheet conductivity of layers.

A treatment for the use of this technique for the solar cell production and the advantages of it towards a 4PP in detailed in a work by Spitz {Spitz, Belledin et al. 2007}.

A.a.III   Carrier Density Imaging

At room temperature in semiconductors there are usually no electrons jumping from one end of the bandgap to the other, though it is much more common that jumps within a band happen, taking energy from temperature or irradiation. The relaxation of these jumps usually is done by phonon or by photon emission in the infrared area.

This measurement targets the interaction between carriers, which depends on the doping of the DUT, and the mid infrared part of the spectrum

Isenberg proposes a review of the method {Isenberg, Schubert et al. 2005} while detailing also application areas in photovoltaics. This approach can lead to false interpretation when the effect of free carrier absorption is not taken into account {Schroder, Thomas et al. 1978}.

A.b   *Capacitance Voltage*

Investigations on an insulator-semiconductor system measure the capacitance as function of the voltage since the underlying semiconductor, by being not a metal, will add peculiar and almost entirely surface dependent traits. These will result in the capacitance values. This dependency contains a great amount of information on the insulator layer and on the interface between insulator and semiconductor.
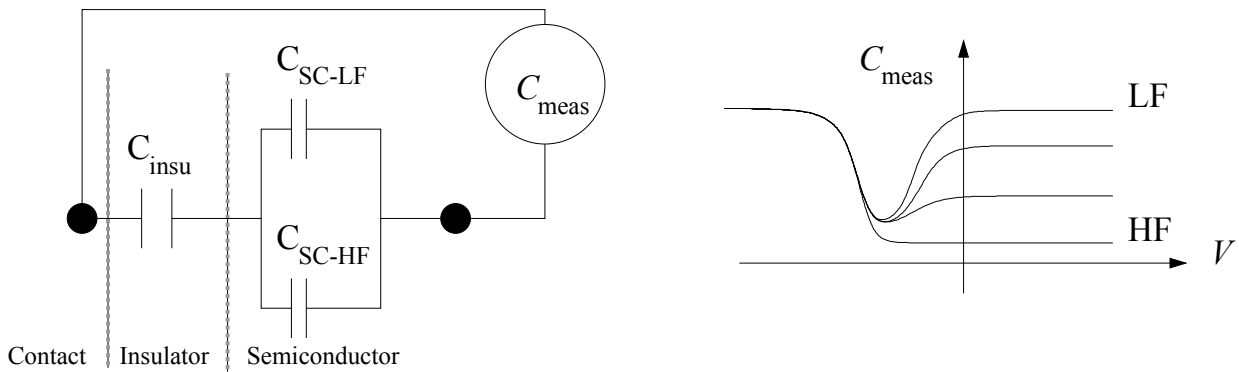
Figure A:1 sketch of a insulator semiconductor system, the tool is able to sweep a voltage and measure the capacitance at each bias. The frequency also plays an important role on the resulting value.

One of the most comprehensive texts on this characterisation is has been published in the 80's {Nicollian and Brews 1982}, and is still a reference nowadays for its rich amount of specific cases.

Recent development of the implementation, namely a mercury drop to create a metal contact on the insulator, reduced drastically the need of processing to deliver a measurable device.

A.c   *SPV*

The method, described in full in {Schroder 2001}, allows to measure the surface voltage in dark and in illuminated condition (see Figure A:2)

The difference of the surface voltage in the two conditions will result in the characteristic surface potential of the structure semiconductor + interface material.
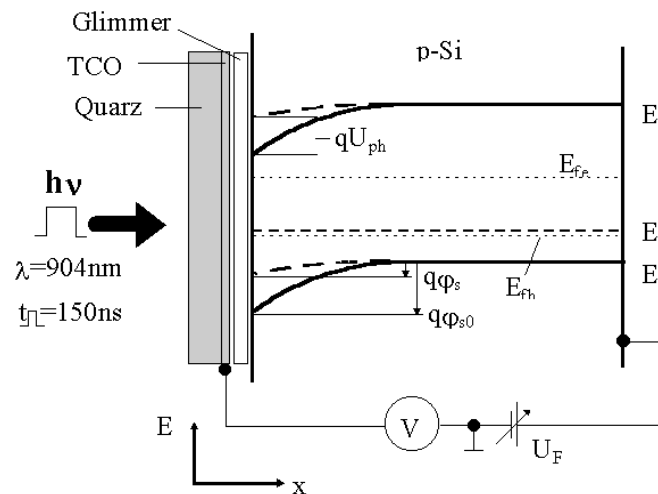
Figure A:2 Detailed sketch of the measurement tool. The material (p-type) is supposed in depletion while in dark. Incoming light with a specific wavelength and length excites EHPs and increase injection at the surface. Monitoring the shift of voltage it is possible to obtain the exact surface potential due to the external conditioning (from {Korte 2006}).

A.d   *Reflection and transmission*

The reflection of a surface can be monitored with the help of a spectrometer. This tool, thanks to grading surfaces can impinge on the target surface a flux of photon having wavelengths in a small range (i.e. 1 nanometre).

The measurement makes use of a UV/Vis/NIR spectrally resolved photometer (Varian Carry 501i). The sample is illuminated by monochromatic light and the intensity of the reflected radiation is measured by a detector. The light sources are a tungsten halogen lamp with a quartz window for the

visual light and a deuterium lamp for the UV light. The detector for the UV and the visual range is a R928 photo multiplier. In the NIR, an electrothermally controlled indium gallium arsenide PIN photodiode is used. In order to characterise the diffusely reflected light as well, an integrating sphere is present. The sphere exhibits an inner radius of 55 mm and is covered with Teflon on the inner walls. The illuminated surface area is 2.01 cm²; the illumination angle is 3°20′. Before each measurement a white standard sample is measured and a dark reference measurement takes place

Finally, reflection can be plotted for each wavelength generated and measured.

One concept particularly helpful for the characterisation of the solar cell based on silicon is the so-called Weighted Reflection. This number takes into account the reflection of the surface, the terrestrial solar irradiation based on a standardized distribution and the internal quantum efficiency (IQE) of an average cell. The reflection at each wavelength is weighted by the probability of absorption and the amount of photons available in that range. The integral of these weighted reflections is normalized on the spectrum and the resulting value is taken as a characterisation value for a surface. Mind that this value is strictly related to the IQE chosen.

The transmission is again measured with the help of the same instrumentation. The photon flux hits the target surface and then enters the integrating sphere after having crossed the entire thickness of the sample.

For the transmission measurement a few further remarks have to be made. The transmission of a structured solar cell can severely differ from an expected value of a silicon slab of the same thickness. The main reason for this is the light trapping structures of a solar cell. This changes the normal direction of rays and in particular of long wavelength photons. Their mean path inside the substrate can reach up to several meters in length, increasing their collection rate.

A.e   *External and internal quantum efficiency*

From the measurement of quantum efficiency it is possible to measure how much of the incoming wavelengths intensity is absorbed and produced photogenerated current.

Indeed the principle is to impose short circuit condition on the cell and shine monochromatic light on the cell. Additionally a white bias light can be present. Thanks to lock-in techniques, this static component is eliminated from the measurements.

$$SR(\lambda) = \frac{J_{SC}}{E(\lambda)} \quad \Rightarrow \quad \begin{cases} EQE(\lambda) = \dfrac{J_{SC}}{q} \dfrac{h \cdot c}{\lambda E(\lambda)} = \dfrac{h \cdot c}{q\lambda} SR(\lambda) \\[4mm] IQE(\lambda) = \dfrac{EQE(\lambda)}{1 - R(\lambda)} = \dfrac{h \cdot c \cdot SR(\lambda)}{q\lambda (1 - R(\lambda))} \end{cases}$$

Equation A−1

From the measurement of the short circuit current and an additional measurement of the wafer reflection it is possible to extract both the external quantum efficiency as well as the internal quantum efficiency.

A.f   *Effective lifetime measurements*

One of the critical parameters of a solar cell is the lifetime of the carrier. Longer lifetimes ensures that EHPs generated far from the junction have the time to diffuse there. In section 0 the several recombination mechanisms have been mentioned. Each of them has a certain dependence on the amount of carriers that can recombine ending therefore their lifetime. Accordingly also the lifetime depends on the amount of carriers. For this reason is interesting to obtain information sweeping the density of carriers over several orders of magnitude.

A.f.I Quasi steady state photo conductance

This method exploits the change in conductance that a semiconductor undergoes as soon as additional mobile carriers are added in sensible number.

The exitation is brought to the wafer with a strong monitored illumination. The change in conductance is monitored by the radio frequency bridge, which transforms the change in coil impedence in a change in voltage. Elaborating the information given by the user, together with the tracked irradiation and the change in conductance, it is possible to deduce how the lifetime changes when the light decreases. The decrease is slow compared with the recombination phenomena, which are usually in the order of microseconds. For this reason it is possible to call the method quasi steady state photo conductance QSSPC.
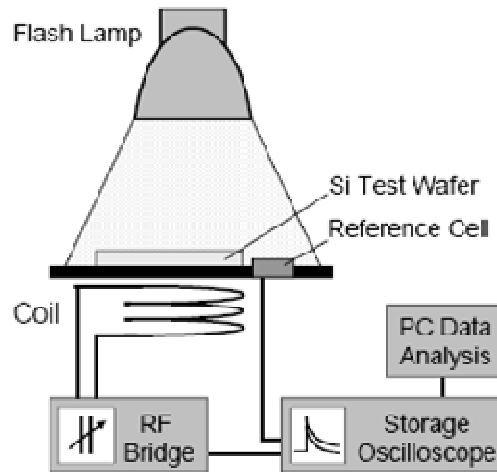
Figure A:3 Sketch of the measurement tool. Of high importance is the calibration of the RF bridge against a known sample.

This tool is one of the most popular for laboratory characterisation, for this reason several review papers are present, worth to mention is a recent publication {Cuevas and Macdonald 2004} and a latest one in which the discussion on the measurement error is reported {McIntosh and Sinton 2008}.

If not otherwise specified, the effective lifetime in this work is measured at an injection level of 5E+14.

A.f.II Characterisation of lifetime, symmetric samples

In the following a structure will be detailed for the characterisation of a silicon wafer. The structure is applied together with the QSSPC lifetime spectroscopy described to gain an insight into the characteristics of the bulk or of the surface of a silicon wafer. It is good practice to take FZ-Si as starting material, and additionally use a substrate doping in the range of the usual photovoltaic solar cell realisation. The example below will make use of numbers which fulfill these criteria.

A typical configuration for the analyses consists of a 250 μm thick Float Zone crystalline silicon substrate with a resistivity of 1 Ohm·cm: this corresponds to a doping level $N_A \approx 1.5E+16$ cm^{-3} and a diffusion constant[47] $D_n \approx 27$ cm²/s. For these starting conditions, using the parameterisation introduced by Kerr {Kerr 2002}, an intrinsic lifetime level of $\tau_{bulk\ Kerr} = 2092$ μs is calculated; this value, in low injection conditions, approximates the lifetime of bulk minority carriers τ_b. This symmetrical structure ensures a good realisation of the condition of symmetrical $S = S_1 = S_2$, which is necessary for the simplification introduced by the mathematical expression

---

[47] Calculated with the PC1D mobility model at 25°C condition.

$$\frac{1}{\tau_{\text{eff}}} = \frac{1}{\tau_{\text{bulk}}} + \frac{2S}{W} \quad \text{for} \quad \frac{SW}{D_{\text{n}}} < \frac{1}{4}$$

<div align="right">**Equation A—2**</div>

which relates the influence of surfaces on effective minority carrier lifetime (**Equation A—2**). This simplification, as demonstrated in the work of Sproul {Sproul 1994}, can be used with a confidence of 4% as long as the calculated S is below a certain value (for this example: $S < 270$ cm/s).
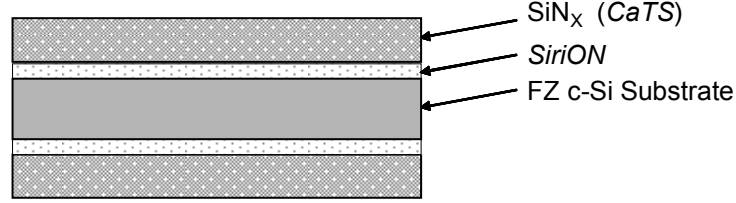
Figure A:4 The symmetric sample is represented here. The bulk is preferably a Float Zone crystalline silicon substrate; on this a passivation layer is symmetrically deposited, in this example the SiriON CaTS can be seen on both side. The sketch is out of scale for representative purposes.

The minority carriers' lifetime is measured resolved to their concentration by means of a Quasi Steady State Photo-conductance Decay (QSSPC) analysis.

Before presenting the measured values, attention must be brought to a collateral effect of field effect passivation on this kind of measurements, as discussed in a dissertation work {Dauwe 2004}. In the case of a p-type material, if charges present at the surfaces induce a space charge region (populated with ΔN charges, see also {Mönch 2004}), the photo-conductance dependency on low illumination level deviates from expected,

$$\tau_{\text{app}} = \tau_{\text{eff}} \left(1 + \frac{2\left(\Delta N - \Delta N_0\right)}{\Delta n_{\text{b}} W} \right)$$

<div align="right">Equation A—3</div>

leading to an apparent lifetime τ_{app}. This value depends on the amount of charges ΔN which are actually at the surface, the amount of charges that would be present in thermal equilibrium ΔN_0 and Δn_b which represents the injection level in the bulk. From Equation A—3 a worst case scenario can be calculated: with a surface in strong inversion the maximum deviation is obtained, even in these conditions the error that can be made with measurements at injection of $5E{+}15 \text{cm}^{-3}$ is well below 5%.

A.f.III   Photoluminescence

A recently developed technique adopts the proportionality of the radiative emission to the amount of injected carriers. The photoluminescence technique illuminates the sample with a monochromatic wavelength $\lambda_{\text{m}} = 790$ nm with a total equivalent intensity of two suns, its energy is slightly higher than the band gap, so that the sensor which measures the radiation from the silicon can be made selective only to those. The cell is not connected to external biasing devices. Therefore, it lays in open circuit conditions. The imaging produces a signal proportional to the effective lifetime. The signal is scaled to τ_{eff} through a coefficient which depends on the optics {Trupke and Bardos 2005}. The measurement instrument implementation is reported elsewhere {Trupke, Bardos et al. 2006}.

The result is an imaging technique. The main advantage of the tool is the amount of information that can be collected within few seconds of signal integration time. Although the method must be calibrated against another measurement tool to obtain quantitative information, already the qualitative comparison of various areas on the cell can be of great help for the identification of local inhomogeneities.

A.g *SunsVOC*

This instrument is able to report the open circuit voltage of a solar cell during a flash of light. During the decay of the flash, the irradiation, as well as the open circuit voltage is tracked. From these informations is possible to understand how much current injection is needed to face recombination losses.

The working principle simply put is that the photo-generator is biasing the device, which can be seen as composed by a diode and a shunt circuit. The device for every amount of irradiation will be autobiased in order to neutralize all the generated EHPs. These autobiases are the important information to collect. This autobias tells us that the device at that specific voltage is able to make a spefic amount of irradiation disappear. Under steady state illumination and at one of the characterized autobiases the cell will make recombine all carriers of which it is capable, but then the rest will be diffused out. The specific literature can be found here {Sinton and Cuevas 2000}
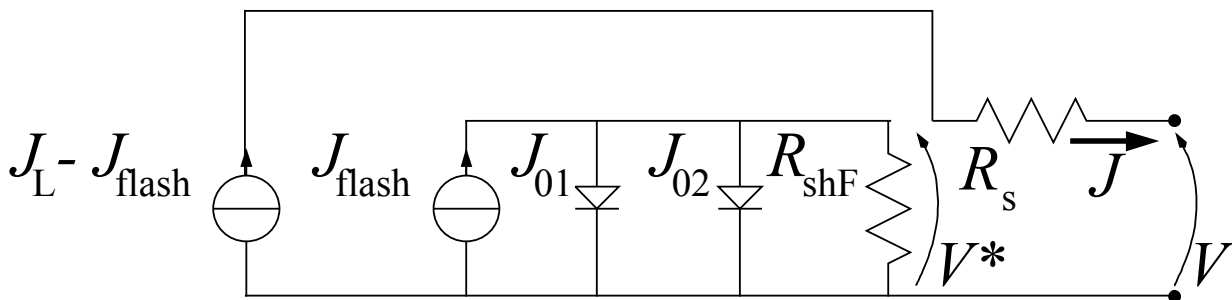
Figure A:5 Equivalent circuit of a SunsVoc measured cell. the voltage V^* is measured on the shunt resistance R_{shF} and on the left side of the dipole series resistance R_s. The flash is creating a J_{flash} current and this polarizes the inner cell. In case the measurement is repeated in light, the same condition can be found, a current equal to J_{flash} polarizes the inner cell and the remaining light can exit the cell.

A.h *Fill Factor Analysis*

A JV1Sun measure can give a value of the *FF*, this parameter though not directly related to a solar cell characteristic, summarizes electrical losses and non ideality of the solar cell diode behaviour.

This term indicates the percentage of the current density / voltage plane between the origin and the two points representing J_{SC} and V_{OC}. In Figure A:6 an example of real current density is traced with a full line. The square on the line represents exactly the maximum power point. The fill factor in this case indicates the area most hatched compared to the empty rectangle with a perimeter of dots.

A.h.I Single cell measurement

The fill factor is an access to the amount of parasitic resistance that is affecting the cell, readily available with a SunsVoc is the *pFF* which gives the value of the *FF* unaffected by the series resistance. Also this quantity is represented in Figure A:6, the vertically and horizontally hatched region is the area which is indicated in percentage. Furthermore, from the V_{OC} it is possible to calculate the J_0 of an ideal diode which has same V_{OC} under the same illumination conditions (Equation A−4).

$$J_0 = \frac{J_1}{\exp(V_{OC}/V_{th}) - 1} \qquad \text{Equation A−4}$$

Furthermore, from the V_{OC} it is also possible to derive the *FF* of this ideal cell.

$$FF_0 = \frac{v_{oc} - \ln\left(v_{oc} + 0.72\right)}{v_{oc} + 1}$$

<div align="right">Equation A−5</div>

This value takes the name of FF_0. A definition of FF_0 is provided in Equation A−5 {Green 1986}, there v_{oc} represents the V_{OC} normalized to the thermal voltage V_{th}. Equation A−5 is an approximation with accuracy of 0.1% for $v_{oc} > 10$.
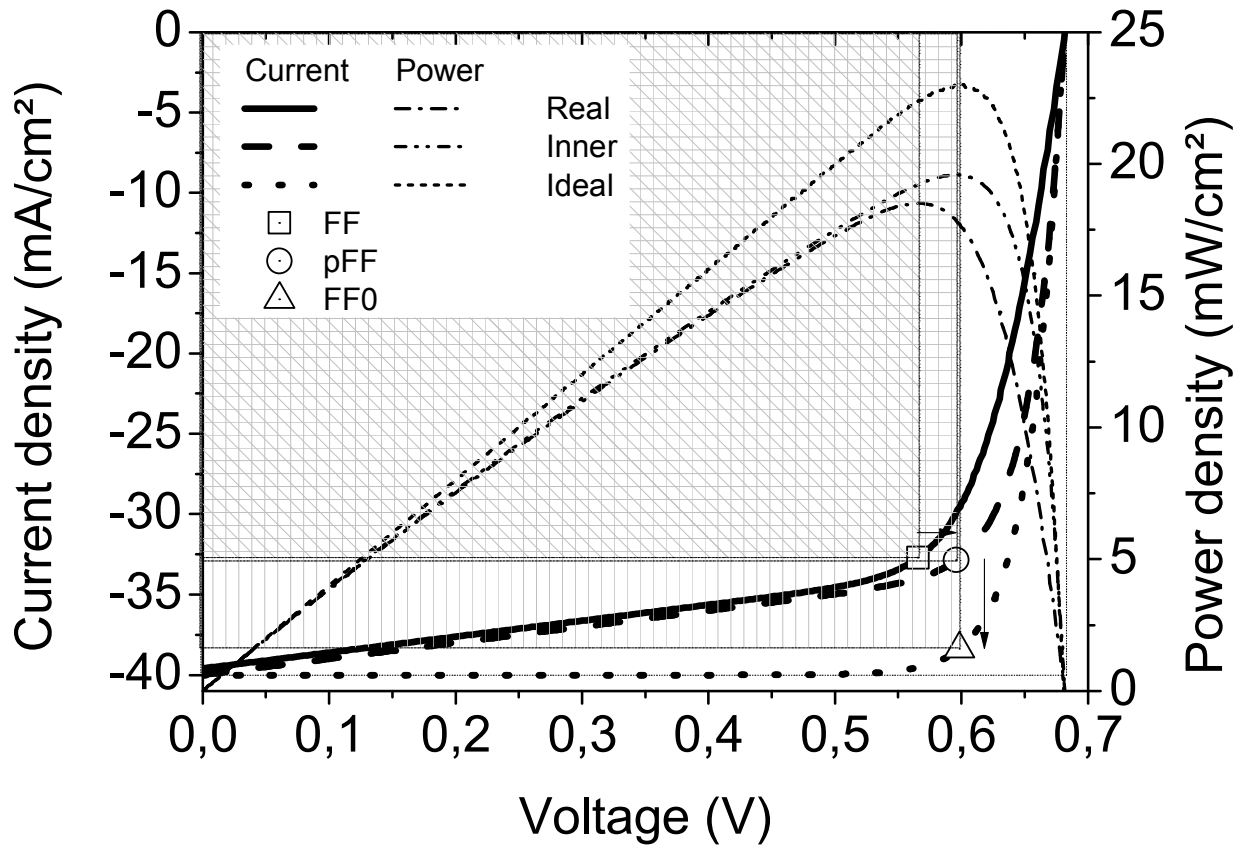
Figure A:6 The picture here presents a cell with the following parameters: $R_s = 1\ \Omega\cdot cm^2$, $R_{shF} = 100\ \Omega\cdot cm^2$, $J_L = 40$ mA/cm², $J_{01} = 1E{-}10$ mA/cm², $J_{02} = 1E{-}9$ mA/cm², $m_2 = 2$, the calculated ideal J_0 is equal to 1.24E-10 mA/cm². The arrows show an almost horizontal and vertical movement of the points, this indicates that they measure a voltage loss and a current loss respectively and indicate symptoms affecting the solar cell.

The difference between *pFF* and *FF* is correlated to and only to the amount of parasitic series resistance in the solar cell, in contrast to the extraction of $R_s = 0$, this value is not obtained from a fit, but as a comparison of two measurements. Furthermore, the difference between *pFF* and FF_0 gives an indication on either the amount of shunt or on divergences from ideality of the solar cell (SCR contamination, edge effects, local recombination sites, etc.) or both. This analysis can help to analyse the symptoms of a single solar cell which lead to efficiency loss.

A.h.II   Production line perspective

Production lines keep this value under strict control, when a correlation with the entity of a parasitic resistance is found, then this parasitic resistance is limiting the overall efficiency and the settings of the line have to be adjusted to remove the trend

Appendix B Mathematical treatises

B.a   *Statistical analysis of experiments*

Often in the scientific world there is a strong disagreement on how experiments should be planned, done and analysed. Most thinkers are biased from their high intellectual capacity and an assumption of low or absent noise. Which translate in the hope that every realisation is highly repeatable and not affected by chance. Though this point of view is interesting, it leads most of the time to a false interpretation of result, it is more than often not possible to distinguish variations imposed from the random distribution of the measured values and the effects that are created in the frame of the experiment. Furthermore, a quantitative analysis of the random component is completely missing.

Luckily this problem has been evident to many and starting from a recent past, a branch of mathematic is giving is best to provide calculation tools that help the analysis of result. The methods are applied in this work to the best knowledge of the author and it is assumed that the reader has the necessary knowledge to follow the presented results. However, an interesting treatment of the methods, with a strong bias for the process control is given by {Kleppmann 2008} (German).

Using these methods the results that are generated by the equipments can be correlated with the values that we are interested in.

B.a.I   Statistical method adopted in the thesis

The statistical method used in this thesis to analyse the results from batches will be described in this short paragraph.

The results of the experiments are analysed to find to which extent the variation performed deliver significant difference on the output value. This is done testing the null hypothesis (how big is the chance that this difference is absent?) and getting the value of this probability, called p_{test}, a value of p_{test} below 0.05 tells that there is a 95% chance that the observed values represent the researched[48].

The direct effects and the interactions are presented with a Pareto diagram, all the effects and interaction which are represented in this graphs are used for the analysis, meaning that the other have not been taken in consideration because they were either not significant (a change of these configuration did not result in a significant change in the output value) or not conceivable to have interaction with each other for any reason.

A second step, towards an empirical understanding of the influence of the parameter is a multi-regression. This can have two methods of formation, we can use as input of the model the values of the factors, which are discreet by nature, or we can input values which are not factor, maybe consequence of them, and they assume continuous values. A regression coefficient will give the confidence of the model prepared; this approach will also help to understand how strong and predictable the output of the system is.

If within the experiment there are at least some repetitions, it is also possible to test if the curvature of the model is corresponding well to the measured value. This additional test consents to give an objective evaluation of the fit. For this reason it takes the name of "Lack of fit test"

Effort is given to assign to factors sound numerical values, in order to define a correct distance, these enable predictions and give meaning to models, to make an example, if a certain comparison is made between samples that were processed for 20 sec and sample that received no processing, the correct naming of the cases is "20 s" and "0 s" instead of the tempting "processed" and "not processed".

After that a model is presented a good proof of its quality for the reader to is visualised by a plane where points represent the observed value and the calculated value, a wealth of point lying on the bisector indicates a good agreement, furthermore, a good distribution of point along this line indicates

---

[48] There is still a 5% chance of being wrong, for example when measuring a value affected by a normal distribution, with mean 50 and standard deviation 5, taking values below 41 and above 58 represents this probability.

that a good spectrum of casus was explored. Lonely points lying completely out from the bisector can be investigated to verify the model; they could be outliers or good questioning moment for the prepared model. Several clustering of points represent a design in which one factor represents more or less the whole variance.

The focus of this method is to extract the highest amount of consistent information from the work that every experiment brings with it. Furthermore it generates a measurable certitude that all questions that brought forth the experiment have either an answer on the system behaviour or an answer which indicates the challenges ahead and how they affect the work.

B.a.II   Data display

Many of the experiment make use of graphs which are named Box-Whisker; the use of each indication of this graph will be elucidated with the help of an Example Data Set. The data set contains values that follow a normal distributed plus some noise. When the usual statistics on the data set are calculated a Box-Whisker graph can be created (Figure B:1). The box top and bottom represent a distance of one standard deviation from the average, which is indicated with a small square in the middle of the box; the line which cuts the box in two is the median this line is not necessarily in the middle of the box, the lines extend to represent the 5% – 95% interval confidence, which means that outside of this line the possibility of having values is below 5%, finally the crosses detail the minimum and the maximum value.
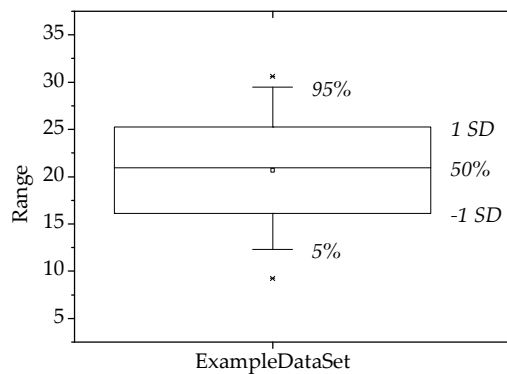
Figure B:1 Box-Whisker diagram on an example dataset

Another useful diagram is the Pareto diagram; there the ANOVA effects estimates are displayed sorted by magnitude, if there is an estimate for the error variability available the effects are standardize and is possible to include the minimum level for a significant effect ($p_{test} < 5\%$). The standardisation procedure multiplies the ANOVA effect by the result of the test distribution.

On this graph the significance of the effect is shown. In case the experiment allows to evaluate a quadratic behaviour, thanks to more than two distinguished cases for the given variable, the linear and the quadratic significance will be tell apart by using two letter: L for linear and Q for quadratic.

Two useful graphics to illustrate the quality of a polynomial fit are the expected observed graph and the residuals plot. The first proposes to plot the height of the observed value by an input combination at the value that the model assumes with the same input. The bisection line is therefore the resulting target of every model. The second instead sorts the diffeences between observed and expected value. These are then plotted on a graph deformed to represent a normal distribution as a line. In one glimpse it is possible to see if the residuals are normally distributed. This is indeed a visual indicator of a good fit.

B.b   *Terms of validity for a complete and an approximated analytical solution*

The differential equation described in 5.3.5 does not result in a known closed form analytical solution. However, the mathematical formulation resembles from close other works for which a solution was found {Chambre 1952; Chen and Luo 2001}. The treatise operates transformations on the differential equation. These transformations bring the system to an expression of known solution. Finally the

boundary conditions are applied an analytical expression is obtained. Below, the same mathematical approach is tested.

The procedure removes the exponential term from the differential equation (Eq. 5–15). In our case, a slightly modified set of transformations that achieves this will be applied (Equation B–1)[49].

$$\beta_m = r \frac{dv(r)}{dr} \qquad \eta_m = r^2 \left(\frac{K_1}{K_2} + e^{v(r)} \right) \qquad \text{Equation B–1}$$

The transformations applied to Eq. 5–15 deliver a different condition with respect to previous treatises. The difference is the presence of a term which directly depends on r (third term of the innest sum of Equation B–2). This extra term refuses the differential equation to be solved with the known procedure.

$$\eta_m \left(K_2 - \beta_m ' \left(\beta_m + 2 - \beta_m r^3 \frac{K_1}{K_2} \right) \right) = 0 \qquad \text{Equation B–2}$$

One idea is to explore the value of the extra term and find a condition to neutralise it. This would guarantee an analytical solution of the system.

$$\eta_m \left(K_2 - \beta_m ' \left(\beta_m + 2 \underbrace{- \beta_m r^3 \frac{K_1}{K_2}}_{\text{term to neutralise}} \right) \right) = 0$$

$$\text{if} \quad \eta_m \neq 0 \quad \text{and} \quad \beta_m r^3 \frac{K_1}{K_2} = 0$$

$$\beta_m ' = \frac{K_2}{\left(\beta_m + 2 \right)}$$

Equation B–3

The extra term is nought on the outermost circumference due to the boundary conditions ($v'(r_{HP}) = 0$ and in turn $\beta_m(r_{HP}) = 0$, see Equation B–1). On the other hand the boundary condition on the innermost circumference does not impose a specific value. The remaining region depends therefore on the value of K_1 and K_2.

Imposing $K_1 / K_2 = 0$ results in negative illumination for positive front bias. This unrealistic condition purports to a necessity of injection absence for the extra term to disappear. A first conclusion is that no exact analytical solution can be found. However, an approximation would also be acceptable if even a small amount of injection were provided. Therefore, instead of looking for the annihilation of the extra term, we will look for the range of injection that keeps it below a certain limit L_m.

$$\left| \beta_m r^3 \frac{K_1}{K_2} \right| < L_m = l_m \cdot r_{HP} \cdot \beta_{max} \Rightarrow \left| \frac{K_1}{K_2} \right| < l_m \qquad \text{Equation B–4}$$

To easily go further, two simplifications are justified and made. The first is that the injection of carriers has no influence on r. Therefore it will be enough to consider its maximum value. Analogously, the term β_m has a maximum value in r_0 which is possible to calculate once a solution is found. Therefore the term l_m is introduced (see Equation B–4).

All values in Equation B–4 belong to the Real set and are positive. With these statements the disequality leads to confinements on l_m and G_L. Our interst contemplates only small values of l_m, close to 0. This choice delivers the conditions on G_L.

---

[49] The transformation are the best guess of the author to perform the solving procedure

$$0 < l_{\mathrm{m}} \le 1 + \frac{U_{\mathrm{brec}} n_{\mathrm{p0}} \left(e^{v_{\mathrm{front}}} - 1 \right)}{J_{\mathrm{0c}} + U_{\mathrm{brec}} n_{\mathrm{p0}} \cosh(w)}$$

$$C + \underbrace{(-1 - l_{\mathrm{m}})}_{\text{negative}} \cdot D < G_{\mathrm{L}} < C + \underbrace{(-1 + l_{\mathrm{m}})}_{\text{negative}} \cdot D$$

Equation B—5

The value of C and D in Equation B—5 is respectively always negative and always positive (see Equation B—6).

$$C = -\frac{n_{\mathrm{p0}} \left(e^{v_{\mathrm{front}}} - 1 \right)}{\tau_{\mathrm{bulk}} \left(\cosh(w) - 1 \right)} < 0$$

$$D = \frac{J_{\mathrm{0c}} + U_{\mathrm{brec}} n_{\mathrm{p0}} \cosh(w)}{U_{\mathrm{brec}} \tau_{\mathrm{bulk}} \left(\cosh(w) - 1 \right)} > 0$$

Equation B—6

In few words Equation B—5 says that any value of l_{m} below 1 will lead to a negative generation. The acceptable range of G_{L} could expand to comprehend positive values of illumination only for l_{m} values larger than unity. Although by that time the value of L_{m} will be enourmous compared to our initial reference.

The system under injection cannot be solved with the procedures that are found in the literature.

Appendix C Lists of Symbols, acronyms and units

C.a   *Symbols*

Symbol	Description	Unit
η	Efficiency, percentage of electrical output power with given input light power (1 sun)	%
a	Radius of the contact	μm
D_{it}	Density of Interface States	cm^{-2}
D_n	Diffusion length of electrons	cm^2/(V s)
d_{SC}	Depth of the surface space charge region.	μm
E_B	Minimum/Maximum of an energy band	eV
E_C	Energy level of the CB	eV
E_F	Fermi energy, average energy of particles added to a system	eV
E_F	Fermi Level	eV
E_{Fn}	Quasi Fermi level for electrons	eV
E_{Fp}	Quasi Fermi level for holes	eV
E_G	Energy Gap (if not otherwise stated, silicon energy bandgap)	eV
E_g	Band Gap	eV
E_S	Surface electric field	V/cm
E_t	Energy level of a trap	eV
E_V	Energy level of the VB	eV
f	Metallic coverage fraction on the back surface of the cell	-
FF	Fill factor, ratio of the product J_{mpp} V_{mpp} over the product J_{SC} V_{OC}	- ∨ %
FF_0	Ideal fill factor, calculated under the assumption that the open circuit voltage observed in the JV1Sun is the result of a single diode device.	- ∨ %
FF_0 - pFF	Difference between the ideal fill factor and the pseudo fill factor	%
G_0	Generation in equilibrium	cm^{-3}
G_L	Generation by light	cm^{-3}
I_{QTOT}	Collected current from the inversion layer	A
J_0	Saturation current density (not ideal diode)	A/cm^2
J_{01}	Base to emitter total saturation current density, $J_{0e}+J_{0b}$, ideal diode	A/cm^2
J_{02}	Base to emitter non ideal saturation current density	A/cm^2
J_{0b}	Saturation current density of emitter minority carrier towards the base	A/cm^2
J_{0c}	Saturation current density of collector minority carriers towards the base	A/cm^2
J_{0e}	Saturation current density of base minority carrier towards the emitter	A/cm^2
J_{0H}	Saturation current density of a local recombination site	A/cm^2
J_L	Photogenerated light at 1 sun intensity	A/cm^2
$J_{L\ total}$	Total photo-generated current potential	A/cm^2
J_{mpp}	Current density at maximum power point	A/cm^2
J_{nbW}	Current escaping the base from the back interface with the depletion region.	A/cm^2
J_{pass}	Recombination current	
J_s	Current density recombining at the surface	A/cm^2
J_{SC}	Short circuit current density	A/cm^2
J_ρ	Current entering the inversion channel, in ideal case corresponds to J_{nbW}	A/cm^2
K_1	Variable of the model in 5.3, correlates to injection in the base	V/μm^2
K_2	Variable of the model in 5.3, correlates with the system properties without injection	V/μm^2
k_B	Boltzmann constant	eV/K
L_{Dn}	Minority carrier diffusion length in p-type silicon	μm

L_{Dp}	Minority carrier diffusion length in p-type silicon	μm
L_m	Acceptable limit value of the extra term for the treatise of Appendix B.b	-
l_m	Acceptable limit value of the extra term for the treatise of Appendix B.b	-
L_p	Pitch between contacts, both for triangular and squared disposition	μm
m_1	Ideality factor of the first diode in a two diode model	-
m_2	Ideality factor of the second diode in a two diode model	-
m_{const}	Constant ideality factor over the whole bias range	-
m_e	Electron mass	g
m_e^*	Electron effective mass	g
m_H	Ideality factor of the diode in an additional branch introduced in the two diode model by Hernando {Hernando, Guitérrez et al. 1998}	-
m_h^*	Effective hole mass in silicon	g
m_{loc}	Local ideality factor	-
N_A	Acceptor density	cm^{-3}
n_{ARC}	Refractive index of the ARC	-
n_{CaTS}	Refractive index of the CaTS	-
N_D	Donor density	cm^{-3}
n_i	Intrinsic carrier density	cm^{-3}
n_s	Volume density of electrons at the surface	cm^{-3}
n_{Si}	Refractive index of the arc	-
n_{SI2N2O}	Refractive index of the stochiometric SI$_2$N$_2$O	
n_{SiriON}	Refractive index of the SiriON	-
n_t	SRH statistical term representing the density of electrons with $E_F = E_t$	cm^{-3}
N_t	Trap density	cm^{-3}
P	Function giving the position d of a potential level ψ_d	μm
pFF	Pseudo fill factor, calculated from open circuit voltages curves on sweeping photo-generated current	- V %
$pFF - FF$	Difference between the pseudo fill factor and the fill factor	%
p_s	Volume density of holes at the surface	cm^{-3}
p_t	SRH statistical term representing the density of holes with $E_F = E_t$	cm^{-3}
p_{test}	Probability of the diametrical event of the tested assumption	-
q	Electron charge	C
Q_f	Fixed charges in the dielectric	cm^{-2}
Q_{it}	Charges trapped in interface states	cm^{-2}
Q_{SC}	Amount of charges accumulated at the silicon surface to equilibrate external loads (potential or ionic).	C/cm^2
Q_{SC}	Surface net charges in the semiconductor	C/cm^2
R_0	Thermal equilibrium recombination	cm^{-3}
r_0	Contact radius exactly equal to a.	μm
R_H	Resistance limiting the recombination of a single spot	Ω cm^2
r_{HP}	Half distance between two contacts	μm
R_s	Series resistance in the one and two diode model - area weighted	Ω cm^2
R_{sFront}	Series resistance in the one and two diode model - area weighted, front component	Ω cm^2
R_{shB}	Shunting of the rear cathode to the anode (collector-base) - area weighted	Ω cm^2
R_{shF}	Shunting of the front cathode to the anode (emitter-base) - area weighted	Ω cm^2
R_{spread}	Spreading resistance component of a dimension limited contact to an infinite bulk.	Ω
$R_{spread-F}$	Spreading resistance component of a density of dimension limited contacts to an infinite bulk.	Ω
R_{sRear}	Series resistance in the one and two diode model - area weighted, rear	Ω cm^2

	component	
S	Surface recombination velocity	cm/s
S_{AlBSF}	Surface recombination velocity of minority carriers facing a surface alloyed with Aluminium	cm/s
S_{eff}	Effective surface recombination velocity, recombination velocity present at an imaginary surface inside the bulk where the field is close to zero resulting from an inhomogeneous S	cm/s
S_{it}	Surface recombination velocity of the interface	cm/s
S_{met}	Surface recombination velocity at a metalized interface	cm/s
S_{pass}	Surface recombination velocity at a passivated interface	cm/s
S_{SC}	Surface recombination velocity due to recombination in a superficial space charge region (SCR)	cm/s
T	Working/measuring temperature	
T_{FFO}	Peak firing temperature	°C
U_{Aug}	Net recombination due to multi-particle Auger phenomena	cm^{-3}
U_i	Generic net recombination	cm^{-3}
U_{rad}	Net recombination due to radiative phenomena	cm^{-3}
U_{scr}	Net recombination, in the space charge region	cm^2/s
U_{SRHb}	Net recombination due to trap assisted phenomena in the bulk	cm^{-3}
U_{SRHdr}	Net recombination due to trap assisted phenomena in depletion regions	cm^{-3}
U_{SRHit}	Net surface recombination, at the interface	cm^2/s
U_{SRHs}	Net recombination due to trap assisted phenomena at the surface	cm^{-3}
$V[r]$	Potential on the rear of the cell, related to the description of 5.3	
V_{front}	Potential on the front of the cell, related to the description of 5.3	
V_{loss}	V_{OC} drop from the beginning to the end of a degradation process	V
V_{mpp}	Voltage at the maximum power point	V
v_{oc}	V_{OC} normalised to the thermal voltage V_{th}	-
V_{OC}	Open circuit voltage	V
V_{OC0}	Measured V_{OC} at the end of a degradation process	V
V_{ocRear}	Maximum voltage of a rear floating junction under illumination	V
V_{th}	Thermal voltage, equal to k_B*T/q	V
v_{therm}	Thermal velocity	cm/s
W	Thickness of the substrate	μm
W_{base}	Thickness of the base, depletion regions at the surfaces are excluded	μm
α_c	Absorption coefficient	cm^{-1}
β_m	Transformation function used in the model in 5.3	V
Δn	Injection level	cm^{-3}
ε_{Si}	Absolute permittivity of Silicon	-
η_m	Transformation function used in the model in 5.3	cm^2
λ_a	Absorption length	μm
λ_m	Wavelegth of a monochromatic Illumination	nm
λ_{Si}	Optimal absorption wavelength for silicon	nm
ρ	Substrate/bulk resistivity	Ω·cm
ρ_{charge}	Charge density	C/cm^{-3}
ρ_{sheet}	Sheet resistance of emitters or inversion layers	Ω/sq.
σ	Substrate/bulk conductivity	(Ω·cm)$^{-1}$
σ_n	Capture cross section of electron	cm^{-2}
σ_p	Capture cross section of holes	cm^{-2}
τ_b	Bulk lifetime	μs
τ_{bulk}	Minority carrier lifetime in the bulk, injection dependent.	μs
$\tau_{bulk\ Kerr}$	Injection dependent parametrical fit of bulk lifetime, from Kerr {Kerr 2002}	μs

τ_{DEG}	Degradation time constant	day
τ_{eff}	Effective lifetime	µs
τ_{n0}	Electrons capture time constant	µs
τ_{p0}	Holes capture time constant	µs
ψ	Potential	V
ψ_d	Potential at a depth $z=d$.	V
ψ_{surf}	Surface potential, defined as the difference between Fermi level in the bulk and at the surface	V

C.b *Acronyms*

Acronym	Brief Description
4PP	4 Point Probe resistance measurement, explained in appendix A.a.I
Al-BSF	Aluminium back surface field
AM1.5g	Standardisation of the light intensity on earth {IEC 2008}. Also referred to as 1 Sun
ARC	Anti-reflecting Coating
a-Si	Amorphous silicon
BNG	Band-gap Narrowing
BSF	Back surface field
CaTS	Capping on Top Surface
CB	Conduction band
Cz-Si	Growing method for Si mono-crystals, from inventor's name: J. Czochralski
DRM	Depletion Region Modulation, change of the depletion width as consequence of injection
DSBC	Double sided buried contact, solar cell structure investigated by **Sunpower**.
EHP	Electron-hole pair
EQE	External quantum efficiency
FCA	Free Carrier Absorption
FFO	Fast Firing Oven, equipment used for RTP of solar cells, peak temperature is indicated by T_{FFO}
FGA	Forming Gas Annealing, an incombustible mixture of hydrogen (in low %) and nitrogen.
FGA	Forming gas annealing
FJP	Floating junction passivation
FZ-Si	Cz Si purified with a Float Zone technique
hli	High level injection
IQE	Internal quantum efficiency
JV1Sun	Measure of current density over a sweep of voltage when a cell is exposed to an illumination of 1 Sun {IEC 2008}.
JVDark	Measure of current density over a sweep of voltage in dark
LBSF	Local back surface field
LFC	Laser Fired Contact, Local melting of aluminium and silicon that recrystallise in a ohmic contact
LID	Light Induced Degradation, light induced recombination sites in Boron doped material
LIP	Light Induced Plating, light assisted galvanisation of front side contacts.
lli	Low-level injection refers to an injection in semiconductor which creates a density of carriers lower than the material doping.
Log	Natural logarithm
mc-Si	Multi-crystalline silicon, referred to wafers having with several mm of extension
MPP	Maximum power point, the product of the potential and current in this working point of the cell is maximum. In this point the *FF* is calculated.
PC1D	PC simulation tool by Paul A. Basore and Donald A. Clugston {Clugston and Basore 1997}
PECVD	Plasma enhanced chemical vapour deposition
PERC	Passivated Emitter and Rear Concept/Cell {Blakers, Zhao et al. 1989}.

PERF   Passivated emitter and rear floating
PSG   Phosphor Silicate Glass, by-product of silicon oxidation surfaces in P rich ambient
PVTEC   Photovoltaik technologie evaluationscenter / photovoltaic technology evaluations centre
QSSPC   Quasi-Steady State Photo-conductance Decay
RCA   Radio Corporation America, a company that first developed and made public a wet chemical sequence to clean silicon surfaces.
RLRC   Resistance-limited Recombination Centres
RT   Room temperature (300 k ~25 °c)
RTP   Rapid Thermal Processing, processing that exploit short exposure of device to high temperature to achieve the execution of metallurgical or chemical reactions
S/N   Signal to noise ratio, used to qualify measurements, *or oral information exchanges, like discussions and conferences.*
SC1   Standard Cleaning 1, first part of a RCA cleaning sequence, designed to remove organic particles from the silicon surface
SC2   Standard Cleaning 2, second part of a RCA cleaning sequence, designed to remove metal particles from the silicon surface
SCR   Space charge region
SE   Stain Etching, see footnote on page 81
SEM   Scanning Electron Microscope
SiNTO SP   Passivation layer: Silicon Nitride capping a Thermal Oxide, Metallisation: Screen Print
SiNTOx   Passivation layer: Silicon Nitride capping a Thermal Oxide
SiN_x Amorphous silicon nitride
SiO_2 Stochiometric silicon oxide
SiO_x Amorphous silicon oxide
SiriON   Silicon rich oxynitride
SRH   Shockley – Read – Hall theory explaining the influence of trap levels on the recombination rate in semiconductors
SRI   Sheet resistance imaging
SRV   Surface recombination velocity, often used instead of *S*
SunsVoc   Measure of open circuit voltage over a sweep of illumination intensity, with few assumptions the measure can be converted in a JV1Sun curve where no series resistance gives contribution, {Sinton and Cuevas 2000}
TLM   Transfer Length Method, often misunderstood with Transmission Line Method
VB   Valence band

C.c   *Units*

This list helps the reader to understand which normalisation are used to display the numerical values, the indications to obtain the SI coherent derived unit are taken from {Taylor and Thompson 2008}

Symbol	Name	SI coherent derived unit
$\Omega \cdot cm$	Resistivity	V cm/A
$\Omega \cdot cm^2$	Resistance per area	V cm²/A
$\Omega/sq.$	Sheet resistance	V cm/(A cm)
ℓ	Litre	(dm)³

Appendix D Bibliography

D.a *Personal publications*

D.a.I As first author

Gautero, L., M. Hoffmann, et al. (2009). All-screen-printed 120-μm-thin large-area silicon solar cells applying dielectric rear passivation and laser-fired contacts reaching 18% efficiency. Proceedings of the 24th European Photovoltaic Solar Energy Conference, Hamburg, Germany.

Gautero, L., M. Hofmann, et al. (2009). All-screen-printed 120-μm-thin large-area silicon solar cells applying dielectric rear passivation and laser-fired contacts reaching 18% efficiency. Proceedings of the 34th IEEE Photovoltaic Specialists Conference, Philadelphia, USA.

Gautero, L., J. Rentsch, et al. (2008). Industrial approach for the deposition, through-vias wet opening and firing activation of a backside passivation layer applied on solar cells. Proceedings of the 23rd European Photovoltaic Solar Energy Conference, Valencia, Spain.

In preparation

Gautero, L., P. Saint-Cast, JM.Sallese, et al. (2010). Semianalytical calculation of injection distribution at depleted and inverted contacted surfaces

D.a.II As co-author

Alemán, M., N. Bay, et al. (2008). Industrially feasible front-side metallization based on ink-jet masking and nickel plating. Proceedings of the 23rd European Photovoltaic Solar Energy Conference, Valencia, Spain.

Biro, D., S. Mack, et al. (2009). Thermal oxidation as a key technology for high efficiency screen printed industrial silicon solar cells. Proceedings of the 34th IEEE Photovoltaic Specialists Conference, Philadelphia, USA.

Hofmann, M., D. Erath, et al. (2008). Industrial type CZ silicon solar cells with screen-printed fine line front contacts and passivated rear contacted by laser firing. Proceedings of the 23rd European Photovoltaic Solar Energy Conference, Valencia, Spain.

Hofmann, M., P. Saint-Cast, et al. (2009). Overview on crystalline silicon solar cells using PECVD rear passivation and laser-fired contacts. Proceedings of the 24th European Photovoltaic Solar Energy Conference, Hamburg, Germany.

John, J., G. Beaucarne, et al. (2009). A review on 5 years cell development within the european integrated project crystal clear. Proceedings of the 24th European Photovoltaic Solar Energy Conference, Hamburg, Germany.

Nekarda, J., S. Stumpp, et al. (2009). LFC on screen printed aluminium rear side metallization. Proceedings of the 24th European Photovoltaic Solar Energy Conference, Hamburg, Germany.

Rentsch, J., L. Gautero, et al. (2008). Single side etching - key technology for industrial high efficiency processing. Proceedings of the 23rd European Photovoltaic Solar Energy Conference, Valencia, Spain.

Rentsch, J., J. Seiffe, et al. (2008). Plasma cluster processing for advanced solar cell manufacturing. Proceedings of the 23rd European Photovoltaic Solar Energy Conference, Valencia, Spain.

Seiffe, J., L. Weiss, et al. (2008). Alternative rear surface passivation for industrial cell production. Proceedings of the 23rd European Photovoltaic Solar Energy Conference, Valencia, Spain.

D.b   *Publications referenced in the work (alphabetically ordered)*

Aberle, A. G., P. P. Altermatt, et al. (1995). "Limiting loss mechanisms in 23% efficient silicon solar cells." Journal of Applied Physics **77**(7): 3491-504.

Aberle, A. G., S. Glunz, et al. (1992). "Impact of illumination level and oxide parameters on Shockley-Read-Hall recombination at the Si-SiO₂ interface." Journal of Applied Physics **71**(9): 4422-31.

Aberle, A. G., S. Glunz, et al. (1993). "Field effect passivation of high efficiency silicon solar cells." Solar Energy Materials and Solar Cells **29**(2): 175-82.

Aberle, A. G., S. J. Robinson, et al. (1993). "High-efficiency silicon solar cells: fill factor limitations and non-ideal diode behaviour due to voltage-dependent rear surface recombination velocity." Progress in Photovoltaics: Research and Applications **1**(2): 133-43.

Aberle, G. A. (1991). Untersuchung zur Oberflächenpassivierung von hocheffizienten Silicium-Solarzellen. Fakultät Für Physik. Freiburg, Universität Freiburg**:** 213.

Agostinelli, G., P. Choulat, et al. (2005). Screen printed large area crystalline silicon solar cells on thin substrates. Proceedings of the 20th European Photovoltaic Solar Energy Conference, Barcelona, Spain.

Agostinelli, G., P. Choulat, et al. (2006). Rear surface passivation for industrial solar cells on thin substrates. Proceedings of the 4th World Conference on Photovoltaic Energy Conversion, Waikoloa, Hawaii, USA.

Agostinelli, G., J. Szlufcick, et al. (2005). Local contact structures for industrial perc-type solar cells. Proceedings of the 20th European Photovoltaic Solar Energy Conference, Barcelona, Spain.

Alemán, M., N. Bay, et al. (2008). Industrially feasible front-side metallization based on ink-jet masking and nickel plating. Proceedings of the 23rd European Photovoltaic Solar Energy Conference, Valencia, Spain.

Altermatt, P., S. Steingrube, et al. (2009). Highly predictive modelling of entire Si solar cells for industrial applications. Proceeding of the 24th European Photovoltaic Solar Energy Conference, Hamburg.

Altermatt, P. P., G. Heiser, et al. (1996). "Rear surface passivation of high-efficiency silicon solar cells by a floating junction." Journal of Applied Physics **80**(6): 3574-86.

Bardeen, J. (1947). "Surface States and Rectification at a Metal Semi-Conductor Contact." Physical Review **71**(10): 717.

Basore, P. A. (1993). Extended spectral analysis of internal quantum efficiency. Proceedings of the 23rd IEEE Photovoltaic Specialists Conference, Louisville, Kentucky, USA, IEEE; New York, NY, USA.

Beaucarne, G., P. Choulat, et al. (2008). Etching, texturing and surface decoupling for the next generation of Si solar cells. Photovoltaics International Journal. **1**.

Beaucarne, G., P. Choulat, et al. (2008). Local Al-Alloyed Contacts for next generation Si solar cells. Workshop on Metallization for Crystalline Silicon Solar Cells, Utrecht.

Becquerel, E. (1839). Mémoire sur les effets électriques produits sous l'influence des rayons solaires. Mémoires lus.

Berger, H. H. (1972). "Contact resistance and contact resistivity." Journal of the Electrochemical Society **119**(4): 507-14.

Biro, D., S. Mack, et al. (2009). Thermal oxidation as a key technology for high efficiency screen printed industrial silicon solar cells. Photovoltaic Specialists Conference (PVSC), 2009 34th IEEE.

Biro, D., R. Preu, et al. (2006). PV-Tec: Photovoltaic technology evaluation center - design and implementation of a production research unit. Proceedings of the 21st European Photovoltaic Solar Energy Conference, Dresden, Germany.

Blakers, A. W., J. Zhao, et al. (1989). 23% efficient silicon solar cell. Proceedings of the 9th European Photovoltaic Solar Energy Conference, Freiburg, Germany.

Born, M. and E. Wolf (1959). Principles of optics. New York, Pergamon Press.

BP (2010). BP Statistical Review of World Energy June 2010. Statistical Review of World Energy. Energy Academy andCentre for Economic Reform and Transformation. Edimburgh, Heriot-Watt University**:** 50.

Breitenstein, O., P. Altermatt, et al. (2006). Interpretation of the commonly observed I-V characteristics of C-Si cells having ideality factor larger than two. Proceedings of the 4th World Conference on Photovoltaic Energy Conversion, Waikoloa, Hawaii, USA.

Breitenstein, O., M. Langenkamp, et al. (2000). Localization of shunts across the floating junction of DSBC solar cells by lock-in thermography. Proceedings of the 28th IEEE Photovoltaics Specialists Conference, Anchorage, Alaska, USA.

Burgers, A. R. (2004). "Fitting flash test curves with ECN's IV curve fitting program IVFIT." Proc. 14 th int. PVSEC Bangkok.

Chambre, P. L. (1952). "On the Solution of the Poisson-Boltzmann Equation with Application to the Theory of Thermal Explosions." The Journal of Chemical Physics **20**(11): 1795-1797.

Chen, F., I. Romijn, et al. (2007). Relationship between PECVD silicon nitride film composition and surface and edge passivation. Proceedings of the 22nd European Photovoltaic Solar Energy Conference, Milan, Italy.

Chen, J. T. C. and D. B. Dimitrov (2007). System and methods of measuring semiconductor sheet resistivity and junction leakage current. United States: 8.

Chen, J. T. C. and R. S. Muller (1974). "Carrier mobilities at weakly inverted silicon surfaces." Journal of Applied Physics **45**(2): 828-834.

Chen, Y. and J. Luo (2001). "A comparative study of double-gate and surrounding-gate MOSFETs in strong inversion and accumulation using an analytical model." Integration **1**(2): 6.

Clement, F. (2009). Die metal wrap through solarzelle- entwicklung und charakterisierung. Fakultät für Angewandte Wissenschaften. Freiburg, Universität Freiburg: 1-256.

Clugston, D. A. and P. A. Basore (1997). "Modelling free-carrier absorption in solar cells." Progress in Photovoltaics: Research and Applications **5**(4): 229-36.

Clugston, D. A. and P. A. Basore (1997). PC1D version 5: 32-bit solar cell modeling on personal computers. Proceedings of the 26th IEEE Photovoltaic Specialists Conference, Anaheim, California, USA, IEEE; New York, NY, USA.

Cornagliotti, E., X. Kang, et al. (2008). Photo-Conductivity Lock-In: A Qualitative and Quantitative Analysis of Measurement Results. 23rd European Photovoltaic Solar Energy Conference and Exhibition, Valencia, Spain.

Cousins, P. J. and J. E. Cotter (2006). "Minimizing lifetime degradation associated with thermal oxidation of upright randomly textured silicon surfaces." Solar Energy Materials & Solar Cells **90**(2): 228-40.

Cousins, P. J., N. B. Mason, et al. (2006). "Loss analysis of DSBC solar cells on FZ(B), MCZ(B), CZ(Ga), and CZ(B) wafers." Transactions on Electron Devices **63**(4): 797-807.

Cousins, P. J., D. H. Neuhaus, et al. (2004). "Experimental verification of the effect of depletion-region modulation on photoconductance lifetime measurements." Journal of Applied Physics **95**(4): 1854-8.

Cox, R. H. and H. Strack (1967). "Ohmic contacts for GaAs devices." Solid-State Electronics **10**(12): 1213-1214, IN7-IN8, 1215-1218.

Cuevas, A. and D. Macdonald (2004). "Measuring and interpreting the lifetime of silicon wafers." Solar Energy **76**(1-3): 255-62.

Cuevas, A., R. Sinton, et al. (2008). QSS Cell Model.

Cuevas, A. and R. A. Sinton (1997). "Prediction of the open-circuit voltage of solar cells from the steady-state photoconductance." Progress in Photovoltaics: Research and Applications **5**: 79-90.

Dauwe, S. (2004). Low-temperature surface passivation of crystalline silicon and its application to the rear side of solar cells. Fachbereich Physik. Hannover, Universität Hannover: 156.

de Wolf, S., G. Agostinelli, et al. (2005). "Influence of stoichiometry of direct plasma-enhanced chmeical vapor deposited SiNx films and silicon substrate surface roughness on surface passivation." Journal of Applied Physics **97**.

del Canizo, C., G. del Coso, et al. (2009). "Crystalline silicon solar module technology: towards the 1€ per watt-peak goal." Progress in Photovoltaics: Research and Applications **17**: 199-209.

Dross, F., A. Milhe, et al. (2008). Stress-Induced Lift-Off Method for kerf-loss-free wafering of ultra-thin (~50μm) crystalline Si wafers. Photovoltaic Specialists Conference, 2008. PVSC '08. 33rd IEEE.

Ebers, J. J. and J. L. Moll (1954). "Large-Signal behavior of junction transistors." Proceedings of the I R E.

Fischer, B. (2003). Loss analysis of crystalline silicon solar cells using photoconductance and quantum efficiency measurements. Fachbereich Physik. Konstanz, Universität Konstanz: 198.

Gatz, S., H. Plagwitz, et al. (2008). "Thermal stability of amorphous silicon/silicon nitride stacks for passivating crystalline silicon solar cells." Applied Physics Letters **93**(17): 173502-3.

Gautero, L., M. Hoffmann, et al. (2009). All-screen-printed 120-μm-thin large-area silicon solar cells applying dielectric rear passivation and laser-fired contacts reaching 18% efficiency. Proceedings of the 24th European Photovoltaic Solar Energy Conference, Hamburg, Germany.

Gautero, L., M. Hofmann, et al. (2009). All-screen-printed 120-μm-thin large-area silicon solar cells applying dielectric rear passivation and laser-fired contacts reaching 18% efficiency. Proceedings of the 34th IEEE Photovoltaic Specialists Conference, Philadelphia, USA.

Gautero, L., J. Rentsch, et al. (2008). Industrial approach for the deposition, through-vias wet opening and firing activation of a backside passivation layer applied on solar cells. Proceedings of the 23rd European Photovoltaic Solar Energy Conference, Valencia, Spain.

Ghannam, M. Y. (1991). A new n⁺pn⁺ structure with back side floating junction for high efficiency silicon solar cells. Proceedings of the 22nd IEEE Photovoltaic Specialists Conference, Las Vegas, Nevada, USA.

Girisch, R., R. P. Mertens, et al. (1982). Limitations of the open circuit voltage of induced junction silicon solar cells due to surface recombination.

Girisch, R. B. M., R. P. Mertens, et al. (1988). "Determination of Si-SiO₂ interface recombination parameters using a gate-controlled point-junction diode under illumination." IEEE Transactions on Electron Devices **35**(2): 203-22.

Glunz, S. W. (1995). Ladungsträgerrekombination in Silicium und Siliciumsolarzellen. Fakultät für Physik. Freiburg, Universität Freiburg**:** 166.

Glunz, S. W., J. Nekarda, et al. (2007). Analyzing back contacts of silicon solar cells by suns-voc-measurements at high illumination densities. Proceedings of the 22nd European Photovoltaic Solar Energy Conference Milan, Italy.

Godlewski, M. P., C. R. Baraona, et al. (1973). Low-high junction theory applied to solar cells. Proceedings of the 10th IEEE Photovoltaic Specialists Conference, Palo Alto, California, USA.

Gore, A. (2006). An Inconvenient Truth. The Planetary Emergency of Global Warming and What We Can Do About It, Rodale Press, Emmaus, Pennsylvania (United States).

Granek, F. (2010). High-efficiency back-contact back-junction silicon solar cells. Technische Fakultät Freiburg, Albert-Ludwigs-Universität Freiburg im Breisgau. **Doktorgrades der Technischen Fakultät** 209.

Grasso, F. S., L. Gautero, et al. (2010). Characterisation of Aluminium Screen-Printed Local Contacts. 2nd Workshop on Metallization for Crystalline Silicon Solar Cells, Konstanz.

Green, M. A. (1986). High efficiency silicon solar cells. Aedermannsdorf, Trans Tech SA,Aedermannsdorf, Switzerland.

Green, M. A. (1986). Solar cells: operating principles, technology and system applications. Kensington, UNSW.

Green, M. A. (1995). Silicon solar cells: Advanced principles and practice. Sydney, NSW, Centre for Photovoltaic Devises and Systems UNSW.

Green, M. A. (1998). Solar cells: operating principles, technology and system applications. Kensington, The University of New South Wales.

Grote, D., M. Hermle, et al. (2008). Analyzing the effects of laterally varying emitter sheet resistance in combination with contact resistance. Proceedings of the 23rd European Photovoltaic Solar Energy Conference, Valencia, Spain.

Haase, F., J. Müller, et al. (2010). Effects of metallization in the semiconductor part - insights from experiments and device modeling. 2nd Workshop on Metallization for Crystalline Silicon Solar Cells, Konstanz.

Hall, R. N. and T. J. Soltys (1980). Polka Dot Solar Cell. Proceedings of the 14th IEEE Photovoltaic Specialists Conference, San Diego, California, USA.

Henley, F., A. Lamm, et al. (2008). Direct film transfer (dft) technology for kerf-free silicon wafering. 23rd European Photovoltaic Solar Energy Conference and Exhibition, Valencia, Spain, WIP.

Herguth, A, et al. (2008). Investigations on the Long Time Behavior of the Metastable Boron-Oxygen Complex in Crystalline Silicon. London, ROYAUME-UNI, Wiley.

Hermle, M. (2008). Analyse neuartiger Silizium- und III-V-Solarzellen mittels Simulation und Experiment. Fachbereich für Physik. Freiburg im Breisgau, Universität Konstanz**:** 198.

Hernando, F., R. Guitérrez, et al. (1998). Humps, a surface damage explanation. Proceedings of the 2nd World Conference on Photovoltaic Energy Conversion, Vienna, Austria.

Hofmann, M. (2008). Rear surface conditioning and passivation for locally contacted crystalline silicon solar cells. Fachbereich Physik. Freiburg im Breisgau, Universität Konstanz**:** 273.

Hofmann, M., D. Erath, et al. (2008). Industrial type CZ silicon solar cells with screen-printed fine line front contacts and passivated rear contacted by laser firing. Proceedings of the 23rd European Photovoltaic Solar Energy Conference, Valencia, Spain.

Honsberg, C. B., K. R. McIntosh, et al. (1997). Characterisation and measurement of silicon solar cells with floating junction passivation. Proceedings of the 26th IEEE Photovoltaic Specialists Conference, Anaheim, California, USA, IEEE; New York, NY, USA.

Hörteis, M. (2009). Fine-line printed contacts on crystalline silicon solar cells. Fachbereich Physik. Konstanz, Universität Konstanz**:** 229.

Huster, F. (2005). Aluminium-back surface field: bow investigation and elimination. Proceedings of the 20th European Photovoltaic Solar Energy Conference, Barcelona, Spain.

Huster, F. (2005). Investigation of the alloying process of screen printed aluminium pastes for the BSF formation on silicon solar cells. Proceedings of the 20th European Photovoltaic Solar Energy Conference, Barcelona, Spain.

Huster, F. and G. Schubert (2005). ECV doping profile measurements of aluminium alloyed back surface fields. Proceedings of the 20th European Photovoltaic Solar Energy Conference, Barcelona, Spain.

IEC (2008). Measurement principles for terrestrial photovoltaic (PV) solar devices with reference spectral irradiance data Photovoltaic devices—Part 3. T. C. 82. Geneva, Switzerland, International Electrotechnical Commission. **International Standard**.

Isenberg, J., M. C. Schubert, et al. (2005). Sheet resistance imaging (SRI) - A contactless and spatially resolved method for the determination of doping inhomogeneities. Proceedings of the 20th European Photovoltaic Solar Energy Conference, Barcelona, Spain.

Jaeger, K., P. Roth, et al. (1992). <u>Thin crystalline silicon 100mm x 100mm MIS-inversion layer solar cells with bifacial sensitivity</u>. Proceedings of the 11th European Photovoltaic Solar Energy Conference, Montreux, Switzerland.

Janz, S., P. Voisin, et al. (2009). <u>Photonic Crystals as Rear-Side Diffusers and Reflectors for High Efficiency Silicon Solar Cells</u>. 24th European Photovoltaic Solar Energy Conference, Hamburg, Germany, WIP.

Jones, S. W. (2008). Diffusion in Silicon, IC Knowledge LLC. **18:** 21.

Kaes, M., G. Hahn, et al. (2007). "Progress in high efficiency processing of EFG silicon solar cells." <u>22nd EC PVSEC</u>: 897.

Kaminski, A., J. J. Marchand, et al. (1998). "Non ideal dark I-V curves behavior of silicon solar cells." <u>Solar Energy Materials and Solar Cells</u> **51**: 221-31.

Kern, W. and D. Puotinen (1970). "Cleaning solutions based on hydrogen peroxide for use in silicon semiconductor technology." <u>RCA Review</u> **31**: 187.

Kerr, M. J. (2002). Surface, emitter and bulk recombination in silicon and development of silicon nitride passivated solar cells, Australian National University. **PhD:** 228.

Kerr, M. J. and A. Cuevas (2002). "General parameterization of Auger recombination in crystalline silicon." <u>Journal of Applied Physics</u> **91**(4): 2473-80.

Kerr, M. J., A. Cuevas, et al. (2003). "Limiting efficiency of crystalline silicon solar cells due to Coulomb-enhanced Auger recombination." <u>Progress in Photovoltaics: Research and Applications</u> **11**(2): 97-104.

Kingston, R. H. and S. F. Neustadter (1955). "Calculation of the Space Charge, Electric Field, and Free Carrier Concentration at the Surface of a Semiconductor." <u>Journal of Applied Physics</u> **26**(6): 718-720.

Kleppmann, W. (2008). <u>Taschenbuch Versuchsplanung: Produkte und Prozesse optimieren</u>, Hanser Verlag.

Korte, L. (2006). Die elektronische Struktur des amorph-kristallinen Silizium-Heterostruktur-Kontakts. <u>Fachbereich Physik</u>. Marburg/Lahn, Universität Marburg**:** 174.

Kränzl, A., A. Schneider, et al. (2004). "Different aspects of back-surface field (BSF) formation for thin multi-crystalline silicon wafers." <u>Asian Journal on Energy and Environment</u> **5**(4): 275-83.

Kray, D. (2004). Hocheffiziente Solarzellenstrukturen für kristallines Silicium-Material industrieller Qualität. <u>Fakultät für Physik</u>. Konstanz, Universität Konstanz**:** 152.

Kray, D., J. Dicker, et al. (2001). <u>20% efficient flexible silicon solar cells</u>. Proceedings of the 17th European Photovoltaic Solar Energy Conference, Munich, Germany, WIP-Munich and ETA-Florence.

Kray, D., H. Kampwerth, et al. (2004). <u>Comprehensive experimental study on the performance of very thin laser-fired high-efficiency solar cells</u>. Proceedings of the 19th European Photovoltaic Solar Energy Conference, Paris, France, WIP-Munich, ETA-Florence.

Kray, D. and K. R. McIntosh (2009). "Analysis of ultrathin high-efficiency silicon solar cells." <u>Physica Status Solidi A</u> **206**(7): 1647-54.

Lemke, A., H. Furtwängler, et al. (2007). <u>Thermal oxidation and wet chemical cleaning of silicon wafers for industrial solar cell production</u>. Proceedings of the 22nd European Photovoltaic Solar Energy Conference, Milan, Italy.

Lölgen, P., C. Leguijt, et al. (1994). <u>Surface passivation by a floating junction</u>. Proceedings of the 12th European Photovoltaic Solar Energy Conference, Amsterdam, The Netherlands, H.S. Stephens & Associates, Bedford, UK, 1994.

Lynch, D. (2009) "Winning the global race for solar silicon." <u>JOM Journal of the Minerals, Metals and Materials Society</u> **Volume**, 41-48 DOI: 10.1007/s11837-009-0166-8

Masetti, G., M. Severi, et al. (1983). "Modeling of carrier mobility against carrier concentration in arsenic-, phosphorus-, and boron-doped silicon." <u>IEEE Transactions on Electron Devices</u> **30**(7): 764-9.

McIntosh, K. R. (2001). Lumps, humps and bumps: Three detrimental effects in the current-voltage curve of silicon solar cells. <u>Centre for Photovoltaic Engineering</u>. Sydney, Australia, University of New South Wales**:** 180.

McIntosh, K. R., P. P. Altermatt, et al. (2000). <u>Depletion-region recombination in silicon solar cells: when does m_{DR} = 2?</u> Proceedings of the 16th European Photovoltaic Solar Energy Conference, Glasgow, UK, James & James, London, UK, 2000.

McIntosh, K. R., G. Boonprakaikaew, et al. (2000). "An experimental technique to measure the shunt resistance across a local region of a floating junction." <u>Solar Energy Materials & Solar Cells</u> **64**: 353-61.

McIntosh, K. R. and C. B. Honsberg (1999). "A new technique for characterizing floating-junction-passivated solar cells from their dark IV curves." <u>Progress in Photovoltaics: Research and Applications</u> **7**(5): 363-78.

McIntosh, K. R., N. C. Shaw, et al. (2004). <u>Light trapping in sunpower's A-300 solar cells</u>. Proceedings of the 19th European Photovoltaic Solar Energy Conference, Paris, France.

McIntosh, K. R. and R. A. Sinton (2008). <u>Uncertainty in photoconductance lifetime measurements that use an inductive-coil detector</u>. Proceedings of the 23rd European Photovoltaic Solar Energy Conference, Valencia, Spain.

McKibben, B., M. Nijhuis, et al. (2009). Energy for Tomorrow. <u>National Geographic</u>.

Mette, A. (2007). New concepts for front side metallization of industrial silicon solar cells. Fakultät für Angewandte Wissenschaften. Freiburg, Universität Freiburg**:** 231.

Metz, B., O. R. Davidson, et al. (2007). "Climate Change 2007: Mitigation. Contribution of Working Group III to the Fourth Assessment Report of the Intergovernmental Panel on Climate Change." Cambridge University Press, Cambridge, UK and New York, NY. Retrieved June **26**.

Mingirulli, N. (2009). Fabrication and Characterisation of Emitter-Wrap-Through Solar Cells. Fachbereich Physik. Konstanz, Universität Konstanz. **Doktor der Naturwissenschaften (Dr. rer. nat.):** 144.

Mönch, W. (2004). Electronic properties of semiconductor interfaces. Duisburg, Germany, Springer-Verlag Berlin, Heidelberg, New York.

Morikawa, H., D. Niinobe, et al. (2010). "Processes for over 18.5% high-efficiency multi-crystalline silicon solar cell." Current Applied Physics **10**(2, Supplement 1): S210-S214.

Mueller, T., S. Schwertheim, et al. (2008). "High quality passivation for heterojunction solar cells by hydrogenated amorphous silicon suboxide films." APPLIED PHYSICS LETTERS **92**: 033504.

Münzer, K. A., K. T. Holdermann, et al. (1999). "Thin monocrystalline silicon solar cells." IEEE Transactions on Electron Devices **46**(10): 2055-61.

Nekarda, J., D. Reinwand, et al. (2009). Industrial pvd metallization for high efficiency crystalline silicon solar cells. Proceedings of the 34th IEEE Photovoltaic Specialists Conference, Philadelphia.

Nekarda, J., S. Stumpp, et al. (2009). LFC on screen printed aluminium rear side metallization. Proceedings of the 24th European Photovoltaic Solar Energy Conference, Hamburg, Germany.

Nekarda, J. F., L. Gautero, et al. (2009). LFC on screen printed Aluminium rear side metallization. 24th European Photovoltaic Solar Energy Conference and Exhibition, Hamburg, Germany

Neuhaus, D. H., P. J. Cousins, et al. (2003). Trapping and junction-related perturbations of the effective excess carrier lifetime. Proceedings of the 1st World Conference on Photovoltaic Energy Conversion Osaka, Japan.

Nicollian, E. H. and J. R. Brews (1982). MOS Physics and Technology. New York, Wiley.

Niinobe, D., H. Morikawa, et al. (2010). "Large-size multi-crystalline silicon solar cells with honeycomb textured surface and point-contacted rear toward industrial production." Solar Energy Materials and Solar Cells **In Press, Corrected Proof**.

Pankove, J. I. (1975). Optical processes in semiconductors, Dover publications.

Pernau, T., G. Hahn, et al. (2001). Bulk hydrogenation of mc silicon materials and solar cells: from research lab to PV-industry. Proceedings of the 17th European Photovoltaic Solar Energy Conference, Munich, Germany, WIP-Munich and ETA-Florence.

Pinchas, H., R. Yosef, et al. (2004). "Exposure to extremely high concentrations of carbon dioxide: A clinical description of a mass casualty incident." Annals of emergency medicine **43**(2): 196-199.

Podewils, C. (2009). A proton axe for thin silicon. Photon International. **April 2009:** 116.

Popovich, V. A., M. Janssen, et al. (2009). Microstructure and mechanical properties of aluminum back contact layers. Proceedings of the 24th European Photovoltaic Solar Energy Conference, Hamburg, Germany.

Prajapati, V., E. Cornagliotti, et al. (2009). High efficiency industrial silicon solar cells on silicon MONO2 TM cast material using dielectric passivation and local BSF, Hamburg.

Preu, R. (2000). Innovative Produktionstechnologien für kristalline Silicium-Solarzellen. Fachbereich Elektrotechnik. Freiburg, FernUniversität Hagen**:** 228.

Preu, R., D. Biro, et al. (2006). The status of silicon solar cell production technology development at fraunhofer ise. Proceedings of the 4th World Conference on Photovoltaic Energy Conversion, Waikoloa, Hawaii, USA.

Pysch, D., A. Mette, et al. (2009). "Comprehensive analysis of advanced solar cell contacts consisting of printed fine-line seed layers thickened by silver plating." Progress in Photovoltaics: Research and Applications **17**: 101-14.

Rauer, M., C. Schmiga, et al. (2009). Passivation of screen-printed aluminium-alloyed emitters for back junction n-type silicon solar cells

Proceedings of the 24th European Photovoltaic Solar Energy Conference, Hamburg, Germany.

Rein, S. (2005). Lifetime spectroscopy: a method of defect characterization in silicon for photovoltaic applications, Springer Verlag.

Rein, S., T. Rehrl, et al. (2001). Electrical and thermal properties of the metastable defect in boron-doped Czochralski silicon (Cz-Si). Proceedings of the 17th European Photovoltaic Solar Energy Conference, Munich, Germany.

Rentsch, J. (2005). Trockentechnologien zur Herstellung von kristallinen Siliziumsolarzellen. Freiburg, Albert-Ludwigs Universität, Freiburg**:** 253.

Rentsch, J., L. Gautero, et al. (2008). Single side etching - key technology for industrial high efficiency processing. Proceedings of the 23rd European Photovoltaic Solar Energy Conference, Valencia, Spain.

Rentsch, J., J. Seiffe, et al. (2008). Plasma cluster processing for advanced solar cell manufacturing. Proceedings of the 23rd European Photovoltaic Solar Energy Conference, Valencia, Spain.

Ritter, F. E. and L. J. Schooler (2002). "The learning curve."

Robbins, H. and B. Schwartz (1961). "Chemical etching of silicon I." J. Electrochem. Soc **106**: 505-508.

Robinson, S. J., A. G. Aberle, et al. (1994). "Recombination saturation effects in silicon solar cells." IEEE Transactions on Electron Devices **41**(9): 1556-69.

Rohlfing, M., P. Krüger, et al. (1993). "Quasiparticle band-structure calculations for C, Si, Ge, GaAs, and SiC using Gaussian-orbital basis sets." Physical Review B **48**(24): 17791.

Romijn, I. G., W. J. Soppe, et al. (2005). Passivation mc-Si solar cells using SiN_x:H: from magic to physics. Proceedings of the 20th European Photovoltaic Solar Energy Conference, Barcelona, Spain.

Roth, T., J. Hohl-Ebinger, et al. (2008). Improving the accuracy of suns-VOC measurements using spectral mismatch correction. Proceedings of the 33rd IEEE Photovoltaic Specialists Conference, San Diego, USA.

Runyan, W. R. (1975). Semiconductor measurements and instrumentation. Tokyo, McGraw-Hill Companies.

Saint-Cast, P., A. Wolf, et al. (2010). to be published.

Schmidt, J., A. G. Aberle, et al. (1997). Investigation of carrier lifetime instabilities in Cz-grown silicon. Proceedings of the 26th IEEE Photovoltaic Specialists Conference, Anaheim, California, USA, IEEE; New York, NY, USA.

Schmidt, J., A. Cuevas, et al. (2001). Fill factor limitations and non-ideal diode behaviour of Czochralski silicon solar cells due to light-induced recombination centres. Proceedings of the 17th European Photovoltaic Solar Energy Conference, Munich, Germany, WIP-Munich and ETA-Florence.

Schmidt, J., A. Cuevas, et al. (2001). "Impact of light-induced recombination centres on the current-voltage characteristic of Czochralski silicon solar cells." Progress in Photovoltaics: Research and Applications **9**(4): 249-55.

Schneiderlöchner, E., A. Grohe, et al. (2005). Status and advancement on transferring the laser-fired contact technology to screen-printed silicon solar cells. Proceedings of the 20th European Photovoltaic Solar Energy Conference, Barcelona, Spain.

Schneiderlöchner, E., R. Preu, et al. (2002). "Laser-fired rear contacts for crystalline silicon solar cells." Progress in Photovoltaics: Research and Applications **10**: 29-34.

Schroder, D. K. (2001). "Surface voltage and surface photovoltage: history, theory and applications." Measurement Science and Technology **12**(3): R16-31.

Schroder, D. K., R. N. Thomas, et al. (1978). "Free carrier absorption in silicon." IEEE Transactions on Electron Devices **ED-25**(2): 254-61.

Schubert, G. (2006). Thick film metallisation of crystalline silicon solar cells Konstanz, Universität Konstanz**:** 142.

Schultz, O., M. Hofmann, et al. (2005). Silicon oxide / silicon nitride stack systems for 20% efficient silicon solar cells. Proceedings of the 31st IEEE Photovoltaic Specialists Conference, Orlando, Florida, USA.

Schumann, M., M. Singh, et al. (2009). Reaching a Kerf Loss below 100 µm by Optimizing the Relation Between Wire Thickness and Abraxive Size for Multi-Wire Sawing. 24th European Solar Energy Conference and Exhibition, Hamburg, Germany.

Seiffe, J., L. Gautero, et al. (2010). "Surface Passivation of crystalline silicon by PECVD double layers of silicon-rich silicon oxynitride and silicon nitride." To be published.

Seiffe, J., L. Weiss, et al. (2008). Alternative rear surface passivation for industrial cell production. Proceedings of the 23rd European Photovoltaic Solar Energy Conference, Valencia, Spain.

Seren, S., M. Kaes, et al. "Efficiency potential of RGS silicon from current R&D production." Proc. 22nd EU PVSEC, Milan 2007 **854**.

Shockley, W. and W. T. Read (1952). "Statistics of the Recombinations of Holes and Electrons." Physical Review **87**(5): 835.

Sinton, R. A. and A. Cuevas (2000). A quasi-steady-state open-circuit voltage method for solar cell characterization. Proceedings of the 16th European Photovoltaic Solar Energy Conference, Glasgow, UK, James & James, London, UK, 2000.

Solmi, S., A. Parisini, et al. (1996). "Dopant and carrier concentration in Si in equilibrium with monoclinic SiP precipitates." Physical Review B **53**(12): 7836-41.

Specht, J., D. Biro, et al. (2008). Using hotmelt-inkjet as a structuring method for higherefficiency industrial silicon solar cells. Proceedings of the International Conference on Digital Printing Technologies and Digital Fabrication, Pittsburgh, PA, USA.

Spitz, M., U. Belledin, et al. (2007). Fast inductive inline measurement of the emitter sheet resistance in industrial solar cell fabrication. Proceedings of the 22nd European Photovoltaic Solar Energy Conference, Milan, Italy.

Sproul, A. B. (1994). "Dimensionless solution of the equation describing the effect of surface recombination on carrier decay in semiconductors." Journal of Applied Physics **76**(5): 2851-4.

Sritharathikhun, J., C. Banerjee, et al. (2007). "Surface passivation of crystalline and polycrystalline silicon using hydrogenated amorphous silicon oxide film." Japanese Journal of Applied Physics **46**(6A): 3296-3300.

Sunpower (2010). SunPower Announces New World Record Solar Cell Efficiency, PR Newswire.

Sze, S. M. and K. K. Ng (2006). Physics of semiconductor devices, Wiley-Blackwell.

Taylor, B. N. and A. Thompson (2008). The international system of units (SI). Gaithersburg, US Dept. of Commerce, Technology Administration, National Institute of Standards and Technology.

Trupke, T. and R. A. Bardos (2005). Photoluminescence: a surprisingly sensitive lifetime technique. Proceedings of the 31st IEEE Photovoltaic Specialists Conference, Orlando, Florida, USA.

Trupke, T., R. A. Bardos, et al. (2006). "Photoluminescence imaging of silicon wafers." Applied Physics Letters **89**(044107): 1-3.

Uruena, A., J. John, et al. (2009). Local Al-Alloyed Contact for Next Generetion Si Solar Cells. 24th European Photovoltaic Solar Energy Conference, Hamburg.

van der Heide, A. S. H., J. H. Bultman, et al. (2001). Contact resistances measured using the corescan: relations with cell processing. Proceedings of the 17th European Photovoltaic Solar Energy Conference, Munich, Germany.

Van der Pauw, L. J. (1958). "A method of measuring the resistivity and Hall coefficient on lamellae of arbitrary shape." Philips Technical Review **20**(8): 220–224.

Van Zeghbroeck, B. (2007). Principles of Semiconductor Devices. B. Van Zeghbroeck.

Volta, A. G. A. A. (1782). Lettere sullo svolgimento dell'elettricità nell'evaporazione. Bosscha Corr., Letter, . original manuscript in Harlem Soc. Holl. Sc.

Warabisako, T., K. Matsukuma, et al. (1993). Bifacial multicrystalline silicon solar cells. Proceedings of the 23rd IEEE Photovoltaic Specialists Conference, Louisville, Kentucky, USA, IEEE; New York, NY, USA.

Wenham, S. R., S. J. Robinson, et al. (1994). Rear surface effects in high efficiency silicon solar cells. Proceedings of the 1st World Conference on Photovoltaic Energy Conversion, Hawaii, USA, IEEE; New York, NY, USA.

Winderbaum, S., I. Romijn, et al. (2006). MW PECVD A-SI$_X$N$_Y$H$_Z$: the road to optimum silicon nitride coatings. Proceedings of the 21st European Photovoltaic Solar Energy Conference, Dresden, Germany.

Wiseman, R. (2010). 59 seconds: think a little, change a lot, Pan.

Wolf, A., S. Mack, et al. (2009). The SiNTO Process: Utilizing a SiNX Anti-Reflection Layer for Emitter Masking During Thermal Oxidation. Proceedings of the 34th IEEE Photovoltaics Specialists Conference (PVSEC), Philadelphia, PA.

Würfel, P. (2005). Physics of solar cells: from principles to new concepts, Vch Verlagsgesellschaft Mbh.

Xu, Y.-N. and W. Y. Ching (1995). "Electronic structure and optical properties of alpha and beta phases of silicon nitride, silicon oxynitride, and with comparison to silicon dioxide." Physical Review B **51**(24): 17379.

Yu, A. Y. C. (1970). "Electron tunneling and contact resistance of metal-silicon contact barriers." Solid-State Electronics **13**(2): 239-247.

Ze-Qiang, Y., H. B. Harrison, et al. (1994). High-quality sub-5-nm oxynitride dielectric films grown on silicon in a nitric oxide ambient using rapid thermal processing, SPIE.

Zimmer, M., A. Oltersdorf, et al. (2007). In-line analysis and process control in wet chemical texturing processes. Proceedings of the 22nd European Photovoltaic Solar Energy Conference, Milan, Italy.

D.c   *Acknowledgements*

Appendix E   Curriculum Vitae

♦ *Work experience*

4/2007 - now	Doctoral research project, <u>Fraunhofer ISE</u> Institut für Solare Energiesysteme, Freiburg, (Germany) Working contract for the development of a doctoral research theme on industrial realisation of solar cells based on bulk silicon.
10/2006 - 2/2007	Research assistant, <u>ECN</u> Energieonderzoek Centrum Nederland, Petten, (The Netherlands) Develop measuring concepts to quickly certify the efficiency of different kind of PV modules.
3 - 9/2006	Master thesis, "Electrical (mathematical) modelling of a solar module using back-contacted photovoltaic cells", <u>ECN</u> Master thesis on PV modules, development of tool for analysis and synthesis.
7 - 10/2005	Internship, "T shape contacts", <u>IMEC</u> Interuniversity MicroElectronics Center, Leuven, (Belgium) Research program about 3D interconnects, Improvement of interlayer via contacts.
07 - 09/2003	Visiting pre-doctoral fellow, "Growth and characterisation of nitride semiconductor", <u>NU</u> Northwestern University, Department of electrical and computer engineering, <u>CQD</u> (Center for Quantum Devices), Evanston IL (USA) First experience with laboratories' instrumentations and optical semiconductor devices.

Education

4/2007 - now	Doctoral program in Microsystems and Microelectronics at <u>EPFL</u> "Ecole Polytecnique Fédérale de Lausanne" The research lead during the work at ISE Fraunhofer is collected and reported to the University.
9/2004 - 9/2006	Master of Science degree: "Nanotech, Intenational Master on micro and nanotechnologies": final mark 110/110 cum Laude. Courses are held at <u>TOP</u> Politecnico di Torino, 3rd Faculty, University school of I.T. Engineering, Torino (Italy), <u>INPG</u> Institut National Polytecnique de Grenoble and <u>EPFL</u>. A newborn international master adopting english as common language and experiencing three types of knowledge spreading on a relatively recent field of the IT world.
9/2001 - 7/2004	Bachelor Degree "LIFI, French-Italian double diploma in I.T. engineering": final mark 105/110. Courses had been held at top and INPG (faculty <u>ENSPG</u>) "Ecole National Superieure de Physique de Grenoble, Grenoble (France) The courses have shifted over a large view on the Information Technology field, starting from electronic and programming the first and second year with a final plunge in telecommunications and material physics.

Languages and Skills

English	Fluent: Several long stays in different anglophone countries, and multiple working experiences based on written and spoken english communications
French	Fluent: Attended in France and in Switzerland university courses for more than a year
German	Fluent: Worked in Germany for more than 3 years
Italian	Mother tongue
Software	CAD for analysis and sinthesis for electronic purpose(PSpice, VHDL, FemLab, MatLab), knowledge of various office suites (<u>LATEX2</u>, MS Office 2003), Programming languages (C/C++, 'Java', Wolfram Mathematica), CAD (Originlab Origin, Xfig, AutoCAD)
General	<u>Touch typing</u> (average 37 WPM), <u>Speed reading</u> (average 350 WPM)

Extra curricular activities and personal

Travels, various expressions of art, sports, entertaining friends.

I agree to the treatment and collection of my personal data according to D. Lgs. 30 giugno 2003 n.196 (Testo Unico Privacy) of the Italian Privacy Code.

Freiburg, Sunday, 24 October 2010